

Thermally altered microbialites of the terminal Ediacaran Dengying
Formation, Sichuan Basin, South China

By
© 2020

Adrienne Seiden
B.S., Tulane University, 2016

Submitted to the graduate degree program in Geology and the Graduate Faculty of the
University of Kansas in partial fulfillment of the requirements
for the degree of Master of Science.

Chair: Alison Olcott

Jennifer A. Roberts

Randy Stotler

Date Defended: 11 May 2020

The thesis committee for Adrienne Seiden certifies that this is the approved version of the following thesis:

Thermally altered microbialites of the terminal Ediacaran Dengying Formation, Sichuan Basin, South China

Chair: Alison Olcott

Date Approved: 15 May 2020

Abstract

In the Sichuan Basin and surrounding areas, the terminal Ediacaran Dengying Formation hosts diverse microbialite forms. Interest in this formation has mainly centered around oil and gas reservoir development, but recent research aims to characterize its paleobiology via petrographic and molecular fossil analysis. This study aims to characterize the paleobiology and diagenetic history of samples from the Moxi area (central basin), Micangshan Uplift (NW basin margin), and Dabashan thrust belt (N basin margin). Moxi samples are all core samples of Dengying Member 4. Michangshan and Dabashan samples are from outcrop; the Micangshan samples are from Dengying Member 3 and the Dabashan samples are from unknown members of the Dengying Formation and underlying the Doushantuo Formation. All samples were photographed using a petrographic microscope in plane-polarized light (transmitted and reflected), with crossed nicols and in blue-violet light. Hydrocarbon geochemistry and extractable biomarkers were isolated from outcrop samples and characterized.

Microbialites in the core samples are mostly stromatolitic and occasionally thrombolitic in texture, while outcrop microbialites are oncolitic and thrombolitic. All samples show putative evidence of hydrothermal alteration and tectonic strain. Extractable biomarkers were limited to a low concentration of n-alkanes with an abnormal distribution of chain lengths. Kerogen geochemical data confirms the samples' low amenability to biomarker extraction; the maximum hydrogen index (HI) is 51 for all Dengying samples and among the samples with acceptable total organic carbon (> 0.5%) the maximum HI is only 6. Based on mass spectra and free oil measurements, extracted hydrocarbons can be attributed to contamination. The Dengying Formation represents a microbially-dominated system that preserves no convincing evidence of eukaryotes, despite the presence of putative metazoans in nearby sections of the Doushantuo.

Extraction of saturated alkanes produced poor yields in the outcrop samples and would likely not be feasible for the core samples based on petrographic analysis showing thermal and tectonic stress. Literature has drawn mixed conclusions about the Dengying Formation's potential as a source of geologic biomarkers; this study provides more evidence that the Dengying is unlikely to yield any significant biomarker information.

Acknowledgments

Thank you to my advisor, Dr. Alison Olcott and to the rest of my committee, Dr. Jennifer Roberts and Dr. Randy Stotler. This research was supported by a grant from PetroChina.

Table of Contents

Abstract.....	iii
Acknowledgments.....	v
List of Figures.....	viii
List of Tables	xii
Introduction.....	1
Background.....	1
Microbialites	2
Neoproterozoic biomarkers.....	3
Geologic setting	6
Methods.....	13
Sample collection.....	13
Biomarker extraction	14
Microscopy	14
Geochemical analysis	15
Results.....	16
Biomarkers.....	16
Geochemistry	17
Petrography.....	20
Discussion.....	46
Microbial evidence	46
Paleoecological interpretation.....	51
Hydrothermal alteration.....	51

Tectonic stress.....	52
Biomarkers.....	54
Reliability of geochemical data	59
Conclusions.....	60
Future work.....	61
References.....	63
Appendix A: Thin sections	76
Dengying Member 4, central uplift, well core (ordered by depth).....	76
Dengying Member 3 (dn ³), Micang mountains (106°32'E, 32°26'N), outcrop.....	94
Doushantuo & Dengying (unknown member), Daba Mountain thrust belt (108°35'E, 31°58N'), outcrop	102
Doushantuo, Daba Mountain thrust belt, (108°46'E, 31°56'N), outcrop.....	108
Appendix B: GC-MS data.....	113
Appendix C: Biomarker reference table	116
Appendix D: Supplemental geochemical data statistics	119
Appendix D: Comparison of biomarker analysis methods.....	120

List of Figures

Figure 1. Map of field site and sample localities	8
Figure 2. Stratigraphic profile for core sites	10
Figure 3. Profile of Ediacaran strata at the Yangba outcrop.....	11
Figure 4. Gas Chromatography/Mass Spectrometry data from outcrop sample 1b.....	17
Figure 5. Mass spectrograms of Sample 1b.....	17
Figure 6. Stromatolite morphology.....	27
Figure 7. Microstructure of Sample 25.....	28
Figure 8. Microtexture of Sample 29.....	29
Figure 9. Microtexture of Sample 28.....	30
Figure 10. Microtexture of Sample 26.....	32
Figure 11. Microtexture of samples 24, 22 and 20	33
Figure 12. Microtexture of samples 19 and 30	35
Figure 13. Microstructure of thrombolites and oncoids in Sample 2a-f.....	38
Figure 14. Sample group 1.....	39
Figure 15. Sample 1f.....	39
Figure 16. Hydrothermal sulfide minerals	41
Figure 17. Oxidized sulfide minerals.....	41
Figure 18. Hydrothermal minerals (non-sulfides)	44
Figure 19. Deformation microstructures.....	45
Figure 20. Comparison of oncolite in dn^2 and dn^3	47
Figure 21. Comparison of dn^3 and Beck Spring dolomite.....	47
Figure 22. Comparison of aggregated coccooid laminations.....	49

Figure 23. Microbialite morphology with depth.....	50
Figure 24. Pseudo-Van Krevelen diagram.....	54
Figure 25. Hydrogen Index vs Total Organic Carbon (TOC).....	56
Figure 26. Venn diagram comparing biomarkers extracted from Dengying carbonate.	57
Figure 27. Hydrogen Index vs Free Oil	59
Figure 28. Sample 18	76
Figure 29. Sample 17	77
Figure 30. Sample 25x	78
Figure 31. Sample 25y	79
Figure 32. Sample 24	80
Figure 33. Sample 22x	81
Figure 34. Sample 22y	81
Figure 35. Sample 20	82
Figure 36. Sample 19x	83
Figure 37. Sample 19y	84
Figure 38. Sample 16	84
Figure 39. Sample 14	85
Figure 40. Sample 29x	86
Figure 41. Sample 29y	87
Figure 42. Sample 15	88
Figure 43. Sample 30	89
Figure 44. Sample 13	89
Figure 45. Sample 28x	91

Figure 46. Sample 28y	91
Figure 47. Sample 27	92
Figure 48. Sample 31	93
Figure 49. Sample 26	93
Figure 50. Sample 1a	94
Figure 51. Sample 1b	95
Figure 52. Sample 1c	96
Figure 53. Sample 1d	96
Figure 54. Sample 1e	97
Figure 55. Sample 1f	98
Figure 56. Sample 2a	99
Figure 57. Sample 2b	99
Figure 58. Sample 2c	100
Figure 59. Sample 2d	101
Figure 60. Sample 2e	101
Figure 61. Sample 2f	102
Figure 62. Sample 4a	103
Figure 63. Sample 5a	103
Figure 64. Sample 5b	104
Figure 65. Sample 5c	105
Figure 66. Sample 6a	105
Figure 67. Sample 7a	106
Figure 68. Sample 8a	107

Figure 69. Sample 9a	107
Figure 70. Sample 9b	108
Figure 71. Sample 9c	108
Figure 72. Sample 10(a-c).....	109
Figure 73. Sample 11(a-b)	110
Figure 74. Sample 12a	111
Figure 75. Sample 12b	112
Figure 76. Chromatogram and n-alkane trace for Sample 1a	113
Figure 77. Chromatogram and n-alkane trace for Sample 1c	114
Figure 78. Chromatogram and n-alkane trace for Sample 1d.....	114
Figure 79. Chromatogram and n-Alkane trace for Sample 1f	115

List of Tables

Table 1. Sample locations	13
Table 2. Geochemical data of outcrop samples.....	Error! Bookmark not defined.
Table 3. Statistics on geochemical data.	20
Table 4. Description and photos of slides with microbial features	Error! Bookmark not defined.
Table 5. Descriptions and photos of microbialite samples from dn ³ of MCS.	355
Table 6. Properties of sulfide minerals identified in Dengying samples.	Error! Bookmark not defined.2
Table 7. Biomarkers identified in Neoproterozoic hydrocarbons	1166
Table 8. Statistics on T _{max} , Oxygen Index (OI), S1, S2, S3, and Free Oil by outcrop site ..	11919
Table 9. Comparison of methods used in other studies on the Dengying Formation	1200
Table 10. Comparison of GCMS instrumentation used in other studies.....	1200

Introduction

The lack of biomarker information from Precambrian microbialites limits our understanding of the conditions leading up to the Cambrian explosion of metazoan biodiversity and the coincident decline of stromatolites. Ancient molecular fossils previously labeled as syngenetic have been called into question (e.g., Brocks et al., 2003; French, 2015), casting doubt on the utility of biomarker analysis as a tool for paleoenvironmental reconstruction in the Precambrian. Petrographic analysis of microbialites, however, enables some paleoenvironmental interpretation; morphology and microtexture offer evidence of biogenicity (Awramik & Grey, 2005), accretion mechanism (Tosti & Riding, 2017), sea level change (Patranabis Deb, et al., 2018) and other metrics.

Researchers have attempted to identify biomarkers from the Dengying Formation (Li et al, 2006; Duda et al., 2014a, b; Fan et al., 1999; Chen, Z. et al., 2017) at various locations with limited results. The question remains whether stromatolites from the Ediacaran that have been subjected to significant thermal stress could still contain syngenetic extractable biomarkers. Alternatively, in the absence of biomarkers, what information can we glean about the microbes that built these microbialites and their involvement in lithification?

This study investigates the feasibility of biomarker study on outcrop from the Dengying Formation in the Micangshan uplift with implications for analysis of Dengying Formation core from the central Sichuan Basin. Both outcrop and core samples were subjects of petrographic inquiry into the activity of syndepositional microorganisms, and the nature of post depositional alteration. Results have implications for the biogenicity of microbial textures in the Dengying and microbial influence on precipitation of dolomite in the Precambrian.

Background

The Ediacaran (635 – 541 Ma) Period separates the Cryogenian “Snowball Earth” and the Cambrian “Explosion” of biodiversity. During this time, Earth experienced a dramatic increase in temperature (Hoffman & Schrag, 2002; Evans, 2003). Rapid oxygenation of the oceans and increased nutrient input throughout the Ediacaran facilitated diversification of multicellular eukaryotes and the development of biomineralization (Gould, 1989; Shields, 2007).

Microbialites

“Microbialite” is a term encompassing several forms of microbially-influenced sedimentary deposits including (but not limited to) stromatolites, thrombolites and oncolites. Stromatolites, which are laminated structures resulting from the lithification of microbial mats, originate approximately 3.5 Ga and are regarded as the earliest evidence of life on Earth (Schopf, 2006). The mats responsible for stromatolites are complex algal-bacterial and sometimes fungal (Riding, 2000) communities. Mat microbes self-organize by metabolism, with phototrophs at the top of the mat and heterotrophs at the bottom. Byproducts of each layers’ metabolism help sustain the other layers. Several of these metabolisms create localized alkalinity (the so-called Alkalinity Engine) which induces mineral precipitation in a process called organomineralization (Dupraz et al., 2009; Konhauser & Riding, 2012). Stromatolites from the Archean through the Paleoproterozoic are exclusively produced in this way via in situ organomineralization (Grotzinger & Knoll, 1999).

Around the Mesoproterozoic (1.6 Ga – 1 Ga), there is a steep drop in atmospheric CO₂ concentration. This in turn shifts the CaCO₃ saturation state in seawater to favor carbonate precipitation in the water column, rather than on the seafloor (Knoll & Swett, 1990; Riding, 2006). Carbonate in the water column nucleates on planktonic cyanobacteria, producing white clouds of carbonate mud called whittings (Riding, 2006). Neoproterozoic stromatolites grow by

trapping this carbonate sediment and growing through it, driven by the need to access sunlight. Mat metabolisms are still capable of inducing in situ carbonate minerals, but grain-trapping and binding becomes the dominant accretion mechanism from the Neoproterozoic onward (Grotzinger & Knoll, 1999). The middle Neoproterozoic (ca. 700 Ma) also contains the first thrombolites, which are microbialites with clotted structure (Aitken & Narbonne, 1989; Halverson, 2007).

The structure and microfabric of microbialites is dependent on several factors, including but not limited to accretion mechanism (agglutinated or precipitated), sedimentation rate, wave energy, biology of the community, and timing of lithification (Riding, 2000, 2011; Harwood & Sumner, 2011; Mata et al., 2012). In precipitated microbialites, mat microbes can become calcified, leaving behind microfossils (Riding, 2011b, Van Lith et al., 2003). Dead microbes may also become pyritized, especially sulfate-reducing bacteria (SRB) (Cosmidis et al., 2013; Konhauser & Riding, 2012; Folk, 2005). In the absence of microfossils, it can be difficult to confirm the biogenicity of stromatolites since several abiotic formations mimic their structure (Riding, 2011a). Under the microscope, some good indicators of microbial origin include clotted peloidal texture, irregular contact between dark and light layers, signs of mat cohesion, and certain crystal morphologies (i.e., nanospherules, needles, dumbbells, smooth rhombs—Dupraz et al., 2009). Diagnostic biomarkers of mat-forming organisms offer corroboratory evidence for biogenicity (Allen et al., 2010; Greinert et al., 2002); however, extractable biomarkers are rare in Proterozoic stromatolites.

Neoproterozoic biomarkers

Geologic biomarkers, also known as molecular fossils, are stable hydrocarbon skeletons of biosynthesized lipids that can be extracted from sedimentary rock and used to identify the taxa

present at deposition and the depositional environment. Molecular fossils have been extracted from sedimentary rocks as old as 1.6 billion years (Summons et al., 1988) and under appropriate diagenetic conditions there are several biomarkers that could help elucidate the paleoenvironment of the Dengying Formation. Biomarker evidence can diagnose anoxia, hypersalinity or photic zone euxinia (Summons & Walter, 1990; Grice et al., 1998; Kenig et al., 1995; Koopmans et al., 1996; Grice et al., 1996; Gaines et al., 2009). Additionally, methanotrophic and methanogenic Archaea produce diagnostic biomarkers (Gaines et al., 2009; Bian et al., 2001; Thiel et al., 1999; Elvert et al., 1999; Schouten et al., 1997). These organisms would be expected to dwell in a shallow marine dolomite platform, since many models of dolomitization are associated with methane release (Mazzullo, 2000; Meister, 2018). Sulfate-reducing bacteria (SRB), also considered facilitators of dolomite precipitation (Vasconcelos, et al., 1995; Warthmann, et al., 2000), are more difficult to diagnose. However, C_{15} and C_{15} *iso-*, *anteiso-* and mid-chain branched fatty acids as well as mono-O-alkyl glycerol ethers are considered moderately specific evidence for SRB (Tosti et al., 2014; Heindel et al., 2010, 2012; Gaines et al., 2009) and would be even more convincing if found alongside framboidal pyrite. Cyanobacteria, which are common mat organisms, may also produce diagnostic biomarkers (Summons et al., 1999; Kenig et al., 1995), although this remains under debate (Rashby et al., 2007). While there is no biomarker for metazoans, steranes are diagnostic of eukaryotes (Brocks & Summons, 2003), and the sterane 24-isopropylcholestane is exclusive to demosponges (one of the oldest metazoans) in pre-Silurian rocks (Gold et al., 2016).

Biomarkers are useful for interpreting paleobiology in Precambrian rocks because most organisms living during this period lack hard parts that fossilize. However, like physical fossils, molecular fossils still require specific depositional and diagenetic conditions to be preserved.

Biomarkers are particularly sensitive to post-depositional heating, as covalent bonds in the hydrocarbon skeleton will break at temperatures exceeding 220°C under otherwise ideal conditions (Brocks & Summons, 2003). The maximum temperature for preservation of biomarkers varies and depends on other environmental conditions. For example, transition metals and sulfur radicals are known to catalyze degradation of hydrocarbons to methane (Mango & Hightower, 1997; Lewan, 1998). Maximum survivable temperature is also positively correlated to the rate of heating (Waples, 2000). Contamination by younger material (migrated hydrocarbons or anthropogenic surface contaminants) is common, especially in permeable rock and exposed outcrops (Brocks et al., 2008; Duda et al., 2014a).

Geologic setting

The Sichuan Basin is a large lowland basin (230,000 km²) in western Sichuan and eastern Chongqing provinces, near the northwestern margin of the Yangtze Plate. The basin is the center of complex tectonic activity, enclosed by mountain ranges on all sides, namely the Longmen Mountains to the west, the Micang Mountains to the north and the Daba Mountains to the northeast (Fig. 1). The basin and surrounding areas are popular study sites for the Dengying Formation (ca. 551-541 Ma) and underlying Doushantuo Formation (ca. 635-551 Ma) (Cui et al., 2019; Condon et al., 2005).

The Doushantuo Formation is well-known for its assemblages of so-called Ediacaran biota, including some of the earliest multicellular eukaryotes. The Weng'an, Wenghui and Miaohu fossil lagerstätte in northern Guizhou are the subject of extensive paleoecological research (e.g., Cunningham et al., 2017; Xiao et al., 2014; Wang et al., 2016; Zhao et al., 2004). The controversial fossil *Megasphaera* (Xiao et al., 2014) is believed by some to be the oldest fossilized animal embryo. The younger Dengying Formation also contains several well-preserved fossil assemblages (Tang et al., 2008; Chen et al., 2014; Xiao et al., 2005; Hua et al., 2007; Cai et al., 2010, 2019), some of which include biomineralizing metazoans and even “Cambrian-style” small shelly fossils (Cai et al., 2019). These Lagerstätte are all >50 km outside the margins of the Sichuan Basin. Inside the basin and at its margins, the Dengying Formation is dominated by diverse microbialites (Li et al., 2013; Song et al., 2018).

In the Sichuan Basin, the Dengying Formation is divided into four Members: dn¹, dn², dn³ and dn⁴. The Doushantuo Formation is also divided into Members 1 through 4, which will be referred to here as do¹, do², do³ and do⁴. Core samples used in this study are from dn⁴ in the Moxi area (i.e., the northern portion of the Gaoshiti-Moxi area), central Sichuan Basin. The cores were

drilled from two sites, at (105°26'E, 30°28'N) and (105°47'E, 30°31'N). In this area, the Dengying Formation is up to 1400 m thick with 2500 – 6000 m burial depth (Feng et al., 2017). Outcrop site 1 is in the Micang mountain (Micangshan) uplift, NE Sichuan Province (106°32'E, 32°26'N); samples from this site are all dn³. The location of outcrop site 1 coincides with the location of Yangba on maps from other studies (e.g., Wang et al., 2019; Zhu et al., 2017; Zhou et al., 2017), but it could also be Qiaoting (Liu et al., 2019) or Dalianghui (Zhou et al., 2017). Sites 2 and 3 are in the Daba mountain (Dabashan) thrust belt in northern Chongqing Province near Chengkou (108°35'E, 31°58'N and 108°46'E, 31°56'N). Samples from site 2 are from unknown members of the Doushantuo and Dengying Formations. Samples from site 3 are all Doushantuo (unknown member). In the text, MCS refers to outcrop site 1, DBS-1 is outcrop site 2, and DBS-2 is outcrop site 3.

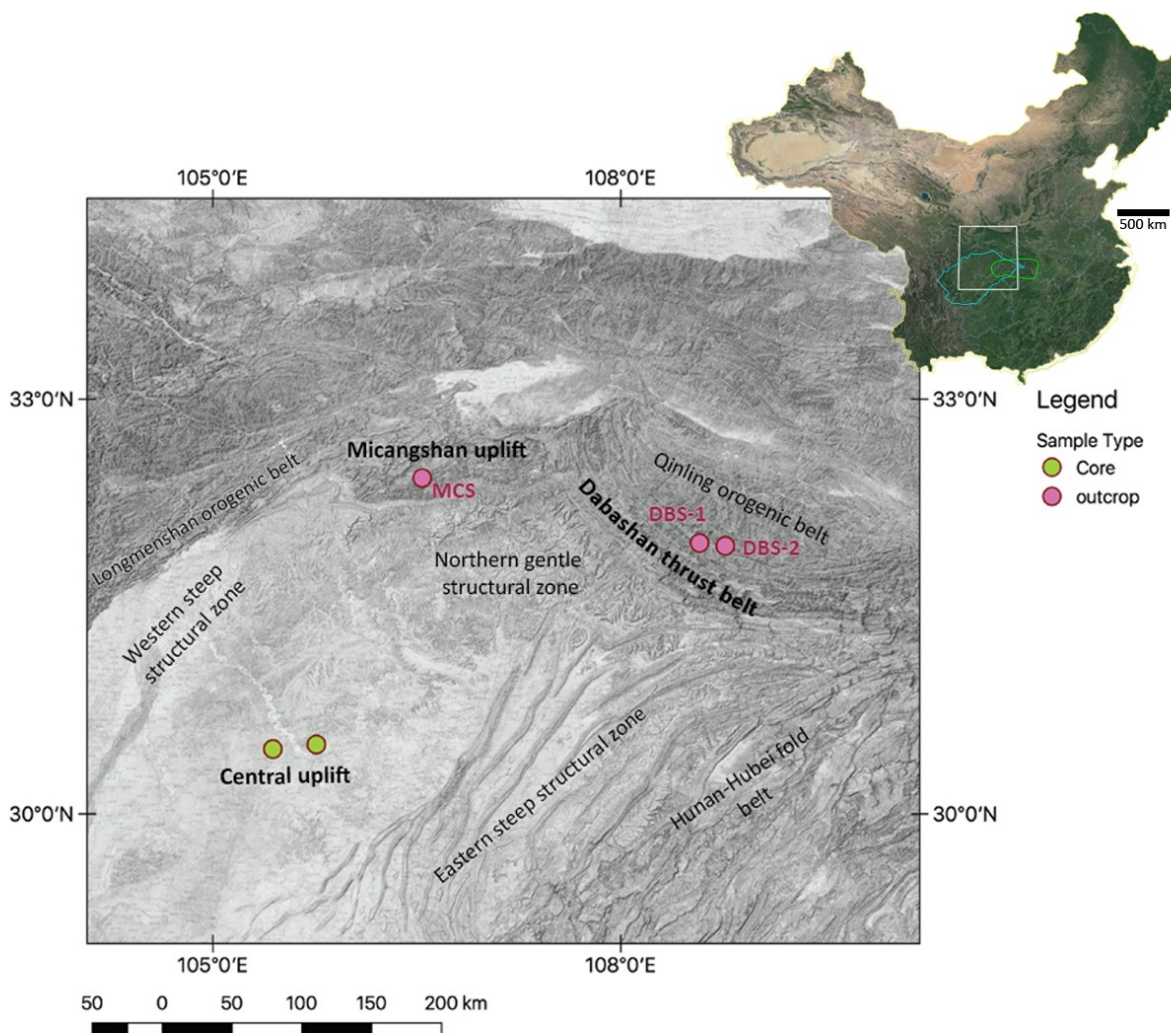


Figure 1. Map of field site and sample localities. The map of China is from a screenshot of Google Earth; the white box marks the study area represented by the larger map at left; the cyan outline (west) represents the Sichuan Basin and the green outline (right) represents the Yangtze Gorges area. On the zoomed in map, green circles are core sites and pink circles are outcrop sites.

The Doushantuo Formation overlies glacial tillite deposits from the Marinoan glaciation: the Chengjiang Formation in the central basin (Jiang et al., 2016), and the Nantuo Formation in the Daba mountain thrust belt (Wang et al., 2019). In the Micang mountain uplift, do^4 overlies the Shangliang Formation, consisting of marble and volcanic rock (Wang et al., 2019). Where do^1 is present, it consists of thin (~5 - 10 m) cap carbonate deposited during glacial retreat (Li et al., 2016; Xiao et al., 2017; Gregory et al., 2017) interbedded with volcanic ash (Gregory et al.,

2017). During the deposition of $do^2 - do^4$, DBS-1 and DBS-2 were on the margin of the Chengkou sag (Wang et al., 2019), also known as the Chengkou rift (Liu et al., 2019), where the environment progressed from shallow in do^2 to deep continental shelf-basin by do^3 (Wang et al., 2019). do^4 consists of organic-rich black shale capped by an ash bed (Gregory et al., 2017). In the central basin and the Micang mountain uplift $do^1 - do^3$ are missing. At the core sites do^4 consists of a shallow marine shale bed and littoral interbedded sandstone siltstone and mudstone capped by dolomicrite (Chen, Y. et al., 2017, Figure 2). At MCS, do^4 facies evolve from foreshore to lagoon to backshore (Wang et al., 2019, Fig. 3).

The Dengying Formation is mainly gray dolomite, with some shale-mudstone layers during transgressive intervals and microbial features during regressions (Figure 2, Fig. 3; Chen, Y. et al., 2017; Song et al., 2018). All members of the Dengying Formation are present at the 3 localities. During this interval, sea level cycled between transgressive (dn^1 and dn^3) and regressive (dn^2 and dn^4). The Deyang-Anyue rift (N-S) was opening just East of the core sites (Zhou et al., 2017; Chen, Y. et al., 2017), and DBS-1 and 2 were situated in the Wanyuan-Dazhu (Zhao et al., 2017) AKA Chengkou (Liu et al., 2019) rift (NW-SE). The new rifts created more platform margin beach environments (Gu et al., 2016), which served as habitat for microbial mats and reefs. DBS-1 and -2 were in the slope between the paleoplatform and the surrounding basin; MCS was on the platform margin (Zhou et al., 2017). By dn^4 , the core sites were situated on the margin of the Deyang-Anyue rift.

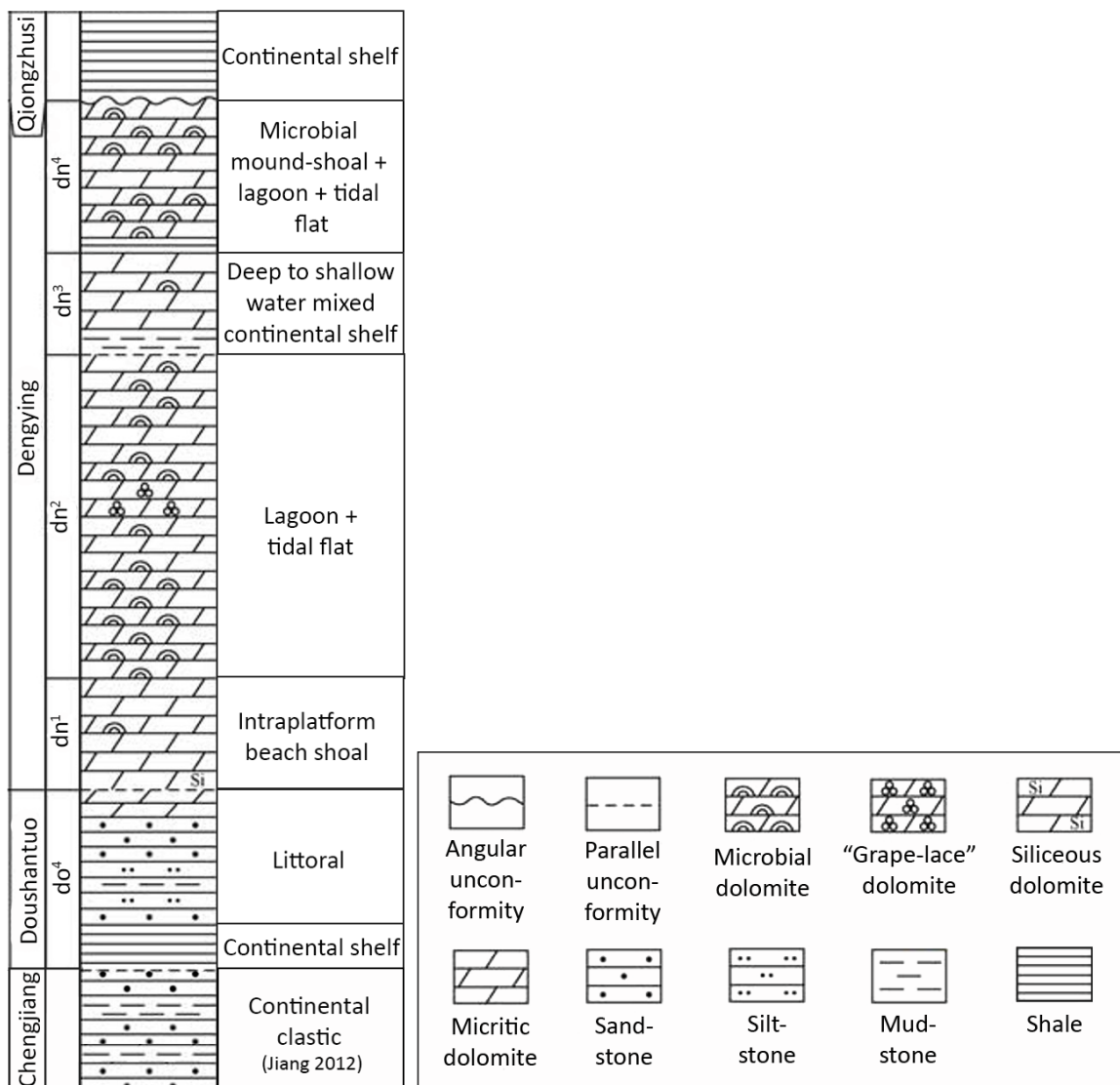


Figure 2. Stratigraphic profile for core sites (Moxi area), based on Chen, Y. et al. (2017), Jiang et al. (2016) and Jiang et al. (2012). Samples for this study are from dn⁴.

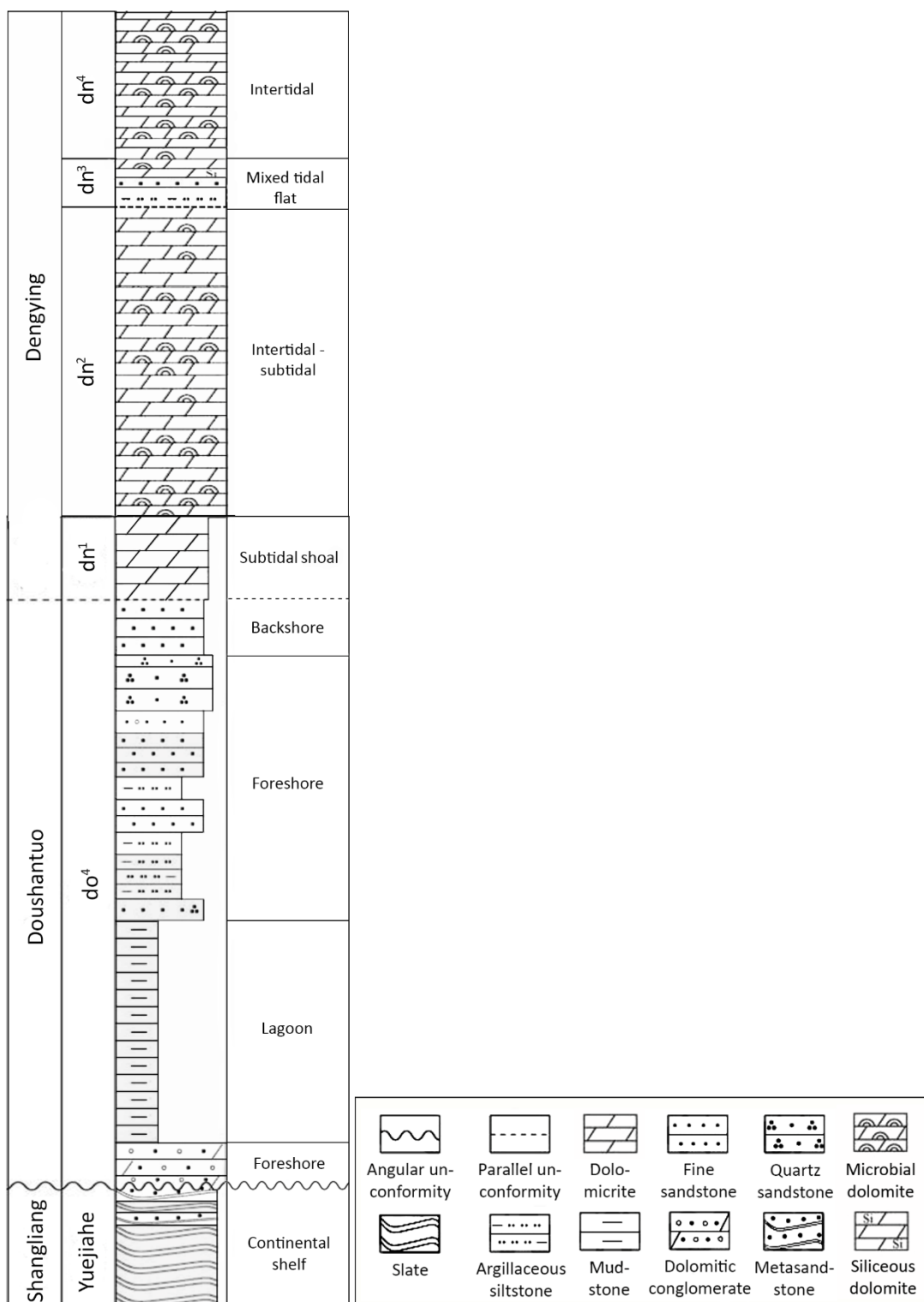


Figure 3. Profile of Ediacaran strata at the Yangba outcrop (MSC) based on Wang et al. (2019), Song et al. (2018) and Li et al. (2014). Samples for this study are from dn^3 .

Following the deposition of dn^2 , Episode I of the Tongwan Movement uplifted Ediacaran strata in the Sichuan Basin and exposed the carbonate to meteoric water. The water dissolved the dolostone, forming pores and caves in the rock and creating the parallel unconformity between dn^2 and dn^3 (Figure 2; Chen, Y. et al., 2017; Zhou et al., 2017; Gu et al., 2016). Following deposition of dn^4 , the strata were uplifted and eroded again during Tongwan Episode II (Chen, Y. et al., 2017; Liu et al., 2019). The Tongwan movement also caused extensive faulting in the region and at least one hydrothermal silica chimney eruption, which created chert interlayers and nodules, and may have contributed to the flourishing of benthic microorganisms (Chen et al., 2009; Fan, 2013; Liu et al., 2014; Feng et al., 2017; Zhu et al., 2017; Peng et al., 2018; Liu et al., 2019). At the start of the Cambrian, sea level rose considerably and the Dengying Formation was buried under dense, organic-rich shales, namely the Qiongzhusi Formation in the central basin (Chen, Z. et al., 2017; Feng et al., 2016), the Guojiaba Formation in the Micang mountain uplift (Guo et al., 2007) and the Shuijingtuo Formation in the Daba mountain thrust belt (Liu et al., 2015).

Basement-rooted faults generated in the late Ediacaran – early Cambrian expanded during the Emei taphrogeny (~390 - 230 Ma), accompanied by more hydrothermal fluid events (Derkowski et al., 2013; Liu et al., 2014; Jiang et al., 2016; Zhu et al., 2017; Peng et al., 2018; Xu et al., 2018) and a massive basalt intrusion in the eastern part of the basin (Shellnutt, 2014). Compressional forces during the following ~ 200 million years created the Micangshan uplift and Dabashan thrust belt (Xu et al., 2009; Shi et al., 2012; Xu et al., 2018).

Methods

Sample collection

A total of 46 outcrop and core samples (17 core, 29 outcrop) were collected from the Dengying Formation (551-541 Ma) and underlying Doushantuo Formation (635-551 Ma) in March 2018. Samples were chosen that had microbial textures and/or high organic content. The depth of sampled core ranges from 5397.8 m – 5224.8 m. Of the 29 outcrop samples fifteen were from the Dengying Formation and fourteen from the Doushantuo. Hand samples were wrapped in aluminum foil to avoid contact with plastic.

Table 1. Sample locations; MX = Moxi area; MCS = Micangshan outcrop; DBS = Dabashan outcrop; dn = Dengying; do = Doushantuo; superscript numbers represent the Member, and [?] indicates an unknown Member.

Sample #	Type	Fm.	Site
18	core	dn ⁴	MX
17	core	dn ⁴	MX
25	core	dn ⁴	MX
24	core	dn ⁴	MX
22	core	dn ⁴	MX
20	core	dn ⁴	MX
19	core	dn ⁴	MX
16	core	dn ⁴	MX
14	core	dn ⁴	MX
29	core	dn ⁴	MX

15	core	dn ⁴	MX
30	core	dn ⁴	MX
13	core	dn ⁴	MX
28	core	dn ⁴	MX
27	core	dn ⁴	MX
31	core	dn ⁴	MX
26	core	dn ⁴	MX
1a	outcrop	dn ³	MCS
1b	outcrop	dn ³	MCS
1c	outcrop	dn ³	MCS
1d	outcrop	dn ³	MCS
1e	outcrop	dn ³	MCS
1f	outcrop	dn ³	MCS
2a	outcrop	dn ³	MCS
2b	outcrop	dn ³	MCS
2c	outcrop	dn ³	MCS
2d	outcrop	dn ³	MCS
2e	outcrop	dn ³	MCS
2f	outcrop	dn ³	MCS
4a	outcrop	do ^{1?}	DBS-1
5a	outcrop	do ^{1?}	DBS-1
5b	outcrop	do ^{1?}	DBS-1
5c	outcrop	do ^{1?}	DBS-1
6a	outcrop	do [?]	DBS-1
7a	outcrop	do [?]	DBS-1
8a	outcrop	do [?]	DBS-1
9a	outcrop	dn [?]	DBS-1
9b	outcrop	dn [?]	DBS-1
9c	outcrop	dn [?]	DBS-1
10a	outcrop	do [?]	DBS-2
10b	outcrop	do [?]	DBS-2
10c	outcrop	do [?]	DBS-2
11a	outcrop	do [?]	DBS-2
11b	outcrop	do [?]	DBS-2
12a	outcrop	do [?]	DBS-2
12b	outcrop	do [?]	DBS-2

Biomarker extraction

For biomarker extraction, outcrop samples were worked in series to avoid cross-contamination. Samples were first broken into chunks with a solvent-washed rock hammer; vortexed with a 9:1 Dichloromethane (DCM): Methanol (MeOH) solution; dried; and then pulverized to a powder in a Retsch Planetary Ball Mill PM 100. Before and after each crushing, the stainless-steel vessel and balls were cleaned with combusted Ottawa sand, then washed with methanol, DCM, and hexane in series. Once powdered, 90 g of sample was measured out and placed into Teflon vessels, 15 g in each, with 25 mL of 9:1 dichloromethane:methanol (v:v). The powders were reacted with solvents in an 800 W microwave accelerated reaction system (MARS Xpress). The temperature was ramped to 100°C for 5 min, where it was held for 30 min, then cooled back to room temperature for 15 min. The solvent-extracted organic material was then vacuum filtered to remove the powdered rock and evaporated down in a TurboVap[®] evaporation system. Once extracts were nearly completely evaporated, 200 µL of hexane was added to each extract, and the contents were transferred into combusted GC vials using a glass syringe and loaded into a ThermoScientific AS 300 autosampler. One µL of each extract was splitlessly injected into the ThermoFinnigan Trace DSQ GC-MS with a Rtx-5 (G27) fused silica column (length = 30 m, i.d. = 0.25 mm, df = 0.25 µm) through an inlet port heated to 150°C. The GC was heated from 40°C to 130°C at a rate of 20°C per minute, and then ramped at 5°C per minute to 350°C, where it was held for 3 minutes. Analytes were run in full-scan positive ion mode. All glassware used in the lab was combusted overnight at 450°C to remove any potential contaminants.

Microscopy

A total of 17 core and 28 outcrop samples were made into petrographic slides by National Petrographic Service in Rosenberg, TX. All slides were impregnated with blue epoxy to highlight porosity. Samples selected for this analysis had visual indications of potential microbial activity. Petrographic samples were characterized using two Olympus BX51 petrographic microscopes: 1) one with 10x, 20x, 50x, and 100x oil immersion objectives equipped for both reflected and transmitted light microscopy, and 2) one with 4x, 10x, 20x, 60x objectives, a cross-nicols plate with a rotatable analyzer, a sensitive tint plate, a mercury vapor arc-discharge lamp, and two exciter filters designed to transmit in both the UV (330-385 nm wavelength) and violet-blue (400-440 nm wavelength) regions. Both microscopes are equipped with digital cameras (greyscale and color, respectively) and image analysis software. Black and white photos are useful for analyzing organic matter preservation and microbial textural relics. The cross nicols and sensitive tint plate aid mineral identification, whereas the exciter filters make zonation of the minerals visible. Color images of the slides in reflected full spectrum and violet-blue light also helped to distinguish sulfide minerals.

Geochemical analysis

Rock-Eval pyrolysis and determination of total organic carbon in the sample were conducted at National Petrographic (Rosenberg, TX) using a Rock-Eval 6 and LECO Carbon analyzer. T_{max} , S1, S2 and S3 were measured by pyrolysis in the Rock-Eval 6 and Total Organic Carbon (TOC) was determined by the LECO Carbon analyzer. These data are attained by monitoring hydrocarbons released from the source rock during temperature-programmed pyrolysis (Behar et al., 2001). They are useful to assess whether biomarker extraction is feasible. TOC (wt%) represents the amount of organic carbon in the samples, and T_{max} (°C) is a measure of thermal maturity of that carbon (highly mature carbon is unlikely to contain biomarkers). S1,

S2 and S3 (mg/g) are useful to determine whether hydrocarbons are indigenous or migrated from younger strata. S1 represents free hydrocarbons, released at 300°C; S2 represents hydrocarbons bound in kerogen, released between 300 and 650°C, as milligrams per gram of rock; and S3 represents carboxyl groups, released between 300 and 400°C. Free Oil, Hydrogen Index (HI), Oxygen Index (OI), and Production Index (PI) are all calculated ratios of the measured parameters. Free Oil is the parts per thousand (ppt, ‰) of total organic carbon that is free hydrocarbons (i.e., $100 * S1 / TOC$); HI is the ppt of TOC that is kerogenous (i.e., $100 * S2 / TOC$); OI is the ppt of TOC that is in carboxyl groups (i.e., $100 * S3 / TOC$); and PI is the ratio of free hydrocarbons to total hydrocarbons (i.e., $S1 / (S1 + S2)$), meant to represent the host rock's oil producing potential.

Results

Biomarkers

Biomarker results were obtained for five of the outcrop samples (1a – 1d and 1f) from Dengying Member 3. n-Alkanes were found in low concentration ($< .001$) in Samples 1b (Fig. 4) and 1a, but do not display the typical Poisson distribution of chain lengths. n-Alkane concentrations in the other samples were negligible (Appendix B).

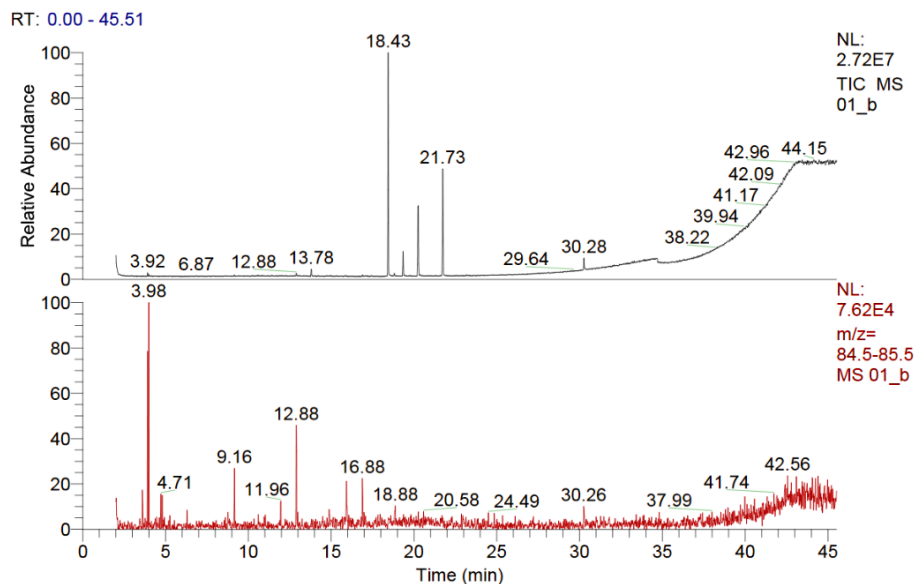


Figure 4. Gas Chromatography/Mass Spectrometry data from outcrop Sample 1b of the Dengying Formation. The bottom trace, in red, shows m/z 85 trace, indicative of n-alkanes, which are not diagnostic for any specific biological precursor. The top trace is the Total Ion Chromatogram, and the large peaks are all phthalates, a common contaminant likely introduced in the lab.

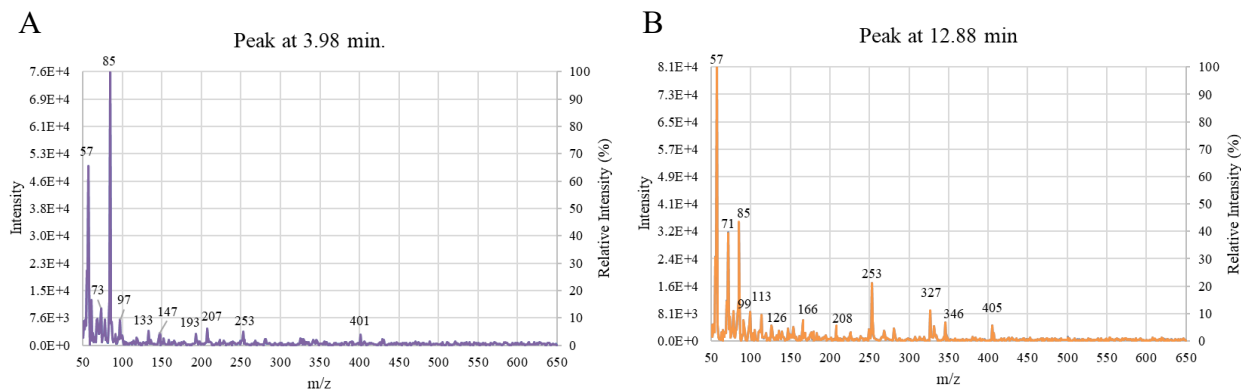


Figure 5. Mass spectrograms of Sample 1b (A) at 3.98 minutes and (B) at 12.88 minutes.

Geochemistry

Geochemical parameters for each individual sample are reported in Table 2. Total Organic Carbon (TOC) of the samples ranges from 0.10% to 2.46% (Table 3; mean = 0.86%, standard dev. = 0.82%, median = 0.39%). The mean TOC of Dengying samples is 0.89% with a standard deviation of 0.92%. Dengying samples from the Micangshan outcrop (black shale and laminated dolostone) have a much greater mean TOC and standard deviation than those from DBS-1 (mostly white limestone and dolomite: 1.08% \pm 0.94% and 0.13% \pm 0.04%, respectively).

The mean TOC of Doushantuo samples is 0.82% with a standard deviation of 0.73%. The Hydrogen Index (HI), which measures the concentration of kerogenous hydrocarbons, ranges from 0 to 51 (Table 3; mean = 10, standard dev. = 14, median = 3). The mean HI of Dengying samples is 15 with a standard deviation of 16 and median value of 6. Samples from MCS have a much lower HI than those from DBS-1 (8 ± 8 and 44 ± 6 , respectively), which contributes to the high standard deviation for these Dengying samples overall. The mean HI of Doushantuo samples is 5 with a standard deviation of 9 and a median value of 1. Samples from DBS-1 (cap carbonate and black shale) have a wide range of HI values (0 – 33), while DBS-2 samples (weathered black shales with high sulfur and copper content) all have $HI \leq 1$. The Production Index (PI), which is the ratio of free hydrocarbons to total hydrocarbons, ranges from 0.44 to 1.00 (Table 3; mean = 0.75, standard dev. = 0.16, median = 0.73). The mean PI of Dengying samples is 0.67 with a standard deviation of 0.11 and median value of 0.71. The mean PI of Doushantuo samples is 0.83 with a standard deviation of 0.16 and a median value of 0.88.

Table 2. Geochemical data of outcrop samples. Leco TOC = total organic carbon in weight %; S1 = free hydrocarbons, released at 300°C; S2 = hydrocarbons bound in kerogen, released between 300 and 650°C; S3 = carboxyl groups, released between 300 and 400°C; Tmax = temperature in °C at which the greatest volume of hydrocarbons is released from the matrix. Greater Tmax generally corresponds to greater thermal maturity; Hydrogen Index (HI) = 100*S2/TOC; Oxygen Index (OI) = 100*S3/TOC; Free Oil = 100*S1/TOC i.e., the parts per thousand of total organic carbon represented by free hydrocarbons; Production Index (PI) = S1/(S1 + S2).

Sample ID	TOC (%)	S1 (mg/g)	S2 (mg/g)	S3 (mg/g)	T _{max} (°C)	Hydrogen Index	Oxygen Index	Free Oil	Production Index	Formation	Site
1a	1.82	0.18	0.07	0.25	323	4	14	10	0.72	dn ³	MCS
1b	1.87	0.17	0.06	0.16	305	3	9	9	0.73	dn ³	MCS
1c	1.89	0.16	0.06	0.24	322	3	13	8	0.71	dn ³	MCS
1d	1.79	0.15	0.06	0.17	309	3	10	8	0.73	dn ³	MCS
1e	2.27	0.17	0.13	0.23	424	6	10	7	0.56	dn ³	MCS
1f	2.14	0.19	0.1	0.2	404	5	9	9	0.65	dn ³	MCS
2a	0.15	0.06	0.02	0.18	419	13	121	40	0.73	dn ³	MCS
2b	0.1	0.04	0.03	0.19	424	30	189	40	0.59	dn ³	MCS
2c	0.46	0.03	0.01	0.19	416	2	41	6	0.85	dn ³	MCS
2d	0.12	0.03	0.02	0.19	426	17	160	25	0.66	dn ³	MCS
2e	0.1	0.05	0.01	0.23	421	10	225	49	0.78	dn ³	MCS
2f	0.19	0.03	0.01	0.16	421	5	84	16	0.77	dn ³	MCS
4a	0.31	0.04	0.01	0.28	335	3	92	13	0.86	do	DBS-1
5a	0.34	0.06	0.01	0.45	337	3	130	17	0.85	do	DBS-1
5b	0.12	0.05	0.02	0.14	318	16	115	41	0.73	do	DBS-1
5c	0.39	0.05	0.01	0.36	362	3	94	13	0.77	do	DBS-1
6a	0.24	0.06	0.08	0.09	438	33	37	25	0.44	do	DBS-1
7a	2.46	0.09	0.01	1.16	311	0	47	4	0.9	do	DBS-1
8a	0.19	0.04	0.02	0.21	319	10	109	21	0.65	do	DBS-1
9a	0.18	0.06	0.07	0.18	428	40	102	34	0.44	dn [?]	DBS-1
9b	0.12	0.06	0.06	0.18	433	51	152	51	0.53	dn [?]	DBS-1
9c	0.1	0.05	0.04	0.21	418	41	214	51	0.54	dn [?]	DBS-1
10a	1.04	0.03	0.01	0.13	346	1	13	3	0.74	do	DBS-2
10b	1.19	0.05	0	0.27	320	0	23	4	0.95	do	DBS-2
10c	0.99	0.05	0	0.13	316	0	13	5	1	do	DBS-2
11a	0.63	0.08	0	0.86	305	0	136	13	0.97	do	DBS-2
11b	0.22	0.08	0	2.18	305	0	986	36	1	do	DBS-2
12a	1.39	0.07	0.01	0.15	313	1	11	5	0.89	do	DBS-2
12b	2.02	0.13	0.01	0.13	340	0	6	6	0.91	do	DBS-2

Table 3. Statistics for total organic carbon (TOC), hydrogen index (HI) and production index (PI). “dn” refers to samples from the Dengying Formation and “do” refers to samples from the Doushantuo Formation.

TOC	MCS	dn DBS-1	do DBS-1	DBS-2	All dn	All do	All
Mean	1.08	0.13	0.58	1.07	0.89	0.82	0.86
Median	1.13	0.12	0.31	1.04	0.19	0.51	0.39
Stdev	0.94	0.04	0.83	0.57	0.92	0.73	0.82
Max	2.27	0.18	2.46	2.02	2.27	2.46	2.46
Min	0.10	0.10	0.12	0.22	0.10	0.12	0.10



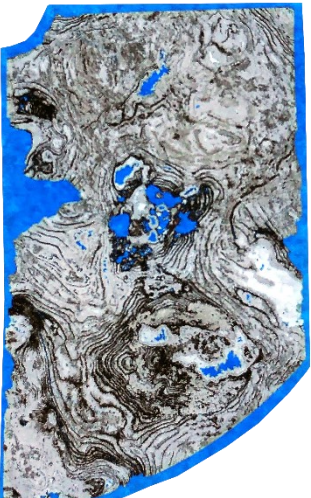
HI	MCS	dn DBS-1	do DBS-1	DBS-2	All dn	All do	All
Mean	8	44	10	0	15	5	10
Median	5	41	3	0	6	1	3
Stdev	8	6	12	0	16	9	14
Max	30	51	33	1	51	33	51
Min	2	40	0	0	2	0	0




PI	MCS	dn DBS-1	do DBS-1	DBS-2	All dn	All do	All
Mean	0.71	0.50	0.74	0.92	0.67	0.83	0.75
Median	0.73	0.53	0.77	0.95	0.71	0.88	0.73
Stdev	0.08	0.06	0.16	0.09	0.11	0.16	0.16
Max	0.85	0.54	0.90	1.00	0.85	1.00	1.00
Min	0.56	0.44	0.44	0.74	0.44	0.44	0.44



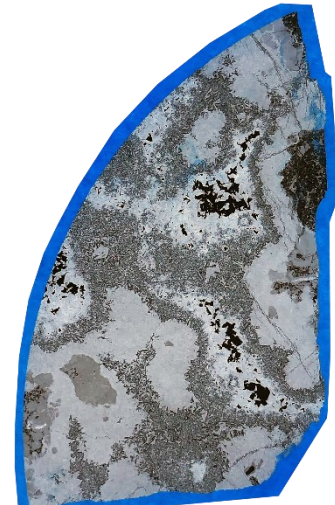
Petrography



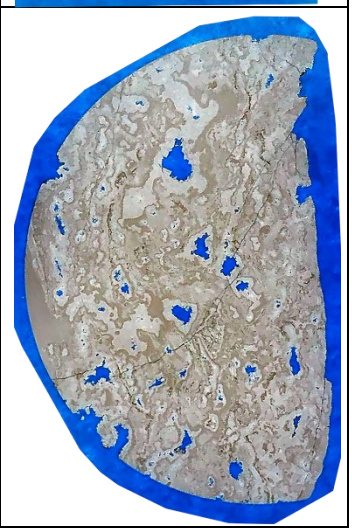
Microbialite samples from dn⁴ core are described, in order of increasing depth, in Table 4. Most of these samples are stromatolites or mat fragments that have been ripped up and re-deposited before lithification (also called “post-depositional thrombolites” (Riding, 2011c)). Some samples have both stromatolitic and thrombolitic textures and one (Sample 30) is a framework thrombolite.


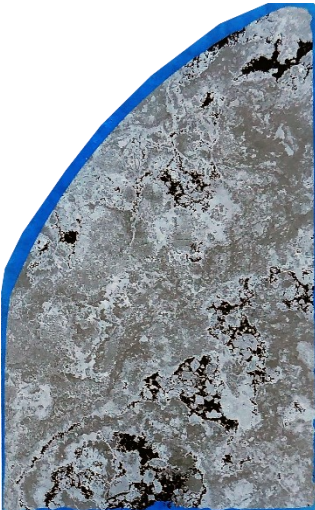

Table 4. Description and photos of slides with microbial features, ordered by depth (increasing). All slides are standard 26mm x 46mm.

ID	Depth (m)	Description	Photo
18	5224.79	<p>Crystalline gray dolomite with stromatolitic features: The organic matter is diffuse laminated or diffuse clotted. The cement is coarse crystalline dolomite, microcrystalline quartz, and hydrothermal sulfate minerals. Saddle dolomite and sulfide minerals fill vugs. This sample also contains stylolites and bitumen-charged or unfilled microfractures.</p>	
25x	5300.13	<p>Composite thrombolite – stromatolite: The stromatolite is a broad domed shape with rhombic ridges. Toward the bottom of the slide, laminations grade into a bushy clotted texture. The matrix is recrystallized coarse crystalline dolomite with anhydrite and barite. The dissolution pore at right is filled with saddle dolomite and sulfide minerals</p>	
25y	5300.13	<p>Bedding plane of Sample 25: concentric bands form lobate, oblong, and crescentic outlines, reflecting the lateral variability of lamina shapes. Pores are lined with saddle dolomite anhydrite and barite. Some areas have been replaced with botryoidal quartz cement.</p>	

24	5308.71	<p>Post-depositional thrombolite: The groundmass is micritic gray dolomite. Irregular, elongate intraclasts are redeposited stromatolite fragments. Stromatolite fragments are either flat-to-moderately convex with smooth laminations or rectangular with wavy laminations. Laminations are of varying thickness and distinctness in both types; several have desiccation cracks implying subaerial exposure. The sample has several large pores, most of which are filled by coarse dolomite or lined by saddle dolomite with pyrite at the center. A few pores are unfilled. Microfractures are charged with bitumen.</p>	
22x	5313.15	<p>Post-depositional thrombolite: the bottom third is a storm deposit of deformed microbial mats. Laminations in the mat fragments are diffuse and clotted with micritic interlayers. Mat chunks have been ripped, folded, rolled up and desiccated (indicated by cracks). Hair-like organic features radiate from a large filled dissolution pore.</p>	
22y	5313.15	<p>Bedding plane of Sample 22: Storm deposit of mat fragments, with filled dissolution pores. Mat fragments are micritic with diffuse clotted laminations. Laminations are smooth and gently to moderately convex. Much of the matrix has been recrystallized to coarse crystalline dolomite; pores are filled with saddle dolomite, anhydrite, and barite.</p>	

20	5317.93	<p>Post-depositional thrombolite: micritic gray dolomite with laminated and clotted organic fragments; laminations are generally wavy and dark although a few are diffuse. Hair-like features are crosscut by desiccation cracks. Pores and veins are filled with coarsely crystalline dolomite, saddle dolomite and sulfide minerals (pyrite or chalcopyrite)</p>	
19x	5320.86	<p>Thrombolitic stromatolite: micritic gray dolomite with both distinct and diffuse organic clots concentrated into pseudo-columnar layers. Planar and circumgranular cracks are filled with coarsely crystalline dolomite, anhydrite, barite and sometimes pyrite. The presence of these cracks could indicate subaerial exposure. Individual pyrite crystals are disseminated throughout the micrite. There are also microstylolites.</p>	
19y	5320.86	<p>Bedding plane of Sample 19: linked lobate and ovate shapes. Black minerals are chalcopyrite.</p>	

29x	5334.64	<p>Stratiform stromatolite: Brecciated micritic dolomite with distinct-clotted laminations containing pyrite framboids. Chunks of laminated micrite are embedded in a coarse hydrothermal cement (mostly dolomite and anhydrite).</p>	
29y	5334.64	<p>Bedding plane of Sample 29: one thick dark lamination takes up ~1/3 of slide space</p>	
30	5335.45	<p>Bedding plane of a porous framework thrombolite with organic-lined chambers and contorted mat fragments. Cement contains quartz, orthoclase, and sericite.</p>	

28x	5351.99	<p>Silicified undulatory stromatolite: laminations are composed of sphalerite microspheroids. Void-filling pyrite and chalcopyrite.</p>	
28y	5351.99	<p>Bedding plane of Sample 28: ovate, lobate, and crescentic outlines formed by clumped spheroidal sphalerite. The groundmass is quartz cement, and pyrite fills void spaces.</p>	
26	5397.81	<p>Branching stromatolite with thick distinct laminations and signs of syndepositional alteration. Walls are absent. Columns are anastomosed at upper right. The sample is mainly micrite with a few large dolomite crystals. Pyrite microcrystals are associated with the organic matter.</p>	

Stromatolites in Samples 25, 29, 28, and 26 (depth = 5300.13 m, 5334.64 m, 5351.99 m, and 5397.81 m, respectively) are mostly intact and their laminations are easily discernible without magnification. Each of these samples represents a different stromatolite morphotype. Sample 25 (Fig. 6a) has densely-packed, relatively thin laminations that form a broad domed shape with small peaks and cusped ridges (red arrows). In the middle-left of the slide, part of the mat folds over itself, forming a wave-like rhombic shape. Overlying laminations echo this shape with diminishing relief. Underlying laminations form smaller, sharper peaks especially on the right side of the slide. Sample 29 (Fig. 6b) contains brecciated chunks of a stratiform stromatolite. Some laminae are wavy and discontinuous, but most are flat and continuous. Laminae vary in distinctness depending on the packing density of the peloids composing them. Sample 28 (Fig. 6c) is another stratiform stromatolite with densely packed undulatory layers. The morphology of Sample 26 (Fig. 6d) is complex. It appears to be a branching columnar stromatolite composed mostly of distinct, dome-shaped laminations, but walls are absent, and many laminations are obscure. The orange dashed lines in Figure 6d are estimations of the column boundaries. Several laminae are cusped in shape; these are generally smaller than the smooth convex laminae.

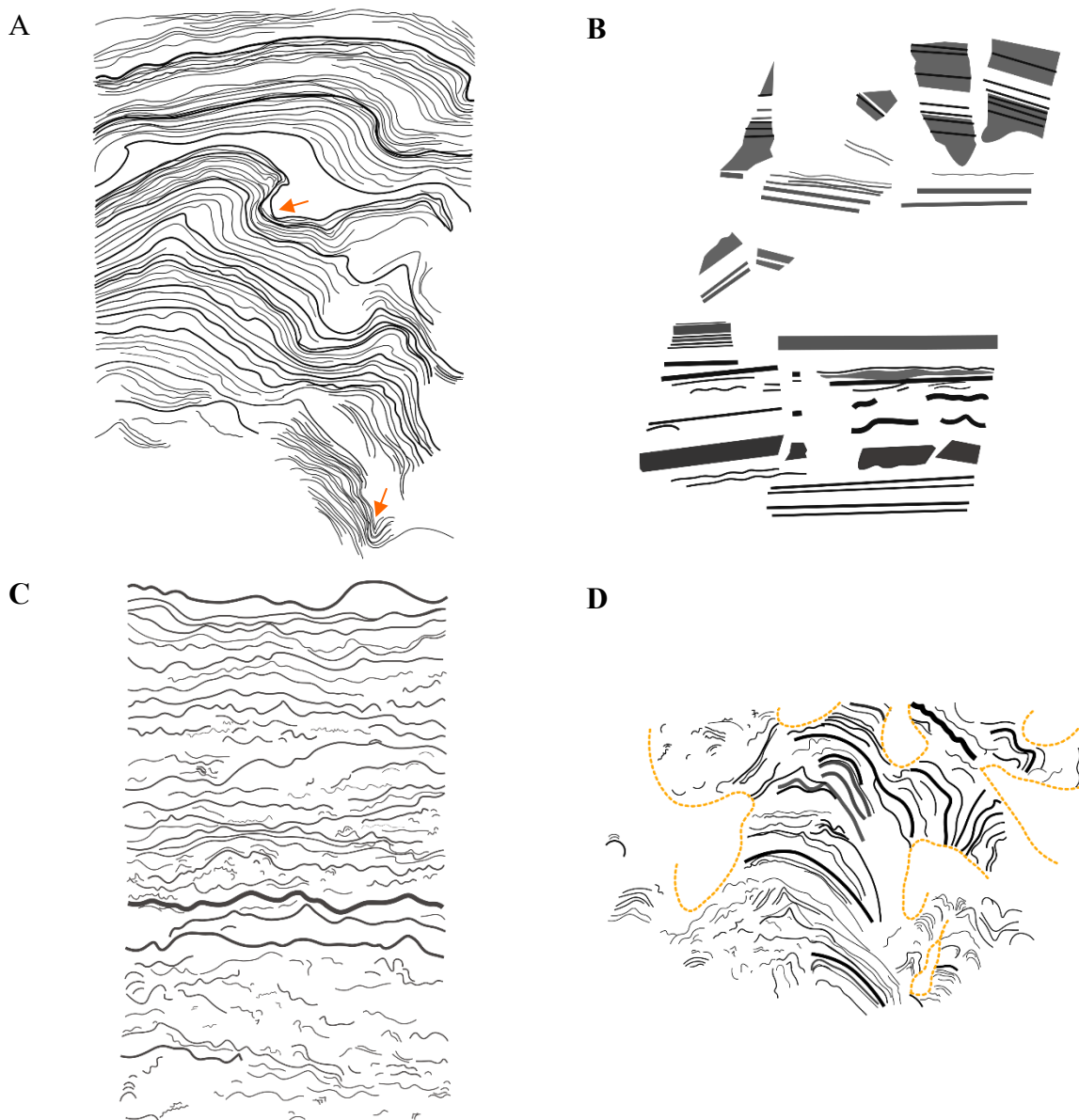


Figure 6. Stromatolite morphology traced from thin sections (26mm x 46mm). (A) Sample 25 (dn⁴, depth = 5300.13 m) is composed of dense thin lamination forming a broad dome shape with sharp peaks and ridges that fold over; toward the bottom, laminations grade into bushy clotted texture (B) Sample 29 (dn⁴, depth = 5334.64 m) contains brecciated laminar microbialite (AKA stratiform stromatolite); laminae vary in thickness and distinctness. Gray lines indicate diffuse laminae (C) Sample 28 (dn⁴, depth = 5351.99 m) is an undulatory stratiform stromatolite with crinkly-wavy laminations of varying thickness (D) Sample 26 (dn⁴, depth = 5397.81 m) is a complex branching columnar stromatolite; the orange dashed line is an estimation of the structure, black lines are laminations. Laminations are mostly domed with some sharp peaks and some wavy flat laminations.

Laminae in Sample 25 are uneven and discontinuous. They change in thickness laterally, often truncating unexpectedly or becoming clotted and diffuse (Fig. 7a, b). Interlaminar space in

the stromatolite is microsparitic (Fig. 7b). Voids are filled with coarse-crystalline dolomite and sulfate minerals (Fig. 7d). Part of the stromatolite has been silicified, i.e., replaced with metasomatic quartz (Fig. 18f). Bushy peloidal aggregates below the stromatolite (Fig. 7c, d), make this sample a composite stromatolite-thrombolite.

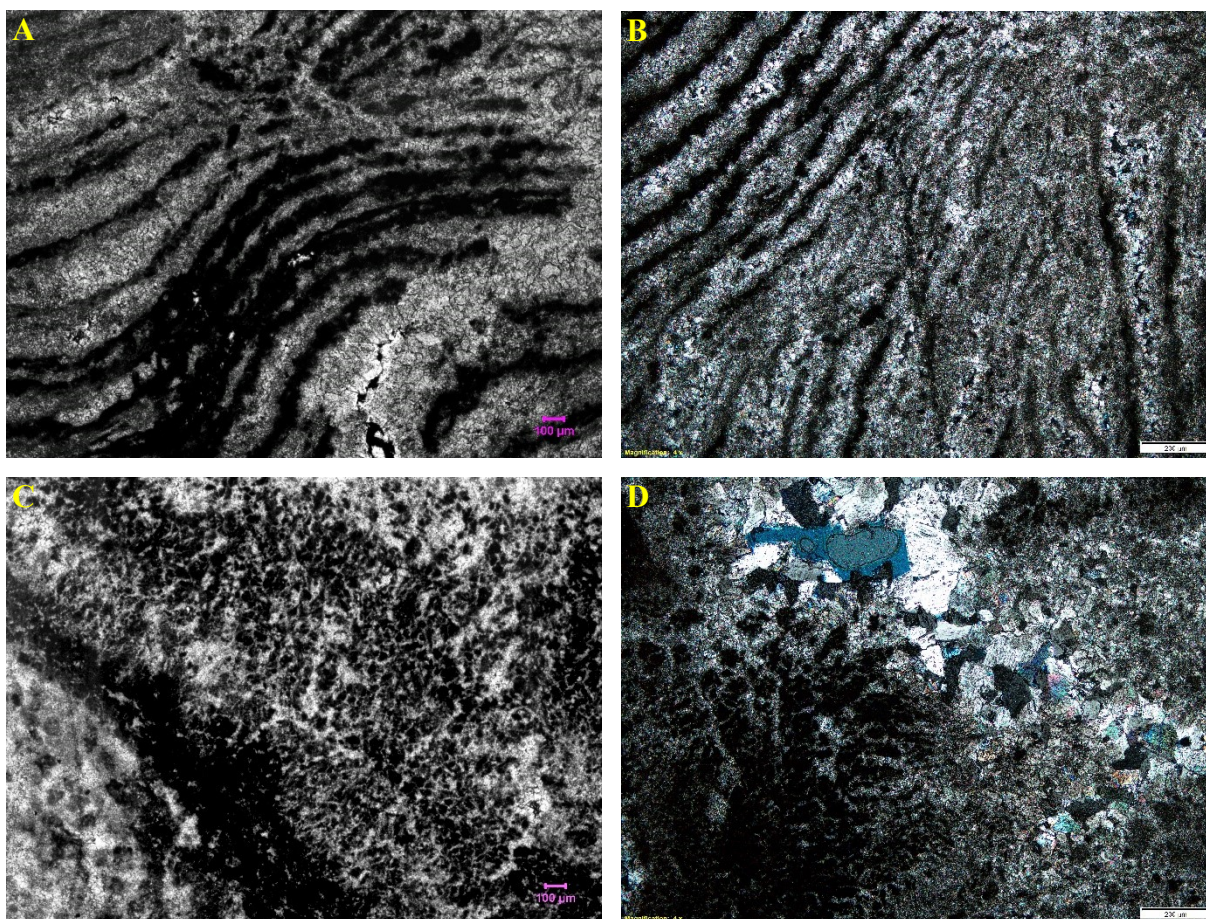


Figure 7. Microstructure of Sample 25 (dn⁴, Depth = 5224.79) (A) domed laminations are dark and discontinuous; sparite interlayers may have resulted from recrystallization of grains and laminations were likely also condensed when this happened. Plane-polarized light (PPL) 4x magnification (B) Laminations form sharp peaks in some areas; laminae here are streaky and diffuse. Cross-polarized light (XPL) 4x magnification (C) Toward the bottom of the slide laminations grade into bushy peloidal fabric. PPL 4x magnification (D) Dense to bushy clotted texture and filled dissolution pore. XPL 4x magnification.

The stratiform stromatolite in Sample 29 can be interpreted as lithified microbial mats rather than chemical lamination because the laminae are made up of clotted peloidal micrite (Fig. 8b-d) and show signs of cohesion during transport (Fig. 8a, c). Fragments in Figure 8a pinch out and curve suggesting they were separated while the mat was still wet and deformable. Pyrite

framboids are distributed throughout the stromatolite (Fig. 8c, d). The framboids have undergone some recrystallization, so their internal morphology is ambiguous, but they do not resemble crystalline pyrite seen in other samples (e.g., Figure 13f, Figure 16d).

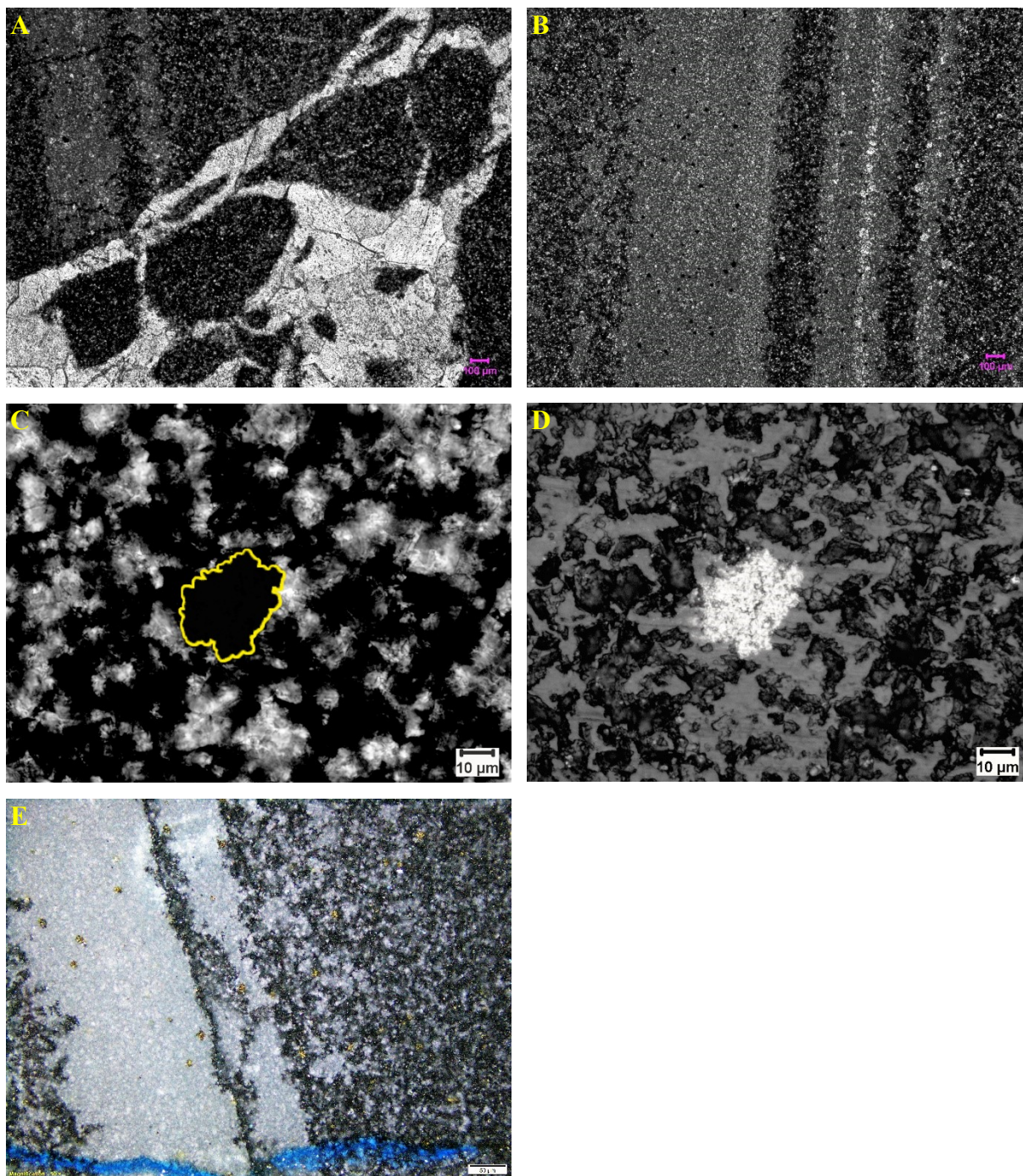


Figure 8. Microtexture of Sample 29 (dn⁴, Depth = 5334.64 m) (A) Microbial mat that has been torn up while still unlithified. PPL 4x magnification (B) Layers are composed of micrite, peloidal micrite (darkest), and microsparite (lightest). PPL 4x magnification (C) Pyrite framboid (outlined) in clotted organic laminations of Sample 29 (dn⁴,

Depth = 5334.64 m). PPL 50x magnification (D) Pyrite framboid in reflected light 50x magnification (E) Clotted laminations with pyrite in reflected light with cross-nicols, 10x magnification.

Sample 28 (dn⁴, Depth = 5351.99 m) is mostly quartz cement, with spheroidal aggregates forming wavy laminae and clumps (Figure 9). The spheroids appear to be composed of sphalerite, which has a dark brown color in plane-polarized light, a greyish-yellow color in reflected light, and red fluorescence in blue-violet light. Laminae have very low synoptic relief; they change in thickness laterally, and frequently cross-cut each other or pinch out. These characteristics point to grain-trapping and binding as an accretion mechanism, rather than mineral precipitation.

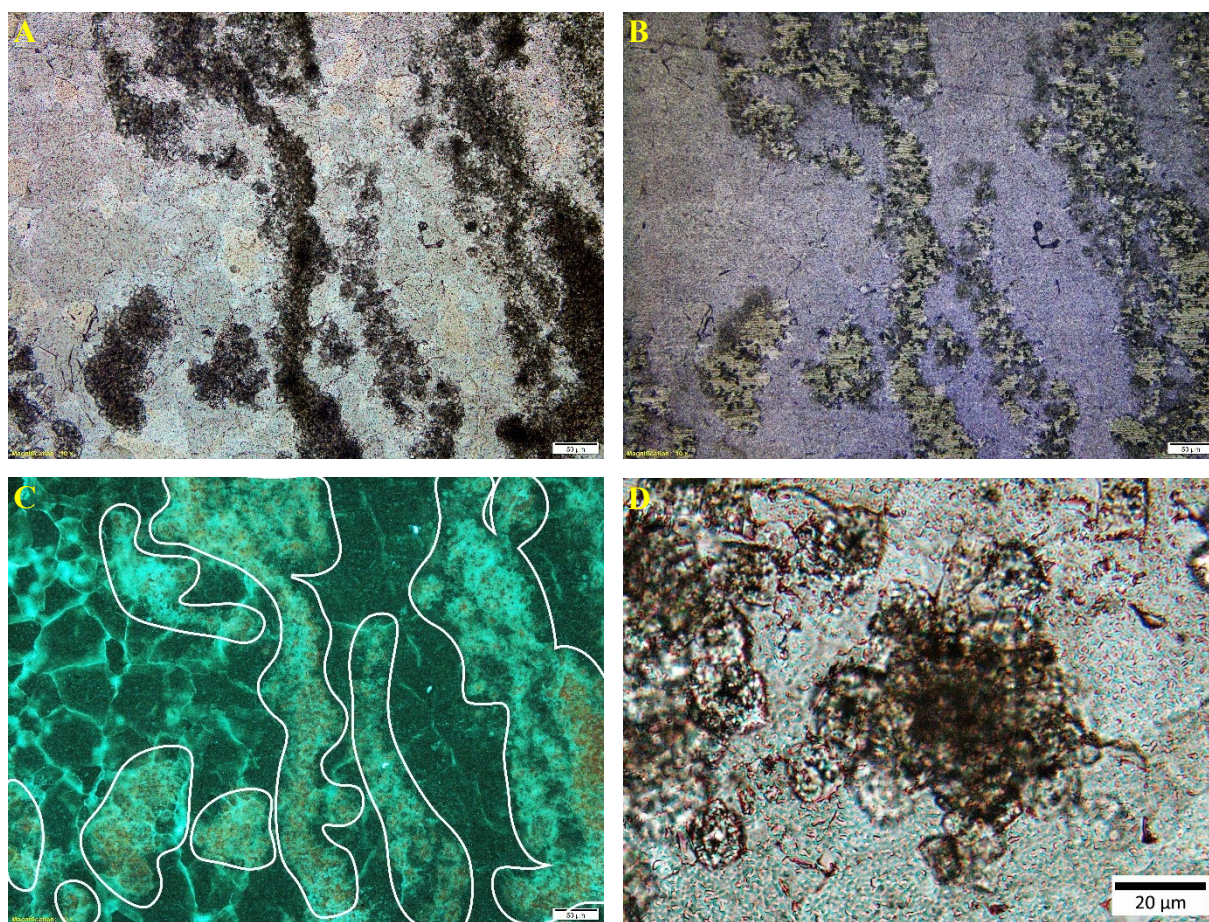
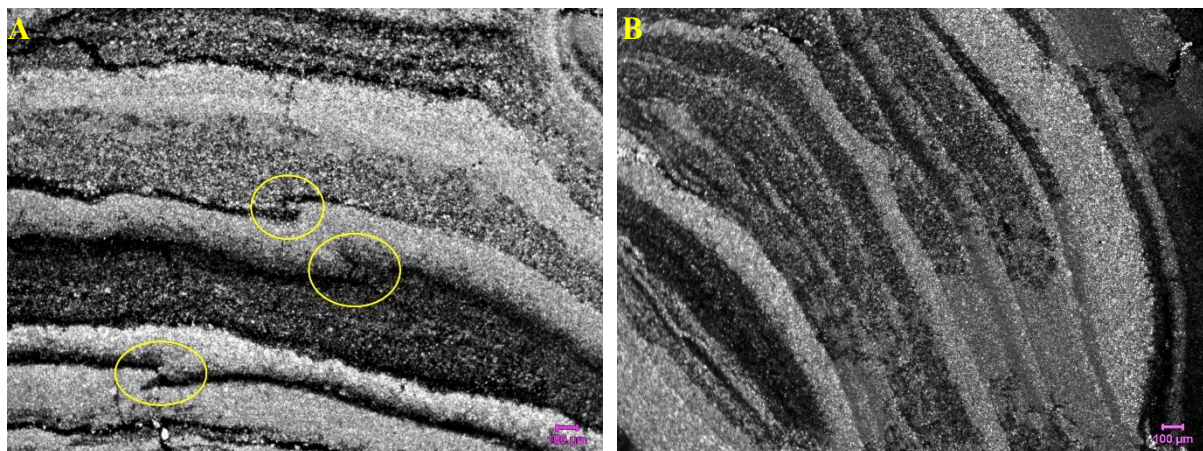


Figure 9. Microtexture of Sample 28 (dn⁴, Depth = 5351.99 m) (A) Wavy laminations of clumped spheroidal sphalerite in quartz cement; individual spheroids are 0.1 – 5.0 µm in diameter. PPL 10x magnification (B) The same view as A in reflected light, revealing sulfide minerals composing the laminations. 10x magnification (C) Same view as A and B in blue-violet light; the spheroidal sphalerite fluoresces red, encased in bluish green fluorescent material. 10x magnification (D) Closer view of spheroids reveals center nuclei. PPL 20x magnification.

Sample 26 is made up of relatively thick, distinct laminations, although disparity in thickness and distinctness is obvious under magnification. Many segments show evidence of deformation and degradation prior to lithification. In Figure 10a, the circled areas show where layers of the mat shifted. Inside the center circle, the overlying lamination curls up, suggesting desiccation following the tear. Laminations in Figure 10b fade from mottled black to gray, a sign of erosional truncation. Figure 10c shows a microbial intraclast in a light interlayer, likely separated from the underlying mat. Enveloping (Figure 10c) and peaked (Figure 10d) laminations thicken toward the top. In the case of peaked laminations, this may suggest the presence of a “tuft” of filamentous cyanobacteria at the top of the mat (Grotzinger & Knoll, 1999). Enveloping laminae indicate accretion via in-situ mineral precipitation; however, enveloping laminae are very rare. Laminae generally have low synoptic relief, cross-cut one another, and truncate (Figure 10b). These characteristics, along with irregular branching columns, point to grain-trapping rather than *in situ* mineralization (Tosti & Riding, 2017).



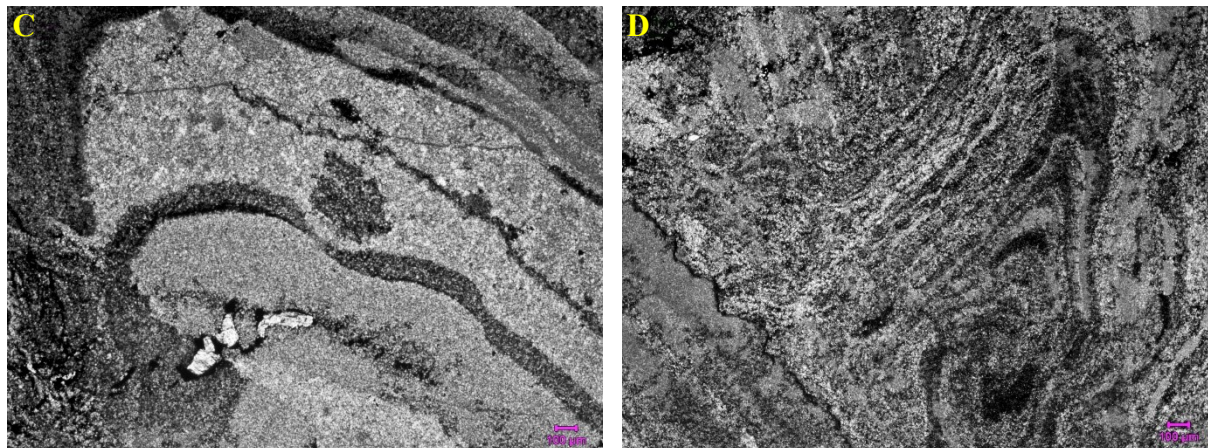


Figure 10. Microtexture of Sample 26 (dn⁴, depth = 5397.81 m) (A) Gently convex laminations: circled features show that the mat has been deformed while still wet. PPL 4x magnification (B) Laminations displaying erosional truncation and cross-cutting. PPL 4x magnification (C) Enveloping rectangular laminae; the thick gap between organic laminations contains a chunk of mat and a few clots. PPL 4x magnification (D) Peaked laminae with high synoptic relief PPL 4x magnification.

Samples 24, 22, 20, and 30 are all thrombolites. Samples 24, 22, and 20 (depth = 5308.71 m, 5313.15 m, and 5317.93 m, respectively) are post-depositional thrombolites, containing mat fragments and clotted intraclasts. Sample 24 (Figure 11a, b) is mostly organic-rich micrite, with sparite veins and filled vugs. Laminations in the mat fragments vary from smooth to wavy and from stratiform to steeply convex. Most of the mat fragments have cracks in them and some areas individual laminae have separated from the mat (Fig. 11b), presumably as a result of desiccation following subaerial exposure. The mat fragment in Figure 11a is wrapped around a cauliflower-like clotted mass, forming a hemispheroidal shape with wavy laminations. Part of the mat fragment folds over itself, suggesting ductile deformation. Mat fragments in Sample 22 (Figure 11c-e) are smaller and more deformed than those in Sample 24. An oncolid in Sample 22 (Figure 11c) is likely the result of mat laminations being rolled into a concentric spherical shape by wave action. Rolled-up mat fragments occur in a sparry layer of a hybrid stromatolite (Figure 11d). The mat fragments form diffuse irregular clasts (Figure 11e) consistent with the reworking and redeposition of mats. Laminated fragments in Sample 20 (Figure 11f) are much darker, but

have the same wavy lamination as seen in Sample 24. In all of these samples, the original micrite has been replaced in areas with hydrothermal cements.

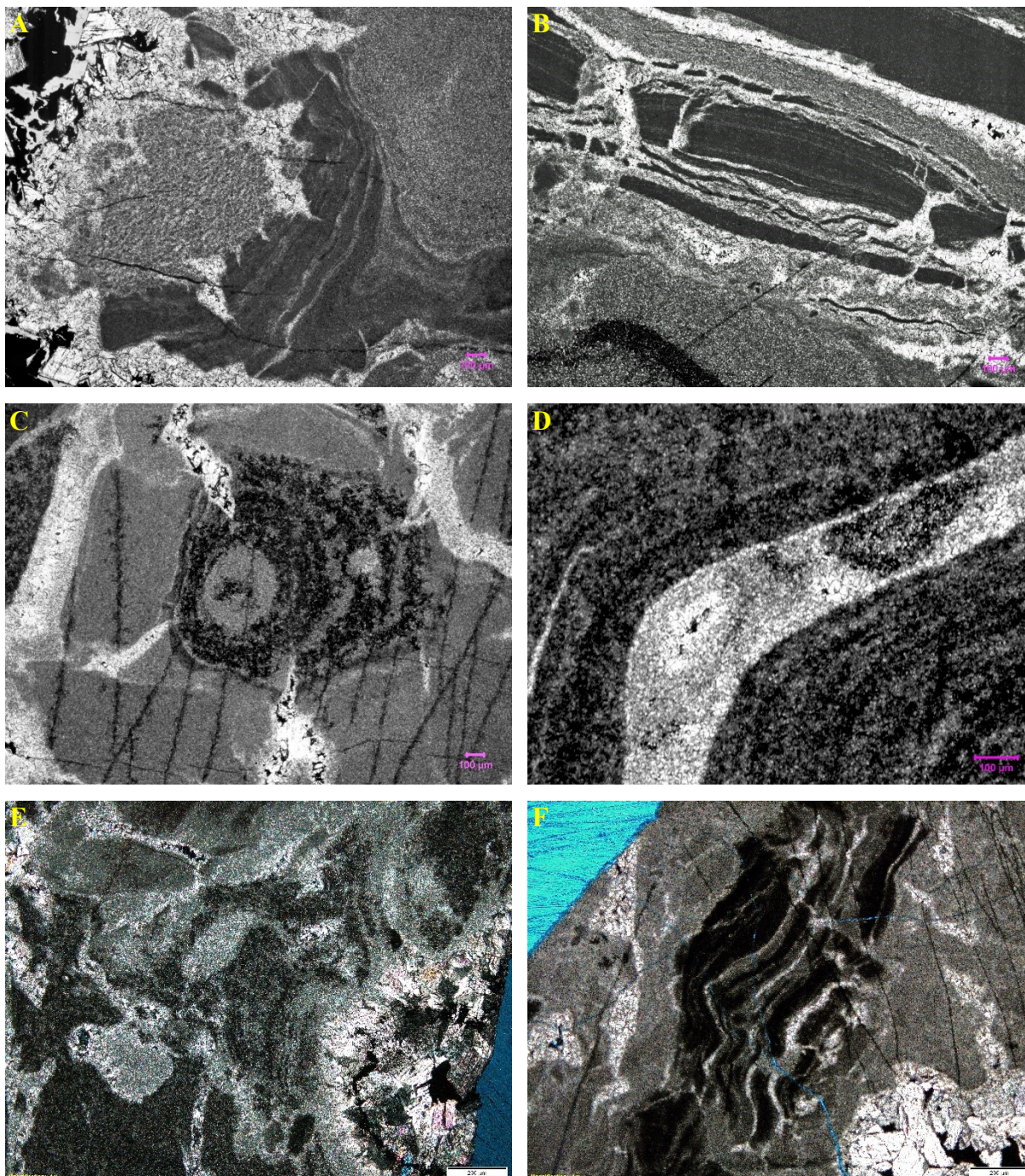
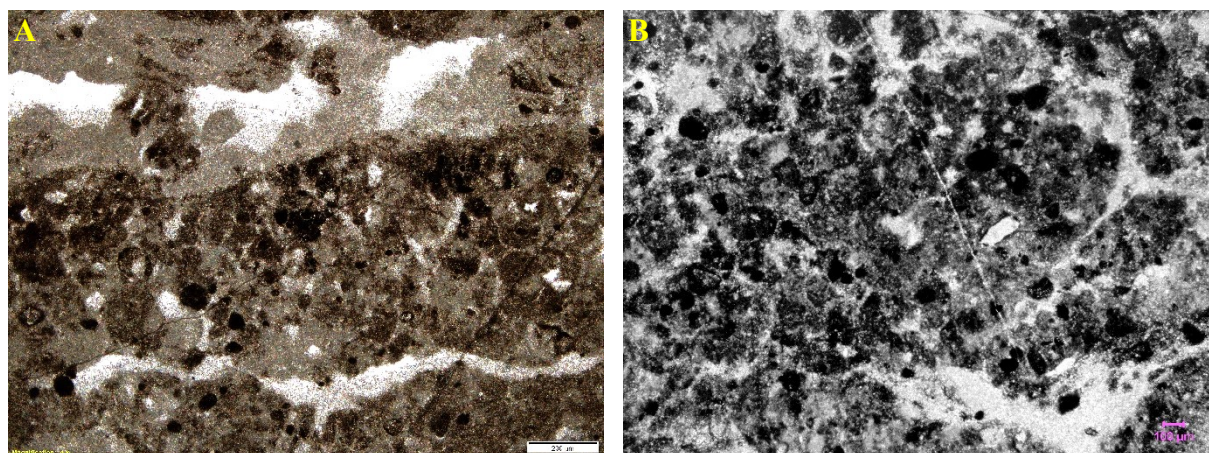


Figure 11. (A) Sample 24 (dn⁴, depth = 5308.71 m) has wavy laminae wrapped around a clotted mass. PPL 4x magnification (B) Desiccated mat fragments in Sample 24. PPL 4x magnification (C) Small oncolite in micrite, Sample 22 (dn⁴, depth = 5313.15 m) parts of the original fabric have been replaced by hydrothermal minerals. PPL 4x magnification (D) Laminated intraclast in Sample 22 with convoluted laminations between laminae suggest that mat pieces were separated while still deformable. PPL 10x magnification (E) An assortment of organic rip-up clasts

in Sample 22. XPL 4x magnification (F) Mat fragment in Sample 20 (dn⁴, depth = 5317.93 m) PPL 4x magnification.

Sample 19 (depth = 5320.86 m) is a thrombolitic stromatolite composed of organic clots and cortoids. The clots are a mix of distinct and diffuse; distinct clots are round and 10 - 100 μ m in diameter. Cortoids are typically sub-rounded, but also form irregular shapes (Figure 12b, c, iii). Sample 19 falls between a stromatolite and a layered thrombolite because the clots composing the layers are larger and less densely packed than typical peloidal texture of stromatolite laminations. Sample 30 (depth = 5335.45 m) is a highly porous framework thrombolite. Hollow chambers are filled with coarsely crystalline dolomite and sulfate minerals (mostly anhydrite) and are lined with dense organic rich micrite. Small wisps of biofilms are visible in micritic areas (Figure 12d, f) which implies that the organic matter in the chamber walls came from decaying microbial mats.



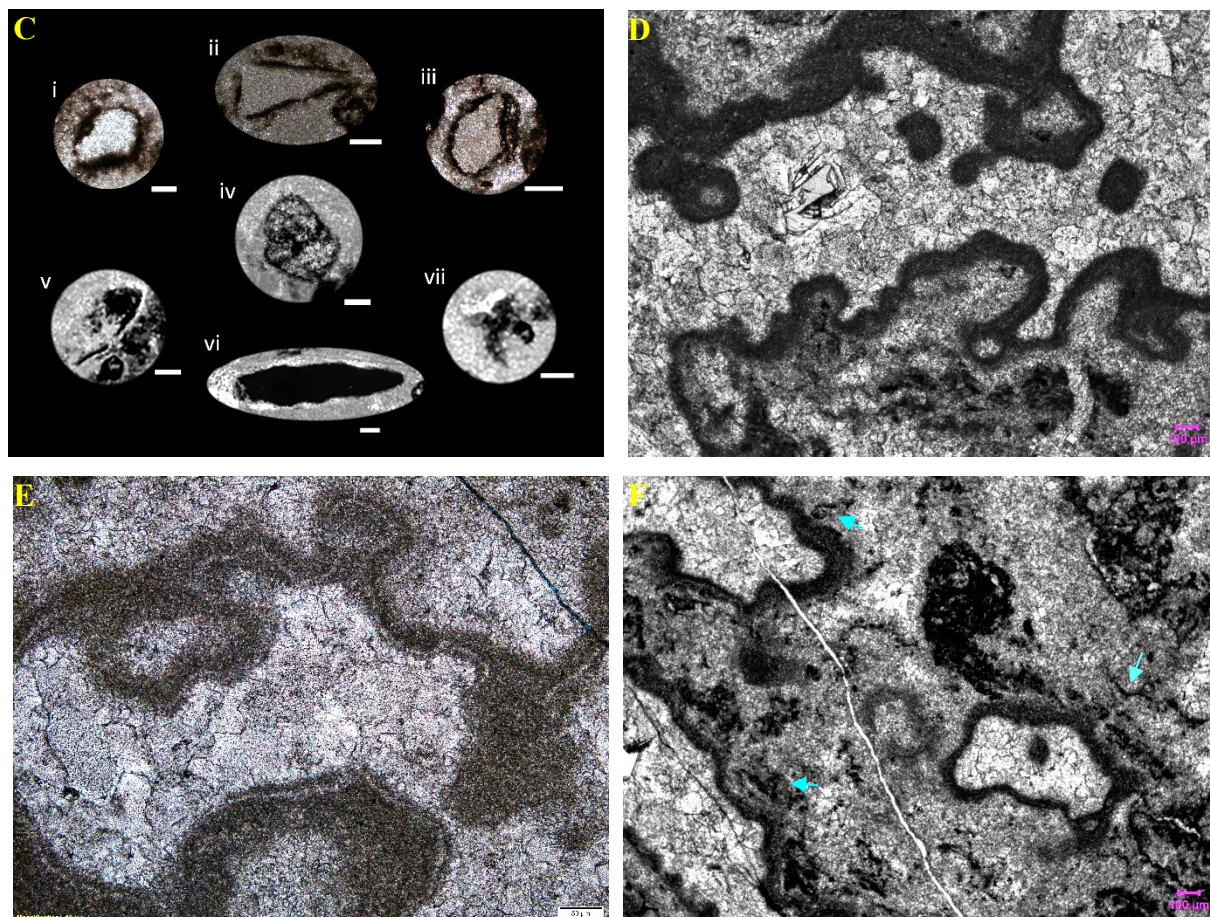


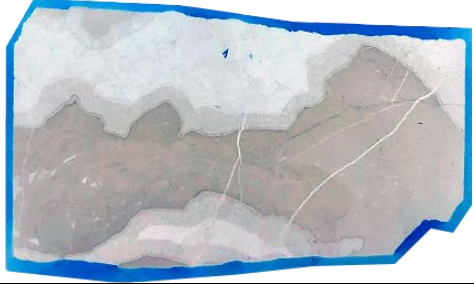


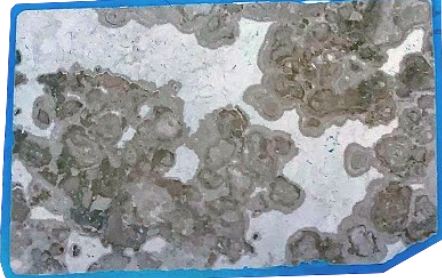


Figure 12. (A) Large organic clots and cortoids form laminations in Sample 19 (dn⁴, depth = 5320.86 m). PPL 4x magnification (B) Sample 19. PPL 4x magnification (C) Noteworthy forms in Sample 19; all scale bars are 50 μ m (D) Framework in Sample 30 (dn⁴, depth = 5335.45 m) Clotted microspar is outlined with thick organic walls and porosity has been filled by hydrothermal cement. PPL 4x magnification (E) Organic chamber walls often contain narrow veins of lighter material. PPL 10x magnification. (F) Organic-rich area of Sample 30 containing contorted fragments of biofilm (arrows). PPL 4x magnification.

In dn³ of the Micangshan outcrop, samples from group 2 appear microbial, despite their low TOC. Sample 2a – 2c are laminites with sparry interlayers, Sample 2d is a framework thrombolite and Sample 2f is mostly oncolitic with areas of clotted and laminated microfabric.

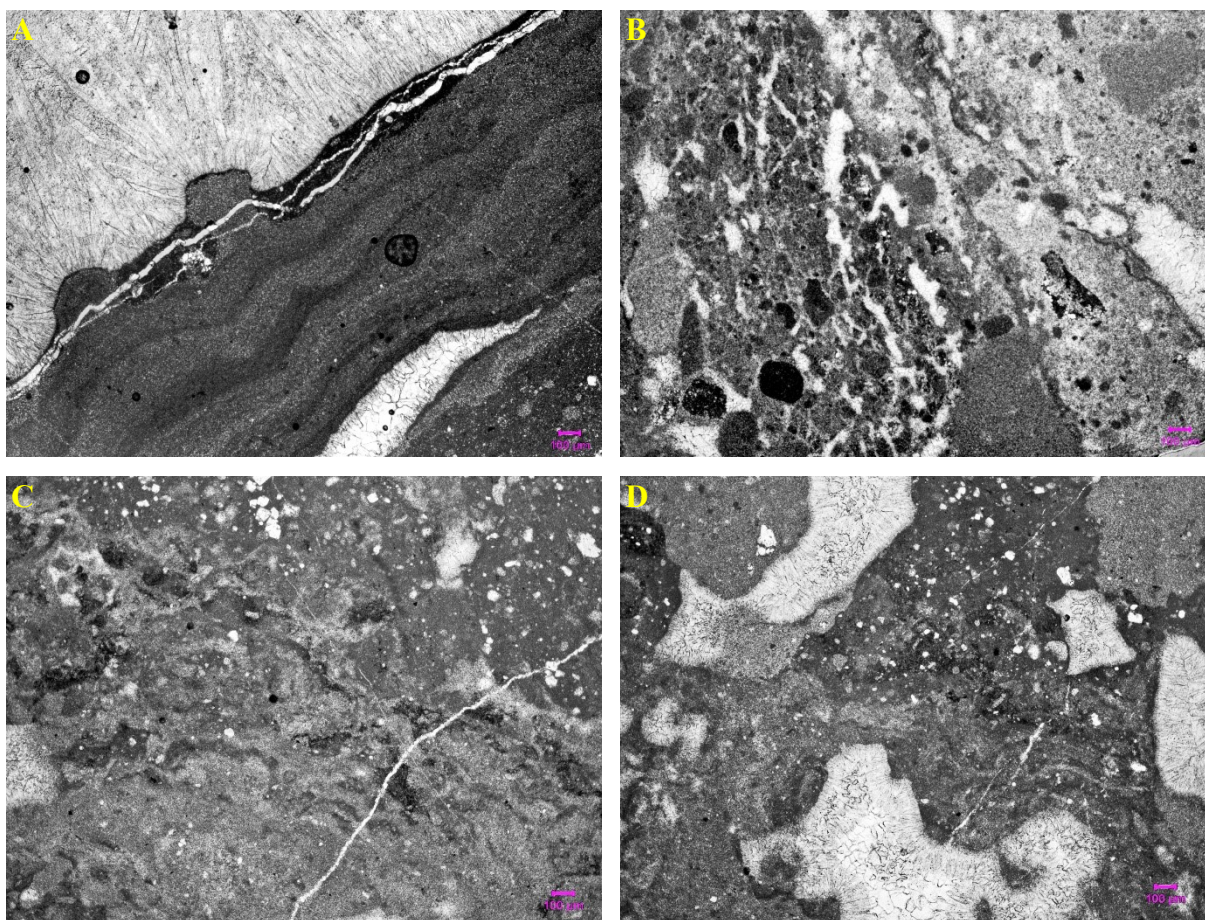
Table 5. Descriptions and photos of microbialite samples from dn³ of MCS.

2a	<p>Banded dolomite: light areas are hydrothermal cement; dark areas are laminated and thrombolitic micrite.</p> <p>TOC = 0.15%; HI = 13‰</p>	
----	--	--

2b	<p>Thrombolitic dolomite with filled fenestral pores</p> <p>TOC = 0.10%; HI = 30‰</p>	
2c	<p>Banded dolomite: light areas are hydrothermal cement; dark areas are organic-rich micrite with clots and vugs.</p> <p>TOC = 0.46%; HI = 2‰</p>	
2d	<p>Framework thrombolite with filled vugs (white)</p> <p>TOC = 0.12%; HI = 17‰</p>	
2e	<p>Fine and coarse crystalline dolomite with botryoidal texture. Filled vugs.</p> <p>TOC = 0.10%; HI = 10‰</p>	
2f	<p>Clumped and composite oncoids in hydrothermal dolomite cement. Clumps are encrusted in laminated carbonate.</p> <p>TOC = 0.19%; HI = 10‰</p>	

The laminations in 2a (Figure 13a) are potentially microbial, but also resemble natural sedimentary stratification. Crystals in the white cement display a radial fibrous growth pattern emanating from the micrite layer. Sample 2b (Figure 13b) is full of clots and fenestral pores

consistent with a microbial thrombolite. Sample 2d (Figure 13c, d) also has abundant dissolution pores and organic clots, as well as colloform laminations. Of sample set 2, Sample 2f (Figure 13e, f) most strongly resembles microbial origin. Laminations in the oncoids are streaky and uneven (Figure 13e). Although the thickness of individual laminations is not uniform there is no obvious trend in thickness of laminae moving outward. Organic clots and oncoids often form mesoclots. In Figure 13f layers of microbial mat have grown over mesoclots. The laminations do not follow the contours of the mesoclots exactly; rather they appear to drape over.



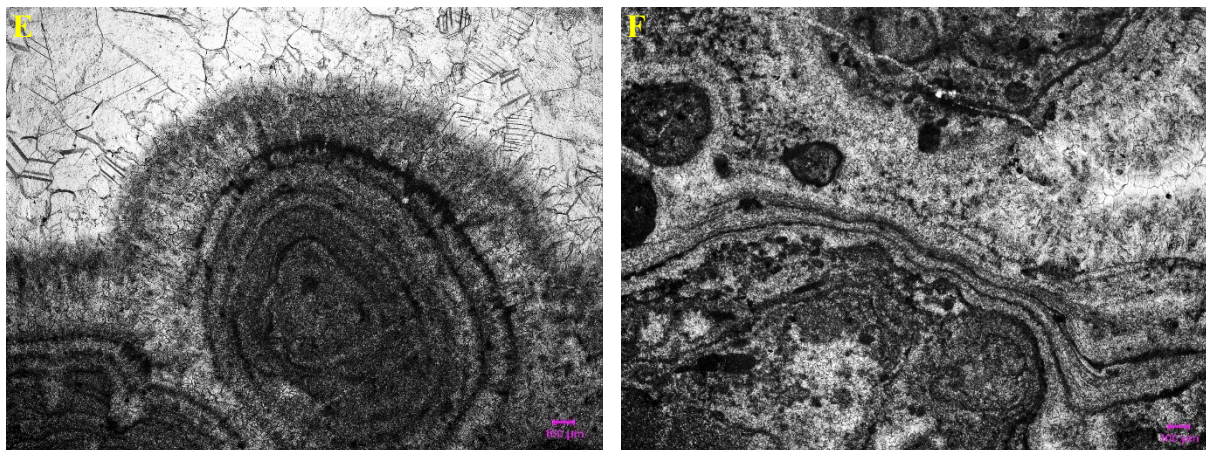
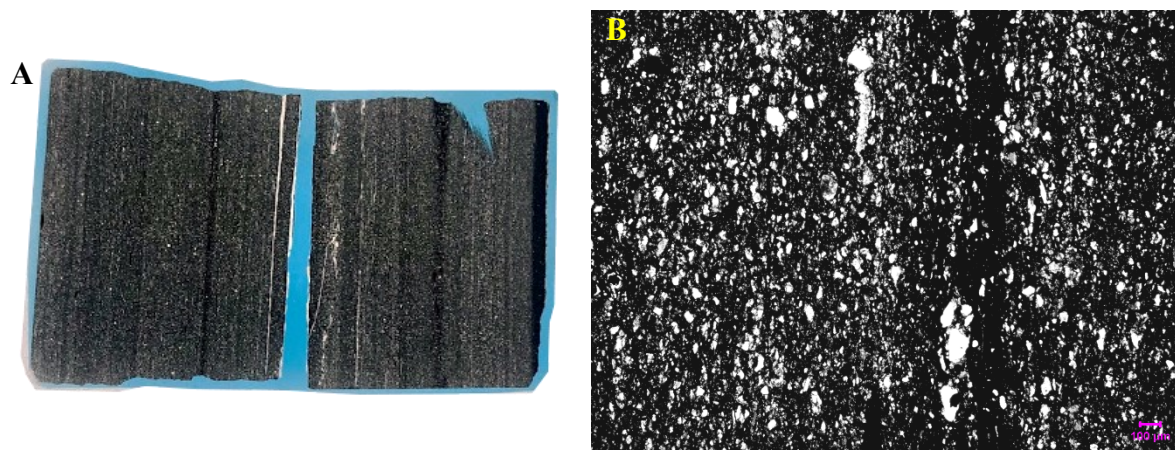


Figure 13. Microstructure of thrombolites and oncoids in Sample 2a-f (A) Laminated organic micrite is encrusted by radial fibrous minerals in 2a. PPL 4x magnification (B) Thrombolite texture in Sample 2b: organic micrite with large distinct clots and fenestral pores. PPL 4x magnification (C) Colloform laminations in Sample 2d. PPL 4x magnification (D) Sample 2d. PPL 4x magnification (E) An oncoid (diameter \approx 2 mm) in Sample 2f is surrounded by isopachous rim cement and coarse dolosparite. PPL 4x magnification (F) Laminae drape over a composite clot in Sample 2f. PPL 4x magnification.

Despite samples from group 2 being the only microbialite at the MCS site, sample group 1 has the highest total organic carbon value of all the dn³ samples (1.79% - 2.27%, mean = 1.96%). All seven of the group 1 samples are siliceous black shales with organic lenses and disseminated sulfide crystals (pyrite and galena). Laminations in Sample 1f look vaguely stromatolitic (Figure 14c, d; Fig. 15) but are too ambiguous to identify as such.



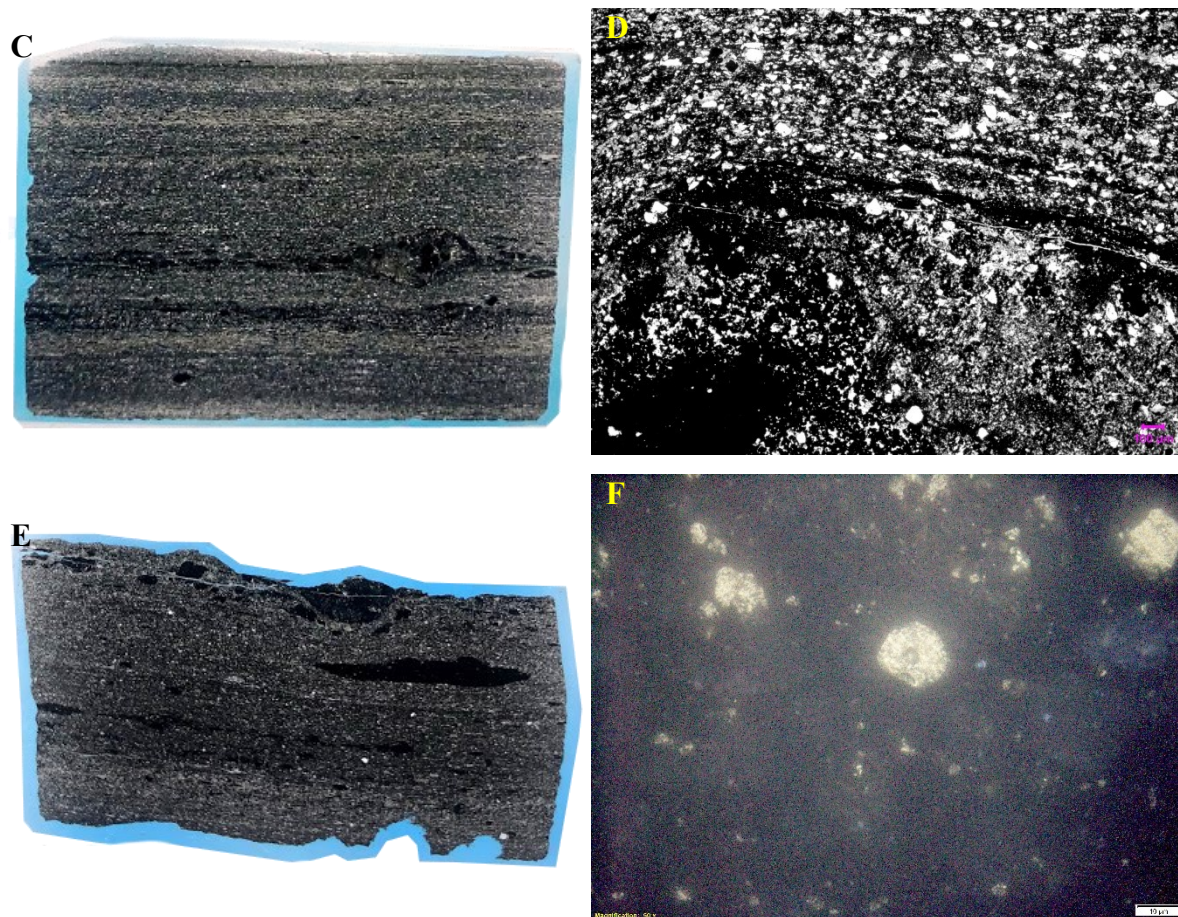


Figure 14. Sample group 1; dn^3 , MCS (A) Sample 1e, TOC = 2.27%; HI = 6% (B) Dark lamination in Sample 1e. PPL 4x magnification (C) Sample 1f, TOC = 2.14%; HI = 5% (D) Middle right of Sample 1f. PPL 4x magnification (E) Sample 1c, TOC = 1.89%; HI = 3% (F) Pyrite in Sample 1c. Reflected light (RL) 50x magnification.

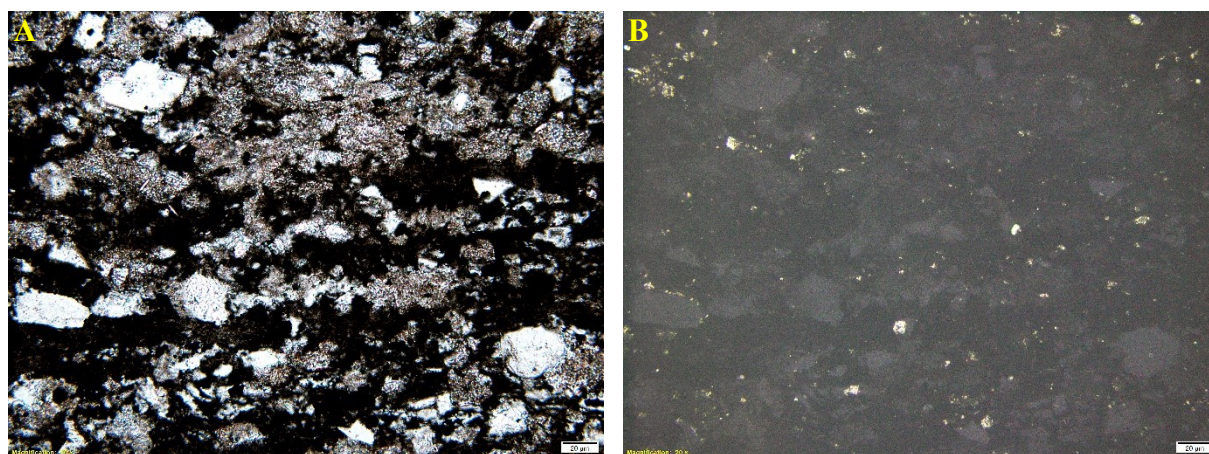
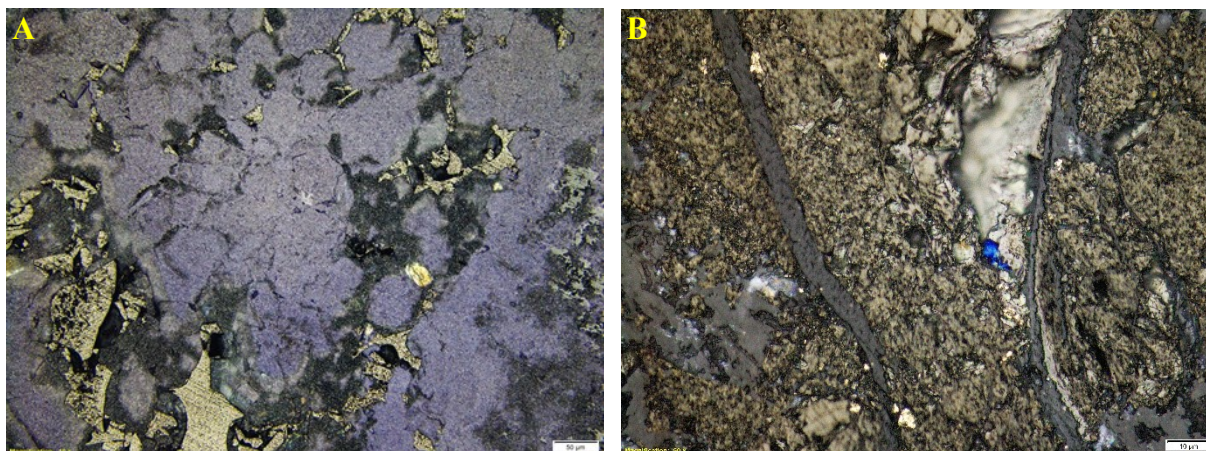


Figure 15. Sample 1f 20x magnification (A) transmitted white light (B) reflected white light.

Hydrothermal alteration is evident in samples from the central basin and all three outcrop sites. Secondary sulfide minerals are especially common in the dn⁴ well core. Sulfides are typically void-filling (Figure 16a), massive deposits (Figure 16b) or disseminated crystals (Figure 16d). They also form styolites (Figure 16c). The dark-yellow hackly-textured sulfide in Figure 16b–d is likely chalcopyrite. Chalcopyrite is not as bright as pyrite in reflected light, and since it is a softer mineral, its surface texture was more obviously affected by slicing and grinding of the thin sections. The brighter, smoother yellow sulfide is pyrite. Covellite (CuS, Figure 16b) is blue in reflected light. Sample 28 also has a small, bright yellow mineral (Fig. 16a) that can be tentatively identified as gold, which is known to precipitate during pyrite oxidation (Koski, 2012). Pyrite is also commonly oxidized to hematite, as seen in two of the samples below (Figure 17b). Criteria used to distinguish sulfide minerals are detailed in Table 6.



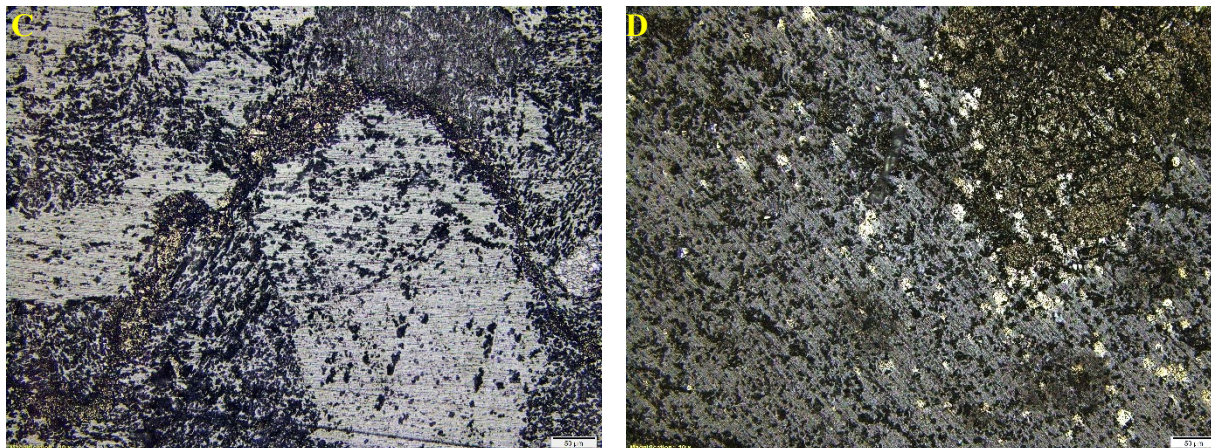


Figure 16. Hydrothermal sulfide minerals (A) Pyrite (brass yellow), sphalerite (grayish yellow), and a bright yellow sulfide (possibly gold?) in Sample 28y (dn⁴ Depth = 5351.99 m), reflected light (RL), 10x magnification (B) Chalcopryite (dark yellow), pyrite (pale yellow) and covellite (blue) in Sample 27 (dn⁴, Depth = 5383.04 m), RL 50x magnification (C) Styolite composed of chalcopryite (likely mixed with bitumen) in Sample 13 (dn⁴, Depth = 5335.77 m), RL 10x magnification (D) Mass of chalcopryite and disseminated pyrite crystals with ambient inclusion trails (AITs) in Sample 27 (dn⁴, Depth = 5383.04 m); the presence of AITs suggests that pyrite crystals have migrated through the matrix dolomite (She et al., 2016), likely during a hydrothermal fluid flow event, RL 10x magnification.

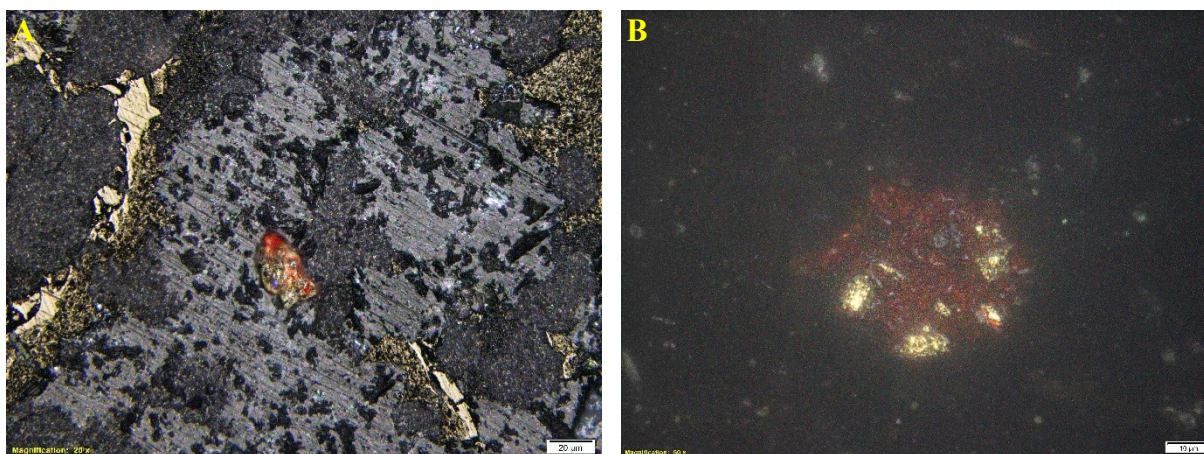
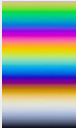


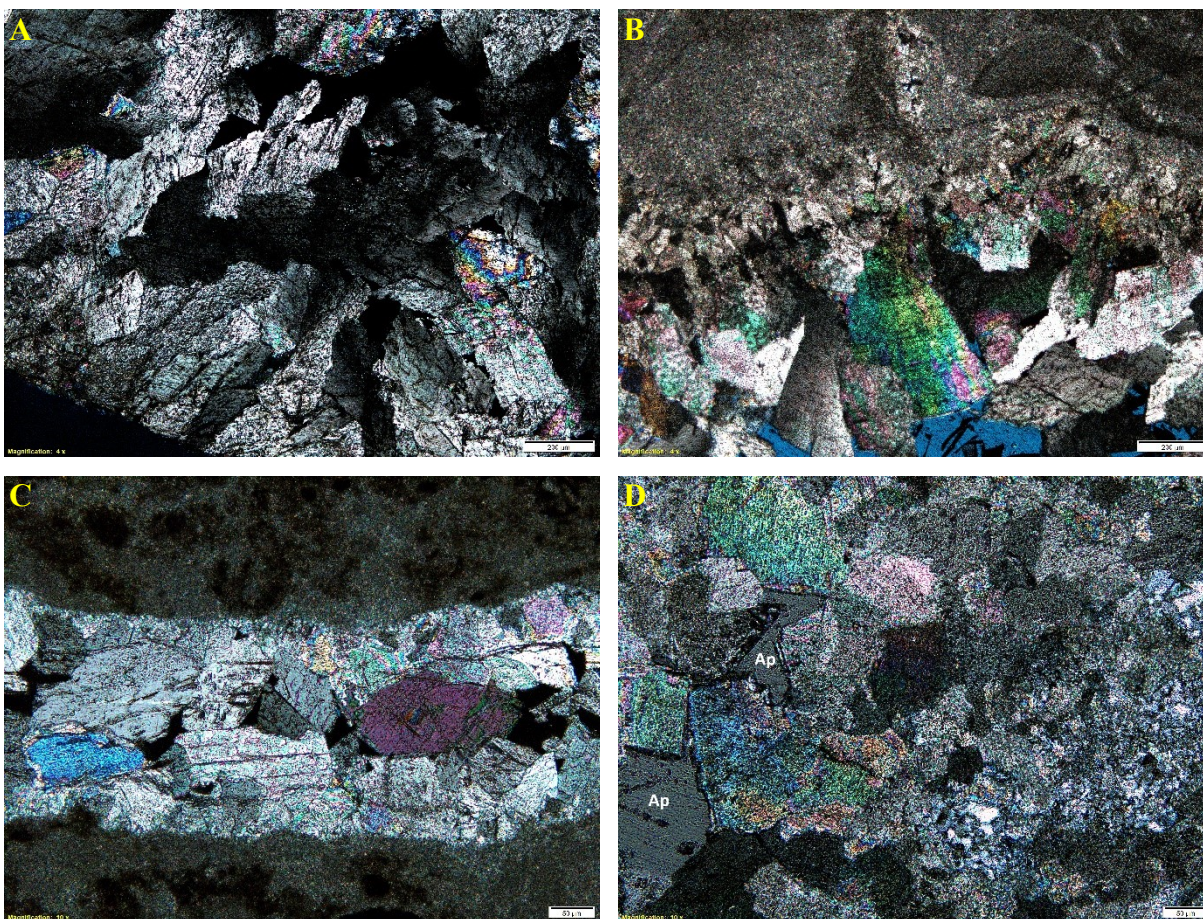
Figure 17. Oxidized sulfide minerals (A) A highly oxidized iron sulfide (lower center) alongside void-filling pyrite and chalcopryite in Sample 31 (dn⁴, Depth = 5385.5 m), RL 20x magnification (B) Oxidized sphalerite with pyrite inclusions in Sample 5c (do, DBS-1), RL 50x magnification.

Table 6. Properties of sulfide minerals identified in Dengying samples.

Mineral	PPL color	Cleavage	Hardness	Twinning	XPL colors	Reflected color	Fluorescent?	Crystal habit	Depositional environment
Sphalerite Zn(Fe)S ⁽¹⁾	gray, yellow, brown ⁽¹⁾	perfect dodecahedral ⁽¹⁾	3.5 – 4 ^(1,2,3)	Contact; lamellar ⁽⁴⁾	Isotropic ⁽¹⁾ ; internal reflections ⁽³⁾	gray (17%) ⁽³⁾	Yes ⁽²⁾	Colloform; euhedral; granular ⁽²⁾	Zinc-sulfide ore ^(2,4)
Galena PbS ⁽⁵⁾	Opaque ^(5,6)	Cubic ⁽⁶⁾	2.5 ^(3,5)	spinel-type or lamellar ⁽⁵⁾	Isotropic ⁽⁵⁾	silvery-gray, white (43%) ^(3,5)	No ⁽⁷⁾	Cubes, octahedrons; massive granular/uniform ⁽⁶⁾	lead sulfide ore ⁽⁵⁾ ; limestone deposits, hydrothermal replacement ⁽⁶⁾
Pyrite FeS ₂ ⁽⁸⁾	Opaque ⁽⁸⁾	Poor ⁽⁸⁾	6 - 6.5 ^(3,8)	penetration and contact ⁽¹⁰⁾	Isotropic ⁽⁸⁾	Pale yellow (55%) ⁽³⁾	No ⁽⁹⁾	Often cubic; pyritohedral with striated faces ⁽¹⁰⁾	sedimentary deposits; hydrothermal veins; metamorphic ⁽¹⁰⁾
Chalcopyrite CuFeS ₂ ⁽¹¹⁾	Opaque ⁽¹¹⁾	Poor ⁽¹¹⁾	3.5 – 4 ^(3,11)	penetration or cyclic ⁽¹¹⁾		Strong yellow (44%) ⁽³⁾ ; purple, blue and/or red tarnish ⁽¹²⁾	No ⁽¹³⁾	Tetrahedrons; octahedrons; massive; grainy; reniform ⁽¹¹⁾	In copper deposits; in hypothermal/ mesothermal veins; hydrothermal replacement deposits ^(11,12)
Covellite CuS ⁽¹⁴⁾	Opaque ⁽¹⁴⁾	perfect on {0001} ^(3,14)	1.5 – 2 ⁽¹⁴⁾	None ⁽¹⁴⁾		Indigo-blue ⁽¹⁴⁾	No ⁽¹⁶⁾	hexagonal plates; foliated; platy ⁽¹⁴⁾	hydrothermal supergene (1°) or weathering product (2°) ⁽⁴⁾

- Sphalerite: Mineral information, data and localities. Retrieved Dec. 7, 2019, from <https://www.mindat.org/min-3727.html>
- Sphalerite Mineral Data. Retrieved Dec. 9, 2019, from <http://webmineral.com/data/Sphalerite.shtml#Xe7NO-hKg2w>
- Lambart, S. (presentation slides). Chapter 7 Reflected light optic. Retrieved from <http://sarahlambart.com/teaching/optmin-07.pdf>
- John W. Anthony, Richard A. Bideaux, Kenneth W. Bladh, and Monte C. Nichols, Eds., Handbook of Mineralogy, Mineralogical Society of America, Chantilly, VA 20151-1110, USA. <http://www.handbookofmineralogy.org/>
- Galena: Mineral information, data and localities. Retrieved Dec. 7, 2019, from <https://www.mindat.org/min-1641.html>
- Galena: The mineral galena information and pictures. Retrieved Dec. 9, 2019, from <https://www.minerals.net/mineral/galena.aspx>
- Galena Mineral Data. Retrieved Dec. 9, 2019, from <http://webmineral.com/data/Galena.shtml#Xe7NB-hKg2w>
- Pyrite: Mineral information, data and localities. Retrieved Dec. 7, 2019, from [ww.mindat.org/min-3314.html](https://www.mindat.org/min-3314.html)
- Pyrite: The mineral pyrite information and pictures. Retrieved Dec. 9, 2019, from <https://www.minerals.net/mineral/pyrite.aspx>
- Pyrite Mineral Data. Retrieved Dec. 9, 2019, from <http://webmineral.com/data/Pyrite.shtml#Xe7M0ehKg2w>
- Chalcopyrite: Mineral information, data and localities. Retrieved Dec. 7, 2019, from <https://www.mindat.org/min-955.html>
- Chalcopyrite: The mineral chalcopyrite information and pictures. Retrieved Dec. 9, 2019, from <https://www.minerals.net/mineral/chalcopyrite.aspx>
- Chalcopyrite Mineral Data. Retrieved Dec. 9, 2019, from <http://webmineral.com/data/Chalcopyrite.shtml#Xe7MeehKg2w>
- Covellite: Mineral information, data and localities. Retrieved Dec. 7, 2019, from <https://www.mindat.org/min-1144.html>
- Covellite: The mineral covellite information and pictures. Retrieved Dec. 9, 2019, from <https://www.minerals.net/mineral/covellite.aspx>
- Covellite Mineral Data. Retrieved Dec. 9, 2019, from <http://webmineral.com/data/Covellite.shtml#Xe7EJehKg2w>

Sulfides commonly fill pores and veins along with saddle dolomite, anhydrite, and barite (Figure 18a-c). Anhydrite displays 2nd and 3rd order interference colors and often has curved faces when filling dissolution pores (Figure 18b). Barite is diagnosed by its 90° cleavage angles, and low (up to 1st order orange) interference colors. Coarse crystalline dolomite, sulfate minerals and occasionally metasomatic quartz also replace original micrite (Fig. 18d, f). Sample 14 also contains a hexagonal mineral with high relief, no cleavage and very low interference colors (dark-medium gray) that is likely apatite (Figure 18d). Dolomite crystals show characteristics of metamorphism, including undulose extinction (Figure 18a) and thick lamellar twins (Figure 18e).



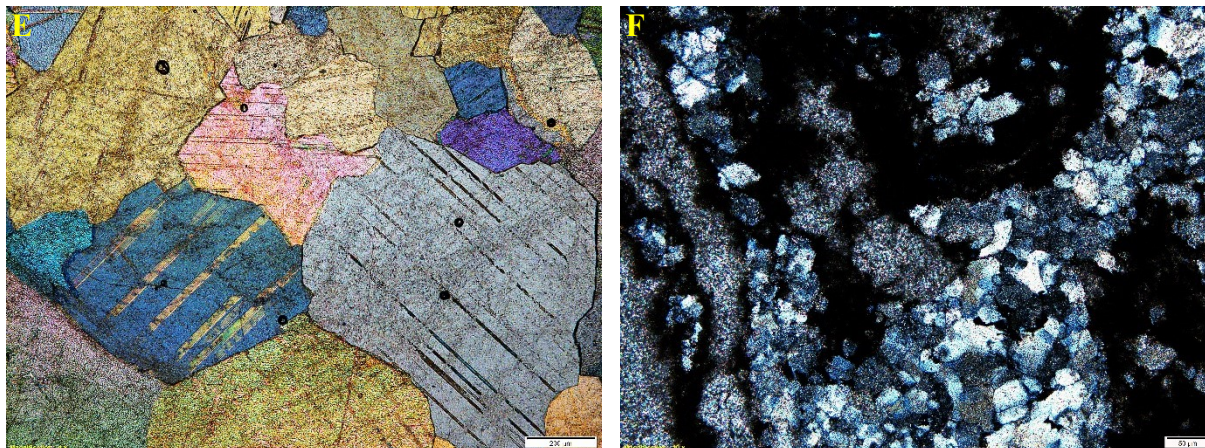


Figure 18. Hydrothermal minerals (non-sulfides) (A) Elongate dolomite crystals with windmill-like undulose extinction in Sample 18 (dn⁴, depth = 5224.79 m). XPL 4x magnification (B) Fine-grained clotted peloidal fabric with dissolution pore filled by saddle dolomite and anhydrite (black chunks in epoxy are pyrite) Sample 22 (dn⁴, Depth = 5313.15 m). XPL 4x magnification (C) Vein filled with polygonal dolomite-barite-anhydrite cement in Sample 19 (dn⁴, Depth = 5320.86 m). XPL 10x magnification (D) Coarsely crystalline dolomite, anhydrite, apatite (Ap) and microcrystalline quartz in Sample 14 (dn⁴, Depth = 5333.17 m) (E) Polygonal cement with large crystals, some of which display lamellar twinning, in Sample 2c (dn³, MCS) XPL 4x magnification (F) Microcrystalline metasomatic quartz in Sample 25 (dn⁴, Depth = 5300.13 m). XPL 4x magnification.

Deformation microstructures also occur at all sites. Nine of the well core samples and 3 of the Dabashan outcrop samples contain stylolites (Figure 16c, Figure 19a), although none of the dn³ samples have them. These are mostly sutured type microstylolites, although size varies considerably (0.5 – 15 mm max. amplitude; 0.05 – 1.7 mm max. thickness). Seven samples contain vertical stylolites, which unlike horizontal stylolites, require compression to form (Van Golf-Racht, 1982). Fractures are ubiquitous throughout the sample set (Figure 19b-e). The most common type of fracture in dn⁴ core is bitumen-filled microcracks (Figure 19b). Larger cracks and veins are filled with blocky mineral cements (Figure 18c, Figure 19c, d) and other cracks remain unfilled. dn³ outcrop samples lack bitumen-filled cracks; mineral-filled cracks are more common in outcrop samples generally. Other petrographic features signal tectonic stress, such as minerals with fibrous surface texture in some of the well core (Figure 19e). Orange arrows in Figure 19c show the direction of shear stress based on misaligned laminae and stepped sigmoidal cracks (Thiele et al., 2015) in Sample 24. Dengying outcrop samples in group 9 contain

cataclastic deformation bands (Figure 19f), with p-foliation, which also result from shear stress (Blenkinsop, 2000). Brecciation (Table 4, Sample 29) implies at least one period of tectonic extension.

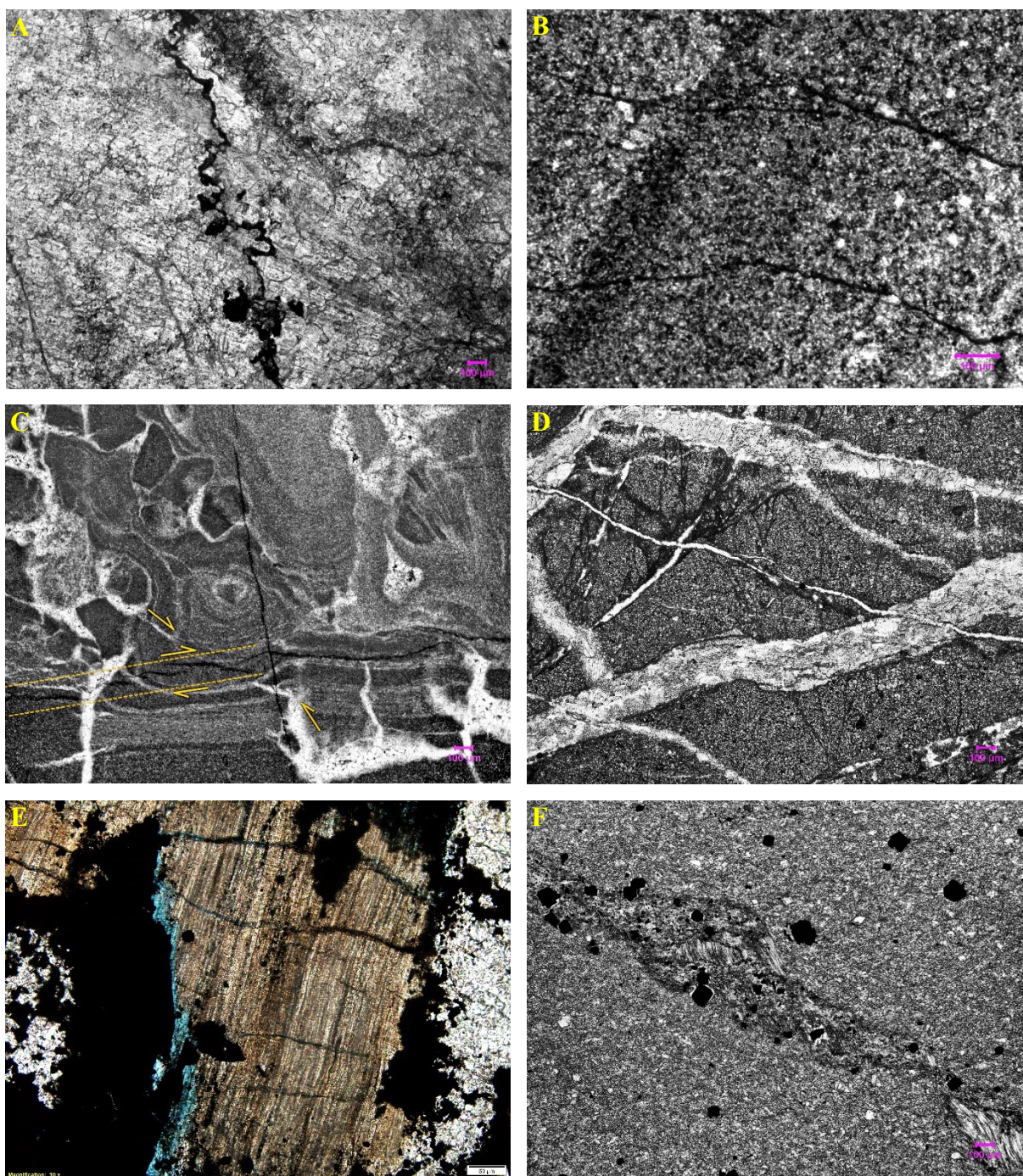


Figure 19. Deformation microstructures (A) Vertical stylolites in Sample 18 (dn^4 , Depth = 5224.79 m). PPL 4x magnification (bedding plane) (B) Bitumen-filled microcracks in Sample 20 (dn^4 , Depth = 5317.93 m). XPL 4x magnification (C) Stepped sigmoidal microcracks with a perpendicular bitumen-filled microfracture; orange arrows

show the direction of displacement; circumgranular cracks at top left, Sample 24 (dn⁴, Depth = 5308.71 m). PPL 4x magnification (D) Intersecting veins and cracks in Sample 4a (do, DBS-1, Dabashan). PPL 4x magnification (E) Fibrous mineral surface in Sample 27, with cracks (dn⁴, Depth = 5383.04 m). PPL 10x magnification (F) Deformation band in Sample 9 with segments of foliation (dn³, DBS-1). PPL 4x magnification.

Discussion

Microbial evidence

Microbial forms identified in dn⁴ of the Gaoshiti-Moxi area are consistent with assessments by other authors (e.g., Li et al., 2013; Chen, Y. et al., 2017; Shan et al., 2017): laminated (except Li et al., 2013), stromatolitic and thrombolitic. Li et al. (2013) mentioned oncolites, but without any reference images. Shan et al. (2017) also found oncolitic samples in dn² core that resemble the oncolite sample in this study from dn³ outcrop (Figure 20). Chen, Y. et al. (2017) mentioned dendrites, but did not provide images. Members 2 and 4 are generally regarded as the microbialite members of the Dengying Formation (Li et al., 2013; Lin et al., 2017; Chen et al., 2017), so it was somewhat surprising to find oncolitic and thrombolitic forms in dn³ (Sample 2, MCS), although they have been identified in dn¹, dn² and dn⁴ at the same site (Song et al., 2018). The oncolites found in dn² (Shan et al., 2017) are about twice the size of oncolites in dn³ (this study), suggesting that they may have accumulated over a greater length of time. Sample 2f also bears a strong resemblance to the ~750 Ma Beck Spring dolomite of Southern California (Harwood & Sumner, 2011, 2012); both have cavity-filling mesoclots surrounded by isopachous cement (Figure 21a, b) and laminations that encase clotted masses (Figure 21c, d). Again, microbialite textures from this study are on a smaller scale; about 1:1.06 for the mesoclots and 1:1.76 for the clotted masses. The oncolites are likely biogenic, based on their resemblance to other microbialites, and the lack of outward-thinning laminae typical of abiotic coated grains (Mariotti, et al. 2018).

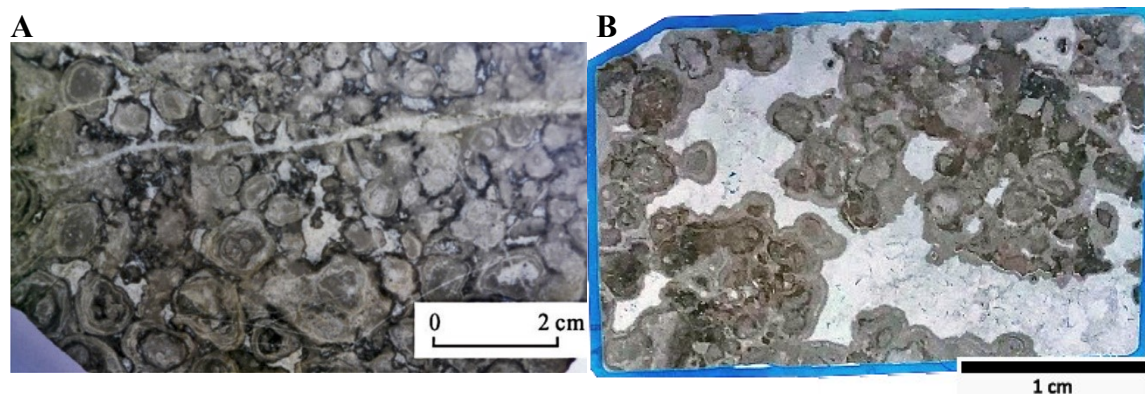


Figure 20 (A) “Oncolite dolomite in the open platform facies of Member 2 of Dengying Formation, at depth of 3396.1 m of Well W117” from Shan et al. (2017) (B) Oncolite in dn^3 from the Micangshan outcrop site (this study).

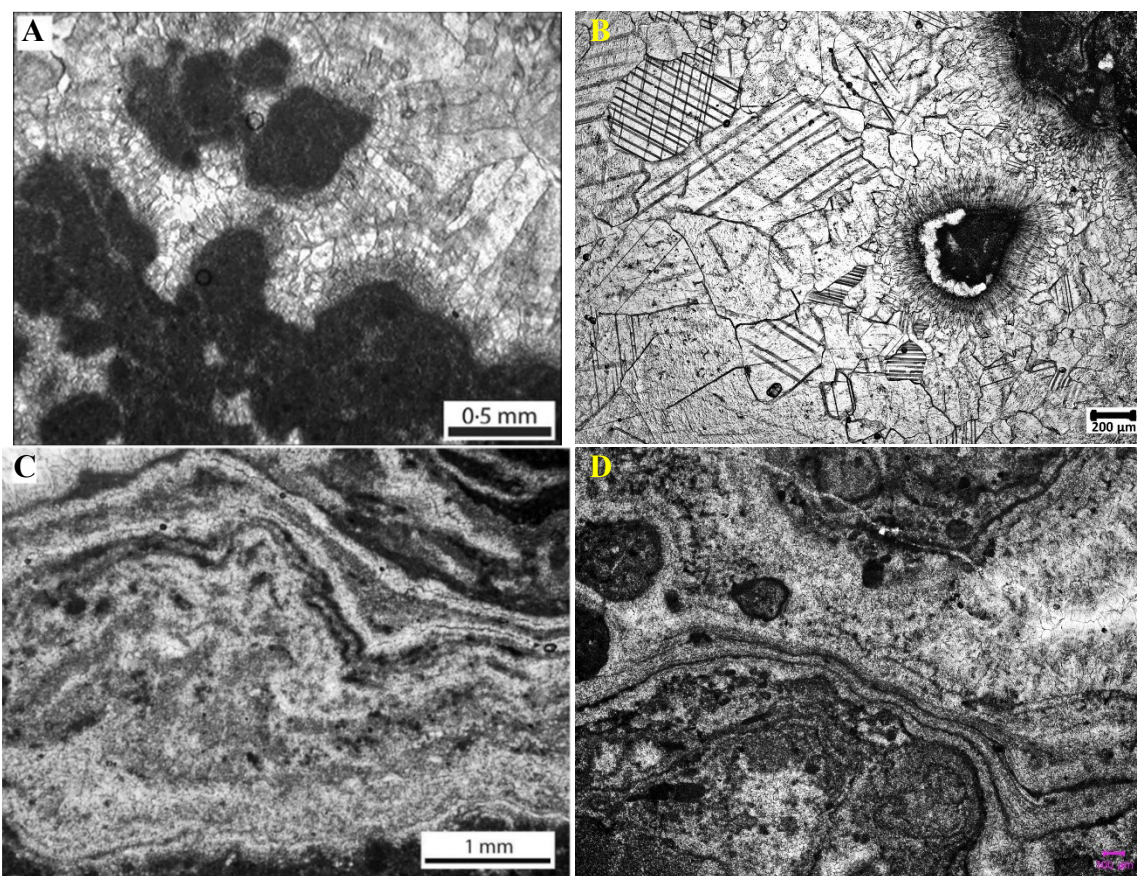


Figure 21 (A) “Distinct micritic mesoclots branch in from the edge of a cavity” from Harwood & Sumner (2011) (B) from Sample 2f (this study) (C) “Laminae with varying distinctness dome over and texturally grade into diffuse and irregular clots” from Harwood & Sumner (2012) (D) from Sample 2f (this study).

Tosti & Riding (2017) lay out criteria for distinguishing precipitated stromatolites from agglutinated stromatolites, even after recrystallization of the original fabric. Agglutinated stromatolites tend to have low synoptic relief, while the laminae of precipitated stromatolites

often have high relief and envelop underlying laminae. Laminae of agglutinated stromatolites have uneven thickness, crosscut one another, end abruptly, or pinch out, while precipitated stromatolites have even continuous laminae. Changes in sedimentation result in branching columns that migrate and change width for agglutinated stromatolites. Precipitated columnar stromatolites stay the same width and rarely branch at all. Clotted peloidal micrite has been attributed to *in situ* precipitation (Chafetz & Buczynski, 1992; Riding & Tomas, 2006). However, precipitated micrite typically has an organic nucleus at the center of each peloid (see Folk & Chafetz, 2000). Only Sample 28 (Figure 9) has nuclei at the center of microspheroid aggregates. In most of the samples organic matter fills intergranular spaces, implying that the micrite precipitated before becoming incorporated into the mat.

The dominance of cocci in the laminae of Sample 28 suggests a low sedimentation rate (Grotzinger & Knoll, 1999). The cocci themselves may be evidence of bacterial sulfate reduction; similar sphaleritic nanospheroids were described by Moreau et al. (2004) as growing in a modern SRB-dominated biofilm. Analogous forms are also present in late Ediacaran to early Cambrian microbial carbonates from the Ara Group in central Oman. These are described by Mettraux et al. (2014) as clumps of microdolospar rather than sphaleritic cocci. Spherules in this study are intermediate in size between the two analogues (Fig. 22) so neither explanation is more likely on the basis of scale. Because the spheroids in the Dengying samples fluoresce red-orange in blue-violet light, while the surrounding cement fluoresces blue-green (as does all the carbonate and quartz), they are likely of a different mineralogy. Samples from Mettraux et al. (2014) are only presented in white transmitted light, making comparison difficult.

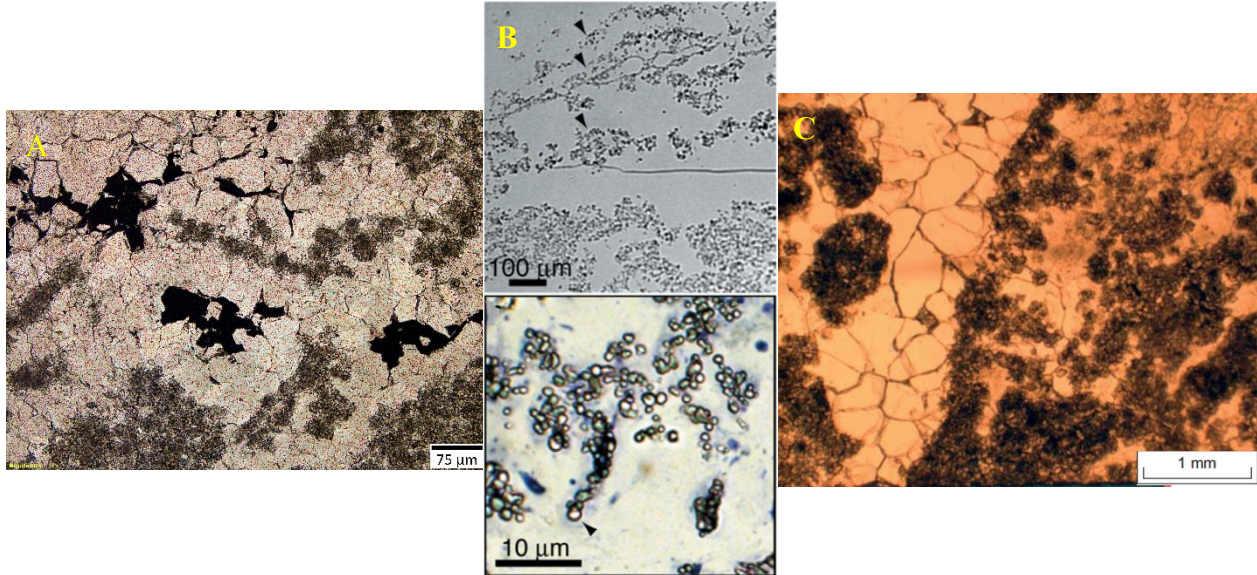


Figure 22. Comparison of aggregated coccoid laminations in (A) Sample 28 of this study (bedding plane, 20x magnification. PPL) (B) A modern SRB biofilm from Tennyson, Wisconsin described by Moreau et al. (2004) (C) Thrombolite from the Ara Group (late Ediacaran – early Cambrian) of Qarn Alam salt dome, Oman (Mettraux et al., 2014).

Tosti & Riding (2017) found that a high sedimentation rate encourages branching columns, which would indicate that the stromatolite represented by Sample 26 was subject to greater sediment supply that then decreased over time. Changes in stromatolite morphology also reflect changes in sea level (Patranabis Deb, 2018). Based on the morphologies in dn⁴ samples, the setting in the Moxi area fluctuated from shallow subtidal, to intertidal to deep subtidal (Fig. 23).

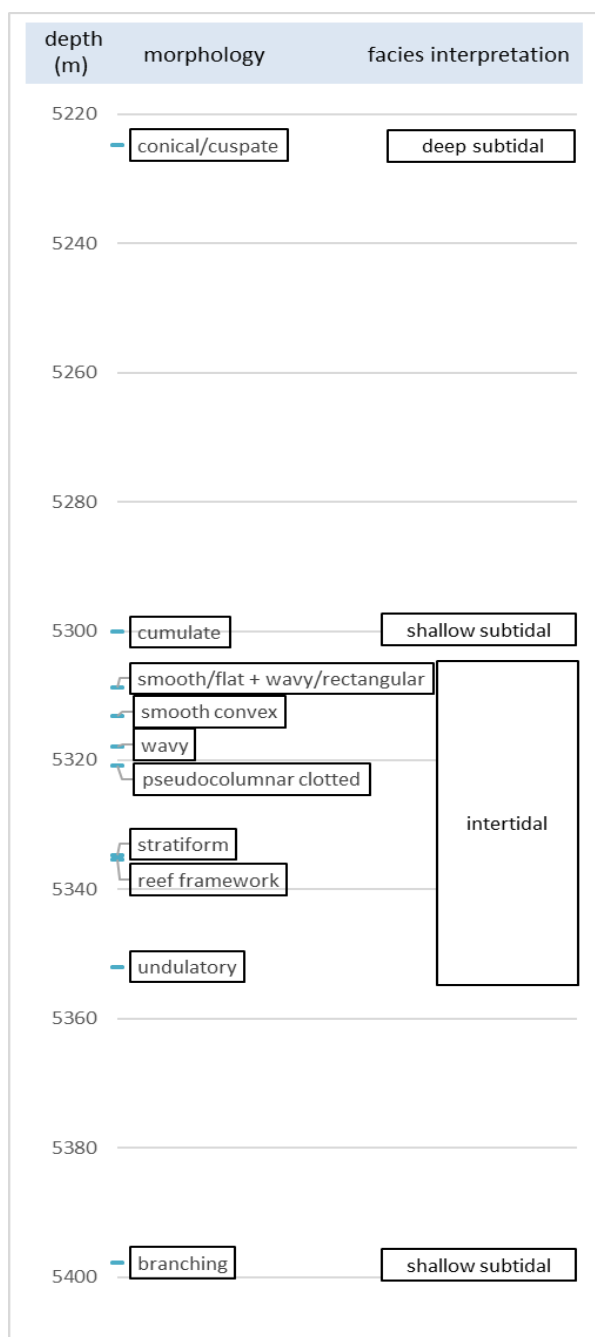


Figure 23. Microbialite morphology with depth in dn^4 samples from the central basin. Each morphotype is labeled with its coinciding facies interpretation, based on Patranabis Deb et al. (2018). Desiccation cracks in Samples 19 through 24 (depth = 5320.86 – 5308.71 m) suggest subaerial exposure, bolstering an intertidal facies interpretation for these samples.

Previous work has not acknowledged the presence of framboidal pyrite in the Dengying Formation although framboids have been identified in the Doushantuo (She et al., 2016; Wang et al., 2012). Framboidal pyrite is often associated with the metabolism of sulfate-reducing bacteria

in early diagenesis (Popa et al., 2004; Folk, 2005; Zhao et al., 2018) or with water column euxinia (Lyons, 1997; Sawłowicz, 2000). Methane oxidation also favors the precipitation of framboidal pyrite with Mg-calcites (Konhauser & Riding, 2012). However, interpretations of framboidal pyrite are dubious since framboids may form long after deposition during late diagenesis, hydrothermal alteration, or metamorphism (Scott et al., 2009; Sawłowicz, 2000). Framboids in these samples are associated with peloidal organic laminations, which give equivocal evidence for biological influence in their formation.

Paleoecological interpretation

It is impossible to make any general interpretations about Ediacaran seawater from these samples. Microbial mats by nature create a microhabitat distinct from the surrounding seawater, and furthermore, the samples from this study have been recrystallized. From the lack of bioturbation in the microbialites we can infer that the system is microbially dominated, and likely lacked eukaryotes entirely. This is somewhat surprising, given the well-preserved putative metazoans in nearby Doushantuo sections. The lack of animal evidence could be due to inhospitable anoxic or euxinic conditions (Beghin et al., 2017), or other factors affecting the distribution of early animals. The dominance of pyrite and lack of non-sulfide iron minerals indicates that the concentration of H_2S exceeded available iron at some point; however, most of the pyrite could have formed after deposition from alteration by sulfidic hydrothermal fluid (Chen et al., 2009), so this is not a reliable metric for paleoenvironmental interpretation. The presence of black shales in dn³ of MCS, a tidal flat environment (Song et al., 2018; Li et al., 2014), could indicate anoxia in shallow water. Anoxia favors the formation of black shales but is not always required.

Hydrothermal alteration

Liu et al. (2016) attribute most of the pyrite in the Dengying to thermochemical sulfate reduction (TSR), based on its morphology and sulfur isotopic composition. This requires that the formation reached or exceeded the temperature window at which TSR occurs, 200° to 350° C (Seal, 2006). Thick lamellar and polysynthetic twins (see Fig. 18e) occur in calcite (and presumably dolomite, since both display “calcite” twinning) at 150° to 300°C (Blenkinsop, 2000).

Several authors have analyzed fluid inclusions to estimate the temperature of hydrothermal fluids that altered the Dengying Formation. Based on data from eight such studies (Jiang et al., 2016; Liu et al., 2016; Chen, Y. et al., 2017; Feng et al., 2017; Zhu et al., 2017; Peng et al., 2018; Xu et al., 2018 & Zhang et al., 2019), the best estimate for the maximum temperature of the hydrothermal fluids is 236°C ±19°C. The fluid would have cooled as it rose, such that fluids in the Doushantuo would have been significantly hotter. Based on clay mineral ratios in the lower Huajipo and Jiulongwan sections of the Doushantuo Formation, Derkowski et al. (2013) estimate that the hydrothermal fluid was 300°C or hotter. Fluid inclusion analysis by Zhou et al. (2015) points to a maximum temperature of 378°C.

Tectonic stress

For biomarker preservation, the rate of heating has a strong influence. Rapid heating from contact with hydrothermal fluid may enhance the preservation of biomarkers, while slow, geothermal heating is more deleterious (Waples, 2000). Because of this, it is significant that even core samples from the gentle structural zone of the Sichuan Basin contain evidence of tectonic stress. Styolites are a symptom of pressure dissolution, which requires both fluid flow and pressure. Horizontal styolites are thought to be diagenetic features, while vertical styolites require tectonic compression (Van Golf-Racht, 1982). Vertical styolites appear in several of the

core samples (Fig. 19a). A few samples contain stepped sigmoidal cracks (Fig. 19c) and fibrous mineral textures (Fig. 19e), both features of shear stress (Bons et al., 2012). Plenty of literature has been published on the complex tectonic history of the Sichuan Basin and its periphery (Gu et al., 2016; Xu et al., 2018), consisting of extension, uplift, folding and compression. All of this would have increased the temperature of the formation more gradually than hydrothermal fluid flow events, and thus contributed to the breakdown of molecular fossils. Indeed, when the HI/OI ratio of kerogen from these samples is plotted on a pseudo-Van Krevelen diagram, they fall into the type IV “inert” range (Fig. 24).

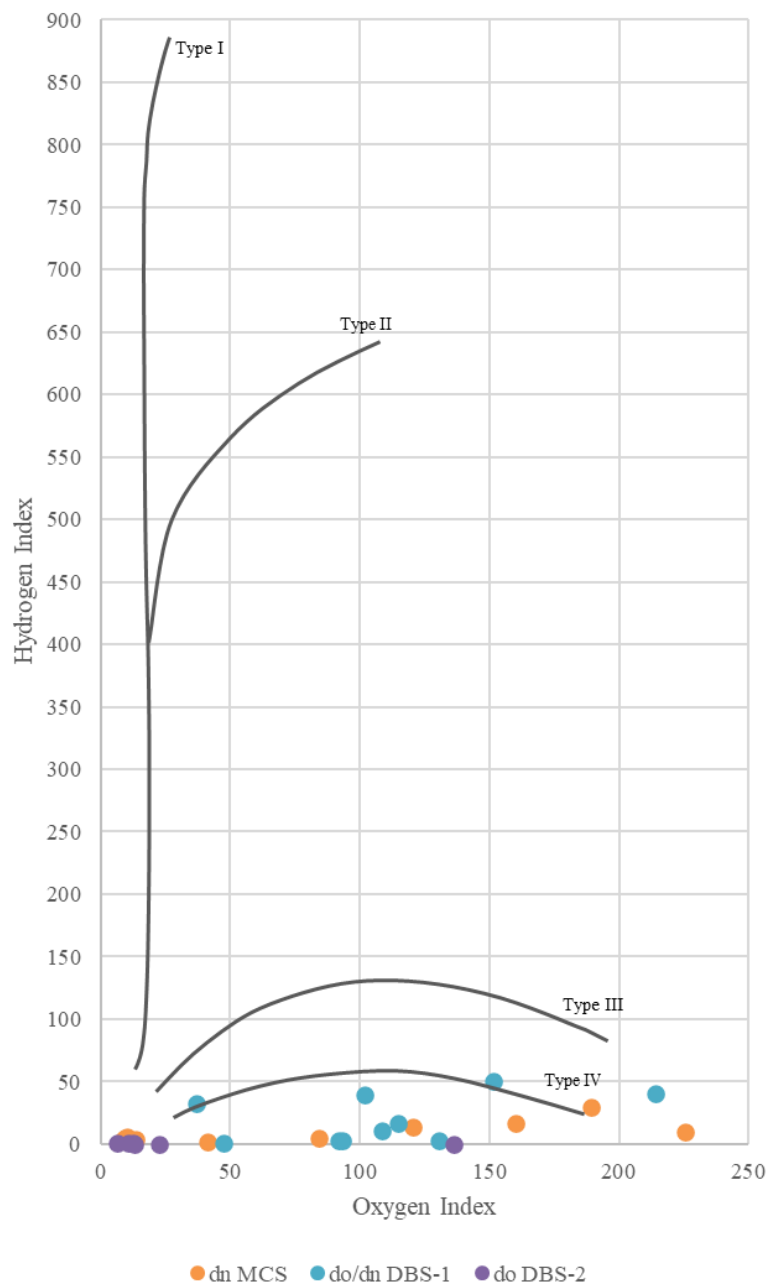


Figure 24. Pseudo-Van Krevelen diagram of kerogen types; x-axis = Oxygen Index ($100 \cdot S_3/TOC$) y-axis = Hydrogen Index ($100 \cdot S_2/TOC$). Type I = Hydrogen-rich, oil-prone; type II = oil and gas prone; type III = gas prone; type IV = inert (kerogen types referenced from AAPG Wiki).

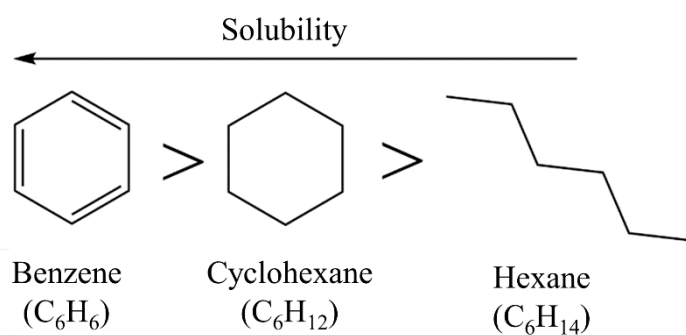
Biomarkers

n-Alkanes are the most commonly preserved biomarkers (Brocks & Summons, 2003) but offer virtually no taxonomic or environmental information, as their precursors are synthesized by most

taxa and they can result from the thermal breakdown of other hydrocarbons. Temperature estimates in both the Dengying and Doushantuo Formations exceed the highest survivable temperature for molecular fossils (220° C; Brocks & Summons, 2003), so the near absence of extractable compounds in these rocks could be entirely explained by thermal alteration (Chen et al., 2009; Shi et al., 2013; Liu et al., 2014; Jiang et al., 2016; Liu et al., 2016; Feng et al., 2017). However, experimental studies suggest that temperature alone is insufficient for complete degradation (Mango et al., 1994; Mango & Hightower, 1997).

HI and TOC are negatively correlated in these data (Fig. 25). Low HI in samples with TOC > 0.5 indicates a high concentration of large aromatic compounds. Hydrocarbons become aromatized with increasing thermal maturity (Gaines et al., 2009) and oxidative weathering (Simoneit, 2004). Light hydrocarbons (< C₁₀) are especially soluble in water (Elliott, 2015), so catalysis of hydrocarbons followed by removal via water washing could be a mechanism to explain low TOC in microbialite samples (i.e., Sample 2). Since unsaturated (aromatic or cyclic) hydrocarbons are more soluble than straight chain hydrocarbons of the same C number, water washing could also explain why HI is greater in samples with low TOC (Fig. 25).

e.g.,



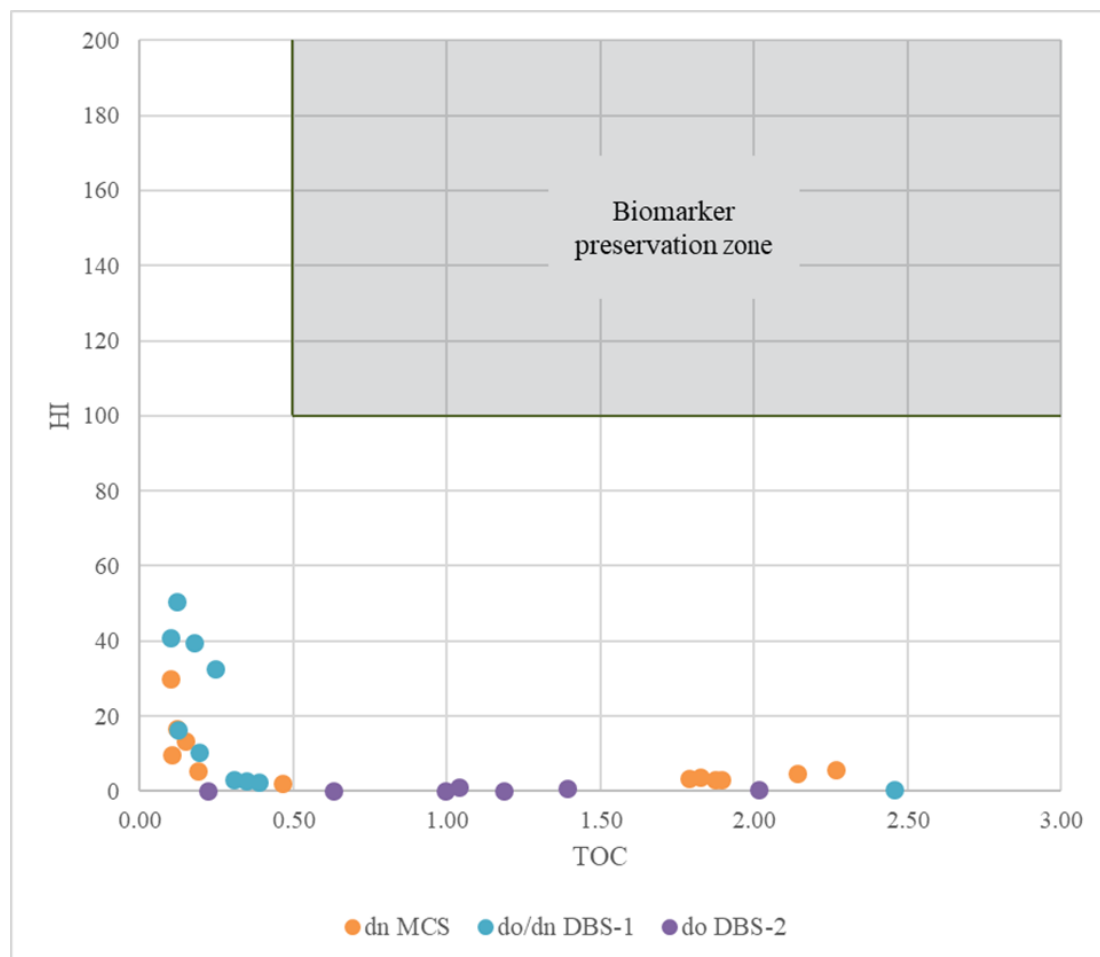


Figure 25. Hydrogen Index ($100 \cdot S_2/TOC$) vs Total Organic Carbon (TOC). Biomarkers generally can be extracted from rocks with $TOC \geq 0.5$ and $HI \geq 100$. Though 13 of the samples have $TOC \geq 0.5$, all fall short of the minimum hydrogen content.

A few other studies have reported on biomarkers extracted from the Dengying Formation. Duda et al. (2014a, b) extracted n-alkanes, PAHs, and trace amounts of steranes and hopanes from the Shibantan Member of the Dengying via HyPy catalytic pyrolysis. This method releases hydrocarbons from kerogen, which enhances biomarker extraction from thermally mature samples and guarantees that the compounds are syngenetic (Love et al., 1995). Although the samples used by Duda et al. (2014a, b) are thermally mature ($T_{max} \geq 500^\circ\text{C}$), they have a hydrogen index equal to 125 mg/g. Despite intense thermal history, other conditions in the Yangtze Gorges area make the site more amenable to biomarker preservation than the Sichuan

Basin. For example, the Dengying Formation in the Yangtze Gorges area is mostly micrite, with no signs of recrystallization (Duda et al., 2014a). Nevertheless, Duda et al. (2014b) found that extractable bitumen from the samples was nearly entirely contamination and that decalcification, in addition to pyrolysis was necessary to isolate indigenous hydrocarbons. They suggest that extensive microfractures could serve as conduits for oil migration. While Duda et al. (2014a, b) acknowledge the dubious origins of solvent-extractable biomarkers in the Shibantan Member, Li et al. (2006) claim that molecular markers they extracted from bitumen in the same area (n-alkanes, regular acyclic isoprenoids, tricyclic terpanes, hopanes, gammacerane, steranes and PAHs) are indigenous.

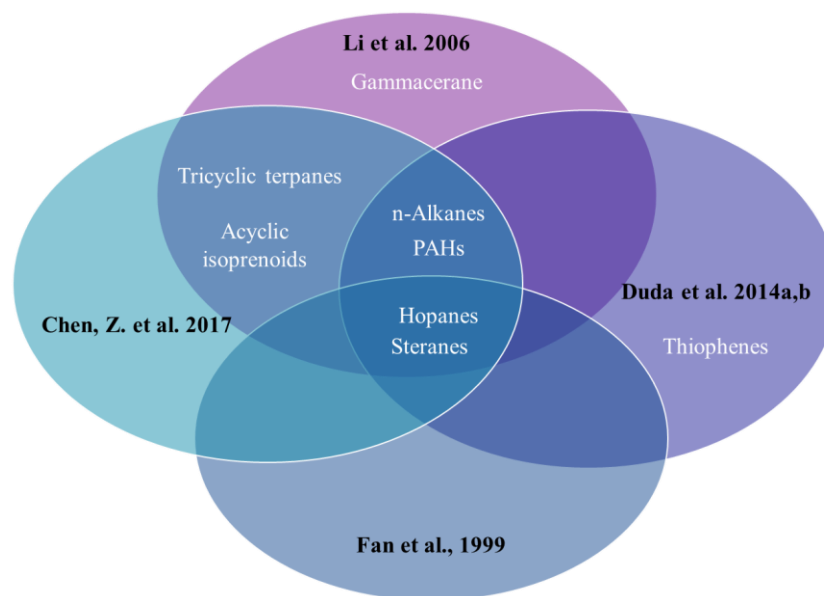


Figure 26. A Venn diagram comparing biomarkers extracted from Dengying carbonate in 4 studies: Fan et al. (1999), Li et al. (2006), Duda et al. (2014) and Chen Z., et al. (2017, 2018).

Fan, et al. (1999) found hopanes and steranes in the Goayan Mn-carbonate deposit (Doushantuo, near DBS-1 of this study), which they interpreted as representing bacterial and algal sources. Although their samples had high TOC (mean 2.84%), the hydrogen index was 0, making it very unlikely that the hopanes and steranes were authigenic. Chen, Z. et al. (2017,

2018) found bitumen from dn⁴ in the Gaoshiti Moxi (G-M) area to be highly thermally mature based on vitrinite reflectance (%Rb \approx 2.96), but managed to extract hopanes, steranes, n-alkanes, PAHs, tricyclic terpanes, and acyclic isoprenoids. Their interpretations are challenged by Huang & Li (2018). Li et al. (2006), Duda et al. (2014) and Chen et al. (2017) used larger capillaries and longer, cooler oven programs to analyze PAHs, while the method used in this study is optimized for identifying saturated hydrocarbons and unable to record large aromatic compounds. See Appendix D for a detailed comparison of methods used in each study (methods from Fan et al., 1999 are not specified).

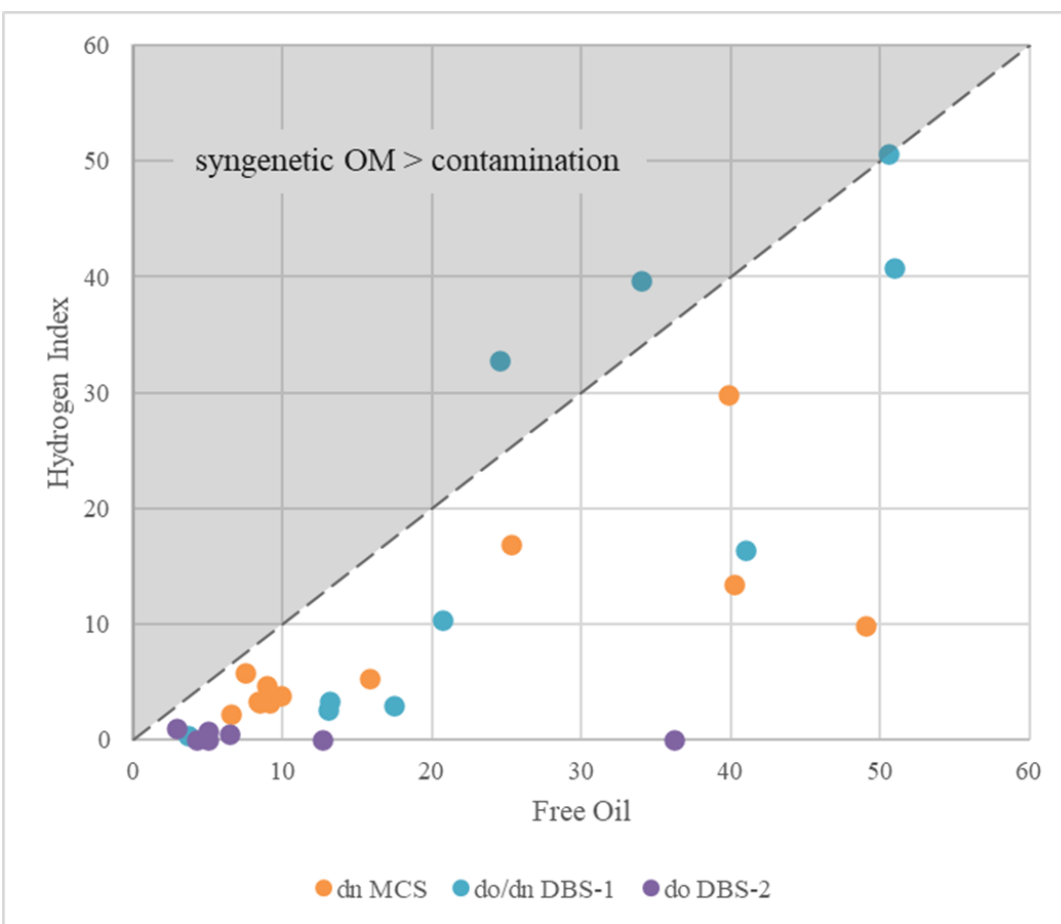


Figure 27. Hydrogen Index ($100 \times S_2/TOC$) vs Free Oil ($100 \times S_1/TOC$). S_2 represents kerogen (i.e. syngenetic organic carbon) while S_1 represents free hydrocarbons. High free oil indicates that biomarkers found in these rocks are likely from post-depositional oil migration. The two points within the area of syngenetic OM > contamination represent 6a (Doushantuo) and 9a (Dengying) which have TOC = 0.24% and 0.18%, respectively.

Reliability of geochemical data

The oxygen index (OI) may be overestimated due to interference of mineral pyrolysis. This happens in samples with high carbonate content and low TOC (Hunt, 1996). Clay minerals may also interfere, causing the HI to be underestimated and the OI to be overestimated (Hunt, 1996). T_{max} is commonly underestimated in samples with mostly inert organic matter (Wilkins, 1999) or migrated oil (King, 2015). T_{max} is typically correlated with $\%R_0$ by the equation:

$$(1) \quad \%R_0 = 0.0180 \times T_{max} - 7.16 \text{ (based on Barnett Shale core samples)}$$

If vitrinite reflectance in the G-M area is 2.96% (Chen, Z. et al., 2017), T_{\max} would be 562.2°C. Measured T_{\max} in this study is significantly lower, and likely inaccurate.

Conclusions

Low HI and high S3 make clear that biomarker extraction is not feasible for the outcrop samples (Table 2, 3). Samples with TOC > 0.5 have extremely low HI, indicating advanced aromatization of hydrocarbons, likely catalyzed by tectonic pressure and/or contact with hydrothermal fluids. Some microbialite samples have surprisingly low TOC, possibly as a result of hydrocarbon catalysis and subsequent removal via water washing. T_{\max} values indicate that the samples are thermally immature, but this is likely underestimated, as is common for samples with low hydrogen and high sulfur content. The production index is 0.75 ± 0.16 in the outcrop samples, indicating that most of the hydrocarbons (~75%) are from migrated oil, unrelated to the formation of the rocks. Extensive microfractures could have served as conduits for oil from overlying Cambrian black shale units into the Dengying and Doushantuo Formations. Since cores have not been exposed to excessive oxidative weathering and the G-M area has a gentler tectonic history than the basin margins, it may be possible to extract biomarkers, via HyPy pyrolysis with decalcification, from core samples. It would be useful to analyze the geochemistry of the G-M area core samples to assess their amenability.

Although biomarker analysis was inconclusive, cores and outcrop samples preserve signs of syndepositional microbial activity. Microbialites include stromatolites, thrombolites, and oncolites (outcrop only). Stromatolites are diverse in their morphology, suggesting change to the environment over the interval. Four stromatolites show signs of subaerial exposure, as well as ductile deformation and redeposition. The original micrite is preserved in some areas. Micritic texture, along with low synoptic relief and lateral inconsistency in the laminations, together

indicate that the stromatolites grew by grain trapping rather than *in situ* precipitation.

Stromatolitic and laminar peloidal fabric is sometimes accompanied by framboidal pyrite, which offers equivocal evidence for bacterial sulfate reduction, as do layered aggregates of sphalerite microspheroids.

Future work

Researchers interested in continuing investigations of the Dengying microbialite in the Sichuan Basin should use core samples from the basin interior rather than outcrop. Had there been more time for this study, it would have been interesting to get TOC, T_{\max} , and kerogen type from the core samples to confirm whether biomarker extraction would be possible. Future studies should use better collection and extraction methods. For this study, samples were wrapped in pre-combusted foil to avoid contamination from plastic bags; however, much of the foil was dissolved when the samples arrived, as is common for samples with high pyrite content (Brocks et al., 2008), so the samples were in contact with plastic regardless. Brocks et al. (2008) recommend the use of combusted glass jars for sample storage to avoid contamination, but since the samples have likely already been contaminated by migrated oil, drilling equipment, etc., glass jars are not worth the extra shipping cost, and polyethylene bags are more appropriate. Solvent cleaning alone is insufficient to remove contaminants, so before solvent washing, the exterior of samples should be sliced off with a sterile rock saw (Brocks et al., 2008). Hydrocarbons from exterior slices may also be extracted and analyzed for comparison with the interior portions; hydrocarbons found exclusively in the interior slices are more likely to be authigenic (Duda et al., 2014b). Using exterior/interior comparison only accounts for surface contamination, however. Kerogen (insoluble organic matter), extracted via decalcification and

hydropyrolysis (HyPy) of previously solvent-extracted samples, is less mobile than bitumen and therefore more likely to be authigenic. Composition of kerogen and bitumen can be compared in the same manner as interior/exterior slices, and the bitumen mass spectra subtracted from the kerogen mass spectra. Considering the age and thermal history of the Dengying Formation, this study would also have benefitted from using a larger GC capillary appropriate for aromatic compounds; 0.32mm internal diameter is recommended (e.g., Duda et al., 2014a, b; Li et al., 2006). Saturated hydrocarbon fractions can be separated from the aromatic fraction by liquid chromatography (e.g., Kelly, 2009) and analyzed separately on full scan mode. Aromatic compounds should be analyzed in selective ion monitoring (SIM) mode (e.g., Kelly, 2009; Brocks et al., 2003). Researchers interested in the hypothetically SRB-preserving sphalerite microspheroids in Sample 28 should start by confirming that the microspheroids are indeed sphalerite, or some other sulfide byproduct of SRB metabolism, using another mineral identification method, such as X-ray diffraction (XRD) or Raman spectroscopy. Images of the coccoids under higher magnification or using a scanning electron microscope may also be useful. Sulfur isotopic composition is used as evidence for or against SRB involvement in pyrite framboid formation (e.g., Schieber, 2002; Popa, 2004), however the isotope signature may be overprinted by hydrothermal alteration (Grassineau et al., 2005). The potential of the Dengying Formation microbialites for hydrocarbon analysis is not as promising as previously hoped, however interpretation of their microstructure yields some important paleoenvironmental information. Dengying Formation microbialites, in the Sichuan Basin and its northern margin, represent a dynamic sub- to intertidal environment, devoid of eukaryotic life and dominated by grain-trapping microbial mats.

References

- AAPG Wiki. (n.d.) Kerogen. Retrieved July 25, 2019, from https://wiki.aapg.org/Kerogen#Kerogen_types
- Aitken, J. D., & Narbonne, G. M. (1989). Two occurrences of Precambrian thrombolites from the Mackenzie Mountains, northwestern Canada. *Palaios* 4, 384–388.
- Allen, M. A., Neilan, B. A., Burns, B. P., Jahnke, L. L., & Summons, R. E. (2010). Lipid biomarkers in Hamelin Pool microbial mats and stromatolites. *Organic Geochemistry* 41(11), 1207–1218.
- Awramik, S. M., & Grey, K. (2005). Stromatolites: Biogenicity, Biosignatures, and Bioconfusion. In *Proceedings of SPIE* (p. 5906). Bellingham, WA, USA.
- Beghin, J., Guilbaud, R., Poulton, S. W., Gueneli, N., Brocks, J. J., Storme, J. Y., Blanpied, C., Javaux, E. J. (2017). A palaeoecological model for the late Mesoproterozoic – early Neoproterozoic Atar/El Mreïti Group, Taoudeni Basin, Mauritania, northwestern Africa. *Precambrian Research* 299(January), 1–14.
- Behar, F., Beaumont, V., & De B. Pentead, H. L. (2001). Rock-Eval 6 Technology: Performances and Developments. *Oil & Gas Science and Technology* 56(2), 111–134.
- Bian L., Hinrichs K.-U., Xie T., Brassell S. C., Iversen N., Fossing H., Jørgensen B. B., Sylva S. P., & Hayes J. M. (2001). Algal and archaeal polyisoprenoids in a recent marine sediment: molecular isotopic evidence for anaerobic oxidation of methane. *Geochemistry, Geophysics, Geosystems* 2, 1023.
- Blenkinsop, T. (2000). *Deformation Microstructures and Mechanisms in Minerals and Rocks*. Kluwer Academic Publishers.
- Bons, P. D., Elburg, M. A., & Gomez-Rivas, E. (2012). A review of the formation of tectonic veins and their microstructures. *Journal of Structural Geology* 43, 33–62.
- Briggs, D., & Summons, R. (2014). Ancient biomolecules: Their origins, fossilization, and role in revealing the history of life. *BioEssays* 36(5), 482–490.
- Brocks, J. J., & Summons, R. E. (2003). Sedimentary Hydrocarbons, Biomarkers for Early Life. *Treatise on Geochemistry* (pp. 63–115). Cambridge, MA, USA: Elsevier.
- Brocks, J. J., Buick, R., Logan, G. A., & Summons, R. E. (2003). Composition and syngeneity of molecular fossils from the 2.78 to 2.45 billion-year-old Mount Bruce Supergroup, Pilbara Craton, Western Australia. *Geochimica et Cosmochimica Acta*, 67(22), 4289–4319.

- Brocks, J. J., Grosjean, E., & Logan, G. A. (2008). Assessing biomarker syngeneity using branched alkanes with quaternary carbon (BAQCs) and other plastic contaminants. *Geochimica et Cosmochimica Acta* 72(3), 871–888.
- Cai, Y., Hua, H., Xiao, S., Schiffbauer, J. D., & Li, P. (2010). Biostratinomy of the late Ediacaran pyritized Gaojiashan lagerstätte from southern Shaanxi, South China: Importance of event deposits. *Palaios* 25, 487–506.
- Cai, Y., Xiao, S., Li, G., & Hua, H. (2019). Diverse biomineralizing animals in the terminal Ediacaran Period herald the Cambrian explosion. *Geology* 47(4), 380–384.
- Chafetz, H. S., & Buczynski, C. (1992). Bacterially Induced Lithification of Microbial Mats. *Palaios* 7(3), 277.
- Chen, D., Wang, J., Qing, H., Yan, D., & Li, R. (2009). Hydrothermal venting activities in the Early Cambrian, South China: Petrological, geochronological and stable isotopic constraints. *Chemical Geology* 258, 168–181.
- Chen, Y., Shen, A., Pan, L., Zhang, J., & Wang, X. (2017). Features, origin and distribution of microbial dolomite reservoirs: A case study of 4th Member of Sinian Dengying Formation in Sichuan Basin, SW China, *Petroleum Exploration and Development* 44(5), 745–757.
- Chen, Z., Zhou, C., Xiao, S., Wang, W., Guan, C., Hua, H., & Yuan, X. (2014). New Ediacara fossils preserved in marine limestone and their ecological implications. *Scientific Reports* 4(4180), 1–10.
- Chen, Z., Simoneit, B. R. T., Wang, T., Yang, Y., Ni, Z., Cheng, B., Luo, B., Yang, C., & Chen, T. (2017). Biomarker signatures of Sinian bitumens in the Moxi – Gaoshiti Bulge of Sichuan Basin, China: Geological significance for paleo-oil reservoirs. *Precambrian Research* 296, 1–19.
- Chen, Z., Simoneit, B. R. T., Wang, T., Ni, Z., & Yuan, G. (2018). Molecular markers, carbon isotopes, and rare earth elements of highly mature reservoir pyrobitumens from Sichuan Basin, southwestern China: Implications for PreCambrian-Lower Cambrian petroleum systems. *Precambrian Research* 317, 33–56.
- Condon, D., Zhu, M., Bowring, S., Wang, W., Yang, A., & Jin, Y. (2005). U–Pb ages from the Neoproterozoic Doushantuo Formation, China. *Science* 308 (5718), 5–98.
- Cosmidis, J., Benzerara, K., Menguy, N., & Arning, E. (2013). Microscopy evidence of bacterial microfossils in phosphorite crusts of the Peruvian shelf: Implications for phosphogenesis mechanisms. *Chemical Geology* 359, 10–22.

- Cui, H., Xiao, S., Cai, Y., Peek, S., Plummer, R., & Kaufman, A. (2019). Sedimentology and chemostratigraphy of the terminal Ediacaran Dengying Formation at the Gaojiashan section, South China. *Geological Magazine* 156, 1924–1948.
- Cunningham, J. A., Vargas, K., Yin, Z., Bengtson, S., & Donoghue, P. C. J. (2017). The Weng'an Biota (Doushantuo Formation): an Ediacaran window on soft-bodied and multicellular microorganisms. *Journal of the Geological Society* 174(5), 793 – 802.
- Derkowski, A., Bristow, T. F., Wampler, J. M., Śródoń, J., Marynowski, L., Elliott, W. C., & Chamberlain, C. P. (2013). Hydrothermal alteration of the Ediacaran Doushantuo Formation in the Yangtze Gorges area (South China). *Geochimica et Cosmochimica Acta* 107, 279–298.
- Dembitsky, V. I., Shkrob, I. & Aki, M. (2001). Branched Alkanes and Other Apolar Compounds Produced by the Cyanobacterium *Microcoleus vaginatus* from the Negev Desert. *Russian Journal of Bioorganic Chemistry* 27(2), 110-119.
- Duda, J. P., Blumenberg, M., Thiel, V., Simon, K., Zhu, M., & Reitner, J. (2014a). Geobiology of a palaeoecosystem with Ediacara-type fossils: The Shibantan Member (Dengying Formation, South China). *Precambrian Research* 255(P1), 48–62.
- Duda, J. P., Thiel, V., Reitner, J., & Blumenberg, M. (2014b). Assessing Possibilities and Limitations for Biomarker Analyses on Outcrop Samples: A Case Study on Carbonates of the Shibantan Member (Ediacaran Period, Dengying Formation, South China). *Acta Geologica Sinica* 88(6), 1696–1704.
- Dupraz, C., Reid, R. P., Braissant, O., Decho, A. W., Norman, R. S., & Visscher, P. T. (2009). Processes of carbonate precipitation in modern microbial mats. *Earth-Science Reviews* 96(3), 141–162.
- Elliott, L. G. (2015). Water Washing: A Major Hydrocarbon Alteration Process. Part 2 – Processes, Controls and Hydrocarbon Type Prediction. *Search and Discovery* Article #41750.
- Elvert M., Suess E., & Whiticar M. J. (1999) Anaerobic methane oxidation associated with marine gas hydrates: superlight C-isotopes from saturated and unsaturated C₂₀ and C₂₅ irregular isoprenoids. *Naturwissenschaften* 31, 1175–1187.
- Evans, D.A.D. (2003) A fundamental Precambrian–Phanerozoic shift in earth's glacial style? *Tectonophysics* 375, 353–385.
- Fan, D., Ye, J., Yin, L., & Zhang, R. (1999). Microbial processes in the formation of the Sinian Gaoyan manganese carbonate ore, Sichuan Province, China. *Ore Geology Reviews* 15, 79–93.

- Fan, H., Wen, H., Zhu, X., Hu, R., & Tian, S. (2013). Hydrothermal activity during Ediacaran – Cambrian transition: Silicon isotopic evidence. *Precambrian Research* 224, 23–35.
- Feng, M., Liu, X., Qiang, Z., Tao, Y., & Xia, Q. (2016). Structural Controlled Hydrothermal dolomite Reservoirs in the Precambrian Dengying Formation of the Central Sichuan Basin, Southwestern China. (Presentation) Bangkok, Thailand: AAPG Asia Pacific Region.
- Feng, M., Wu, P., Qiang, Z., Liu, X., Duan, Y., & Xia, M. (2017). Hydrothermal dolomite reservoir in the Precambrian Dengying Formation of central Sichuan Basin, Southwestern China. *Marine and Petroleum Geology* 82, 206–219.
- Folk, R. L., & Chafetz, H. S. (2000). Bacterially Induced Microscale and Nanoscale Carbonate Precipitates. In R. E. Riding & S. M. Awramik (Eds.), *Microbial Sediments* (1st ed., pp. 40–49). Springer.
- Folk, R. L. (2005). Nannobacteria and the formation of framboidal pyrite: Textural evidence. *Journal of Earth System Science* 114(3), 369–374.
- French, K. L., Hallmann, C., Hope, J. M., Schoon, P. L., Zumberge, J. A., Hoshino, Y., Peters, C. A., George, S. C., Love, G. D., Brocks, J. J., Buick, R., Summons, R. E. (2015). Reappraisal of hydrocarbon biomarkers in Archean rocks. *PNAS*, 112(19), 5915–5920.
- Gaines, S. M., Eglinton, G., & Rullkötter, J. (2009). *Echoes of Life - What Fossil Molecules Reveal about Earth History* (1st ed.). New York, New York: Oxford University Press.
- Gold, D. A., Grabenstatter, J., Mendoza, A. de, Riesgo, A., Ruiz-Trillo, I., & Summons, R. E. (2016). Sterol and genomic analyses validate the sponge biomarker hypothesis. *Proceedings of the National Academy of Sciences* 113(10), 2684–2689.
- Gould, S.J., 1989. *Wonderful World*. Norton, New York. (399 pp.).
- Grassineau, N. V., Appel, P. W. U., Fowler, C. M. R., & Nisbet, E. G. (2005). Distinguishing biological from hydrothermal signatures via sulphur and carbon isotopes in Archean mineralizations at 3.8 and 2.7 Ga. *Geological Society Special Publication* 248, 195–212.
- Gregory, D. D., Lyons, T. W., Large, R. R., Jiang, G., Stepanov, A. S., Diamond, C. W., Figueroa, M.C., & Olin, P. (2017). Whole rock and discrete pyrite geochemistry as complementary tracers of ancient ocean chemistry: An example from the Neoproterozoic Doushantuo Formation, China. *Geochimica et Cosmochimica Acta* 216, 201–220.
- Greinert, J., Bohrmann, G. & Elvert, M. (2002). Stromatolitic fabric of authigenic carbonate crusts: result of anaerobic methane oxidation at cold seeps in 4,850 m water depth. *International Journal of Earth Science* 91, 698–711.

- Grice, K., Gibbison R., Atkinson J. E., Schwark L., Eckardt C. B., & Maxwell J. R. (1996) Maleimides (1H-pyrrole-2, 5-diones) as molecular indicators of anoxygenic photosynthesis in ancient water columns. *Geochimica et Cosmochimica Acta* 60, 3913–3924.
- Grice, K., Schouten S., Nissenbaum A., Charrach J., & Sinninghe Damsté J. S. (1998) Isotopically heavy carbon in the C21 to C25 regular isoprenoids in halite-rich deposits from the Sdom Formation, Dead Sea Basin, Israel. *Organic Geochemistry* 28, 349–359.
- Grotzinger, J. P., & Knoll, A. H. (1999). Stromatolites in Precambrian carbonates: Evolutionary mileposts or environmental dipsticks? *Annu. Rev. Earth Planet. Sci.*, 27, 313–358.
- Gu, Z., Yin, J., Jiang, H., Zhang, B., Li, Q., Yuan, M., Zhai, X., Zhang, L., & Yang, F. (2016). Tectonic evolution from Late Sinian to Early Paleozoic and natural gas exploration in northwestern Sichuan Basin, SW China. *Petroleum Exploration and Development* 43(1), 1–12.
- Guo, Q., Strauss, H., Liu, C., & Goldberg, T. (2007). Carbon isotopic evolution of the terminal Neoproterozoic and early Cambrian: Evidence from the Yangtze Platform, South China. *Palaeogeography, Palaeoclimatology, Palaeoecology* 254, 140–157.
- Halverson, G. P. (2006). A Neoproterozoic Chronology. In S. Xiao & A. J. Kaufman (Eds.), *Neoproterozoic Geobiology and Paleobiology* (pp. 231–271). Springer Science + Business Media.
- Harwood, C. L., & Sumner, D. Y. (2011). Microbialites of the Neoproterozoic Beck Spring dolomite, Southern California. *Sedimentology* 58(6), 1648–1673.
- Harwood, C. L., & Sumner, D. Y. (2012). Origins of Microbial Microstructures In the Neoproterozoic Beck Spring dolomite: Variations In Microbial Community and Timing of Lithification. *Journal of Sedimentary Research* 82(9), 709–722.
- Heindel, K., Birgel, D., Peckmann, J., Kuhnert, H., & Westphal, H. (2010). Formation of deglacial microbialites in coral reefs off Tahiti (Iodp 310) involving sulfate-reducing bacteria. *Palaios* 25(10), 618–635.
- Heindel, K., Birgel, D., Brunner, B., Thiel, V., Westphal, H., Gischler, E., Ziegenbalg, S.B., Cabioch, G., Sjövall, P., & Peckmann, J. (2012). Post-glacial microbialite formation in coral reefs of the Pacific, Atlantic, and Indian Oceans. *Chemical Geology* 304–305, 117–130.
- Hoffman, P.F., & Schrag, D.P. (2002). The Snowball Earth hypothesis: testing the limits of global change. *Terra Nova* 14, 129–155.
- Hua, H., Chen, Z., & Yuan, X. (2007). The advent of mineralized skeletons in Neoproterozoic Metazoa -- new fossil evidence from the Gaojiashan Fauna. *Geological Journal* 42, 263–279.

- Huang, H., & Li, J. (2018). Biomarker signatures of Sinian bitumens in the Moxi – Gaoshiti bulge of Sichuan Basin, China: Geological significance for paleo-oil reservoirs: Discussion. *Precambrian Research* 314, 487–491.
- Hunt, J. M. (1996). *Petroleum geochemistry and geology* (2nd ed.). New York: W. H. Freeman.
- Jiang, X., Wang, J., Cui, X., Zhuo, J., Xiong, G., Lu, J., & Liu, J. (2012). Zircon SHRIMP U-Pb geochronology of the Neoproterozoic Chengjiang Formation in central Yunnan Province (SW China) and its geological significance. *Science China - Earth Sciences* 55(11), 1815–1826.
- Jiang, Y., Tao, Y., Gu, Y., Wang, J., Qiang, Z., Jiang, N., Lin, G., Jiang, C. (2016). Hydrothermal dolomitization in Dengying Formation, Gaoshiti-Moxi area, Sichuan Basin, SW China. *Petroleum Exploration and Development* 43(1), 54–64.
- Kelly, A. E. (2009). *Hydrocarbon Biomarkers for Biotic and Environmental Evolution Through the Neoproterozoic-Cambrian Transition* (Doctoral dissertation, Department of Earth, Atmospheric, and Planetary Sciences. Massachusetts Institute of Technology, Cambridge). Available from ResearchGate.
- Kenig, F., Sinninghe Damsté, J. S., Kock-van Dalen, A. C., Rijpstra, W. I. C., Huc, A. Y., & de Leeuw, J. W. (1995) Occurrence and origin of mono-, di-, and trimethylalkanes in modern and Holocene cyanobacterial mats from Abu Dhabi, United Arab Emirates. *Geochim. Cosmochim. Acta* 59, 2999–3015.
- King, R. R. (2015). Modified method and interpretation of source rock pyrolysis for an unconventional world. *Search and Discovery* Article #41704.
- Knoll, A.H., Swett, K. (1990). Carbonate deposition during the late Proterozoic Era: an example from Spitsbergen. *American Journal of Science* 290-A, 104-132.
- Konhauser, K., & Riding, R. (2012). Bacterial Biomineralization. In A. H. Knoll, D. E. Canfield, & K. O. Konhauser (Eds.), *Fundamentals of Geobiology* (1st ed., pp. 105–130). Blackwell Publishing Ltd.
- Koopmans, M. P., Van Kaam-Peters, H. M. E., Kenig, F., Schouten, S., Sinninghe Damsté, J. S., Hartgers, W. A., & de Leeuw, J. W. (1996). Diagenetic and catagenetic products of isorenieratene: Molecular indicators for photic zone anoxia. *Geochimica et Cosmochimica Acta* 60(22), 4467–4496.
- Koski, R.A. (2012) Supergene ore and gangue characteristics in volcanogenic massive sulfide occurrence model: U.S. Geological Survey Scientific Investigations Report 2010–5070 –C, chap. 12, 6 p.

- Lewan, M. D. (1998). Sulphur-radical control on petroleum formation rates. *Nature* 391(6663), 164–166.
- Li, M., Wang, T., Wang, C., & Zhang, W. (2006). Molecular composition and [indigeneity] of organic matter in Late Neoproterozoic sedimentary rocks from the Yangtze region, South China. *Chinese Journal of Geochemistry*, 25(4), 318–327.
- Li, L., Tan, X., Zeng, W., Zhou, T., Yang, Y., Hong, H., Luo, B., & Bian, L. (2013). Development and reservoir significance of mud mounds in Sinian Dengying Formation, Sichuan Basin. *Petroleum Exploration and Development* 40(6), 714–721.
- Li, Y., Zheng, R., Pang, Y., & Sun, H. (2014). Lithology Characteristic and Sedimentary Environment of the Member 3 of Dengying Formation, in Yangba Area, Northeast Sichuan. *Science Technology and Engineering* 5.
- Li, F.B., Teng, F.Z., Chen, J.T., Huang, K.J., Wang, S.J., Lang, X.G., Ma, H.R., Peng, Y.B., & Shen, B. (2016). Constraining ribbon rock dolomitization by Mg isotopes: Implications for the ‘dolomite problem’. *Chemical Geology* 445, 208-220.
- Liu, P., Xiao, S., Yin, C., Zhou, C., Gao, L., & Tang, F. (2008). Systematic description and phylogenetic affinity of tubular microfossils from the Ediacaran Doushantuo Formation at Weng’an, South China. *Palaeontology* 51(2), 339–366.
- Liu, S., Huang, W., Jansa, L.F., Wang, G., Song, G. Zhang, C., Sun, W., & Ma, W. (2014). Hydrothermal dolomite in the Upper Sinian (Upper Proterozoic) Dengying Formation, East Sichuan Basin, China. *Acta Geologica Sinica* 88(5), 1466–1487.
- Liu, B., Cheng, J., Ye, J., & Wang, S. (2015). Shale Gas Accumulation Conditions and Gas-bearing Properties of the Lower Cambrian Shuijingtuo Formation in Well Chengtan 1 , Dabashan Complex Tectonic Belt. *Acta Geologica Sinica* 89 Supp.(September), 162–163.
- Liu, L., Wu, Y., Yang, H., & Riding, R. (2016). Ordovician calcified cyanobacteria and associated microfossils from the Tarim Basin, Northwest China: Systematics and significance. *Journal of Systematic Palaeontology* 14(3), 183–210.
- Liu, Q., Zhu, D., Jin, Z., Meng, Q., & Li, S. (2019). Influence of volcanic activities on redox chemistry changes linked to the enhancement of the ancient Sinian source rocks in the Yangtze craton. *Precambrian Research* 327(31), 1–13.
- Lin, X., Peng, J., Du, L., Yan, J., & Hou, Z. (2017). Characterization of the Microbial dolomite of the Upper Sinian Dengying Formation in the Hanyuan Area of Sichuan Province, China. *Acta Geologica Sinica* 91(3), 806–821.

- Love, G. D., Snape, C. E., Carr, A. D., & Houghton, R. C. (1995). Release of covalently-bound alkane biomarkers in high yields from kerogen via catalytic hydrolysis. *Organic Geochemistry* 23(10), 981–986.
- Lyons, T. W. (1997). Sulfur isotopic trends and pathways of iron sulfide formation in upper Holocene sediments of the anoxic Black Sea. *Geochimica et Cosmochimica Acta* 61(16), 3367–3382.
- Mango, F. D., Hightower, J. W., & James, A. T. (1994). Role of transition-metal catalysis in the formation of natural gas. *Nature* 368(6471), 536–538.
- Mango, F. D., & Hightower, J. (1997). The catalytic decomposition of petroleum into natural gas. *Geochimica et Cosmochimica Acta* 61(24), 5347–5350.
- Mariotti, G., Pruss, S. B., Summons, R. E., Newman, S. A., & Bosak, T. (2018). Contribution of benthic processes to the growth of ooids on a low-energy shore in cat island, the bahamas. *Minerals*, 8(6).
- Mata, S. A., Harwood, C. L., Corsetti, F. A., Stork, N. J., Eilers, K., Berelson, W. M., & Spear, J. R. (2012). Influence of gas production and filament orientation on stromatolite microfabric. *Palaios* 27(April), 206–219.
- Mazzullo, S. J. (2000). Organogenic Dolomitization in Peritidal to Deep-Sea Sediments. *Journal of Sedimentary Research* 70(1), 10–23.
- Meister, P., Wiedling, J., Lott, C., Bach, W., Kuhfuß, H., Wegener, G., Böttcher, M. E., Deusner, C., Lichtschlag, A., Bernasconi, S. M., Weber, M. (2018). Anaerobic methane oxidation inducing carbonate precipitation at abiogenic methane seeps in the Tuscan archipelago (Italy). *PLoS ONE* 13.
- Mettraux, M., Homewood, P., dos Anjos, C., Erthal, M., Lima, R., Matsuda, N., Souza, A., & Al Balushi, S. (2015). Microbial communities and their primary to early diagenetic mineral phases; the record from Neoproterozoic microbialites of Qarn Alam, Oman. *Geological Society, London, Special Publications* 418(1), 123–154.
- Moreau, J. W., Webb, R. I., & Banfield, J. F. (2004). Ultrastructure, aggregation-state, and crystal growth of biogenic nanocrystalline sphalerite and wurtzite. *American Mineralogist* 89(7), 950–960.
- Patranabis-Deb, S., Majumder, T., & Khan, S. (2018). Lifestyles of the palaeoproterozoic stromatolite builders in the Vempalle Sea, Cuddapah Basin, India. *Journal of Asian Earth Sciences* 157, 360–370.

- Peng, B., Li, Z., Li, G., Liu, C., Zhu, S., Zhang, W., Zuo, Y., Guo, Y., & Wei, X. (2018). Multiple dolomitization and Fluid Flow Events in the Precambrian Dengying Formation of Sichuan Basin, Southwestern China. *Acta Geologica Sinica* 92(1), 311–332.
- Peters, K. E., Walters, C. C., & Moldowan, J. M. (1993). *The Biomarker Guide* (2nd ed.). Cambridge, UK: Cambridge University Press.
- Popa, R., Kinkle, B. K., & Badescu, A. (2004). Pyrite framboids as biomarkers for iron-sulfur systems. *Geomicrobiology Journal* 21(3), 193–206.
- Rashby S.E., Sessions A.L., Summons R.E., & Newman D.K. (2007) Biosynthesis of 2-methylbacteriohopanepolyols by an anoxygenic phototroph. *Proceedings of the National Academy of Sciences, USA* 104, 15099–15104.
- Riding, R. (2000). Microbial carbonates: The geological record of calcified bacterial-algal mats and biofilms. *Sedimentology* 47(SUPPL. 1), 179–214.
- Riding, R. (2006). Cyanobacterial calcification, carbon dioxide concentrating mechanisms, and Proterozoic-Cambrian changes in atmospheric composition. *Geobiology* 4(4), 299–316.
- Riding, R., & Tomás, S. (2006). Stromatolite reef crusts, Early Cretaceous, Spain: Bacterial origin of in situ-precipitated peloid microspar? *Sedimentology* 53(1), 23–34.
- Riding, R. (2011a). The Nature of Stromatolites: 3,500 Million Years of History and a Century of Research. In J. Reitner, N.-V. Quéric, & G. Arp (Eds.), *Advances in Stromatolite Geobiology* Springer, pp. 29-74.
- Riding, R. (2011b). Calcified cyanobacteria. In J. Reitner and V. Thiel (eds), *Encyclopedia of Geobiology*. Encyclopedia of Earth Science Series, Springer, Heidelberg, pp. 211-223.
- Riding, R. (2011c). Microbialites, stromatolites, and thrombolites. In J. Reitner and V. Thiel (eds), *Encyclopedia of Geobiology*. Encyclopedia of Earth Science Series, Springer, Heidelberg, pp. 635-654.
- Roberts, J. A., Bennett, P. C., González, L. A., Macpherson, G. L., & Milliken, K. L. (2004). Microbial precipitation of dolomite in methanogenic groundwater. *Geology* 32(4), 277.
- Sawłowicz, Z. (2000). Framboids: From their origin to application. *Prace Mineralogiczne* 88, 80.
- Schieber, J. (2002). Sedimentary pyrite: A window into the microbial past. *Geology* 30(6), 531–534.
- Schopf J. W. (2006). Fossil evidence of Archaean life. *Philosophical transactions of the Royal Society of London. Series B, Biological sciences* 361(1470), 869–885.

- Schouten, S., van der Maarel, M. J., Huber, R., & Sinninghe Damsté, J. S. (1997) 2,6,10,15,19-pentamethylcosenes in *Methanobolus bombayensis*, a marine methanogenic archaeon, and in *Methanosarcina mazei*. *Organic Geochemistry* 26, 409–414.
- Scott, R.J., Meffre, S., Woodhead, J., Gilbert, S.E., Berry R.F., & Emsbo, P. (2009) Development of Framboidal Pyrite During Diagenesis, Low-Grade Regional Metamorphism, and Hydrothermal Alteration. *Economic Geology* 104 (8), 1143–1168.
- Seal, R. R. (2006). Sulfur isotope geochemistry of sulfide minerals. *Reviews in Mineralogy and Geochemistry* 61, 633–677.
- Shan, X., Zhang, J., Zhang, B., Liu, J., Zhou, H., Wang, Y., & Fu, Z. (2017) Characteristics of dolomite karstic reservoir in the Sinian Dengying Formation, Sichuan Basin. *Petroleum Research* 2(1), 13–24.
- She, Z. B., Zhang, Y. T., Liu, W., Song, J., Zhang, Y., Li, C., Strother, P., & Papineau, D. (2016) New observations of Ambient Inclusion Trails (AITs) and pyrite framboids in the Ediacaran Doushantuo Formation, South China. *Palaeogeography, Palaeoclimatology, Palaeoecology* 461, 374–388.
- Shellnutt, J. G. (2014) The Emeishan large igneous province: A synthesis. *Geoscience Frontiers* 5 (3), 369 – 394.
- Shi, W., Zhang, Y., dong, S., Hu, J., Wiesinger, M., Ratschbacher, L., Jonckheere, R., Li, J., Tian, M., Chen, H., Wu, G., Ma, L., & Li, H. (2012) Intra-continental Dabashan orocline, southwestern Qinling, Central China. *Journal of Asian Earth Sciences* 46, 20-38.
- Shiea, J., Brassell S. C., & Ward D. M. (1990) Mid-chain branched mono- and dimethyl alkanes in hot spring cyanobacterial mats: a direct biogenic source for branched alkanes in ancient sediments? *Organic Geochemistry* 15, 223–231.
- Shields, G.A. (2007). A normalised seawater strontium isotope curve: possible implications for Neoproterozoic–Cambrian weathering rates and the further oxygenation of the Earth. *eEarth* 2, 35–42.
- Simoneit, B. R. T. (2004). Biomarkers (molecular fossils) as geochemical indicators of life. *Advances in Space Research*, 33, 1255–1261.
- Song, J., Liu, S., Qing, H., Jansa, L., Li, Z., Luo, P., Yang, D., Sun, W., Peng, H., & Lin, T. (2018) The depositional evolution, reservoir characteristics, and controlling factors of microbial carbonates of Dengying Formation in upper Neoproterozoic, Sichuan Basin, Southwest China. *Energy Exploration and Exploitation* 36(4), 591–619.

- Summons R. E., Powell T. G., & Boreham C. J. (1988) Petroleum geology and geochemistry of the Middle Proterozoic McArthur Basin, northern Australia: III. Composition of extractable hydrocarbons. *Geochim. Cosmochim. Acta* 52, 1747–1763.
- Summons R. E. & Walter M. R. (1990) Molecular fossils and microfossils of prokaryotes and protists from Proterozoic sediments. *American Journal of Science* 290-A, 212–244.
- Summons, R. E., Jahnke, L. L., Hope, J. M., & Logan, G. A. (1999). 2-Methylhopanoids as biomarkers for cyanobacterial oxygenic photosynthesis. *Nature* 400(6744), 554–557.
- Tang, F., Yin, C., Liu, P., Gao, L., & Zhang, W. (2008). A New Diverse Macrofossil Lagerstätte from the Uppermost Ediacaran of Southwestern China. *Acta Geologica Sinica* 82(6), 1095–1103.
- Thiel V., Peckmann J., Seifert R., Wehrung P., Reitner J., and Michaelis W. (1999) Highly isotopically depleted isoprenoids: molecular markers for ancient methane venting. *Geochimica et Cosmochimica Acta* 63, 3959–3966.
- Thiele, S. T., Micklethwaite, S., Bourke, P., Verrall, M., & Kovesi, P. (2015) Insights into the mechanics of en-échelon sigmoidal vein formation using ultra-high resolution photogrammetry and computed tomography. *Journal of Structural Geology* 77, 27–44.
- Tosti, F., Mastandrea, A., Guido, A., Demasi, F., Russo, F., & Riding, R. (2014). Biogeochemical and redox record of mid-late Triassic reef evolution in the Italian dolomites. *Palaeogeography, Palaeoclimatology, Palaeoecology* 399, 52–66.
- Tosti, F., & Riding, R. (2017). Fine-grained agglutinated elongate columnar stromatolites: Tieling Formation, ca 1420 Ma, North China. *Sedimentology* 64(4), 871–902.
- Van Golf-Racht, T. D. (Ed.). (1982). Basic Geology. In *Developments in Petroleum Science* (12th ed., pp. 5–50). Elsevier.
- Van Lith, Y., Warthmann, R., Vasconcelos, C., & McKenzie, J. A. (2003). Microbial fossilization in carbonate sediments: a result of the bacterial surface involvement in dolomite precipitation. *Sedimentology* 50(2), 237–245
- Vasconcelos, C., McKenzie, J.A., Bernasconi, S., Grujic, D., & Tiens, A.J. (1995). Microbial mediation as a possible mechanism for natural dolomite formation at low temperatures. *Nature* 377, 220–222.
- Wang, L., Shi, X., & Jiang, G. (2012). Pyrite morphology and redox fluctuations recorded in the Ediacaran Doushantuo Formation. *Palaeogeography, Palaeoclimatology, Palaeoecology* 333–334, 218–227.

- Wang, Y., Wang, Y., Du, W., & Wang, X. (2016). New Data of Macrofossils in the Ediacaran Wenghui Biota from Guizhou, South China. *Acta Geologica Sinica* 90(5), 1611–1628.
- Wang, Z., Liu, J., Jiang, H., Huang, S., Wang, K., & Xu, Z. (2019). Lithofacies paleogeography and exploration significance of Sinian Doushantuo depositional stage in the middle-upper Yangtze region, Sichuan Basin, SW China. *Petroleum Exploration and Development* 46(1), 41–53.
- Waples, D. W. (2000). The kinetics of in-reservoir oil destruction and gas formation: constraints from experimental and empirical data, and from thermodynamics. *Organic Geochemistry* 31(6), 553–575.
- Warthmann, R., van Lith, Y., Vasconcelos, C., McKenzie, J. A., & Karpoff, A. M. (2000). Bacterially induced dolomite precipitation in anoxic culture experiments. *Geology* 28(12), 1091–1094.
- Wilkins, R. W. T. (1999). The problem of inconsistency between thermal maturity indicators used for petroleum exploration in Australian basins. *ASGO Journal of Australian Geology and Geophysics* 17(5/6), 67–76.
- Xiao, S., Shen, B., Zhou, C., Xie, G., & Yuan, X. (2005). A uniquely preserved Ediacaran fossil with direct evidence for a quilted bodyplan. *PNAS* 102(29), 10227–10232.
- Xiao, S., Muscente, A. D., Chen, L., Zhou, C., Schiffbauer, J. D., Wood, A. D., Polys, N.F., & Yuan, X. (2014). The Weng'an biota and the Ediacaran radiation of multicellular eukaryotes. *National Science Review*, 1(4), 498–520.
- Xiao, S., Bykova, N., Kovalick, A., & Gill, B. C. (2017). Stable carbon isotopes of sedimentary kerogens and carbonaceous macrofossils from the Ediacaran Miaohu Member in South China: Implications for stratigraphic correlation and sources of sedimentary organic carbon. *Precambrian Research* 302(June), 171–179.
- Xu, H., Liu, S., Qu, G., Li, Y., Sun, G. & Liu, K. (2009), Structural Characteristics and Formation Mechanism in the Micangshan Foreland, South China. *Acta Geologica Sinica* 83, 81-91.
- Xu, Q., Qiu, N., Liu, W., Shen, A., & Wang, X. (2018). Thermal evolution and maturation of Sinian and Cambrian source rocks in the central Sichuan Basin, Southwest China. *Journal of Asian Earth Sciences* 164(March), 143–158.
- Zhang, P., Liu, G., Cai, C., Li, M., Chen, R., & Gao, P. (2019). Alteration of solid bitumen by hydrothermal heating and thermochemical sulfate reduction in the Ediacaran and Cambrian dolomite reservoirs in the Central Sichuan Basin, SW China. *Precambrian Research* 321, 277–302.

- Zhao, Y., Chen, M., Peng, J., Yu, M., He, M., Wang, Y., Yang, R., Wang, P., & Zhang, Z. (2004). Discovery of a Miaohu-type biota from the Neoproterozoic Doushantuo Formation in Jiangkou County, Guizhou Province, China. *Chinese Science Bulletin* 49(20), 2224–2226.
- Zhao, W., Wei, G., Yang, W., Mo, W., Xie, W., Su, N., Liu, M., & Zeng, F. (2017). Discovery of Wanyuan-Dazhou Intracratonic Rift and its significance for gas exploration in Sichuan Basin, SW China. *Petroleum Exploration and Development* 44(5), 697–707.
- Zhao, J., Liang, J., Long, X., Li, J., Xiang, Q., Zhang, J., & Hao, J. (2018). Genesis and evolution of framboidal pyrite and its implications for the ore-forming process of Carlin-style gold deposits, southwestern China. *Ore Geology Reviews* 102, 426–436.
- Zhou, J., Yao, G., Yang, G., Zhang, J., Hao, Y., Wang, F., Gu, M., & Li, W. (2015). Genesis mechanism of the Sinian-Cambrian reservoirs in the Anyue Gas Field, Sichuan Basin. *Natural Gas Industry* 2(2–3), 127–135.
- Zhou, J., Zhang, J., Deng, H., Chen, Y., Hao, Y., & Li, W. (2017). Lithofacies paleogeography and sedimentary model of Sinian Dengying Fm in the Sichuan Basin. *Natural Gas Industry B* 4, 217–224.
- Zhu, D., Zhang, D., Liu, Q., Jin, Z., & Zhiliang, H. E. (2017). Activity of Silica-Rich Hydrothermal Fluid and Its Impact on Deep dolomite Reservoirs in the Sichuan Basin, Southern China. *Acta Geologica Sinica* 91(6), 2214–2229.

Appendix A: Thin sections

Dengying Member 4, central uplift, well core (ordered by depth)

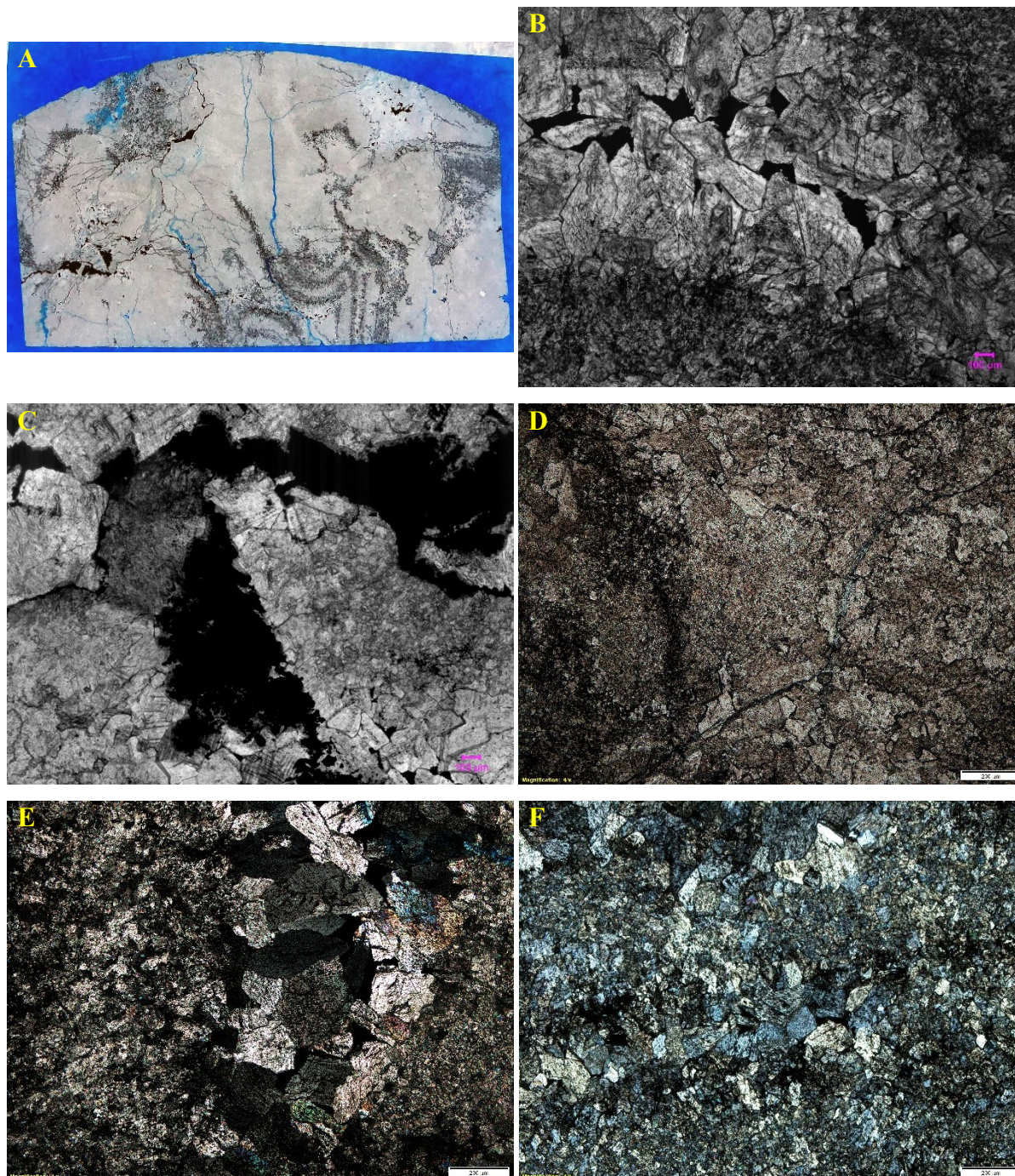


Figure 28. Sample 18 (Depth = 5224.79m) (A) Photo of entire thin section, cut parallel to bedding, transmitted light (B) Saddle dolomite-filled vein with pore-filling organic matter. PPL 4x magnification (C) Dense organic matter, likely void filling oil. PPL 4x magnification (D) Diffuse organic matter and coarse crystalline dolomite cement. PPL 4x magnification (E) organic rich micrite grading into hydrothermal vein cement. XPL 4x magnification (F) Fine to coarse crystalline dolomite with some cloudy organic matter. XPL 4x magnification.

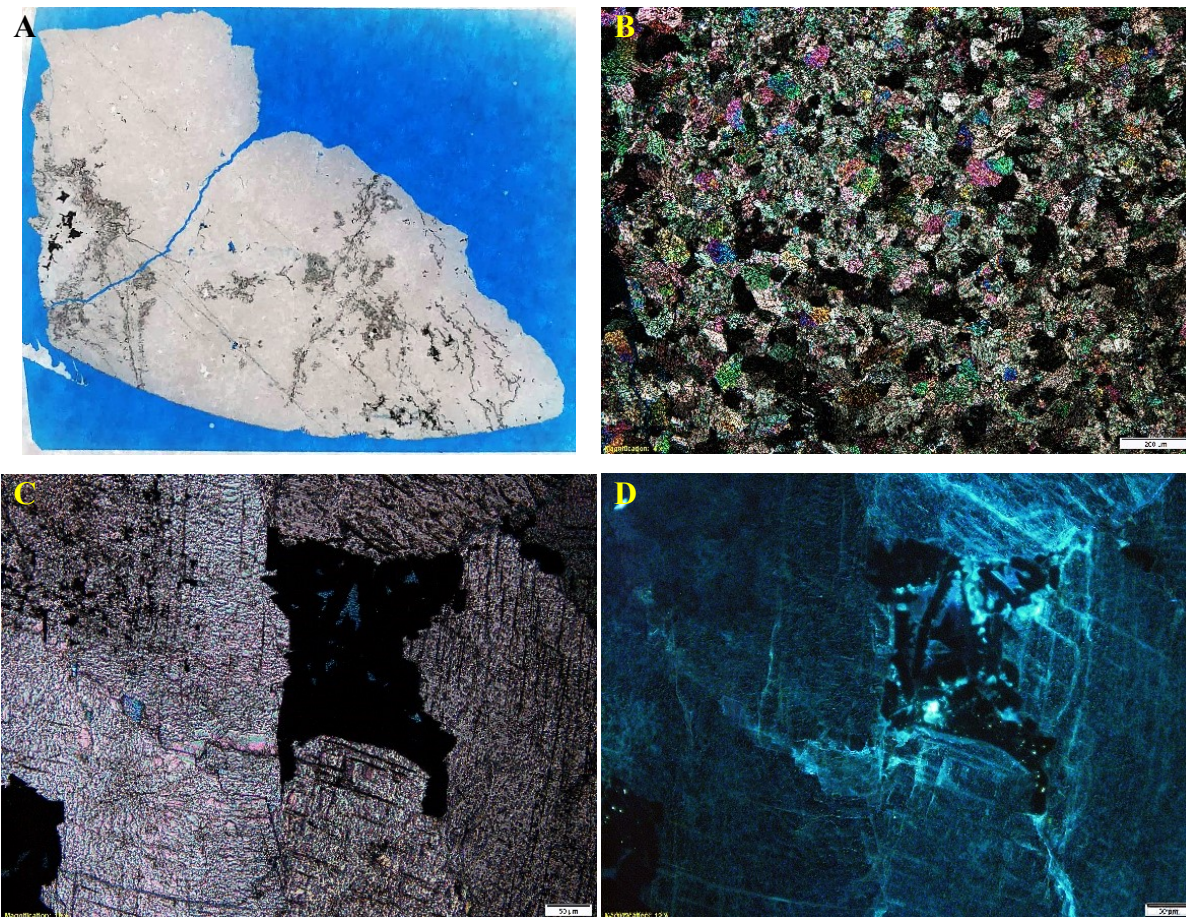
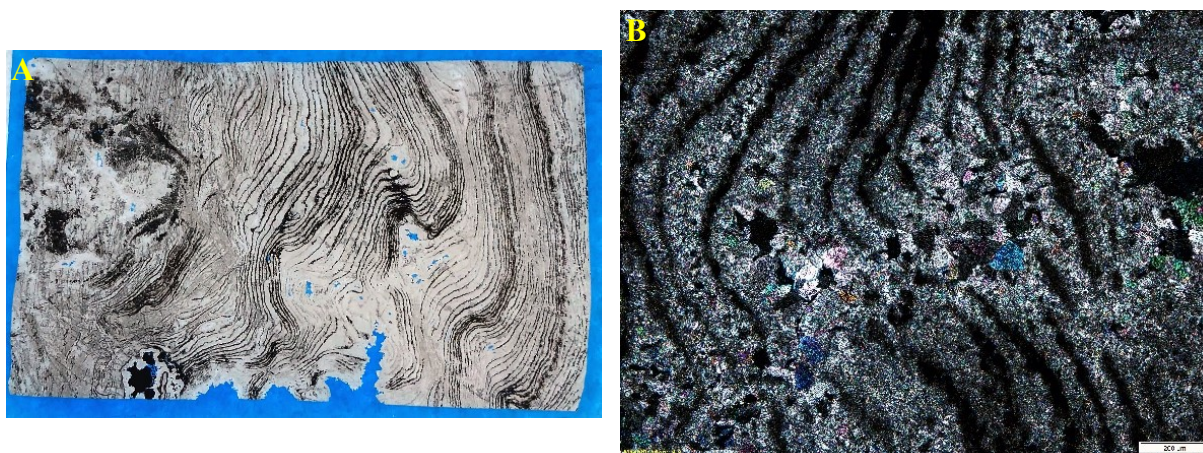


Figure 29. Sample 17 (Depth 5237.49m) (A) Photo of entire thin section, cut parallel to bedding, transmitted light (B) Matrix mineral cement. XPL 4x magnification (C) Pyrite-filled pore PPL 10x magnification (D) same as C in blue-violet reflected light (BV) 10x magnification.



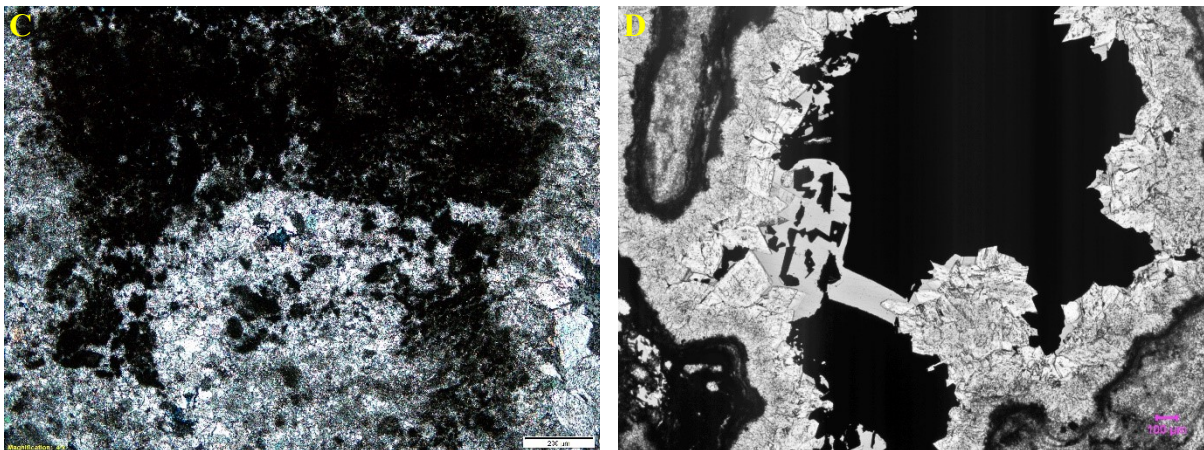
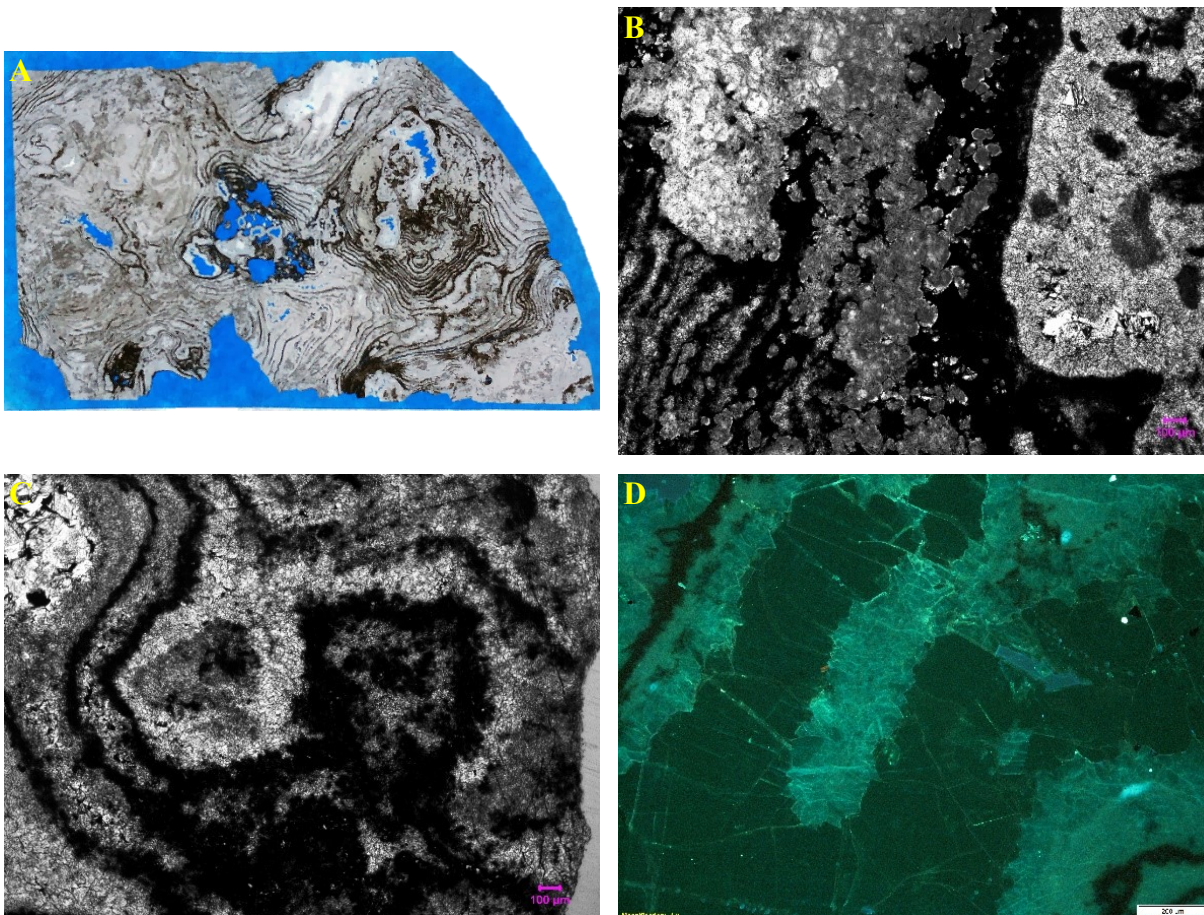


Figure 30. Sample 25x (Depth = 5300.13m) (A) Photo of entire thin section, transmitted light (B) Wispy stromatolitic laminations with coarsely crystalline hydrothermal minerals. XPL 4x magnification (C) Dense and bushy peloids in sparite cement. PPL 4x magnification (D) Dissolution pore lined by dolomite and anhydrite, filled with pyrite. PPL 4x magnification.



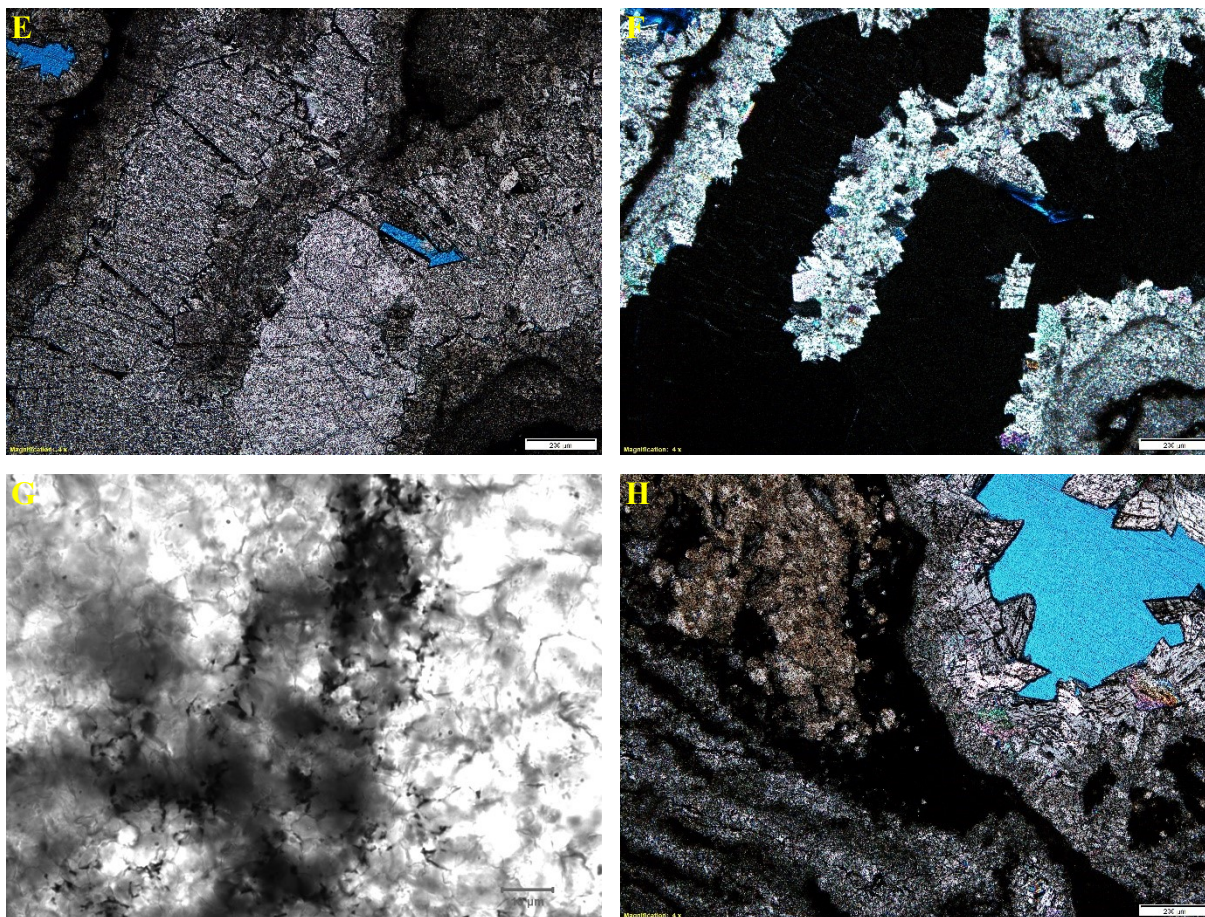
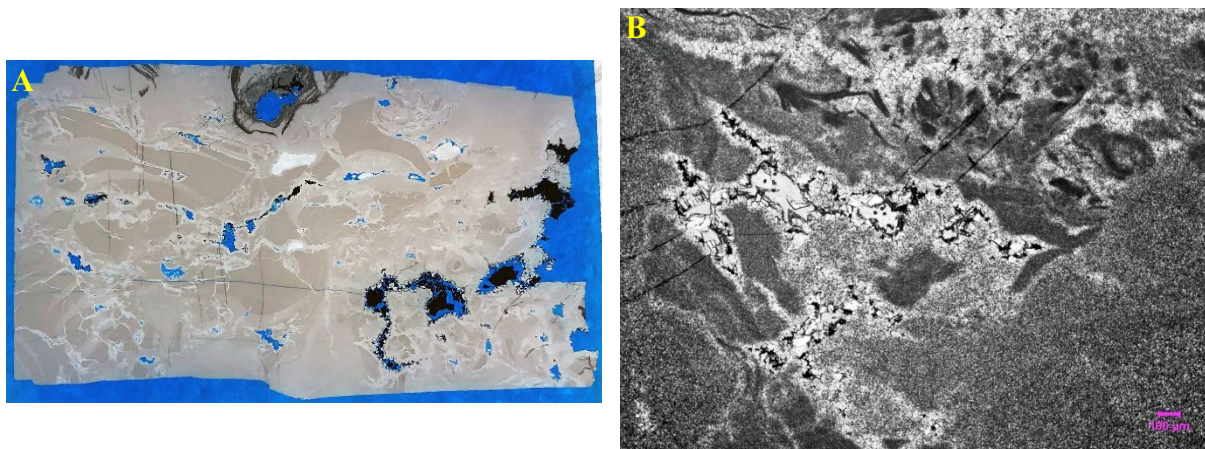


Figure 31. Sample 25y (Depth = 5300.13m) (A) Photo of the entire thin section, transmitted light (B) Left to right: stromatolite, botryoidal cement, coarse crystalline cement. PPL 4x magnification (C) Two domes of the stromatolite PPL 4x magnification. (D) A hydrothermal cement wraps around a peninsula of neomorphic dolomite + sulfates, BV 4x magnification (E) Same view as D in plane-polarized transmitted light, 4x magnification (F) Same view as D and E in with crossed nicols, the sparry peninsula is at maximum birefringence when the surrounding mineral is at extinction and vice versa, 4x magnification (G) Organic matter preservation PPL 100x magnification (H) Partially silicified stromatolite next to a dissolution pore filled by dolomite and anhydrite. XPL 4x magnification.



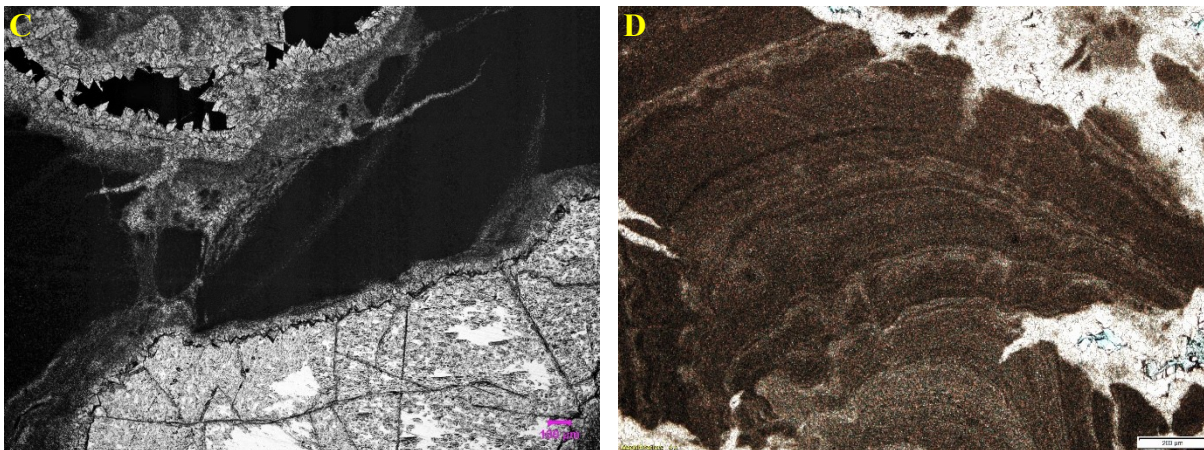
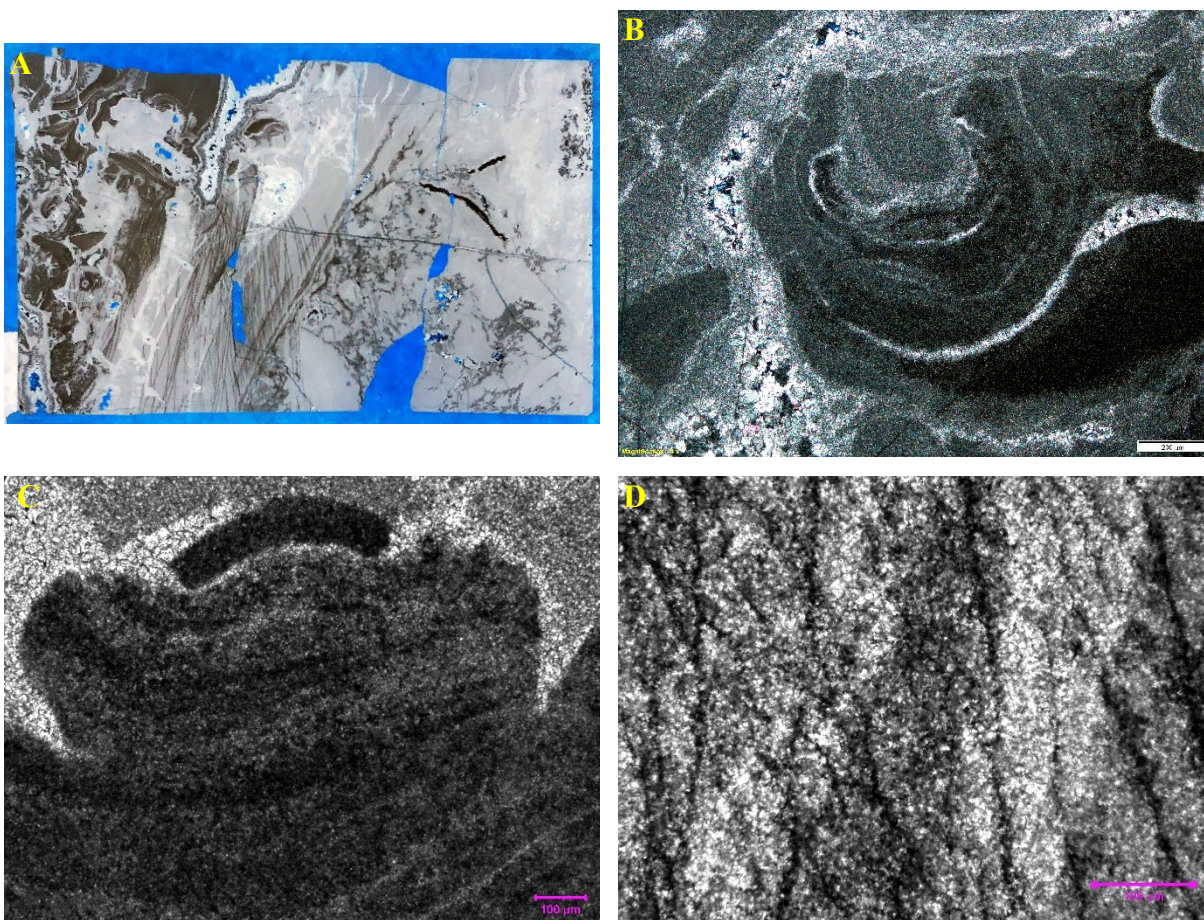


Figure 32. Sample 24 (Depth = 5308.71m) (A) Photo of the entire thin section, cut perpendicular to bedding; rip-up clasts and bitumen-lined dissolution pores visible, transmitted light (B) Micritic fabric with ripped up microbial mats, circumgranular cracks and dissolution pores partially filled with saddle dolomite (SD). PPL 4x magnification (C) SD-lined, pyrite filled dissolution pores, organic clasts, large crystalline cement with hackly texture. PPL 4x magnification (D) Chunk of domed stromatolite with colloform laminations PPL 4x magnification.



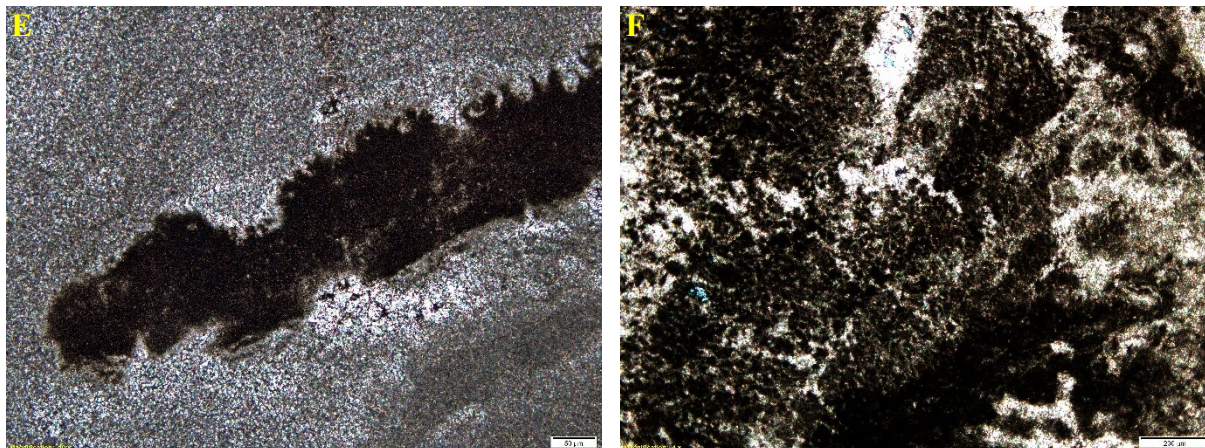


Figure 33. Sample 22x (Depth = 5313.15m) (A) Photo of entire thin section; hair-like fractures, SD-filled dissolution pores and a storm deposit containing ripped and rolled up microbial mats, transmitted light (B) domed or rolled up microbial mats XPL 4x magnification (C) PPL 10x magnification (D) Hair-like fractures appear to be conduits for oil. PPL 20x magnification. (E) Macroalgae or microbial mat fragment PPL 10x magnification (F) Bushy clots with circumgranular cracks suggesting subaerial exposure. PPL 4x magnification.

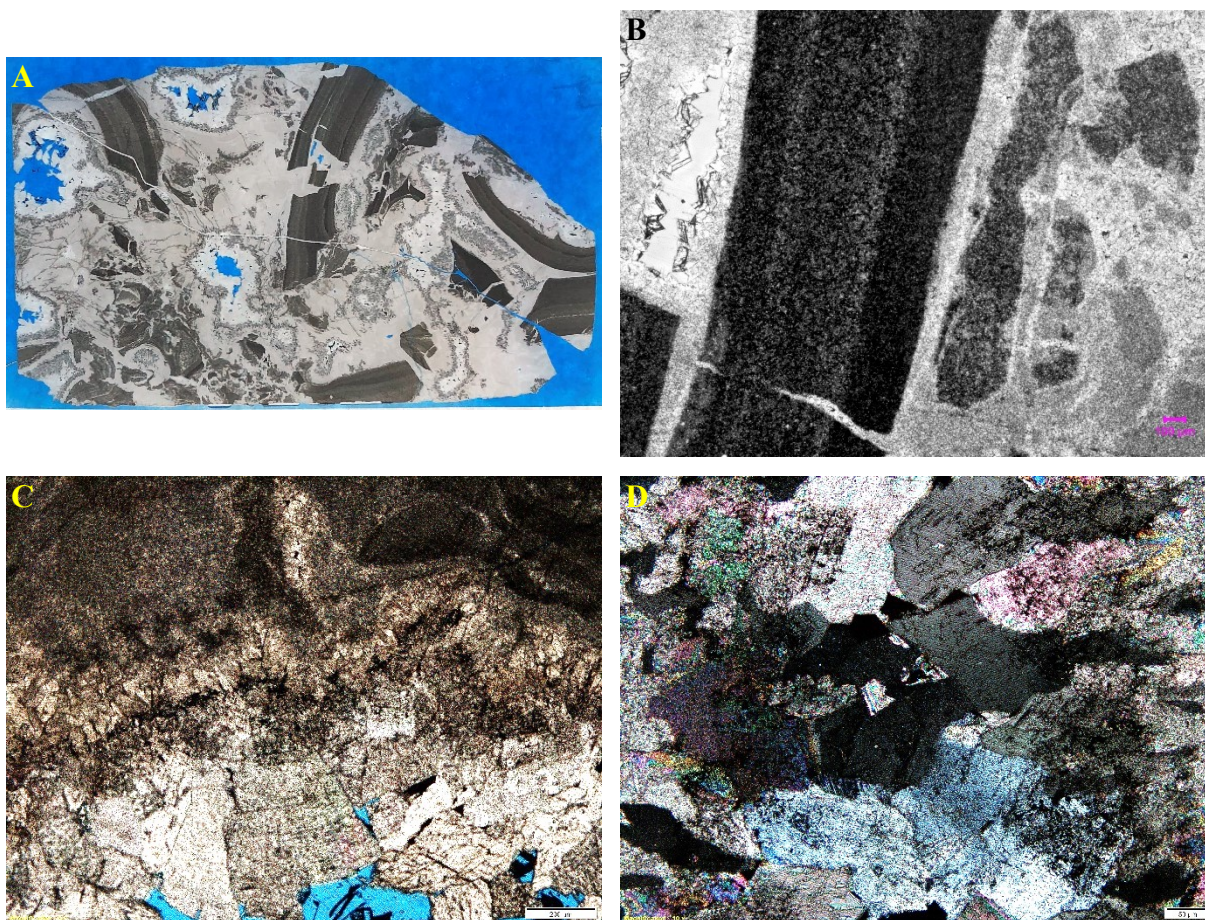


Figure 34. Sample 22y (Depth = 5313.15m) (A) Photo of entire thin section; storm deposit of ripped and deformed microbial mats, coarse crystalline dolomite cement with dissolution pores, transmitted light (B) Torn microbial mat

PPL 4x magnification (C) Fine-grained clotted peloidal fabric transitioning into saddle-dolomite and anhydrite. PPL 4x magnification. (D) Saddle dolomite (gray), anhydrite (colorful) and barite (blue). XPL 10x magnification.

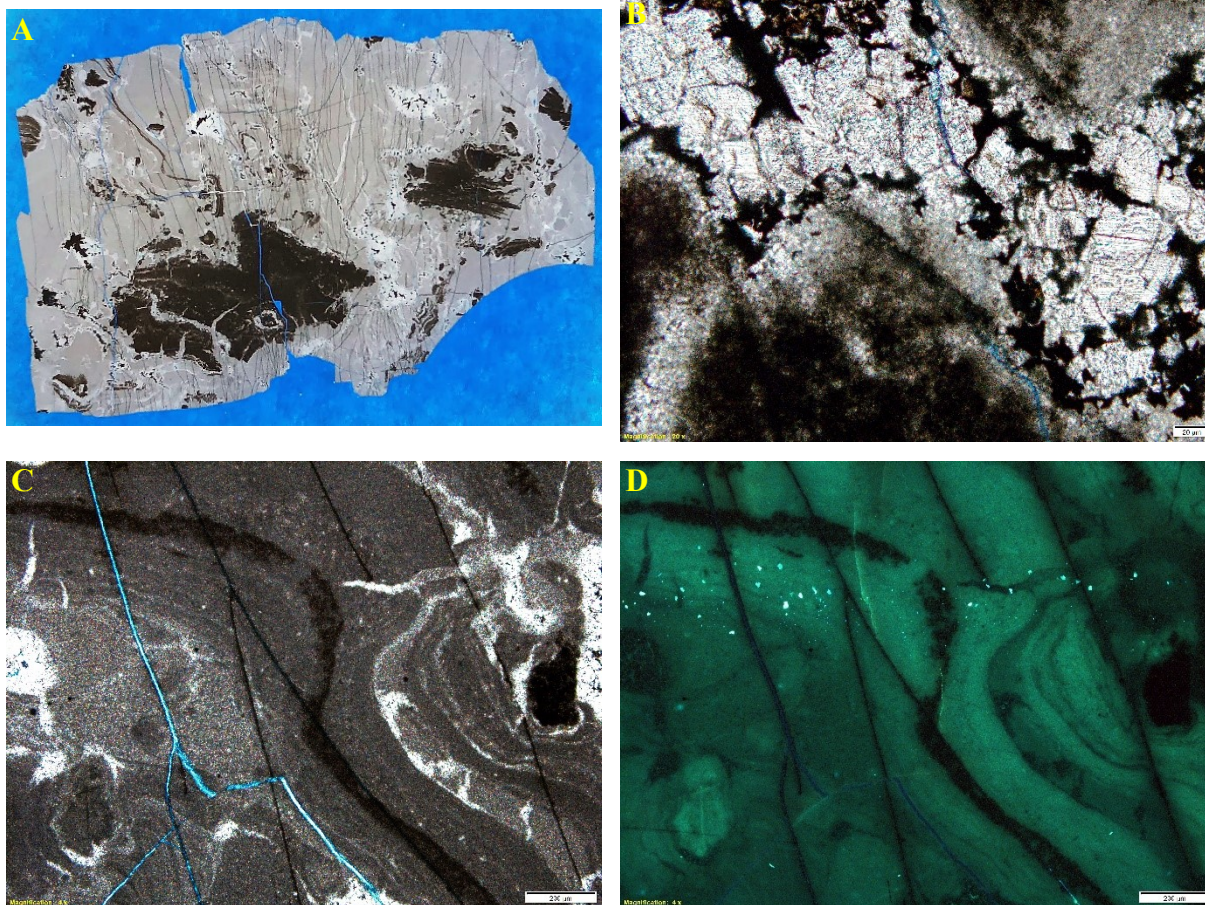
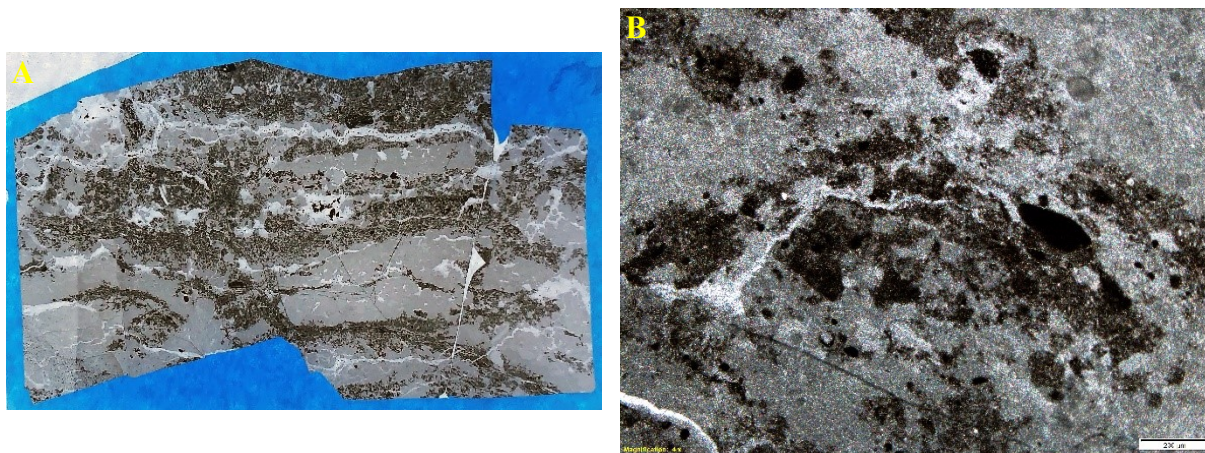


Figure 35. Sample 20 (Depth = 5317.93 m) (A) Photo of entire thin section, transmitted light (B) Cloudy organic matter surrounds a dissolution pore filled with large dolomite crystals, pyrite and bitumen (black). PPL 20x magnification (C) Stromatolitic and clumped organic matter, hair-like fractures and hydrothermal replacive minerals PPL 4x magnification (D) Same view as C but in reflected blue-violet light 4x magnification.



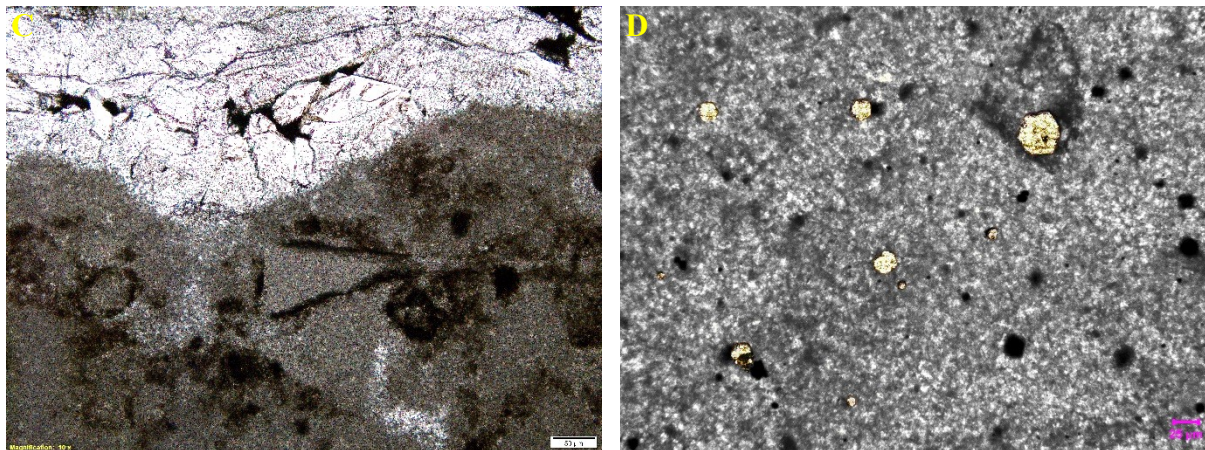


Figure 36. Sample 19x (Depth = 5320.86 m) (A) Photo of entire thin section; fine-grained clotted peloidal laminations clasts and filled veins, transmitted light (B) Fine-grained clotted peloidal fabric with circumgranular cracks. PPL 4x magnification (C) Irregular cortoids and clots fill micrite beside hydrothermal vein filled with polygonal dolomite-barite-anhydrite cement PPL 10x magnification (D) Composite transmitted/reflected light image, showing distribution of pyrite microcrystals in micrite; pyrite has been colorized for contrast. PPL 20x magnification.

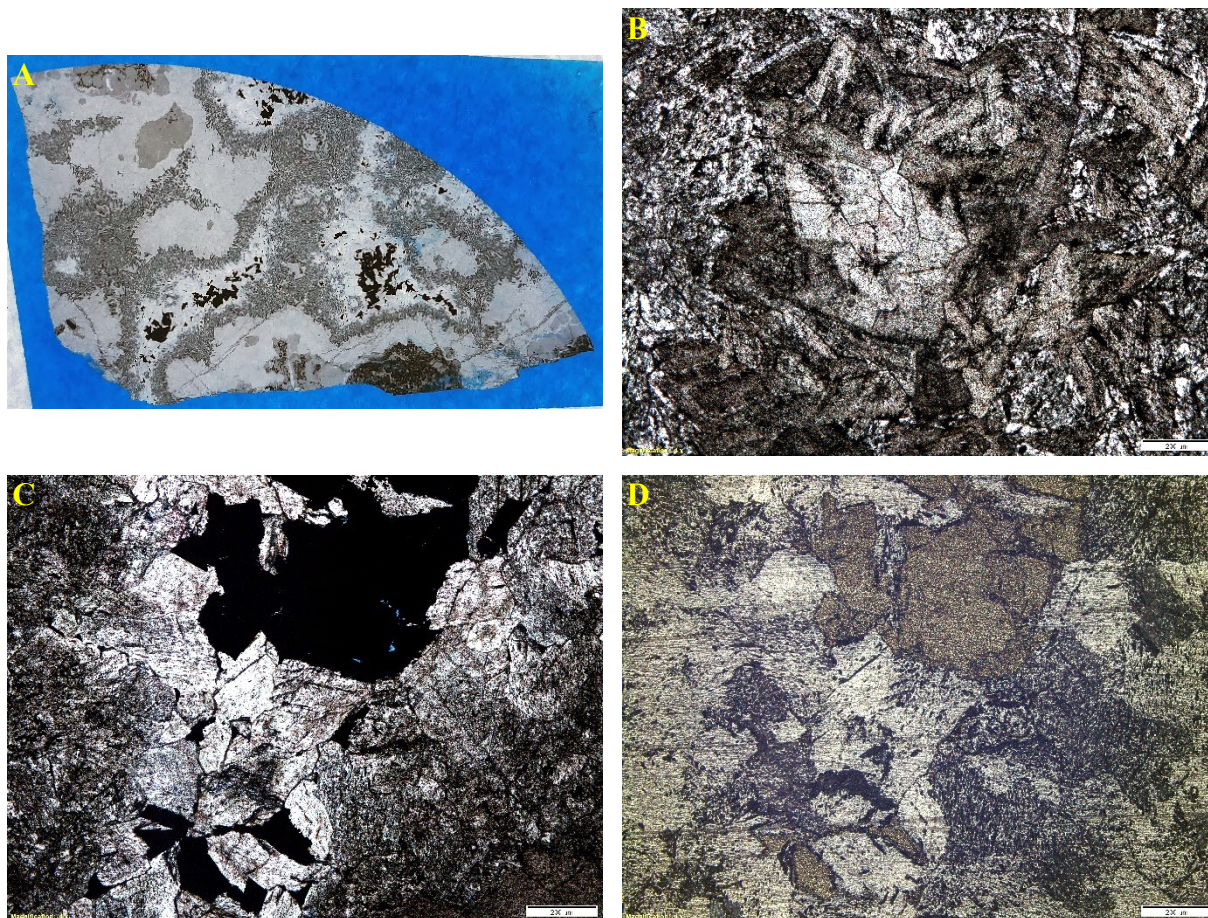


Figure 37. Sample 19y (Depth = 5320.86 m) (A) Photo of the entire thin section, transmitted light (B) cluster of zoned tabular crystals. PPL, 4x magnification (C) Void-filling saddle dolomite and chalcopyrite PPL, 4x magnification (D) Same view as E in reflected light, 4x magnification.

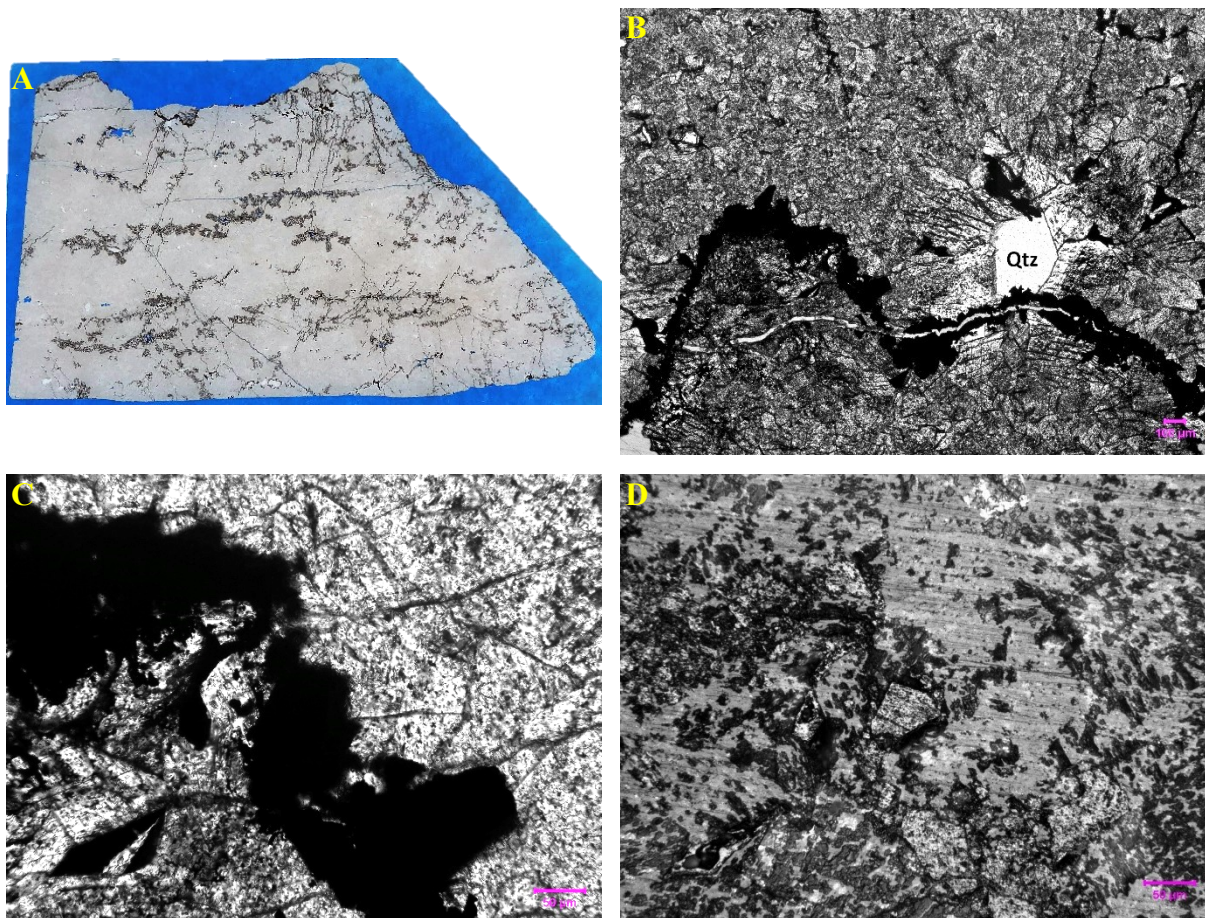


Figure 38. Sample 16 (Depth = 5328.45 m) (A) Photo of entire thin section, transmitted light (B) Micritic matrix dolomite, coarse crystalline dolomite, a single quartz crystal and a stylolite. PPL 4x magnification (C) Stylolite in B in 20x magnification (D) Same view as C but in reflected light, revealing sulfide minerals in the stylolite, 20x magnification.

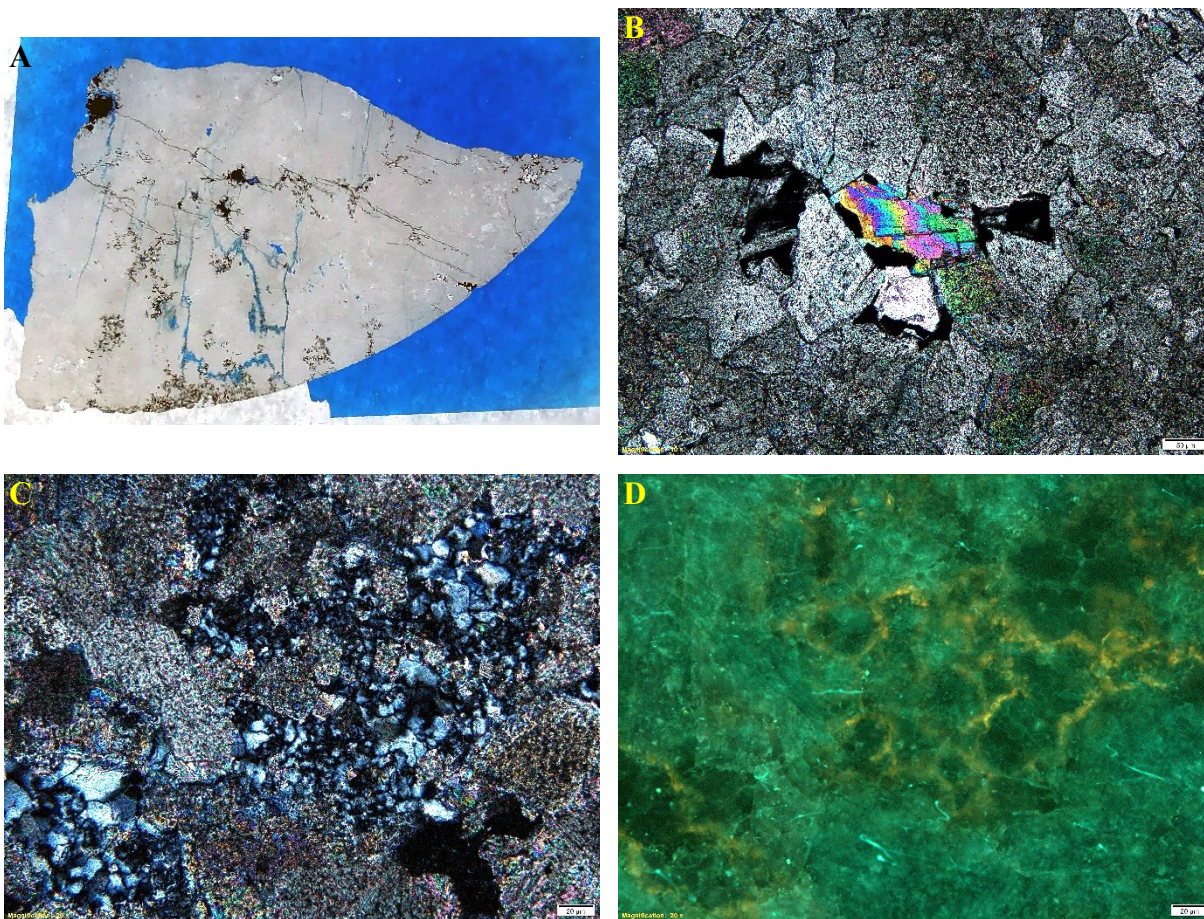
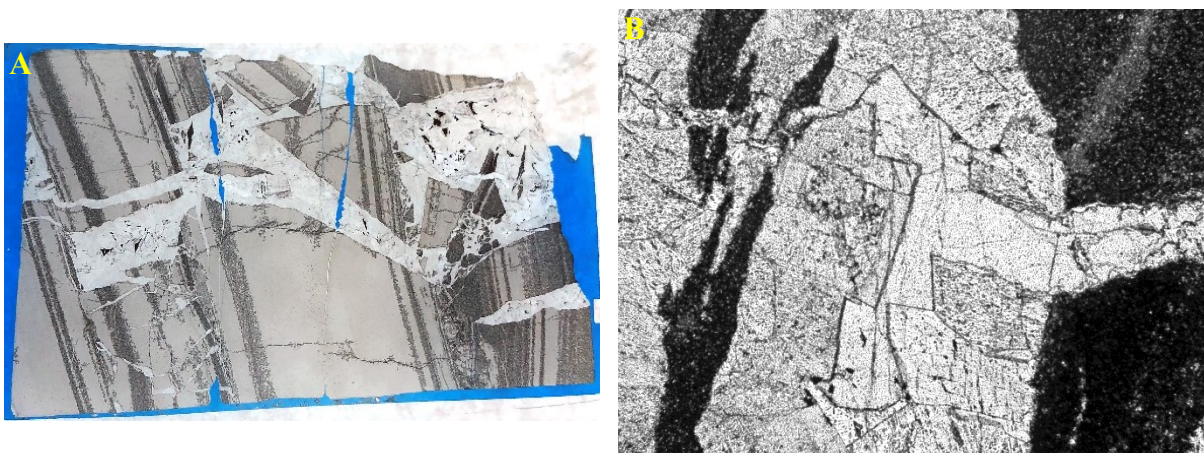


Figure 39. Sample 14 (Depth = 5333.17 m) (A) Photo of the entire thin section, transmitted light (B) Saddle dolomite and anhydrite (displaying lovely interference colors and cleavage), with organic matter and pyrite (black) (C) dolomite, anhydrite and microcrystalline quartz cement. XPL 20x magnification (D) Green and yellow fluorescence, BV 20x magnification.



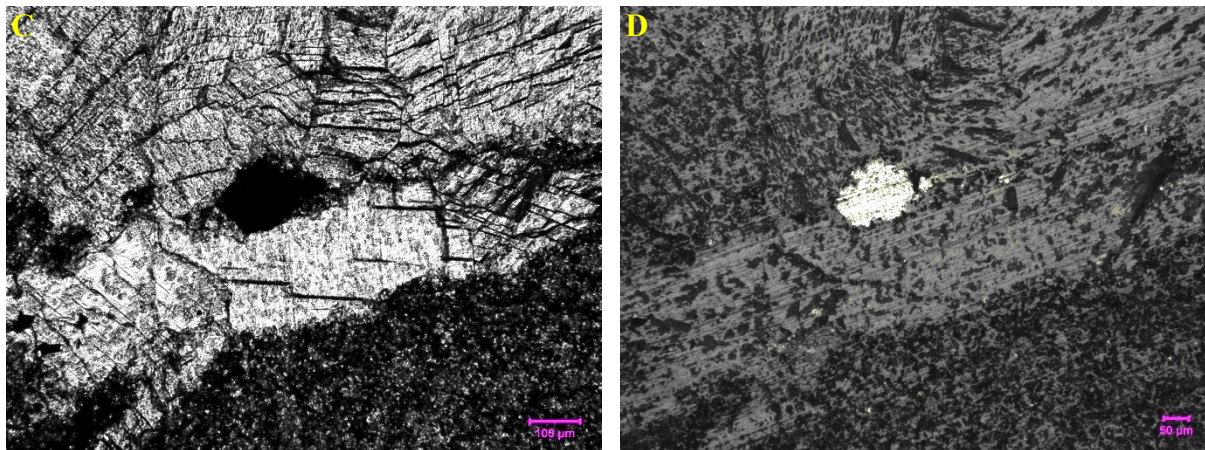
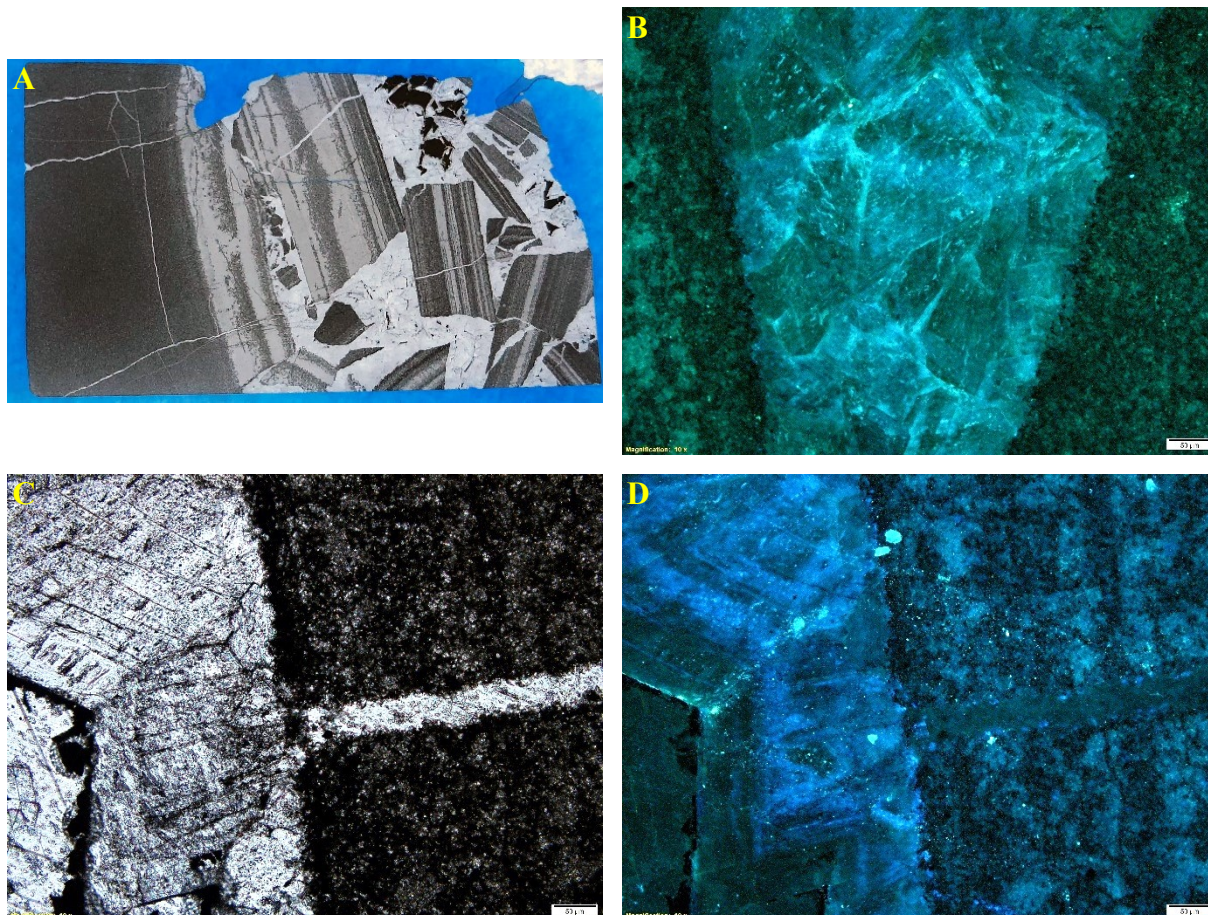


Figure 40. Sample 29x (Depth = 5334.64 m) (A) Photo of entire thin section, transmitted light (B) Stromatolite fragments that appear to have been chipped off before lithification PPL 4x magnification (C) Pyrite framboid with ambient inclusion trail (AIT) implying migration through the matrix (She et al., 2016). PPL 10x magnification (D) Pyrite framboid with AIT, RL 10x magnification.



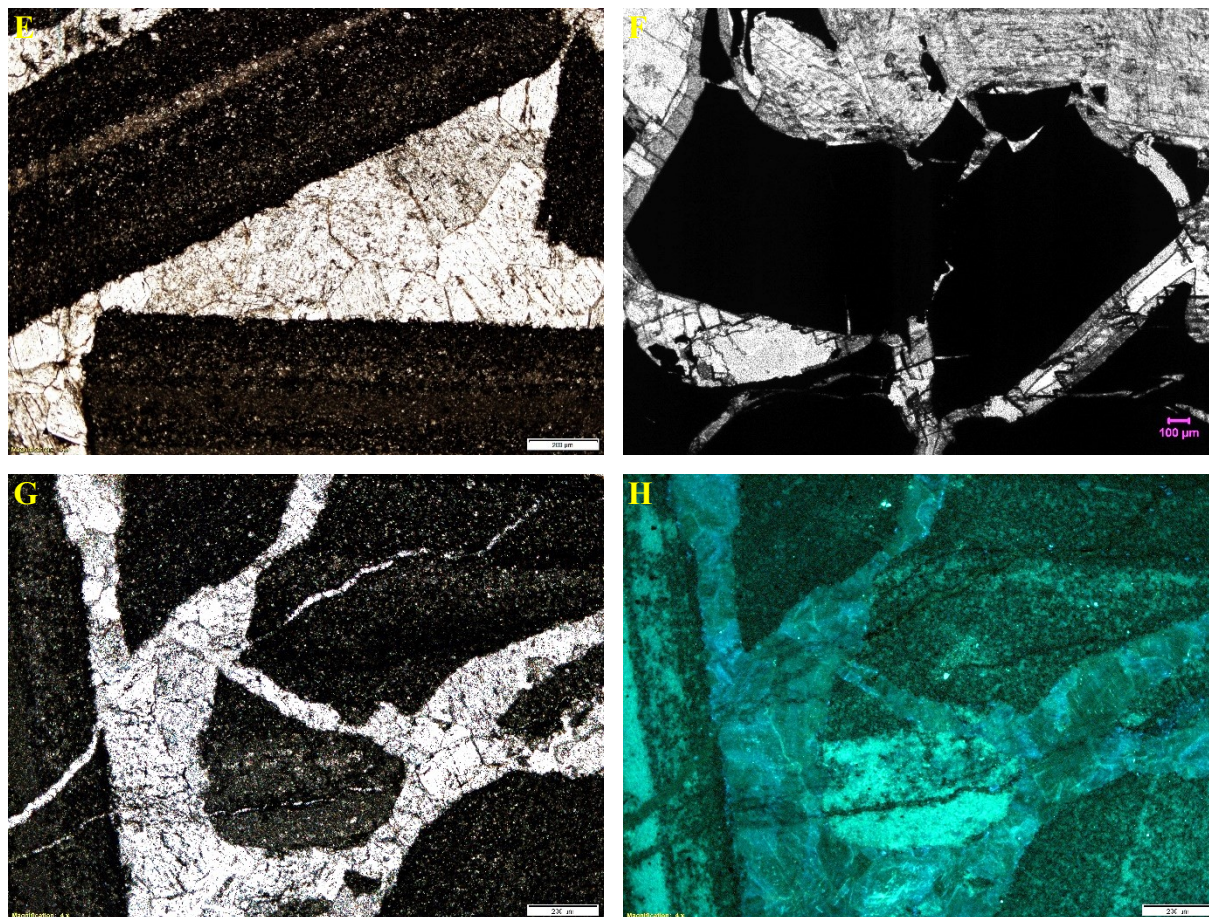


Figure 41. Sample 29y (Depth = 5334.64 m) (A) Photo of entire thin section; deformed and brecciated microbial mats in carbonate cement, transmitted light (B) Carbonate cement without zonation, blue-violet light 10x magnification (C) Carbonate cement and microbial mat. PPL 10x magnification (D) Same as C in blue-violet light, revealing zonation in carbonate cement, 10x magnification (E) Brecciated microbial mat in carbonate cement. PPL 4x magnification (F) Void-filling sulfide mineral. PPL 4x magnification (G) Cracked microbial mat in crystalline cement. PPL 4x magnification (H) Same view as G in blue-violet light, 4x magnification.



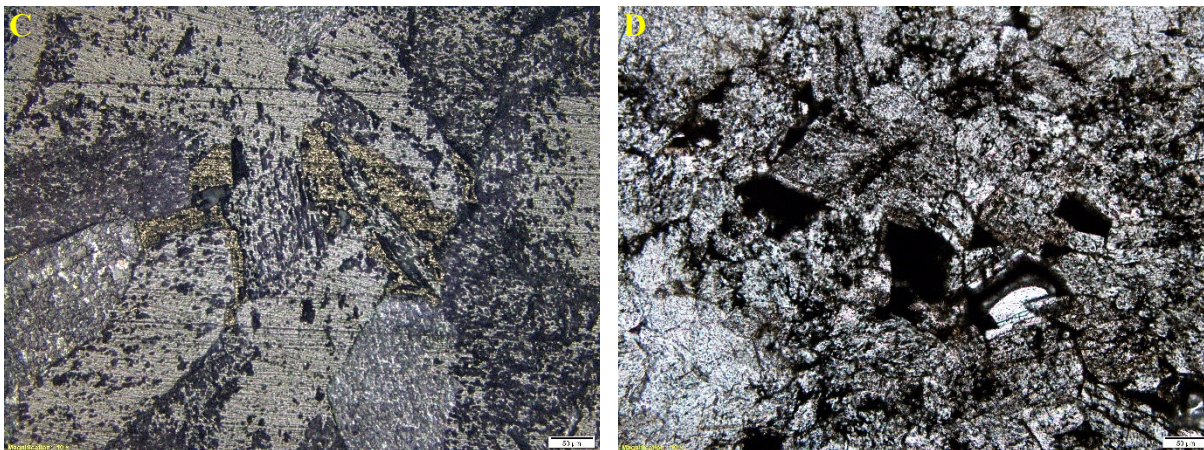
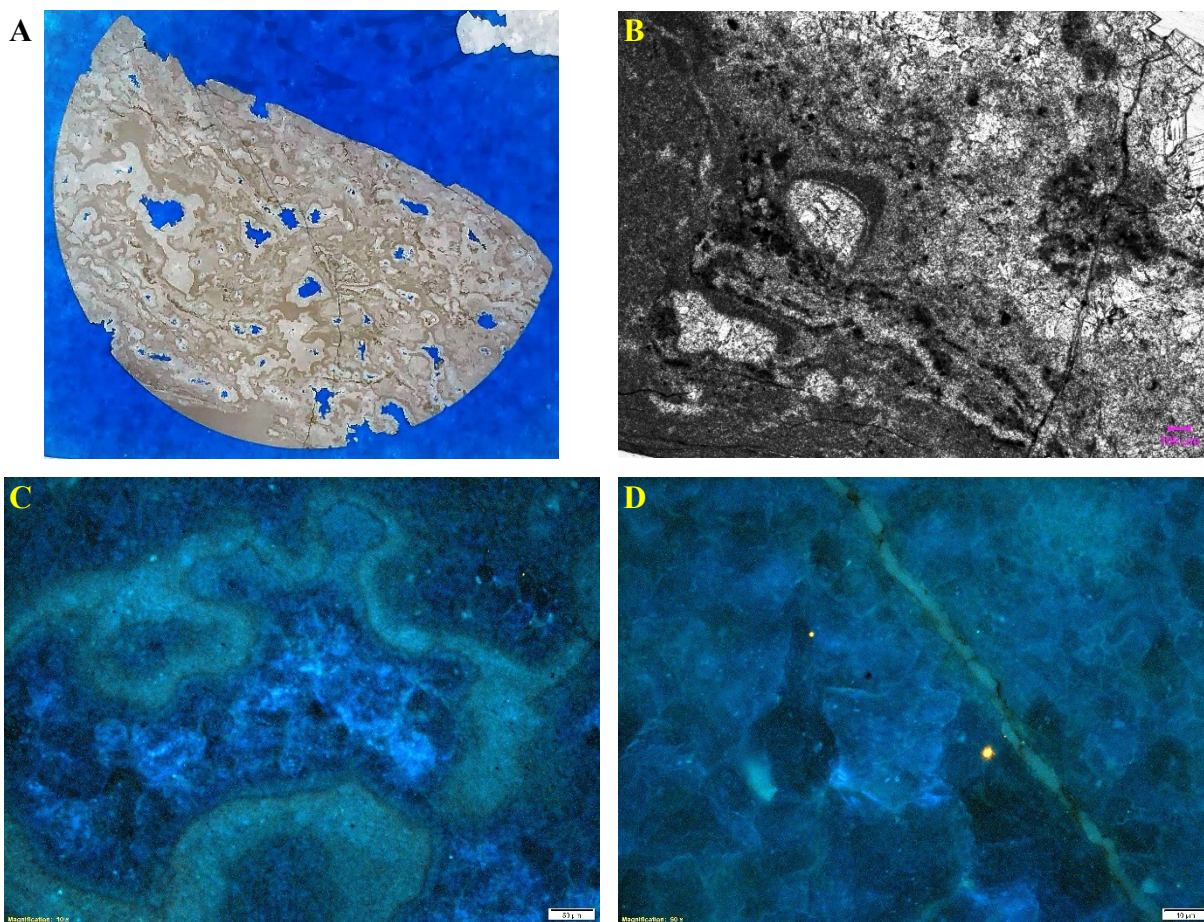


Figure 42. Sample 15 (Depth = 5335.43 m) (A) Photo of entire thin section, transmitted light (B) void-filling carbonate cement with chalcopyrite. PPL 10x magnification (C) Same view as B in reflected light, revealing sulfide minerals, 10x magnification (D) PPL 10x magnification.



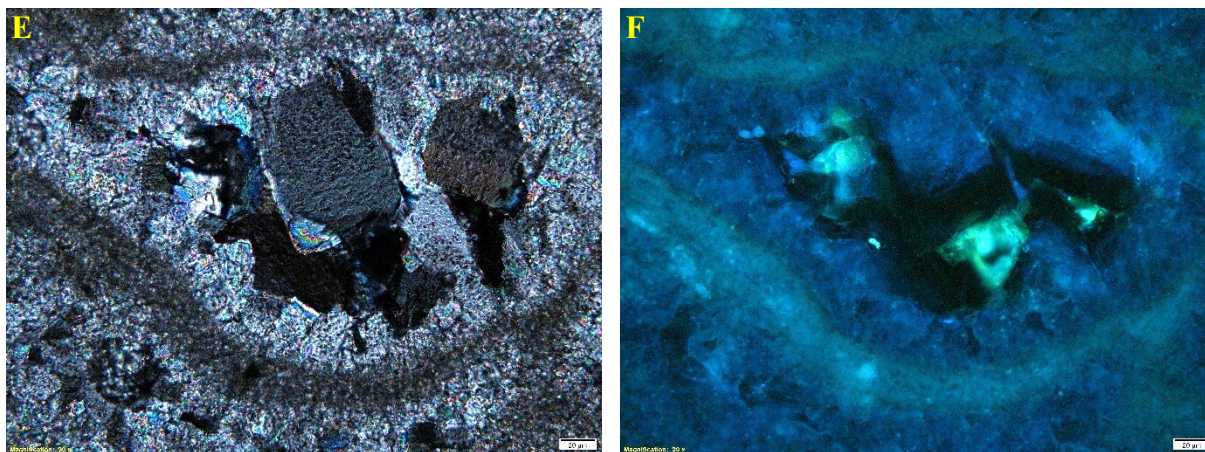


Figure 43. Sample 30 (Depth = 5335.45 m) (A) Photo of entire thin section, microbial framework, transmitted light (B) Clots, mat fragments and hollow chambers PPL 4x magnification (C) Large filled chamber lined with organic matter (green) surrounding cement fluoresces blue BVL 10x magnification (D) Same view as C in blue-violet light, 10x magnification (D) Sphalerite (red-orange fluorescence) BV 50x magnification (E) Deformed diffuse cortoid, filled with coarsely-crystalline dolomite. XPL 20x magnification (F) Same view as F in blue-violet light, organic matter fluoresces green, BV 20x magnification.

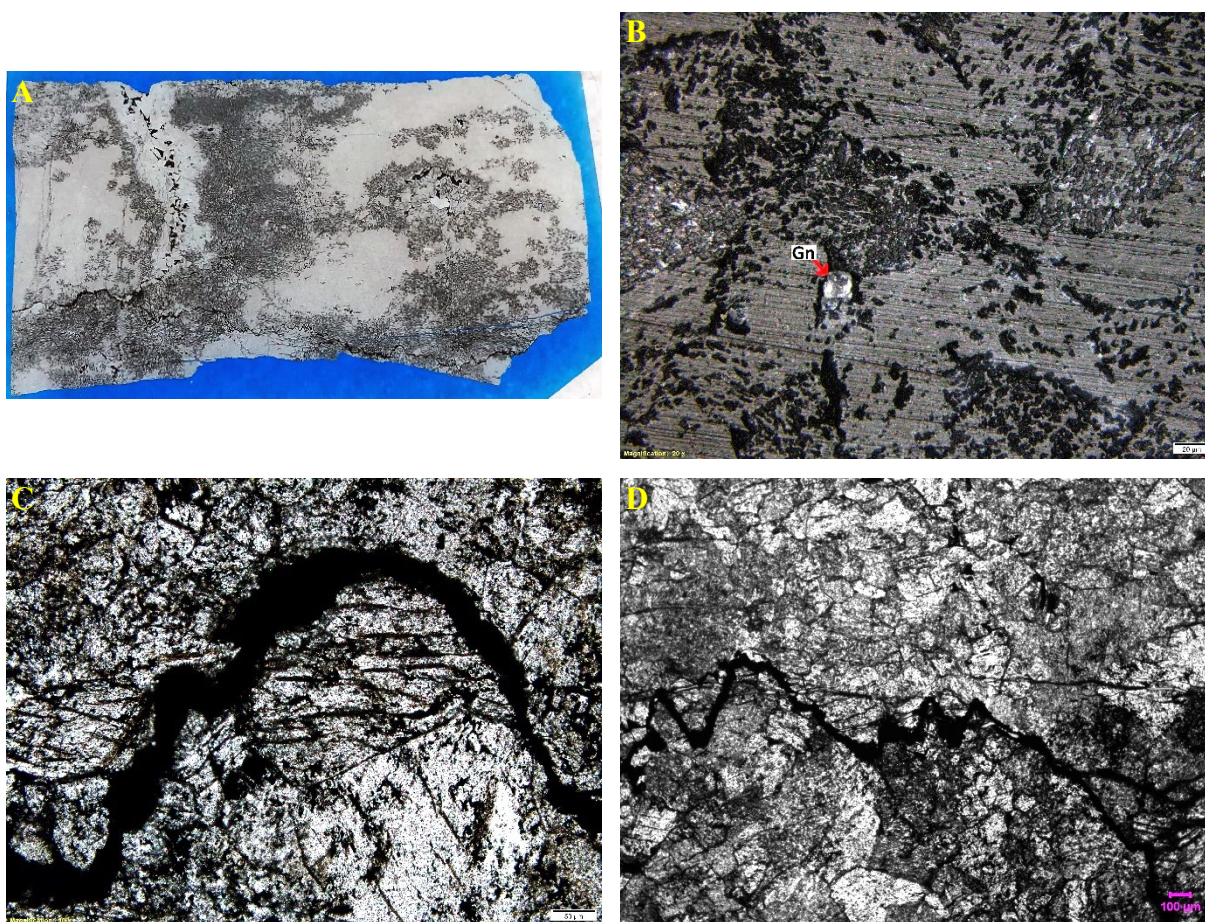
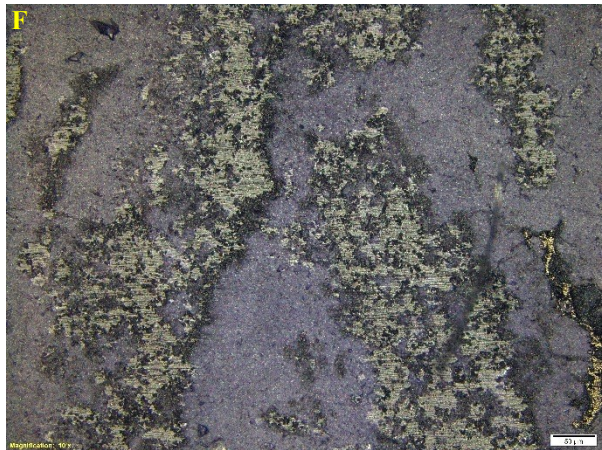
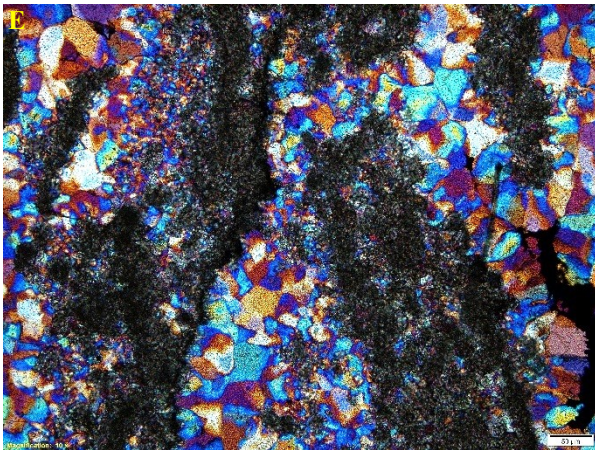
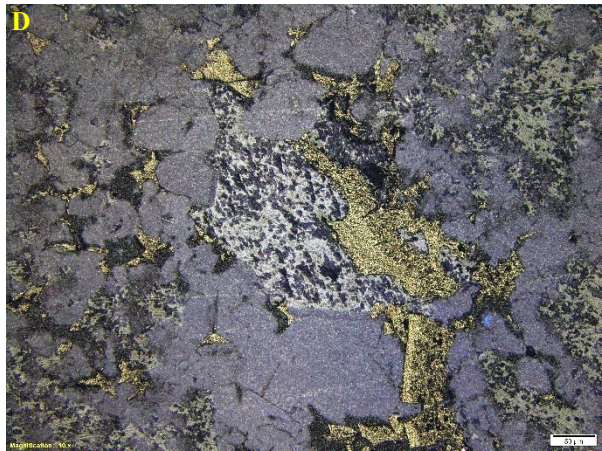
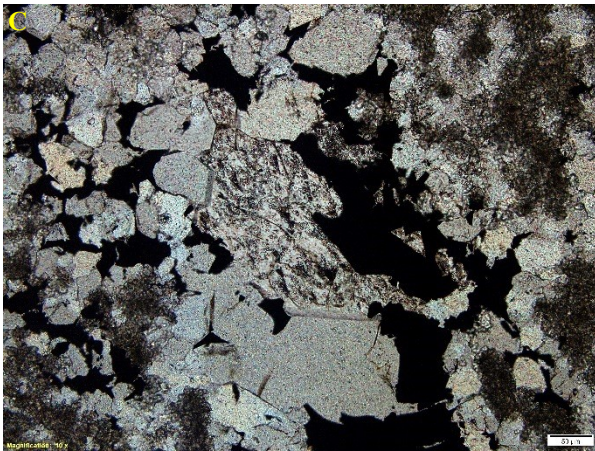
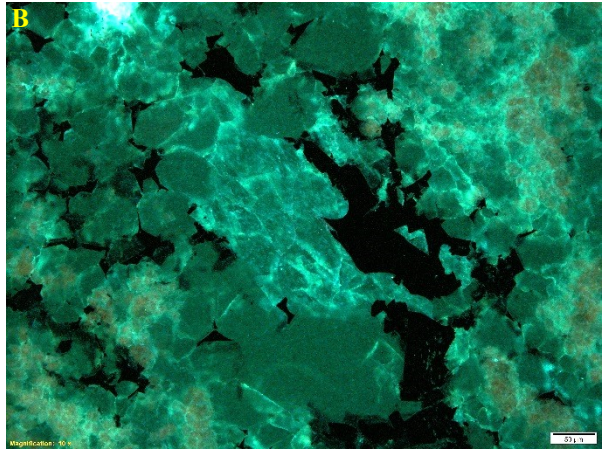


Figure 44. Sample 13 (Depth = 5335.77 m) (A) Photo of entire thin section, transmitted light (B) Cubic galena (GN) in reflected light, 20x magnification (C) Stylolite. PPL 10x magnification (See Fig. 16c for reflected light) (D) Stylolite. PPL 4x magnification.



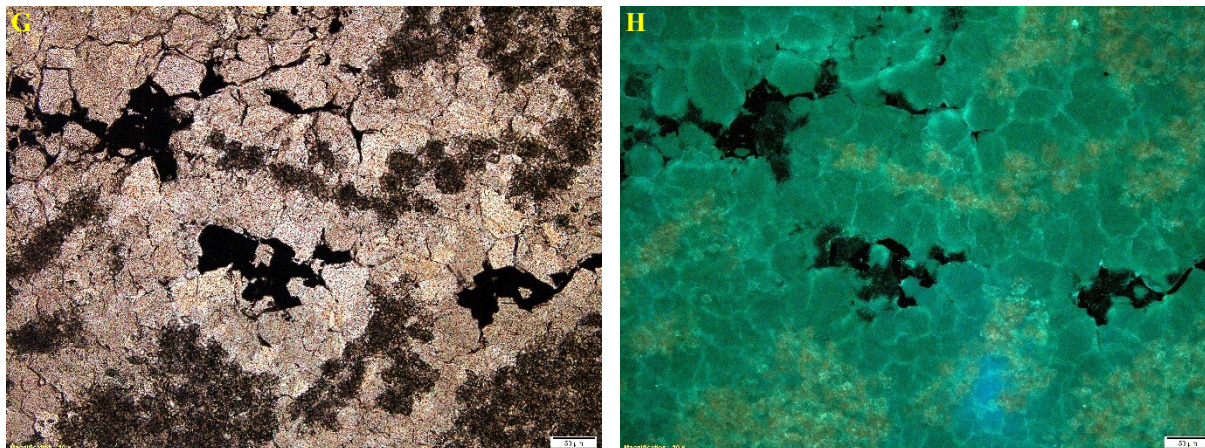


Figure 45. Sample 28x (Depth = 5351.99 m) (A) Photo of entire thin section, transmitted light (B) Clumped spheroidal sphalerite (red-orange) with quartz and other sulfide minerals (black), BV 10x magnification (C) Same view as B. PPL 10x magnification (D) Same view as B and C in reflected light, 10x magnification (E) Spheroidal sphalerite laminations in quartz cement, void-filling chalcopyrite, bottom right. XPL with sensitive tint plate 10x magnification (F) Same view as E in reflected light, 10x magnification (G) Aggregated spheroidal sphalerite. PPL 10x magnification (H) Same view as G in blue-violet light, 10x magnification.

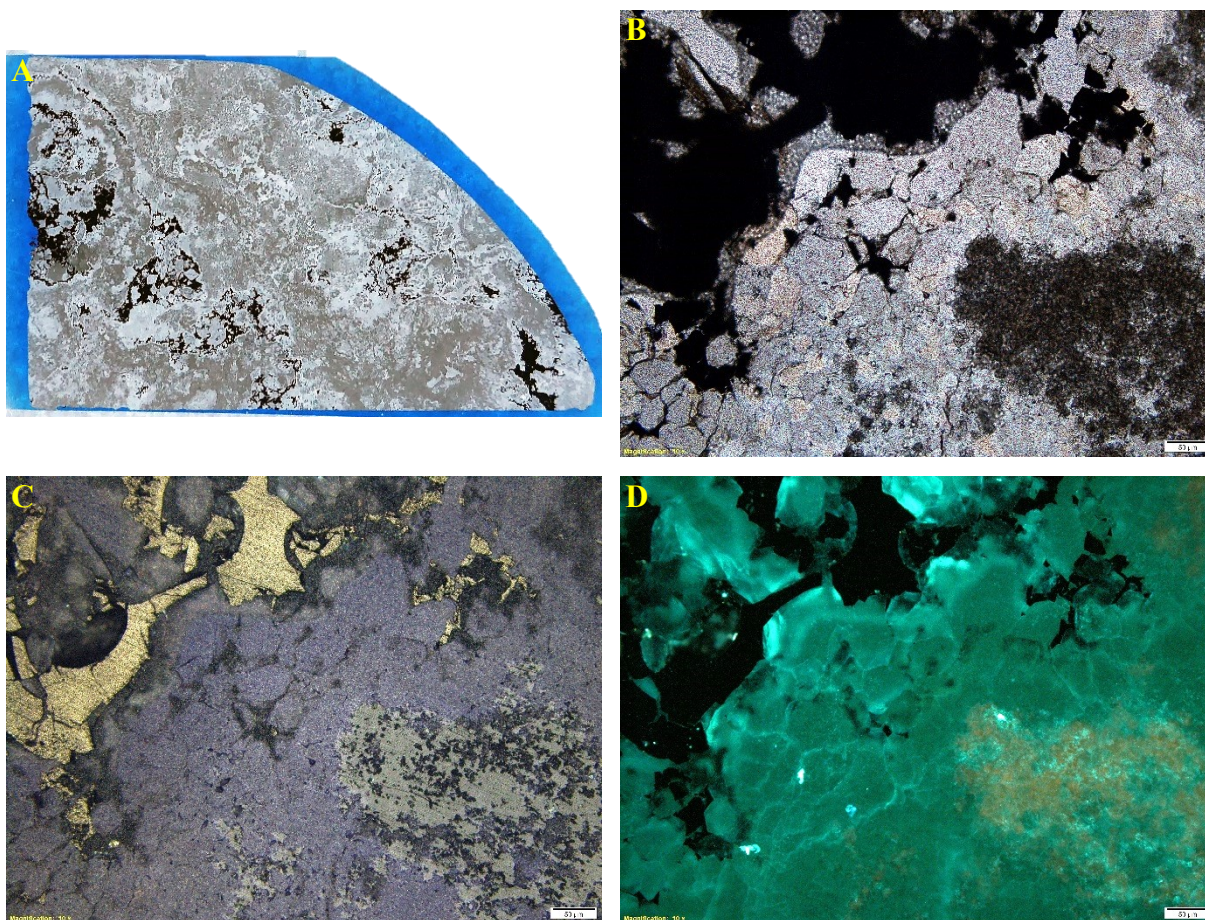


Figure 46. Sample 28y (Depth = 5351.99 m) (A) Photo of entire thin section, transmitted light (B) Quartz cement with void-filling pyrite and clumped spheroidal sphalerite. PPL 10x magnification (C) Same view as B in reflected

light, showing reflectance colors of pyrite and sphalerite (D) Same view as B and C in blue-violet light; some zonation in the quartz; sphalerite fluoresces red.

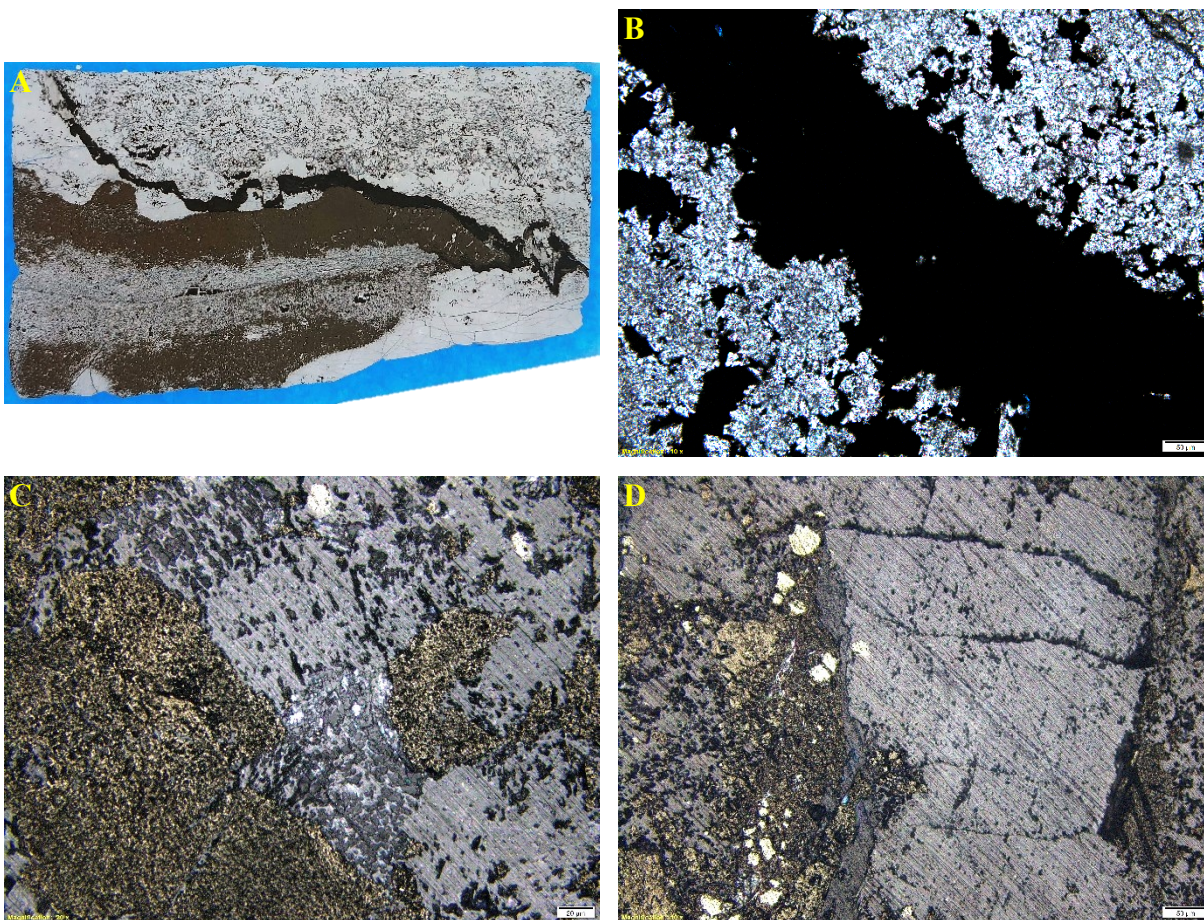
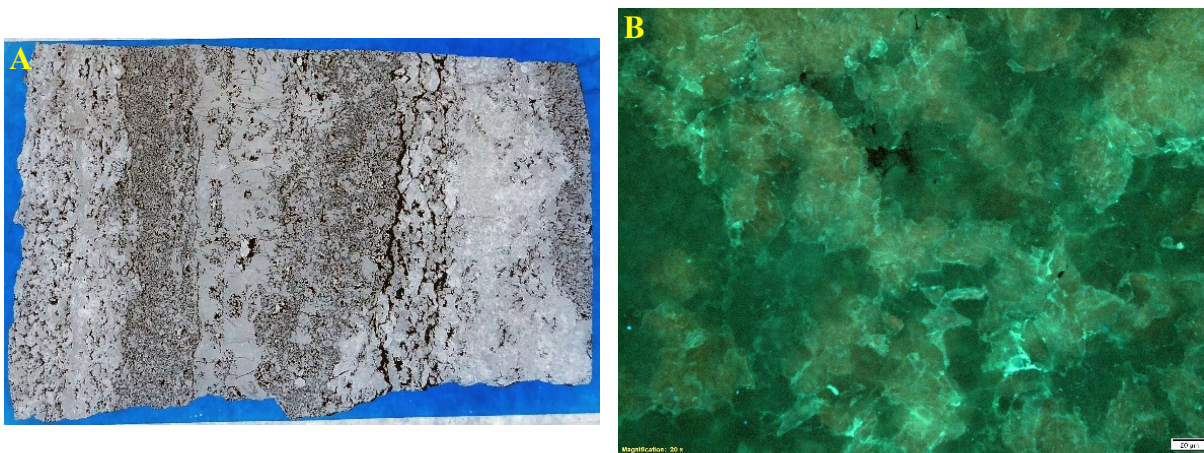


Figure 47. Sample 27 (Depth = 5383.04 m) (A) Photo of entire thin section, cut parallel to bedding; large stylolite and swath of hydrothermal pyrite, transmitted light (B) Stylolite. PPL 10x magnification (C) Chalcopyrite (dark yellow), pyrite (pale yellow) and galena (pale gray), RL 20x magnification (D) Chalcopyrite and pyrite, RL 20x magnification.



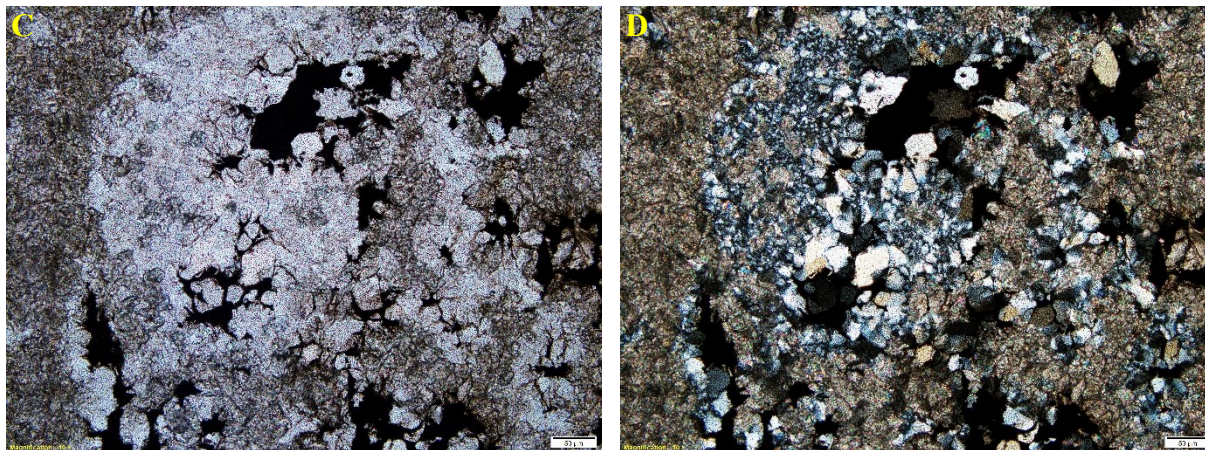


Figure 48. Sample 31 (Depth = 5385.50 m) (A) Photo of entire thin section, transmitted light (B) Red-orange and green fluorescence in blue-violet light, 20x magnification (C) Quartz partially replaces micrite. PPL 10x magnification (D) Same view as C in crossed polar light, 10x magnification.

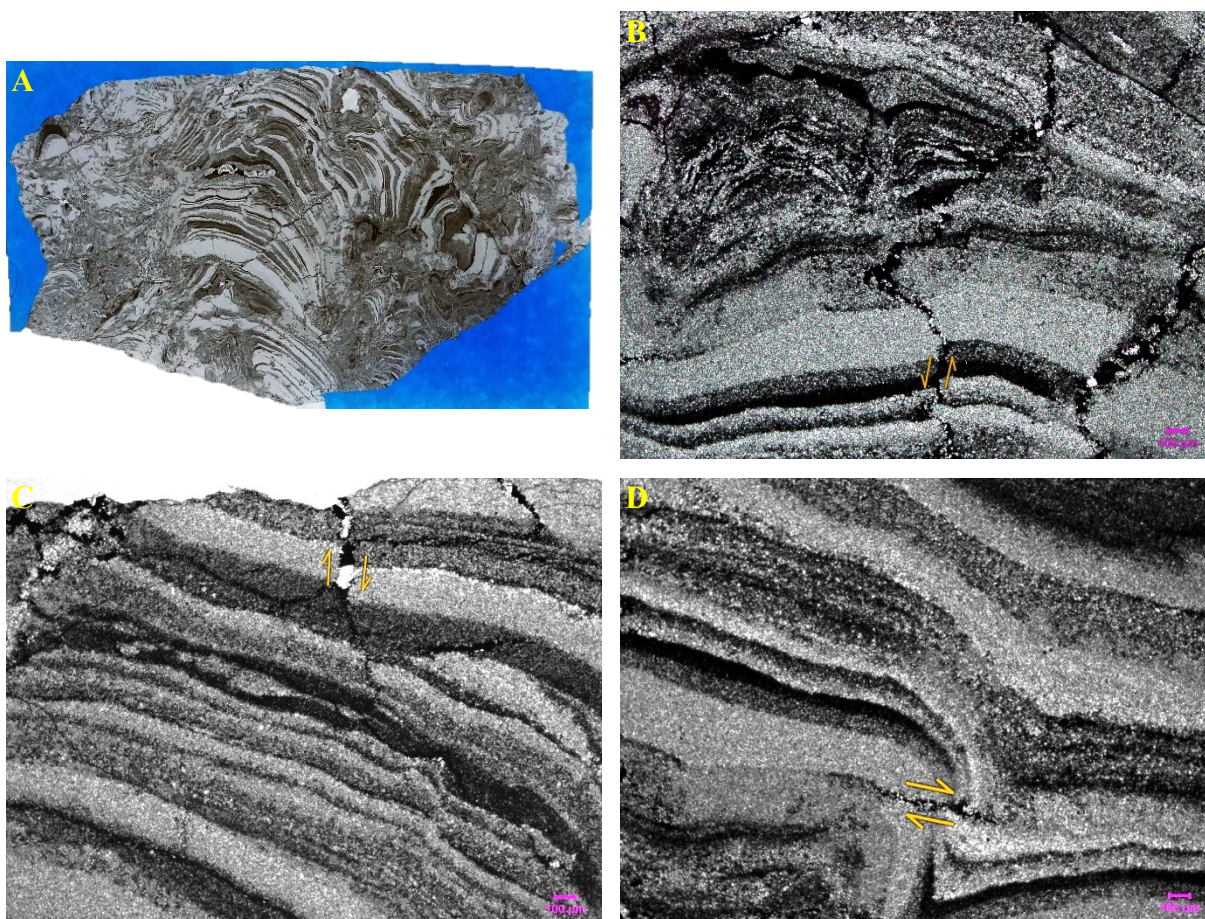


Figure 49. Sample 26 (Depth = 5397.81 m) (A) Photo of entire thin section, branching columnar stromatolite; some laminations are wispy and pinch out, transmitted light (B) Fractured stromatolite, orange arrows show displacement PPL 4x magnification (C) Fine-grained stratiform stromatolite; wavy laminations with post-depositional fractures (orange arrows). PPL 4x magnification (D) Flat stromatolite (right) rises steeply into domical stromatolite (left); fracture and displacement after lithification (orange arrows). PPL 4x magnification.

Dengying Member 3 (dn³), Micang mountains (106°32'E, 32°26'N), outcrop

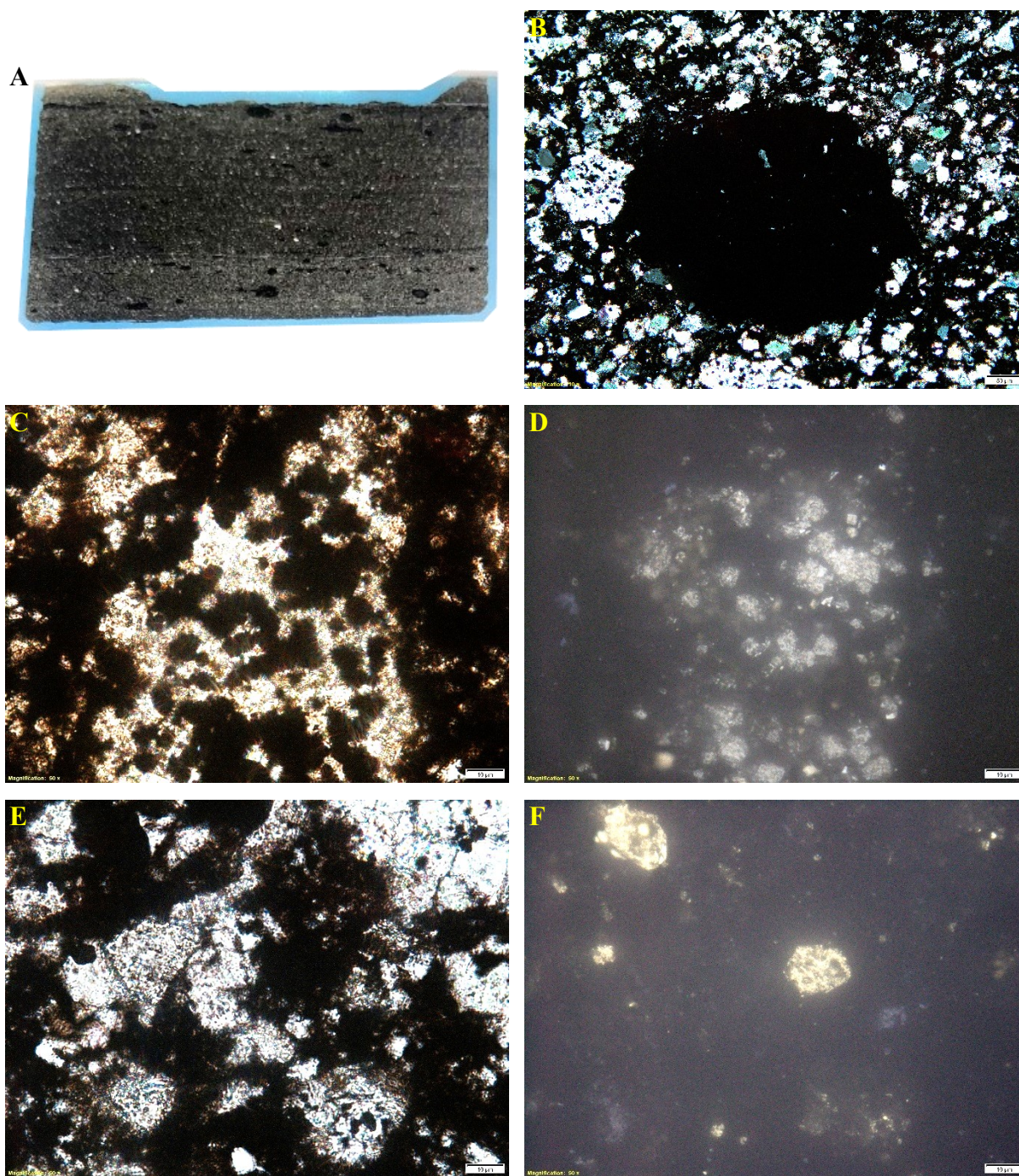


Figure 50. Sample 1a (A) Photo of the entire thin section, thinly laminated carbonate-grain shale with organic clumps, transmitted light (B) Organic clump. XPL 10x magnification (C) Clotted organic matter and sulfide minerals. PPL 50x magnification (D) Same view as C in reflected light, revealing galena and sphalerite, 50x magnification (E) Clotted organic matter and sulfide minerals. PPL 50x magnification (F) Same view as E in reflected light, sulfides are mostly pyrite, 50x magnification.

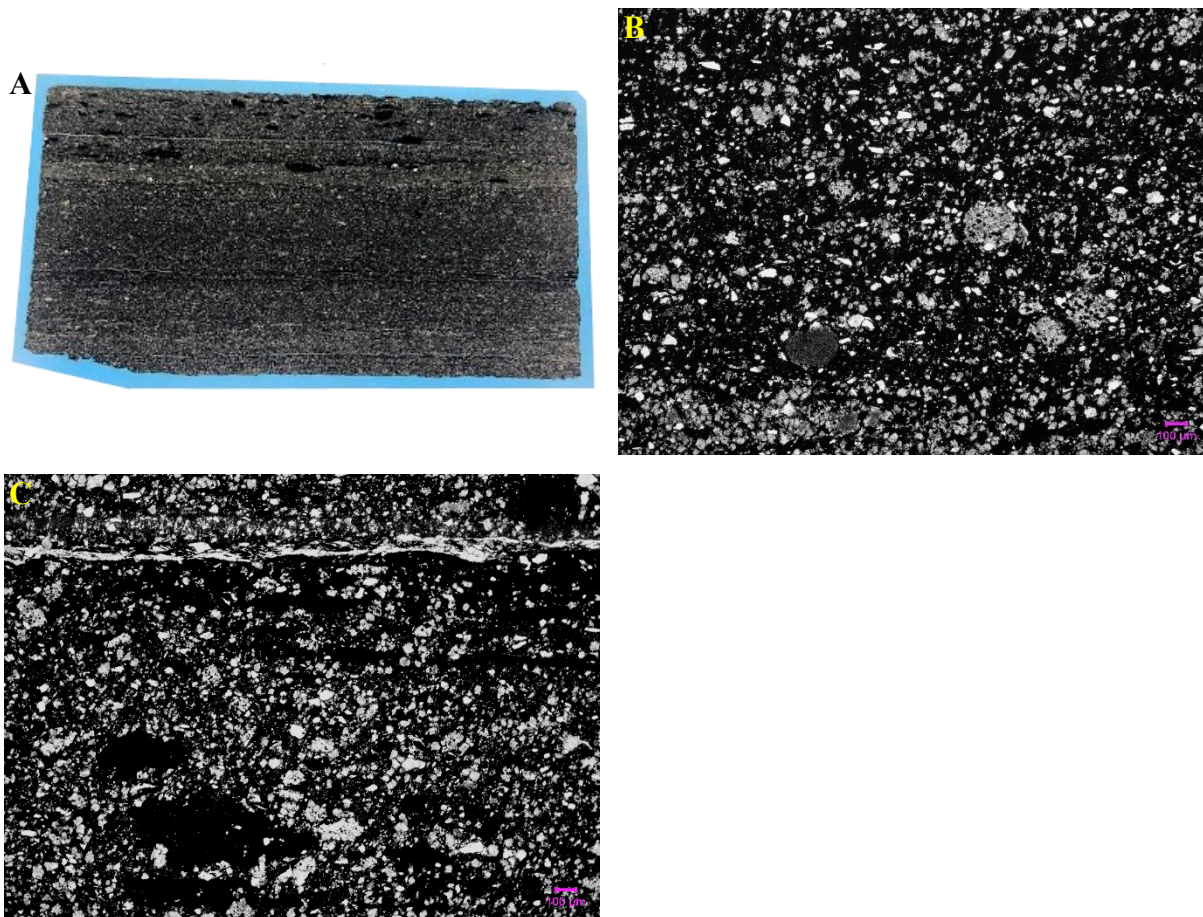
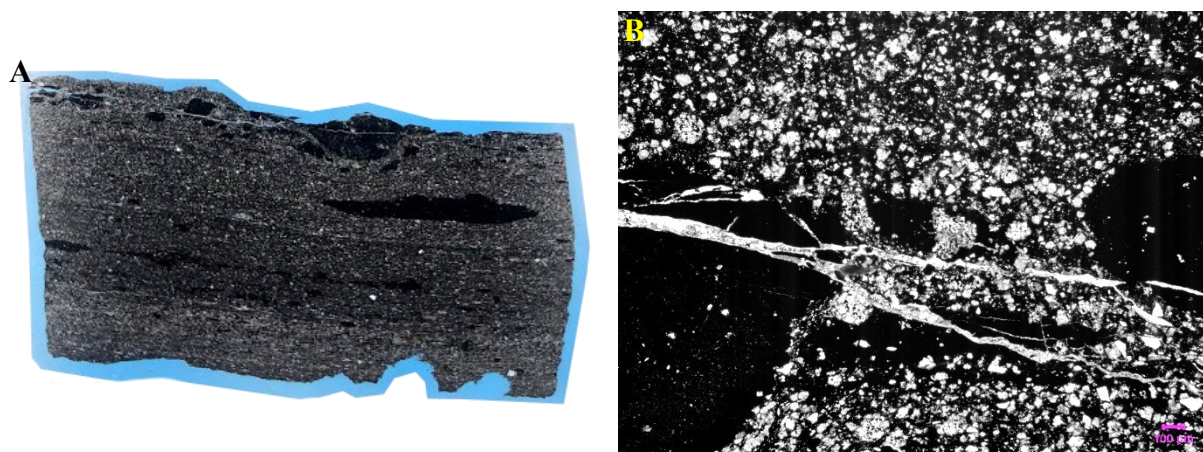


Figure 51. Sample 1b (A) Photo of entire thin section, thinly laminated carbonate-grain shale with organic clumps, transmitted light (B) Coarse silt with quartz and carbonate grains and illite. PPL 4x magnification (C) Laminated shale with organic clumps and a thin clay layer (top). PPL 4x magnification.



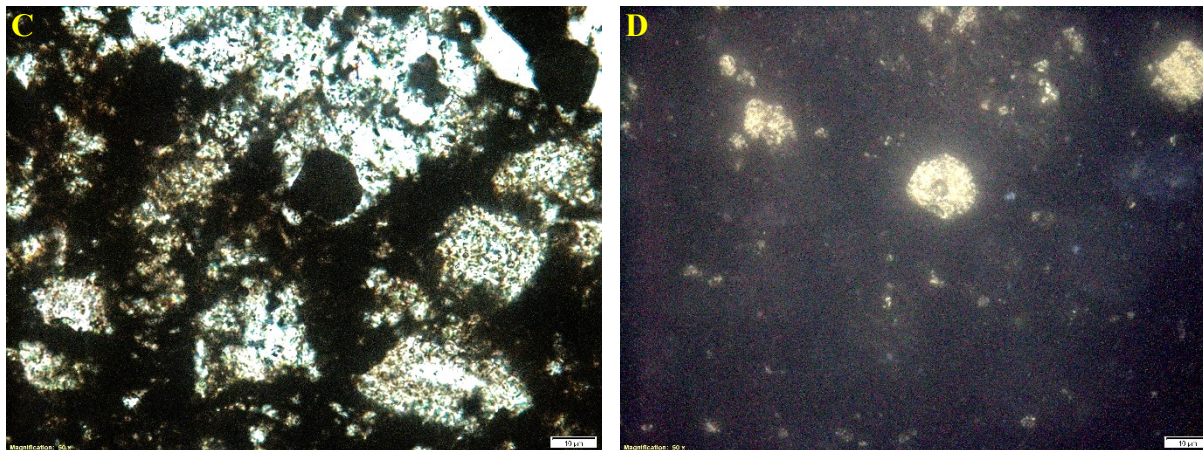


Figure 52. Sample 1c (A) Photo of the entire thin section, coarse-silty shale with thin laminations, thicker light and dark bands, and large organic clasts, transmitted light (B) Organic clasts in grainy laminated shale. PPL 4x magnification (C) Sulfide minerals and intergranular organic matter PPL 50x magnification (D) Pyrite seen in C, RL 50x magnification.

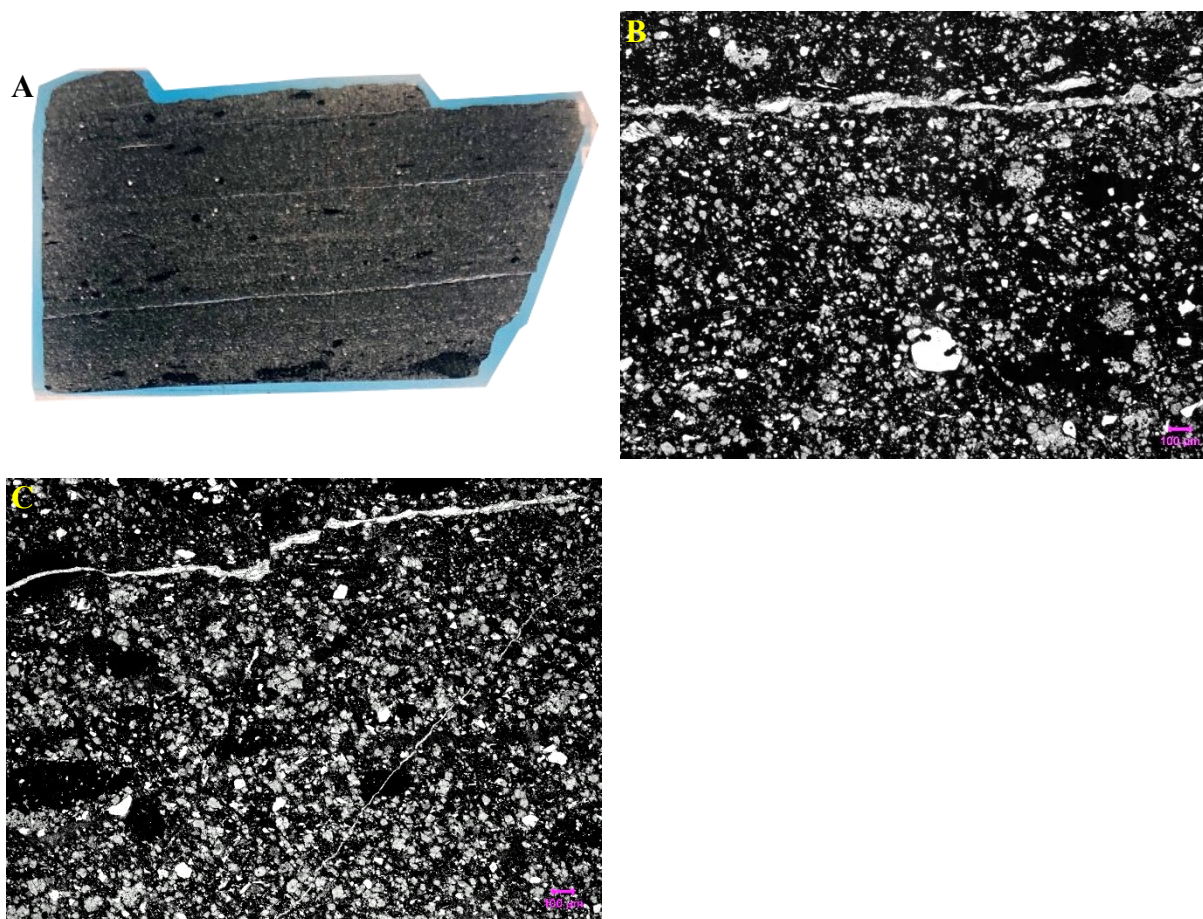


Figure 53. Sample 1d (A) Photo of the entire thin section, laminated black shale with thin clay layers and clumps of organic matter, transmitted light (B) Grainy texture and thin clay layer. PPL 4x magnification (C) Grainy fabric with larger organic clots. PPL 4x magnification.

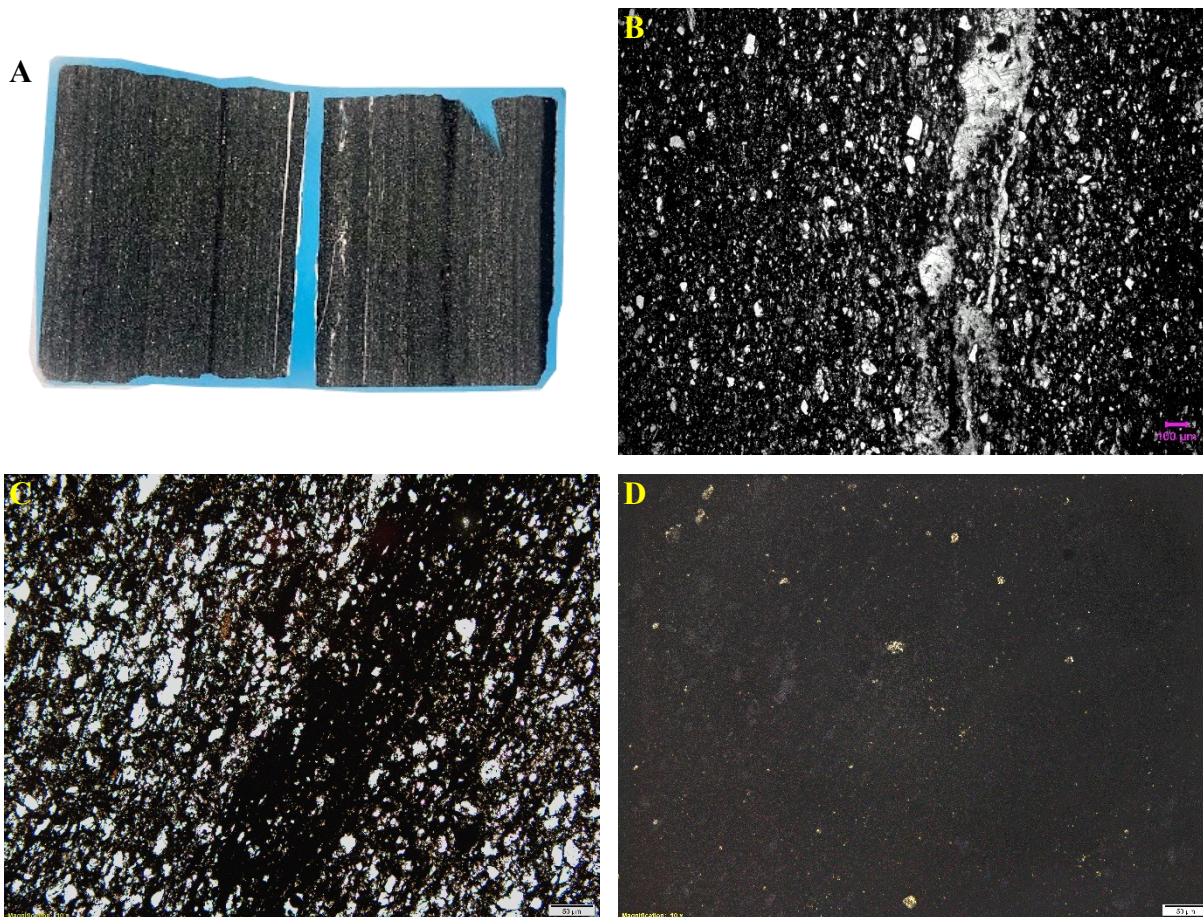
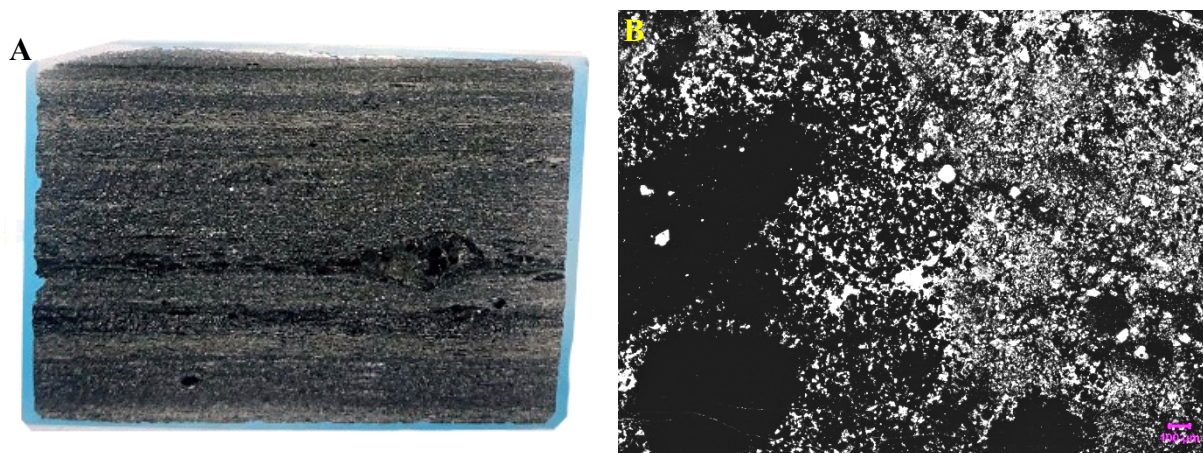


Figure 54. Sample 1e (A) Photo of entire thin section, laminated black shale, transmitted light (B) dolomite-filled vein in grainy groundmass. PPL 4x magnification (C) Organic lamination with grainy quartz (white) and illite (brown). PPL 10x magnification (D) Same view as C in reflected light 10x magnification.



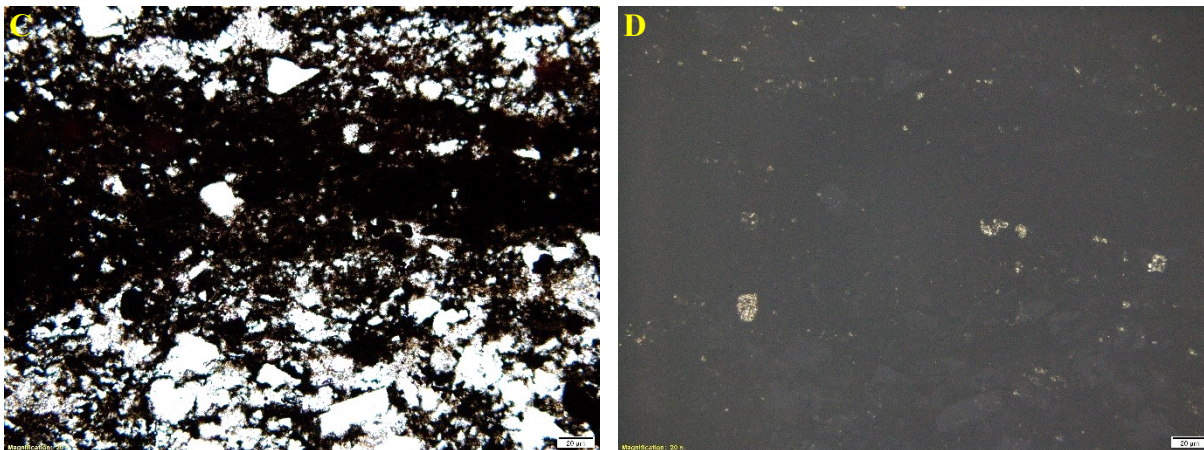
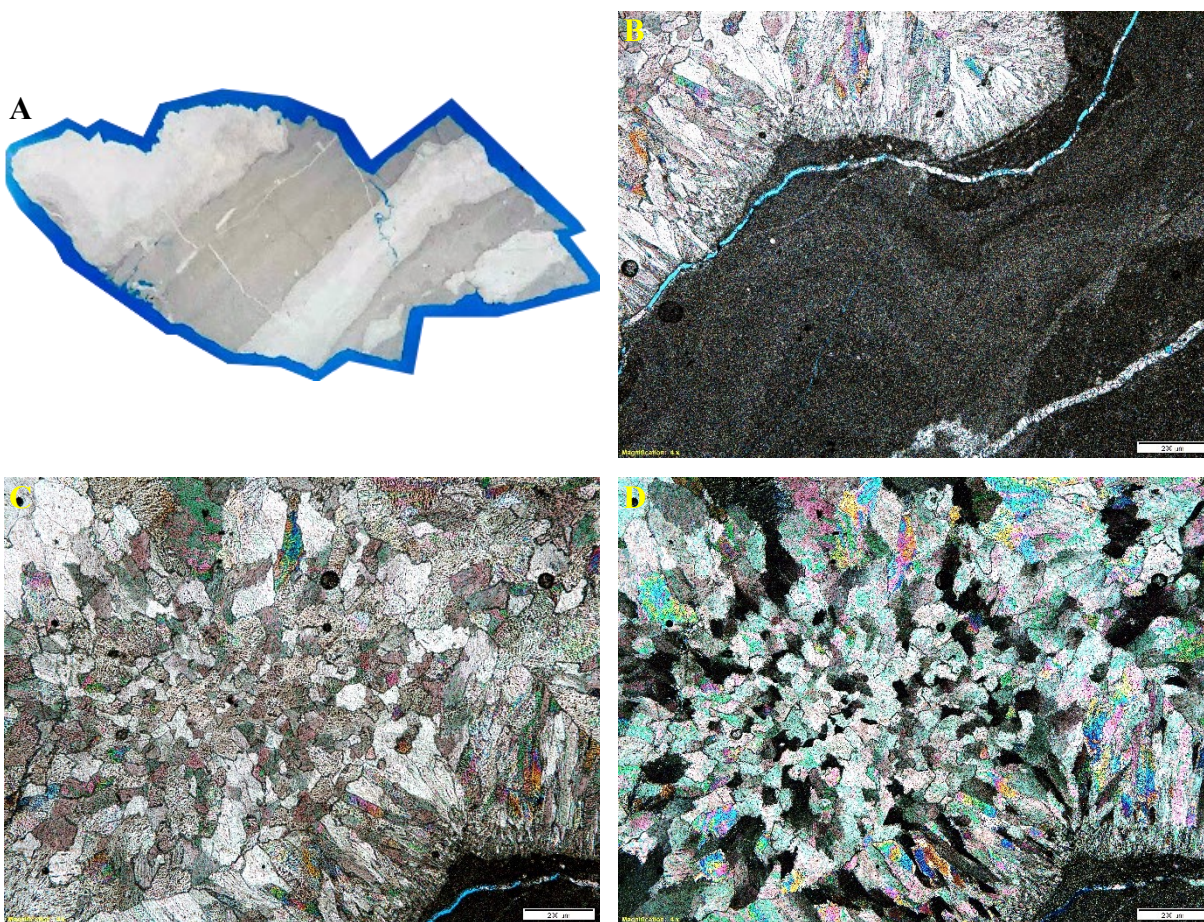


Figure 55. Sample 1f (A) Photo of the entire thin section, black shale with thick light and dark banding, transmitted light (B) Organic clots and sulfide minerals PPL 4x magnification (C) Organic lamination and quartz grains (white), PPL 20x magnification (D) Same view as E in reflected light, revealing pyrite, 20x magnification.



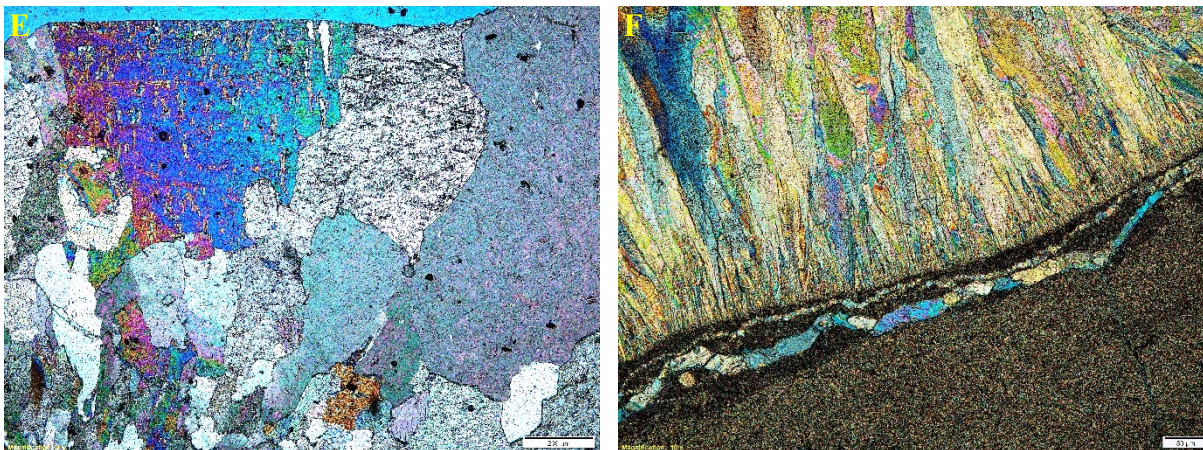
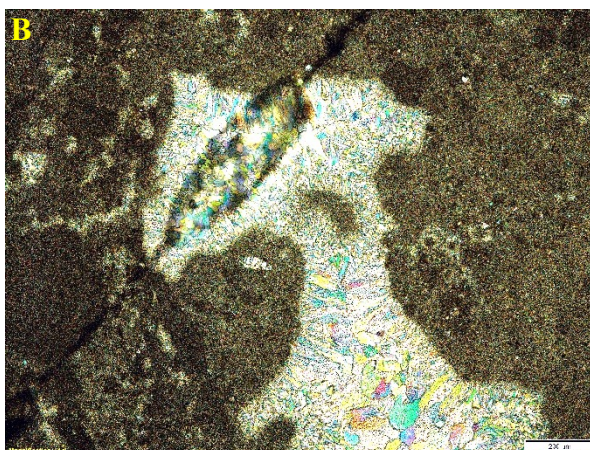


Figure 56. Sample 2a (A) Photo of the entire thin section, transmitted light (B) Ghost laminations in micrite (bottom right) fibrous rim dolomite (top left). XPL 4x magnification (C) Fibrous dolomite transitions into polygonal cement. XPL 4x magnification (D) Same view as C, with minerals at extinction or maximum birefringence. XPL 4x magnification (E) Hydrothermal replacive minerals. XPL 4x magnification (F) Fibrous dolomite and accessory minerals emanating from micrite; 2 filled veins in micrite. XPL 10x magnification.

A



C

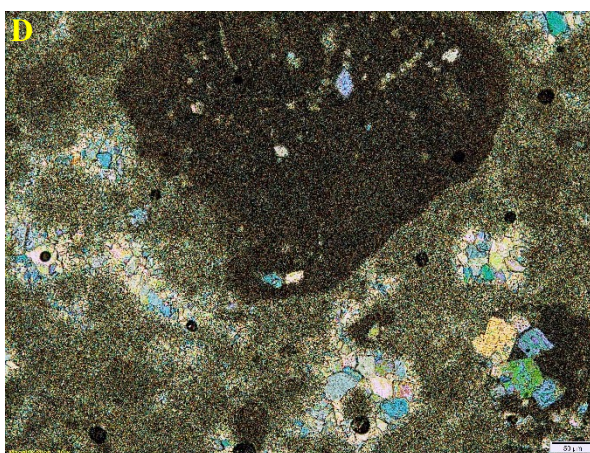
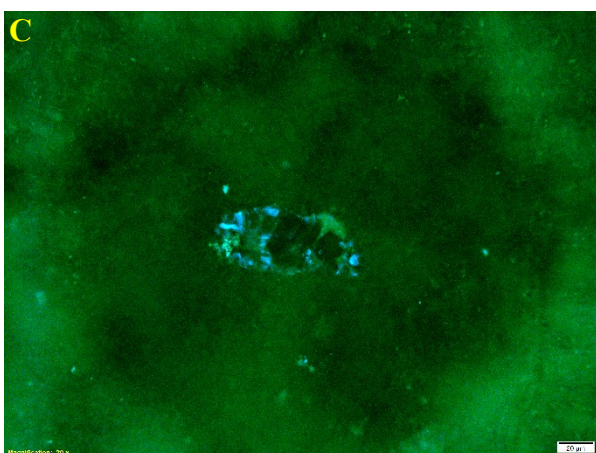


Figure 57. Sample 2b (A) Photo of the entire thin section, transmitted light (B) Thrombolitic texture bottom left, pelimicrite with large organic clasts plus hydrothermal vein with chunk of micrite and confusing overlying feature. PPL 4x magnification (C) Green and blue fluorescence in a hollow chamber, BV 20x magnification (D) Micritized

organic clot or *Protolagena* test (Cai et al., 2010) (diameter = 0.5mm) with replacive dolomite rhombs. XPL 10x magnification.

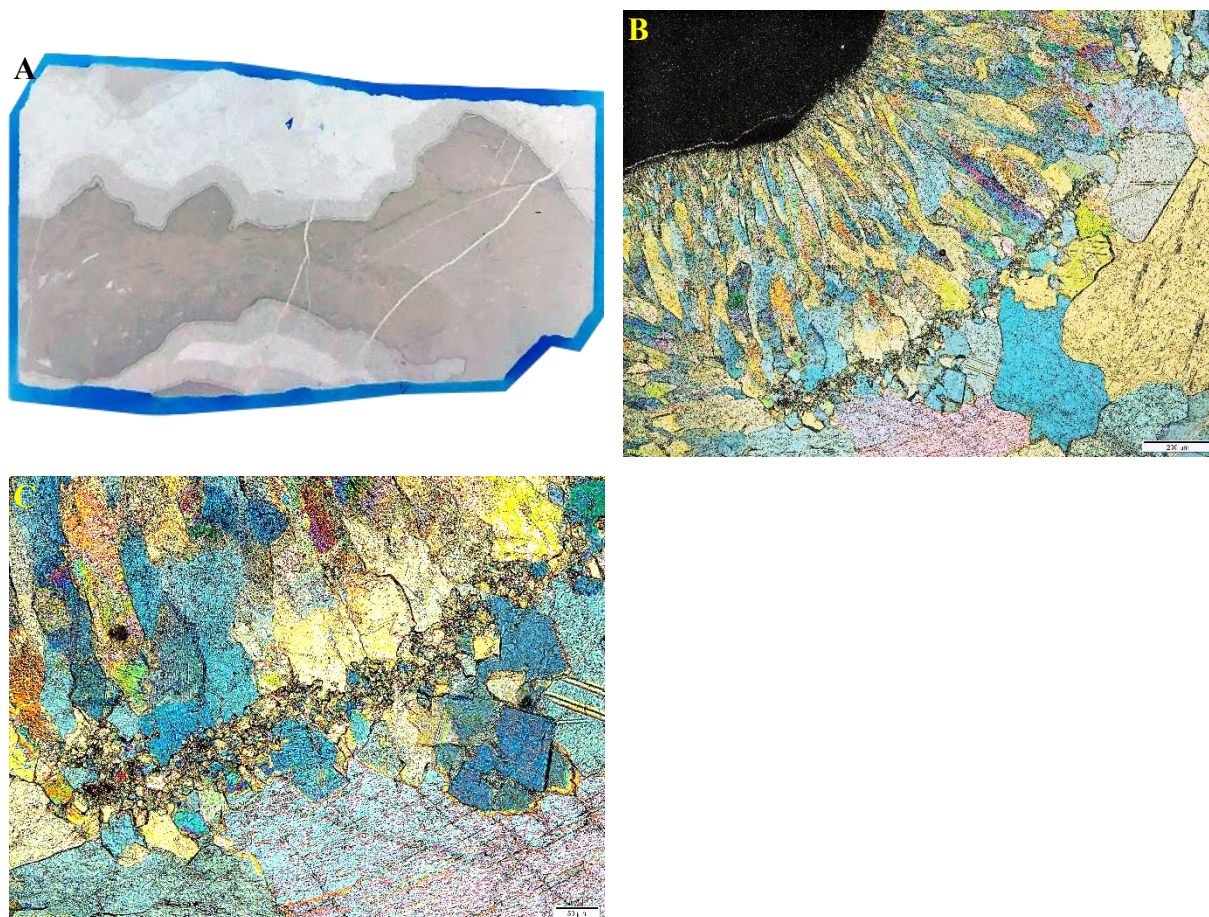
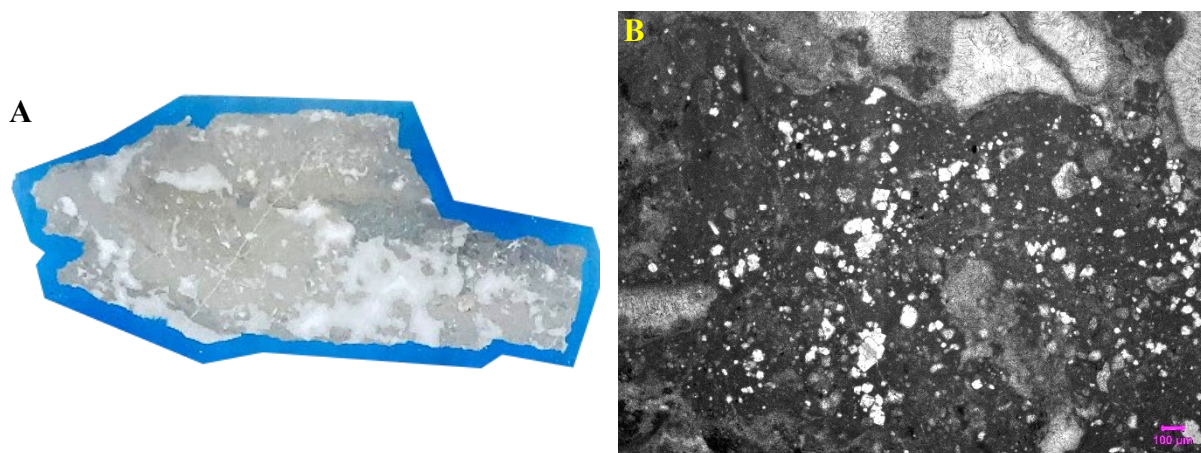


Figure 58. Sample 2c (A) Photo of the entire thin section, transmitted light (B) Fibrous, finely crystalline, and coarsely crystalline hydrothermal minerals. XPL 4x magnification (C) Fibrous, finely crystalline, and coarsely crystalline hydrothermal minerals. XPL 10x magnification



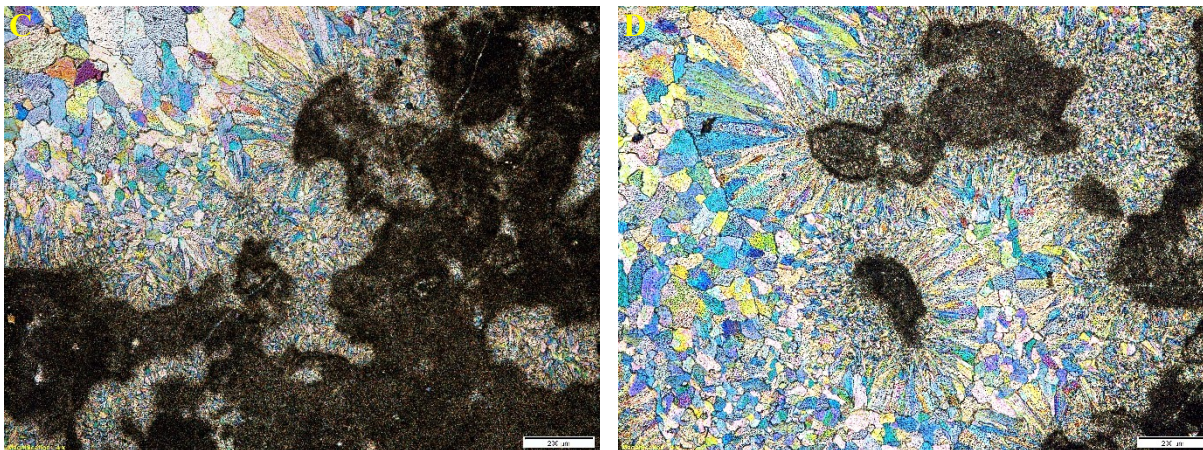


Figure 59. Sample 2d (A) Photo of the entire thin section, transmitted light (B) Thrombolite microtexture; micrite with filled dissolution pores and disseminated quartz crystals. PPL 4x magnification (C) Microbial framework surrounded by fibrous dolomite transitioning into dolosparite XPL 4x magnification (D) Disaggregated microbial framework surrounded by fibrous dolomite transitioning into dolosparite. XPL 4x magnification.

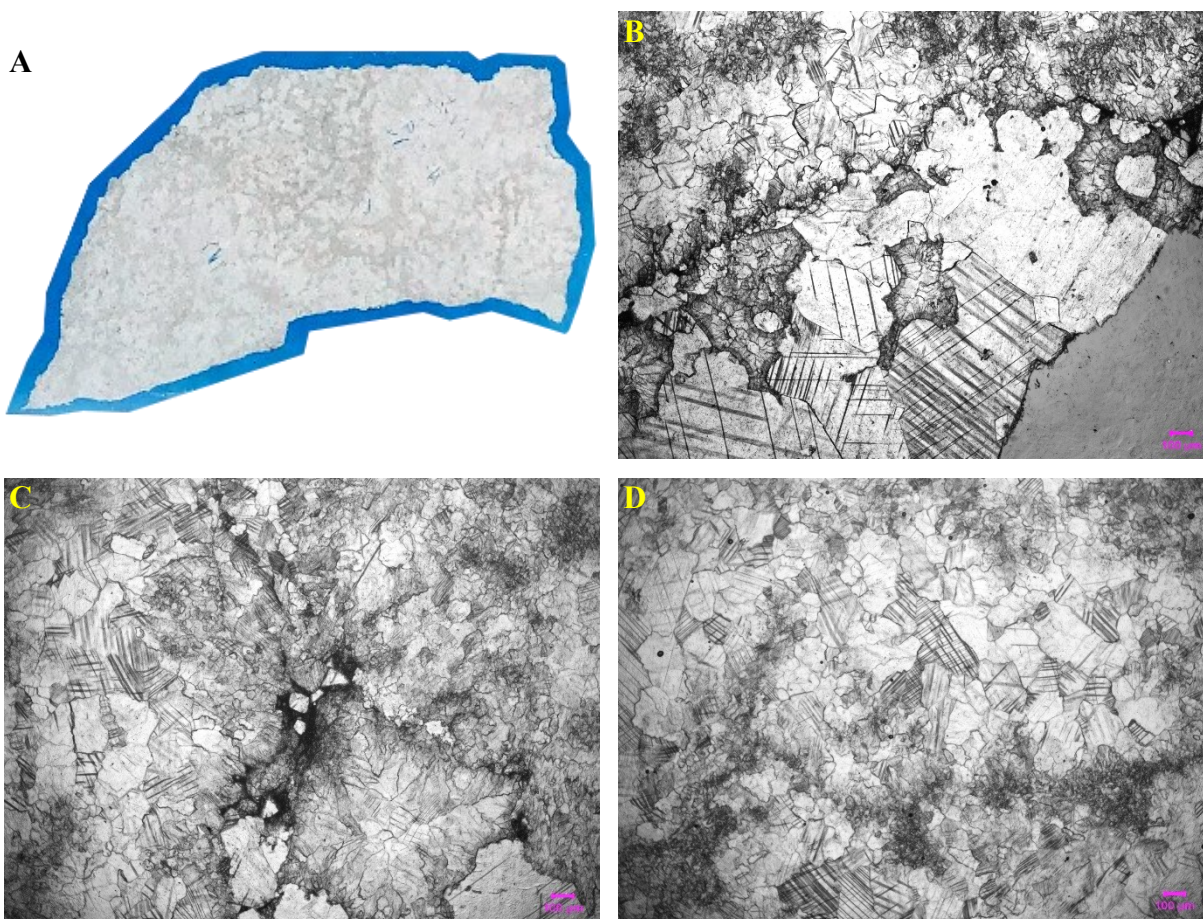


Figure 60. Sample 2e (A) Photo of the entire thin section, transmitted light (B) Coarse to finely crystalline dolosparite with some oil staining; Large crystal at right has botryoidal texture PPL 4x magnification (C) Coarse to finely crystalline dolosparite with oil charge. PPL 4x magnification (D) Coarse to finely crystalline dolosparite with some oil staining. PPL 4x magnification.

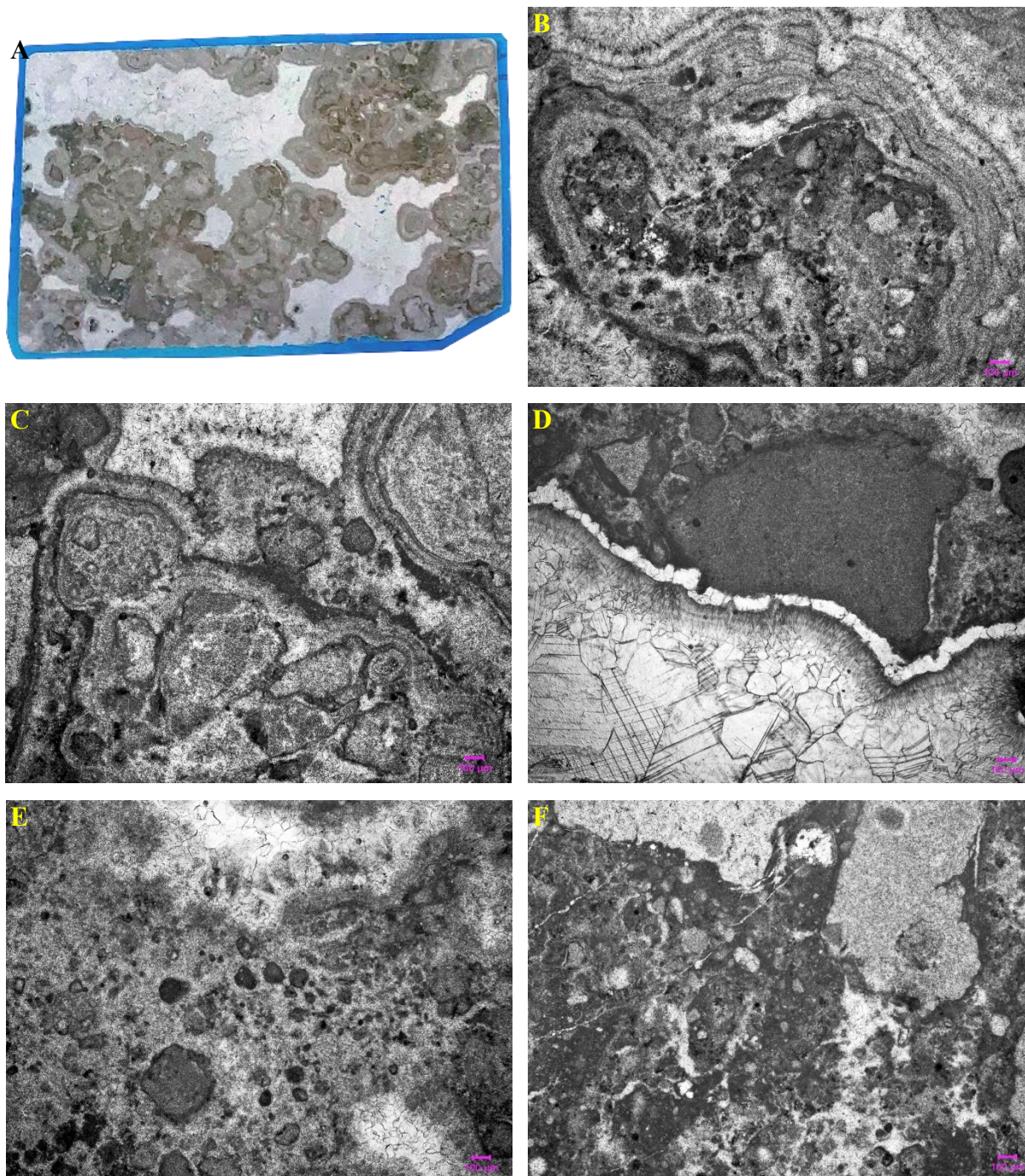


Figure 61. Sample 2f (A) Photo of the entire thin section, grapestone and dolosparite, transmitted light (B) Clotted mesoclots with encrusting laminae, diffuse organic matter and peloids. PPL 4x magnification (C) Thrombolite. PPL 4x magnification (D) Leolite, peloids and hollow chambers (top), dolosparite (bottom) and crystalline aggregate lining dolosparite cement. PPL 4x magnification (E) Clots and cortoids with dissolution. Crown-shaped feature near top center vaguely resembles *Mengeosphaera eccentrica* (Xiao et al., 2014) PPL 4x magnification (F) Large intraclasts, extensive circumgranular cracks. PPL 4x magnification.

**Doushantuo & Dengying (unknown member), Daba Mountain thrust belt (108°35'E,
31°58N'), outcrop**

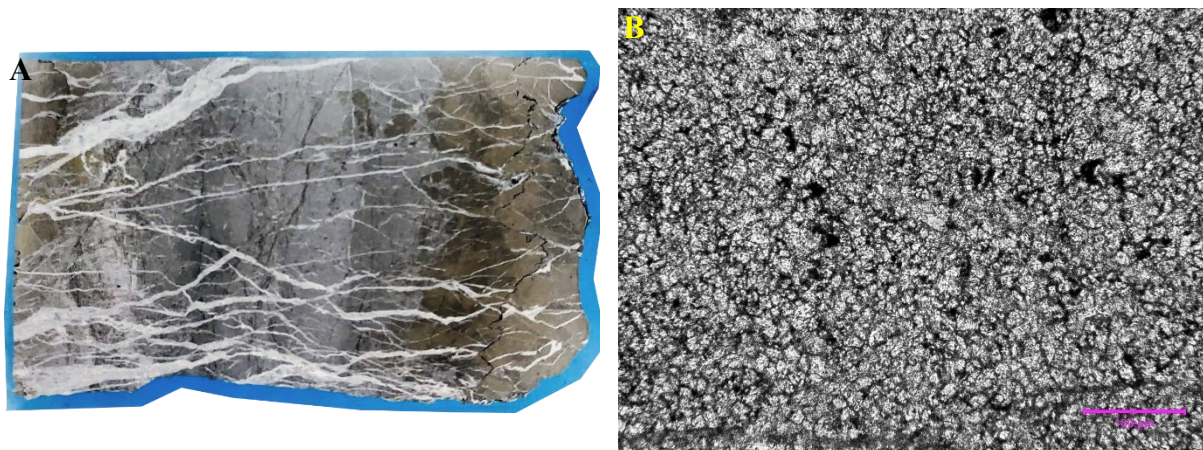


Figure 62. Sample 4a Doushantuo (A) Photo of the entire thin section, transmitted light (B) Oil-rich dolomitic marl. PPL 20x magnification.

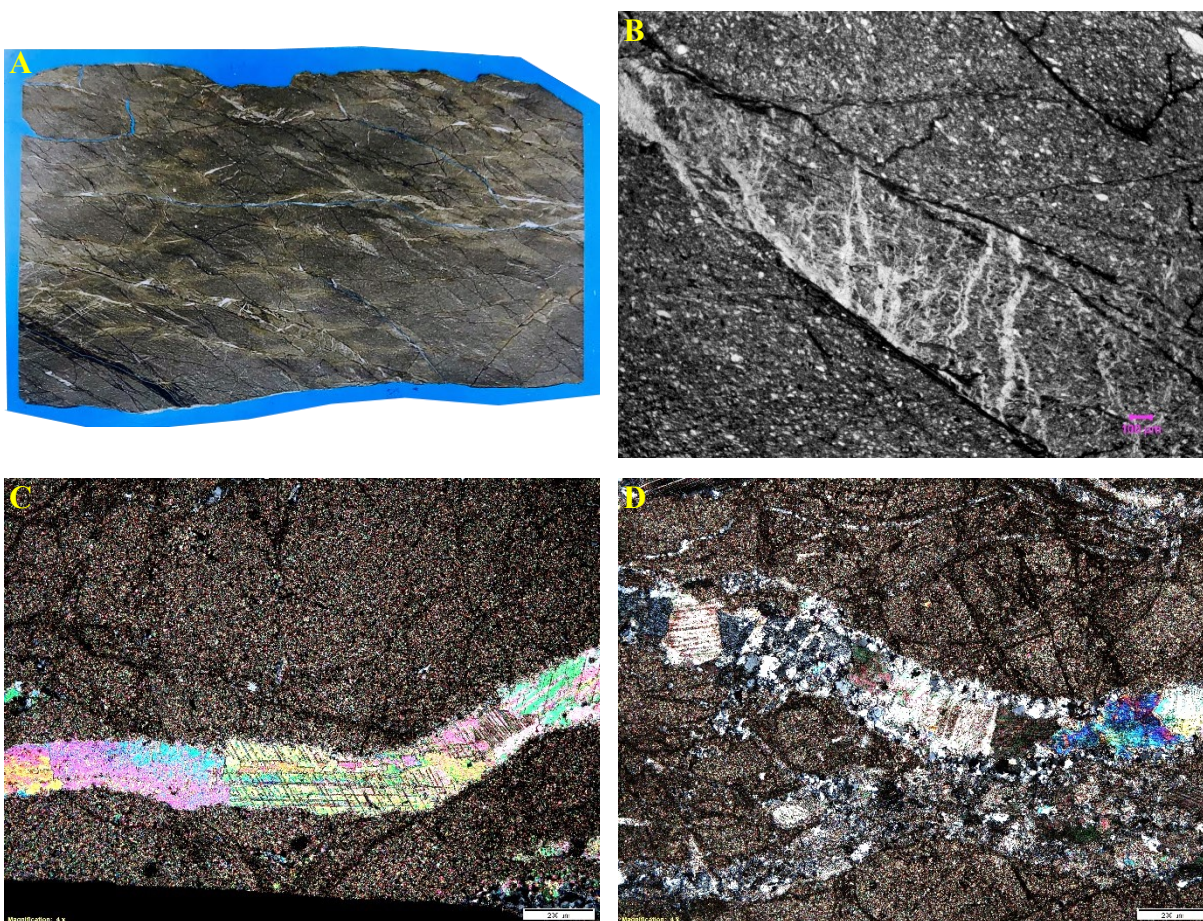


Figure 63. Sample 5a Doushantuo (A) Photo of the entire thin section, transmitted light (B) Vertical veins between cracks. PPL 4x magnification (C) Anhydrite-filled vein, some polysynthetic twinning. XPL 4x magnification (D) Hydrothermal vein lined with microcrystalline quartz filled with dolomite and anhydrite. XPL 4x magnification.

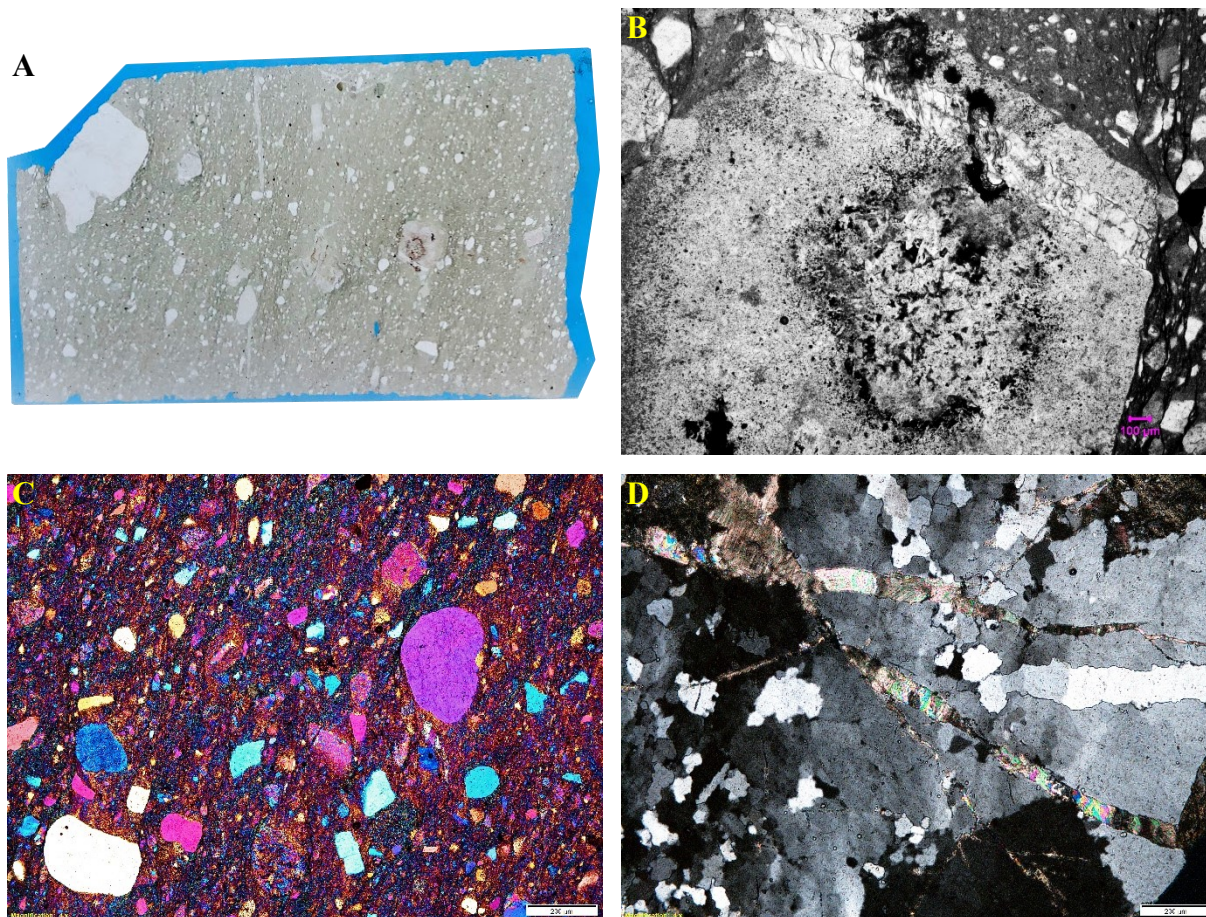
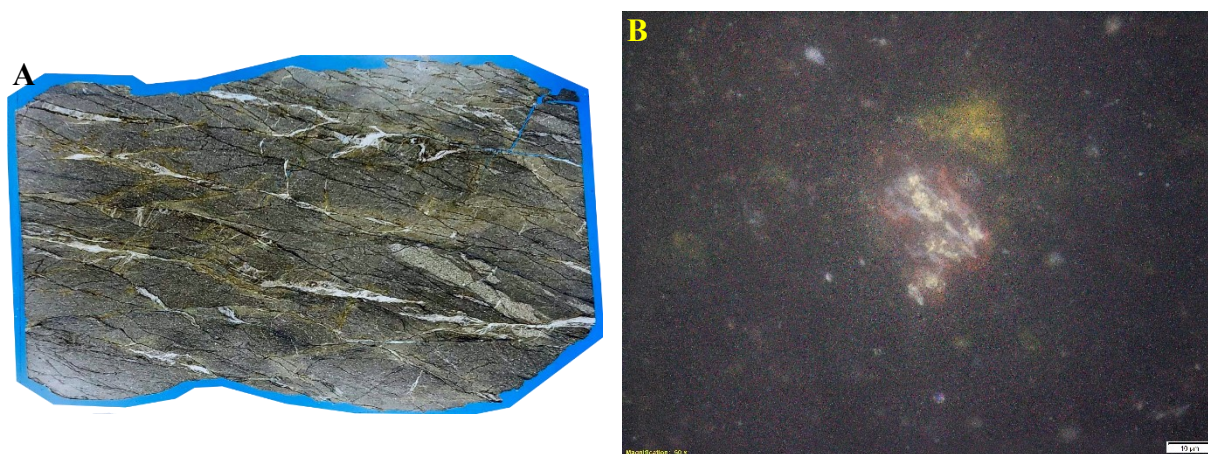


Figure 64. Sample 5b Doushantuo (A) Photo of the entire thin section, transmitted light (B) Chert nodule at center right in A contains a tubular metazoan microfossil(?) with diameter = $155\mu\text{m}$, the structure is made up of segments with a groove running down its length. This groove could be a longitudinal ridge as seen in tubular metazoans of the genus *Crassitubus* (Liu et al., 2008), the center of an antiaxial vein, or some diagenetic feature. PPL 4x magnification (C) Poorly sorted rounded quartz grains in fine-grained cement. XPL with sensitive tint plate 4x magnification (D) Quartz cement with anhydrite-filled cracks. XPL 4x magnification.



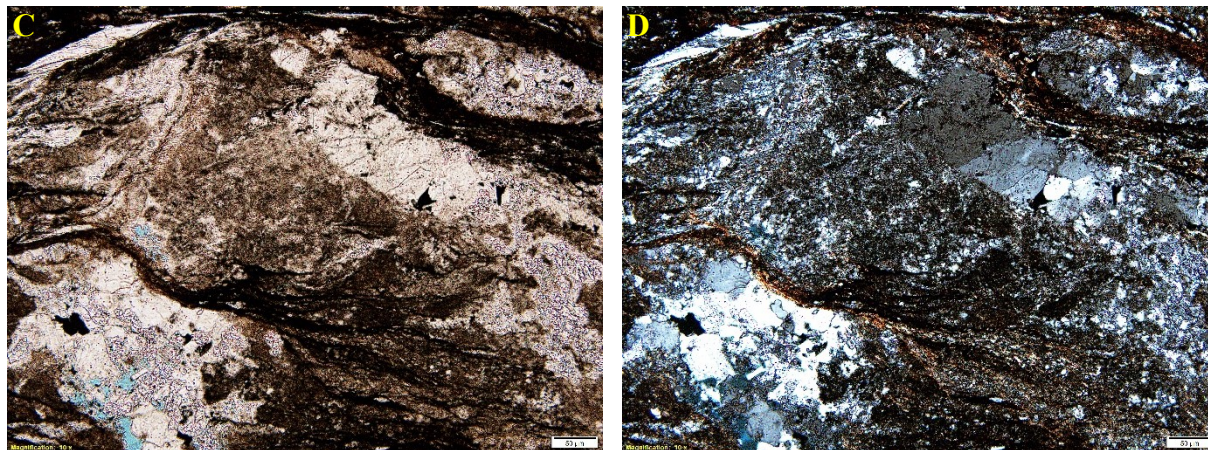


Figure 65. Sample 5c Doushantuo (A) Photo of the entire thin section, transmitted light (B) Oxidized sphalerite with pyrite inclusions, RL 50x magnification (C) Quartz with mica-rich interlayers; ghost thrombolitic texture (center, upper left). PPL 10x magnification (D) Quartz with mica-rich interlayers. XPL 10x magnification.

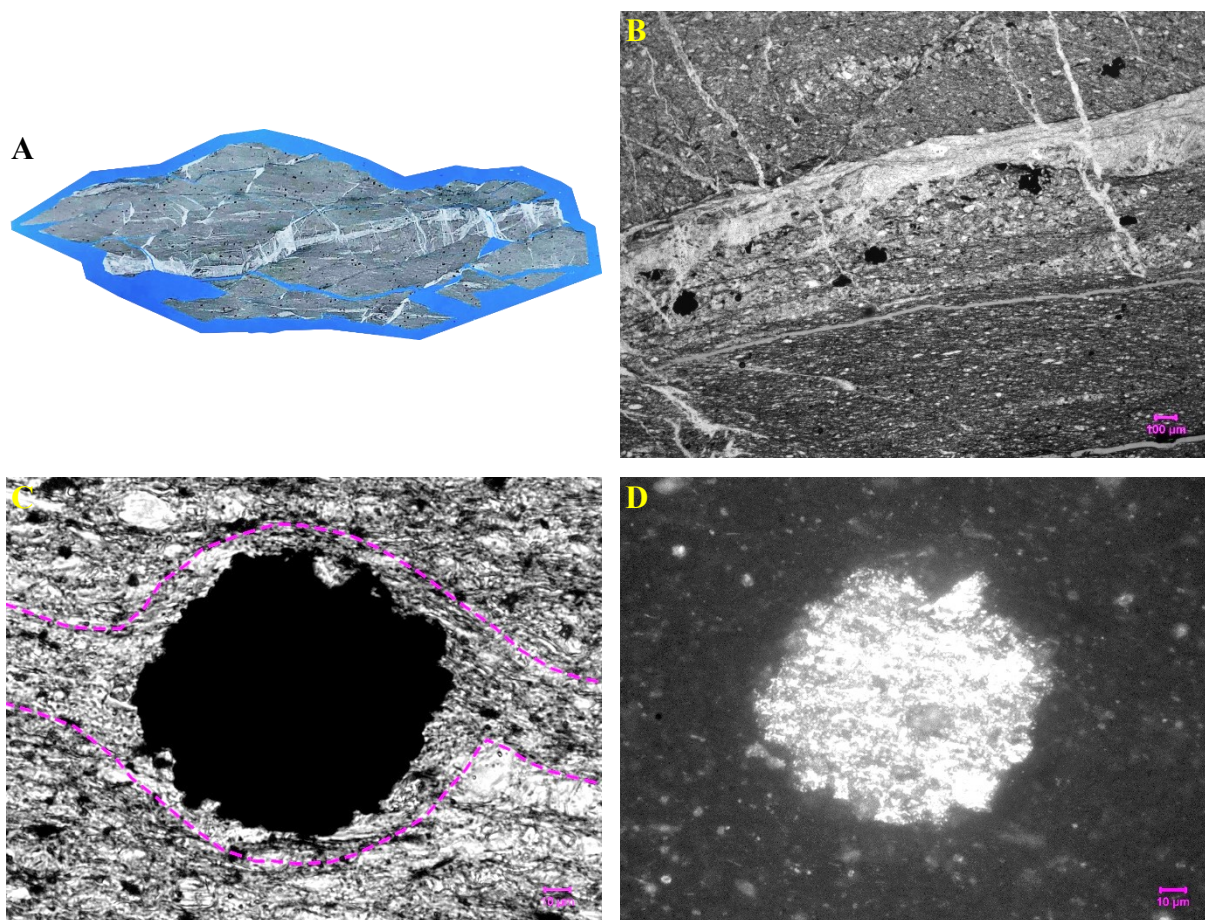


Figure 66. Sample 6a Doushantuo (A) Photo of the entire thin section, transmitted light (B) Banded shale with parallel and perpendicular veins and pyrite nodules. PPL 4x magnification (C) Pyrite porphyroblast with δ -type tails (pink dashed line). PPL 50x magnification (D) Pyrite RL 50x magnification.

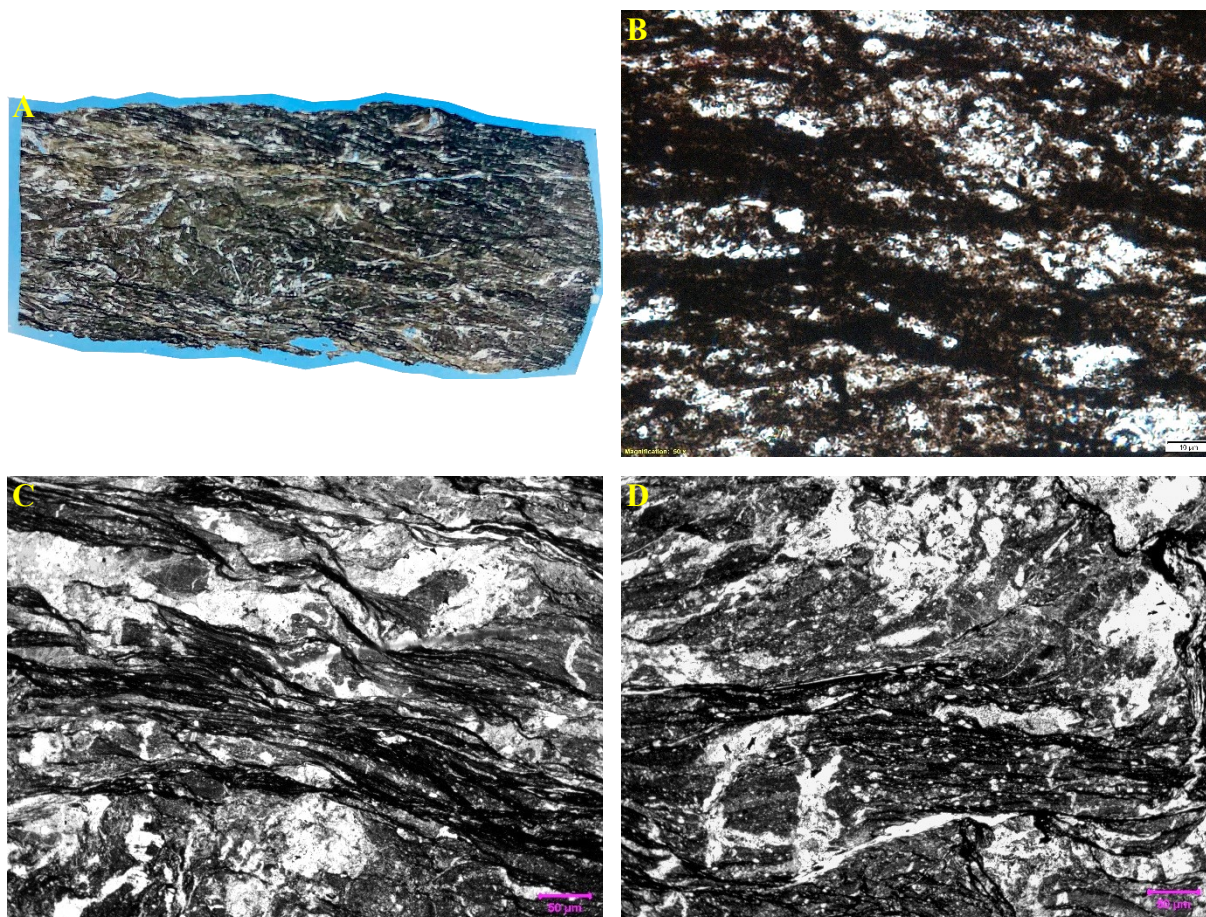
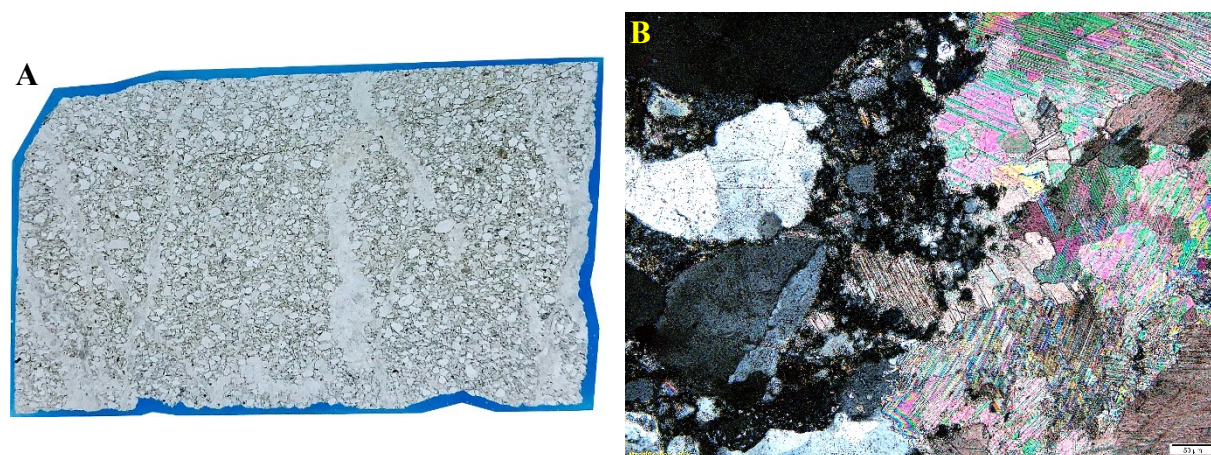


Figure 67. Sample 7a Doushantuo (A) Photo of the entire thin section, transmitted light (B) Foliated dolostone PPL 50x magnification (C) Foliated dolostone with organic clasts. PPL 20x magnification (D) Stromatolite showing symsedimentary cracking (bottom left) surrounded by foliated dolomite PPL 20x magnification.



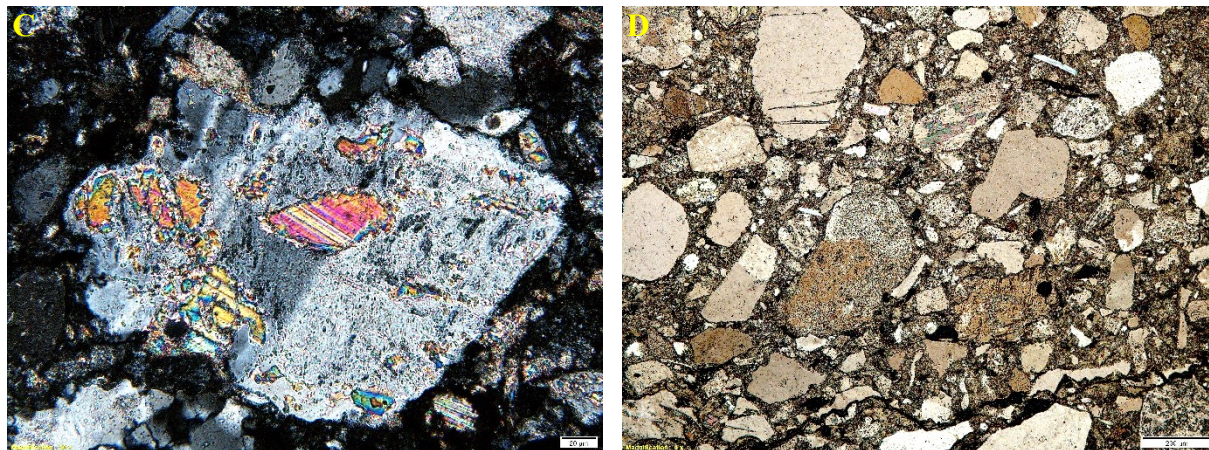


Figure 68. Sample 8a Doushantuo (A) Photo of entire thin section, transmitted light (B) Gypsum (notice cleavage on large crystal) and anhydrite. XPL 10x magnification (C) Anhydrite partially hydrated to gypsum (or vice-versa). XPL 20x magnification (D) Subangular grains. XPL 10x magnification.

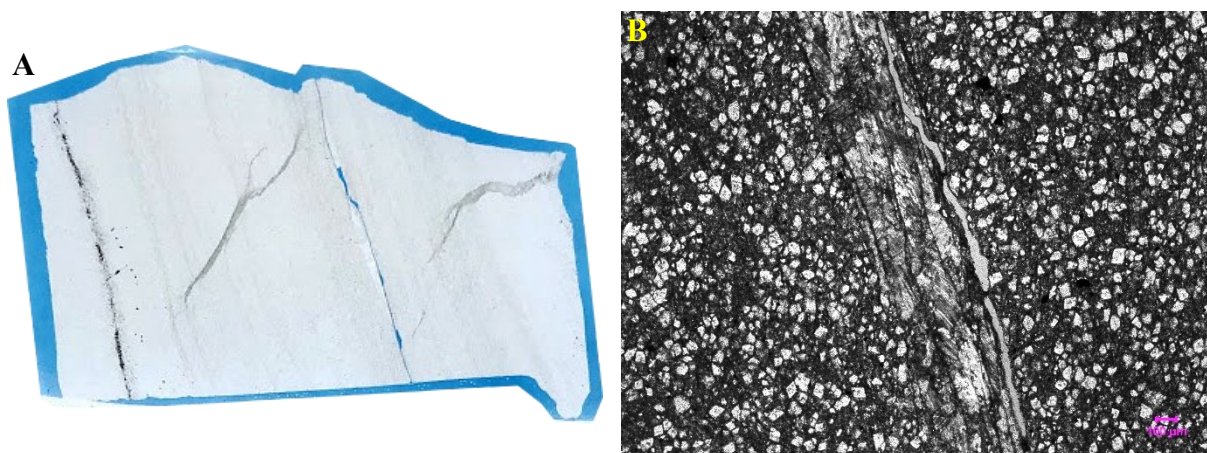
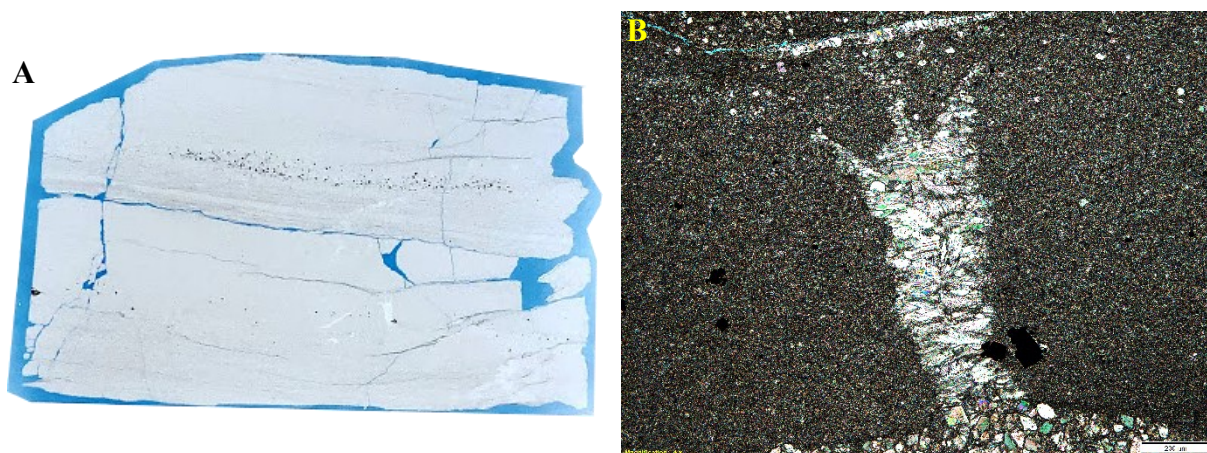


Figure 69. Sample 9a Dengying (A) Photo of entire thin section, transmitted light (B) dolomite marlstone with vein of "chevron" gypsum PPL 4x magnification.



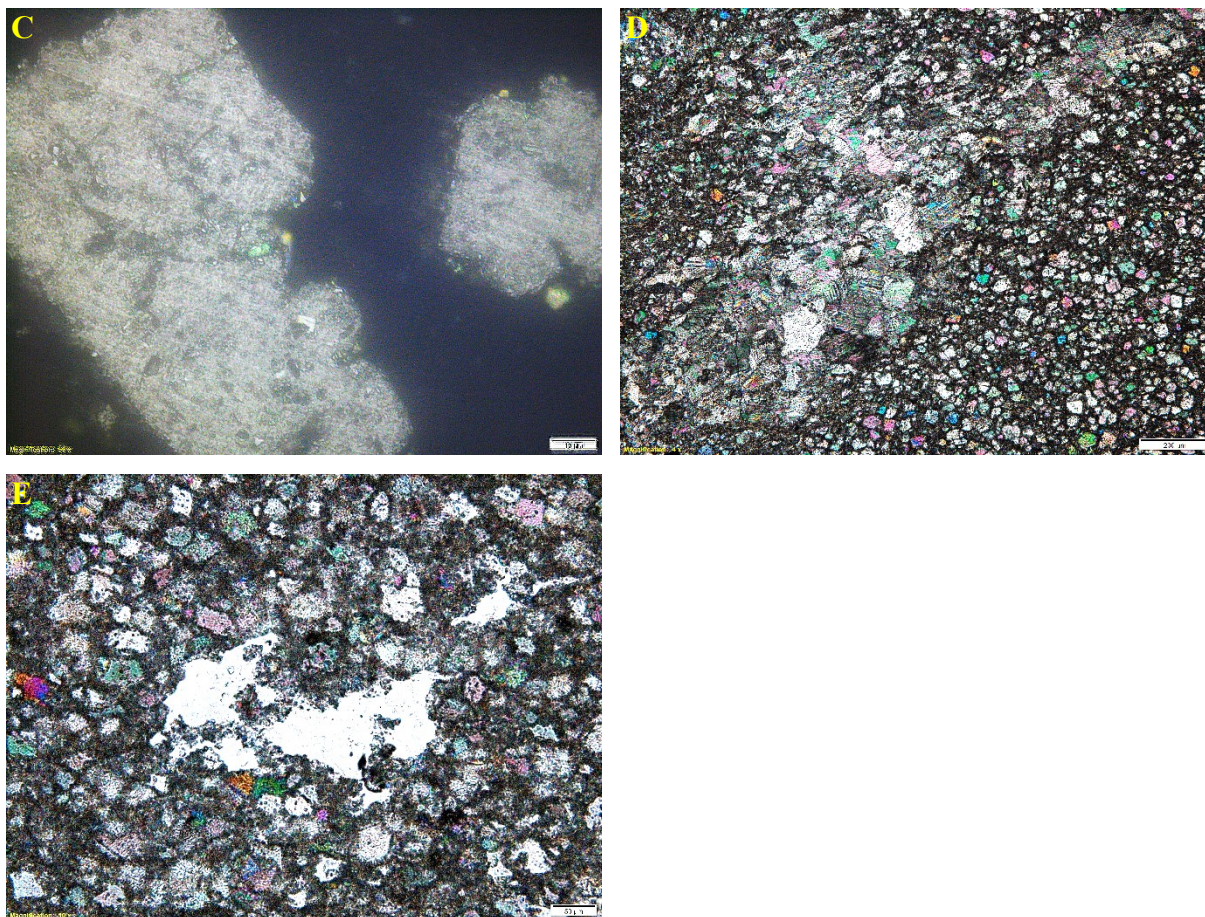


Figure 70. Sample 9b Dengying (A) Photo of the entire thin section, transmitted light (B) Hydrothermal vein. XPL 4x magnification (C) Galena with other sulfide minerals, RL 50x magnification (D) dolomite rhomb mosaic with coarse cement XPL 4x magnification (E) Amorphous silica. XPL 10x magnification.

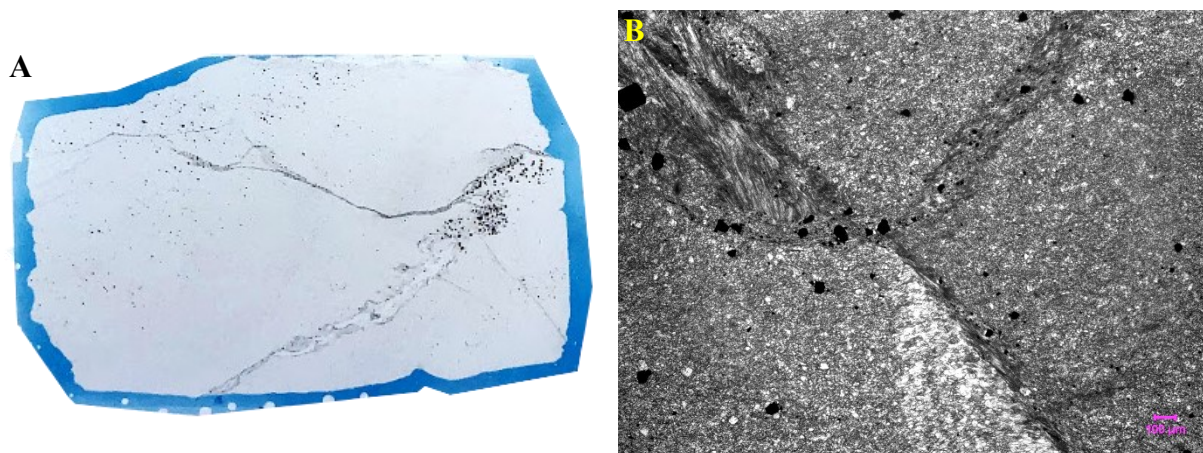


Figure 71. Sample 9c Dengying (A) Photo of the entire thin section, transmitted light (B) intersecting deformation bands. PPL 4x magnification.

Doushantuo, Daba Mountain thrust belt, (108°46'E, 31°56'N), outcrop

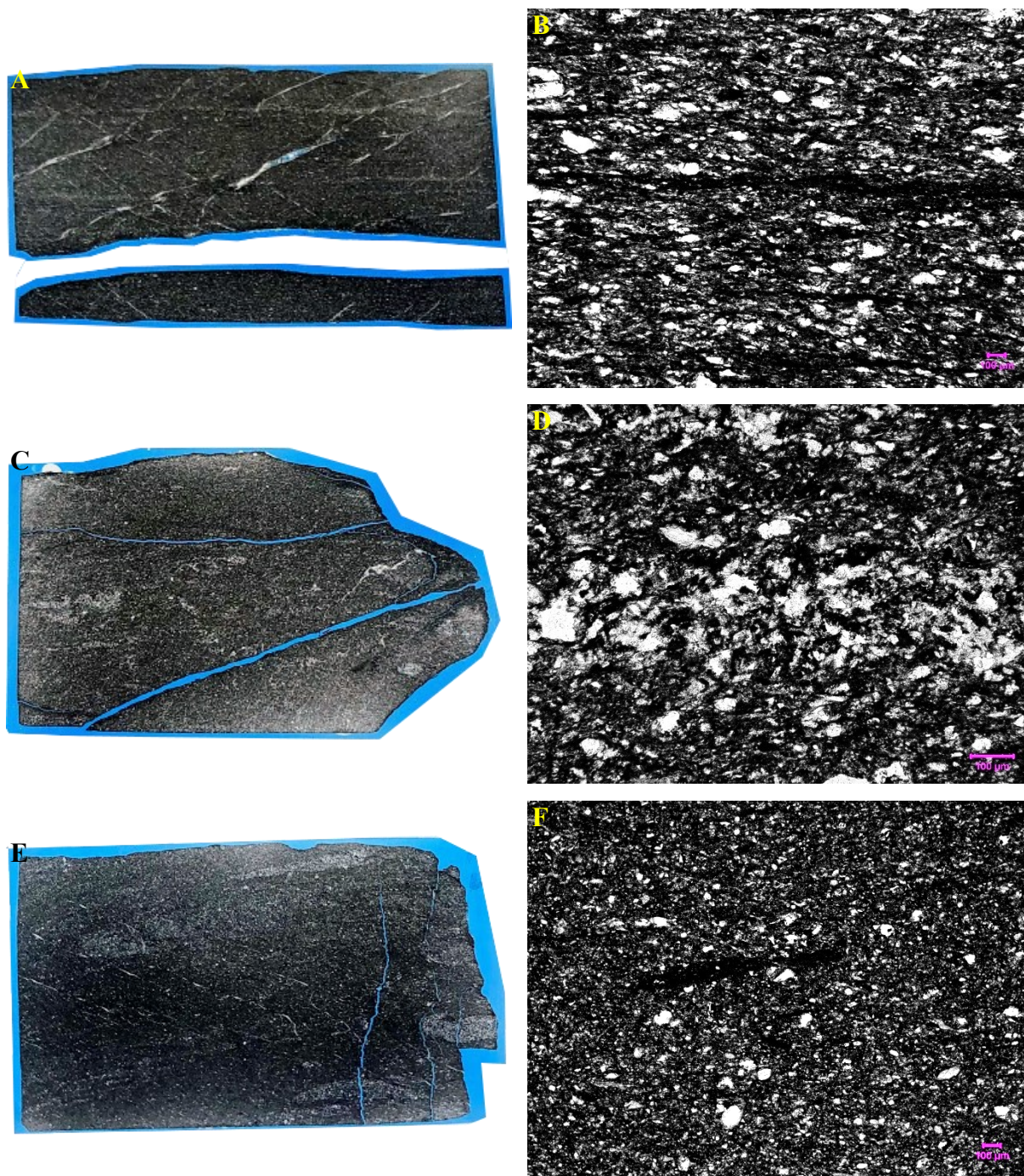


Figure 72. Sample 10(a-c) (A) A photo of thin section 10a, laminated black shale , transmitted light (B) Organic laminations in 10a. PPL 4x magnification (C) A photo of thin section 10b, laminated black shale, transmitted light (D) Organic lamination in 10b. PPL 10x magnification (E) A photo of thin section 10c, laminated black shale, transmitted light (F) Organic clast in 10c. PPL 4x magnification.

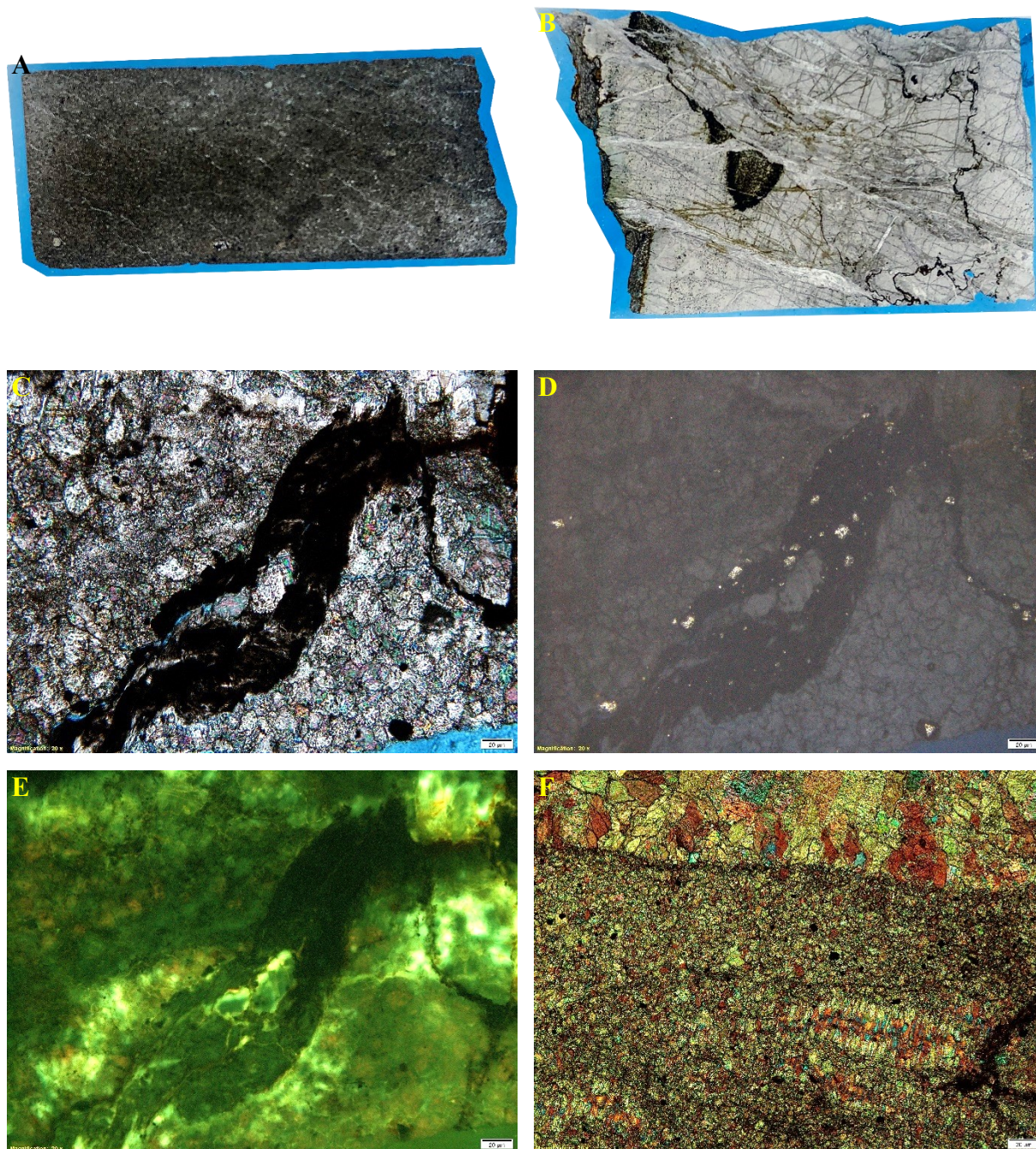


Figure 73. Sample 11(a-b) (A) Photo of thin section 11a , transmitted light (B) Photo of thin section 11b (C) Organic stylonite with pyrite, 11b. XPL 20x magnification (D) Same view as C in reflected light, revealing pyrite, 20x magnification (E) Same view as C and D in blue-violet light; the matrix fluoresces green and orange, 20x magnification (F) Microsparite with antiaxial vein (bottom right), sparry cement (top). XPL 20x magnification.

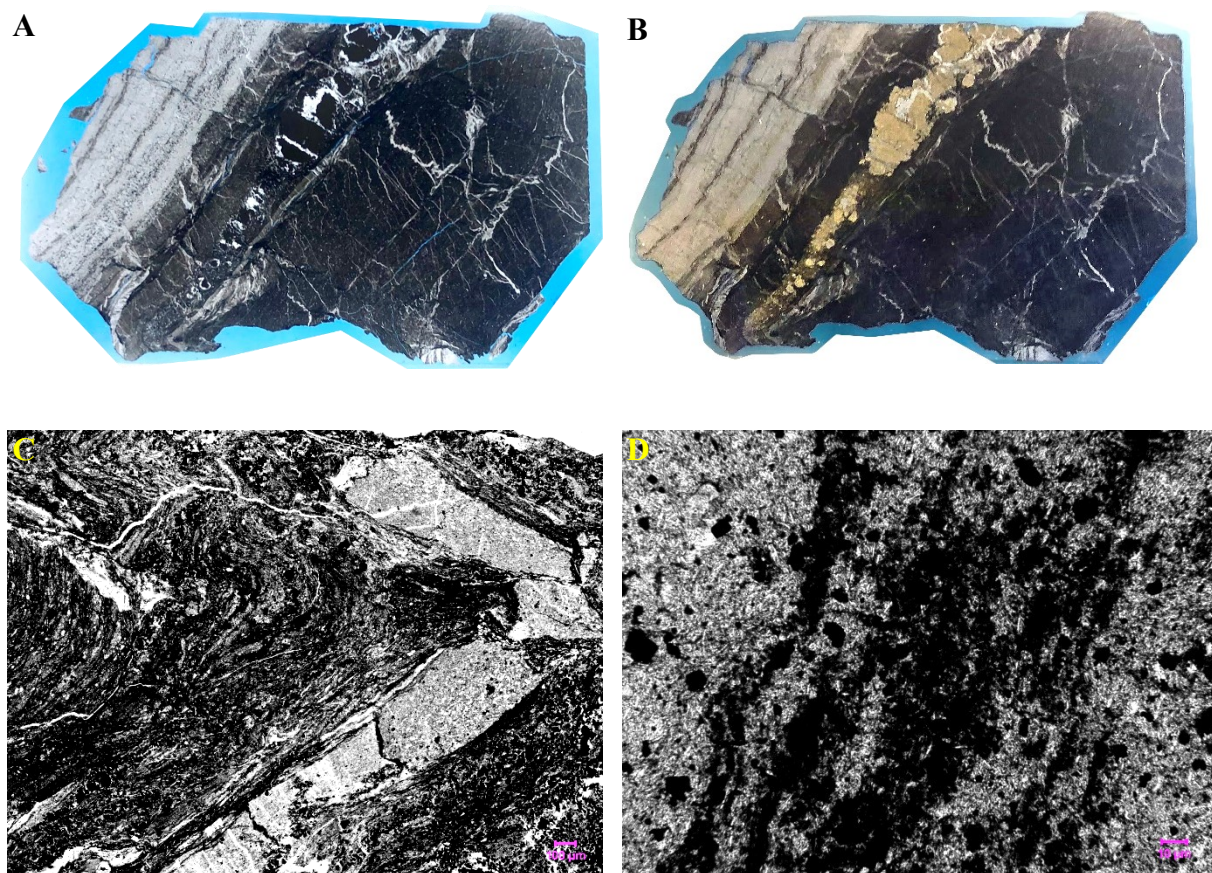
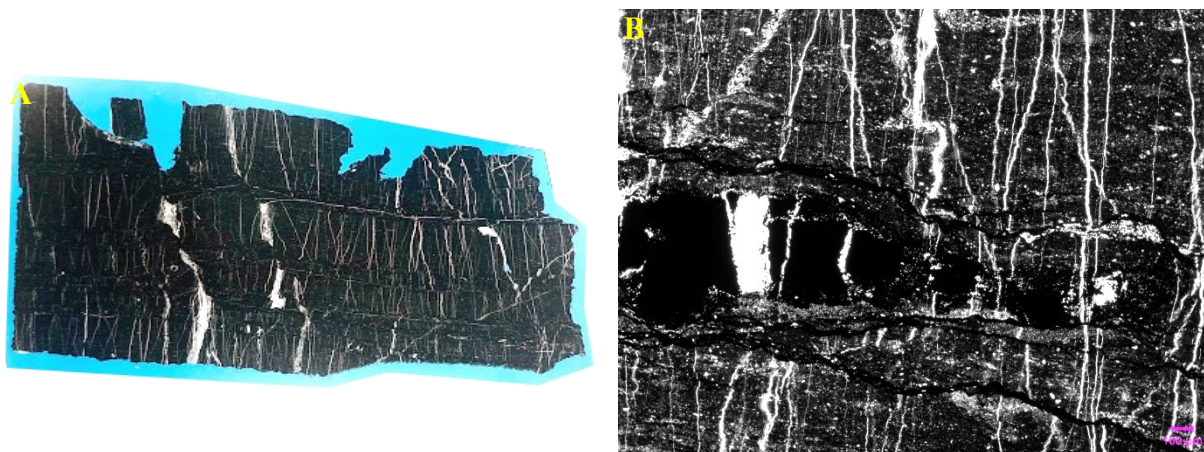


Figure 74. Sample 12a (A) Photo of thin section 12a, transmitted light (B) Photo of thin section 12a, reflected light, showing large pyrite deposit, likely from post-depositional thermal sulfate reduction (TSR) (C) Conical hybrid stromatolite, possibly *Conophyton garganicum* (Riding, 2011c). PPL 4x magnification (D) Biolamination with pyrite minerals. PPL 50x magnification.



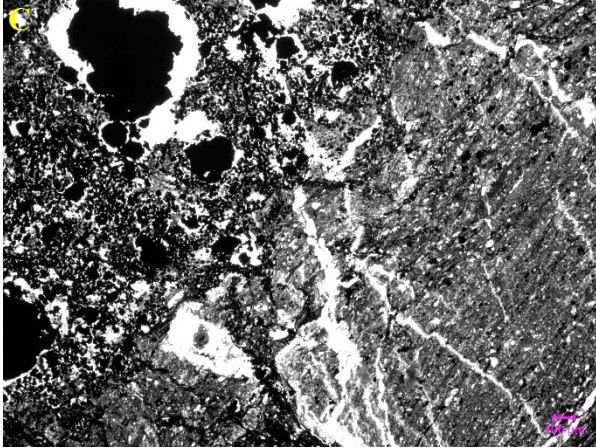


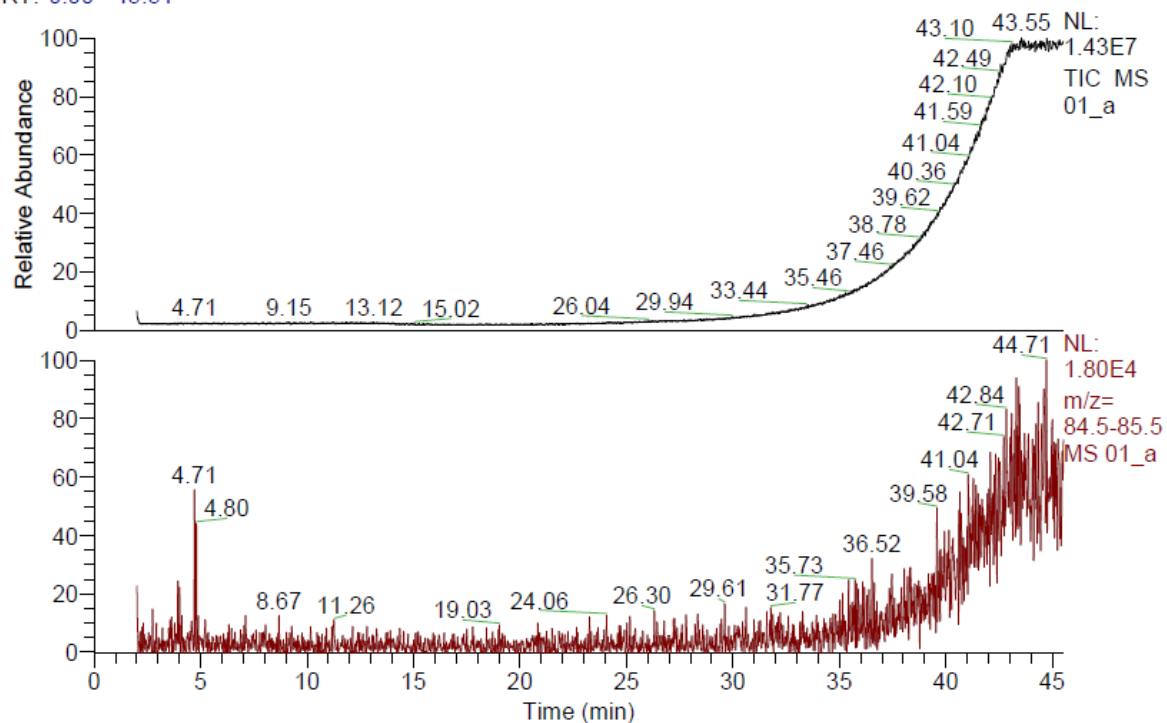
Figure 75. Sample 12b (A) Photo of the entire thin section, transmitted light (B) dolomitic shale with abundant cracks. PPL 4x magnification (C) Sulfide minerals and dessication cracks. PPL 4x magnification.

Appendix B: GC-MS data

C:\Xcalibur\data\2019\March\201_a
laminated black shale

3/3/2019 10:39:26 PM

RT: 0.00 - 45.51



01_a #130 RT: 4.71 AV: 1 NL: 1.03E4

T: + c Full ms [50.00-650.00]

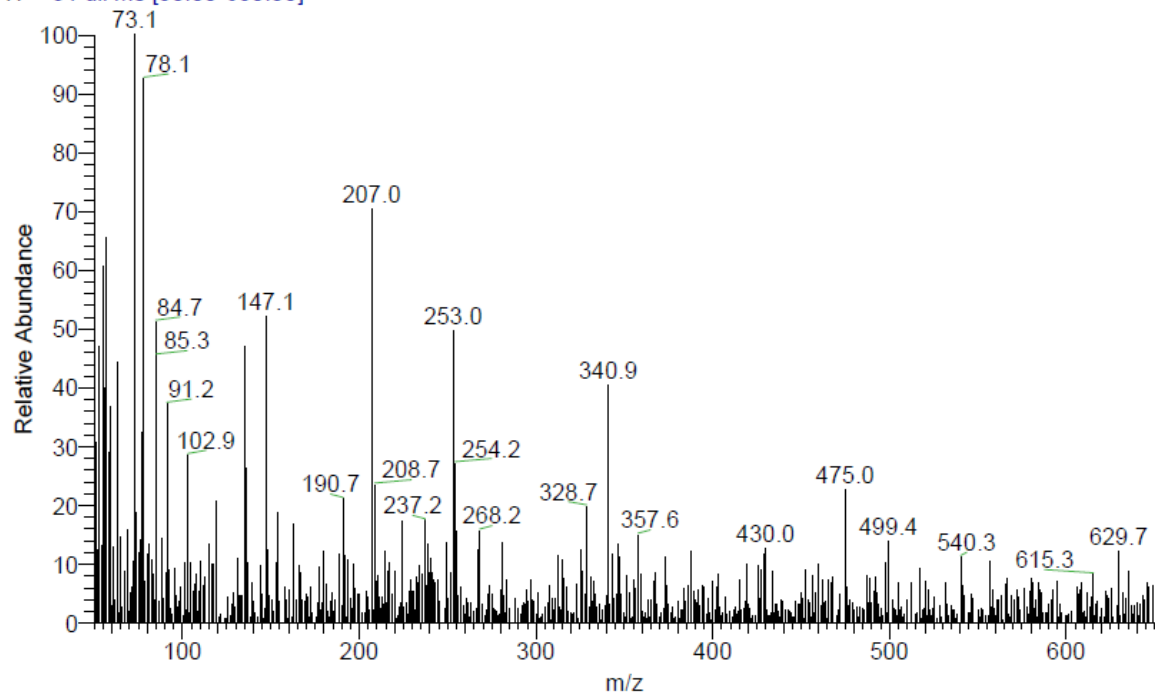


Figure 76. Chromatogram and n-alkane trace for Sample 1a (top); spectrogram of the peak at 4.71 min (bottom).

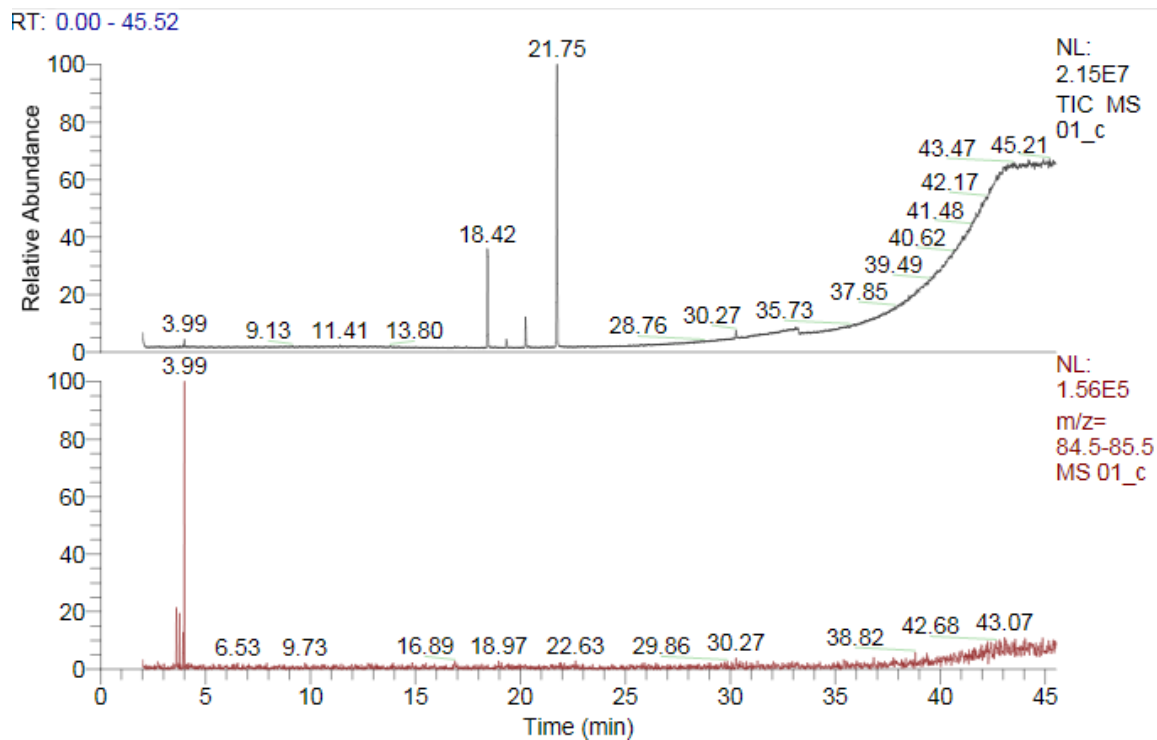


Figure 77. Chromatogram and n-alkane trace for Sample 1c

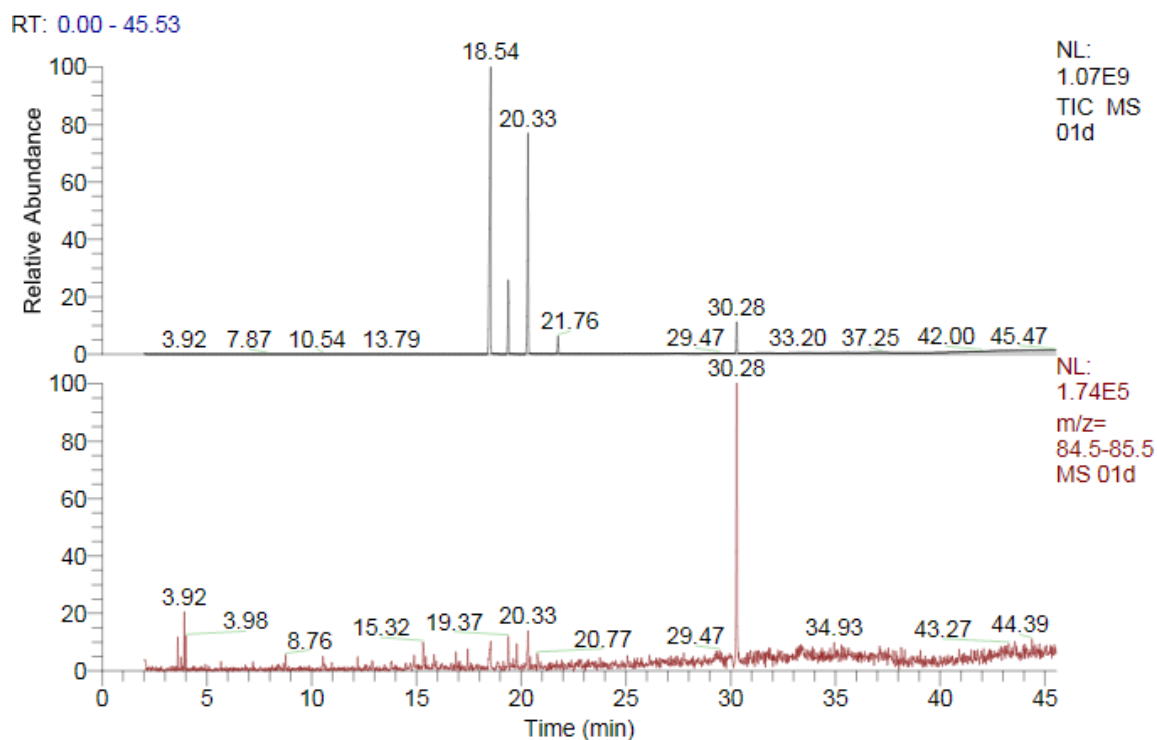


Figure 78. Chromatogram and n-alkane trace for Sample 1d

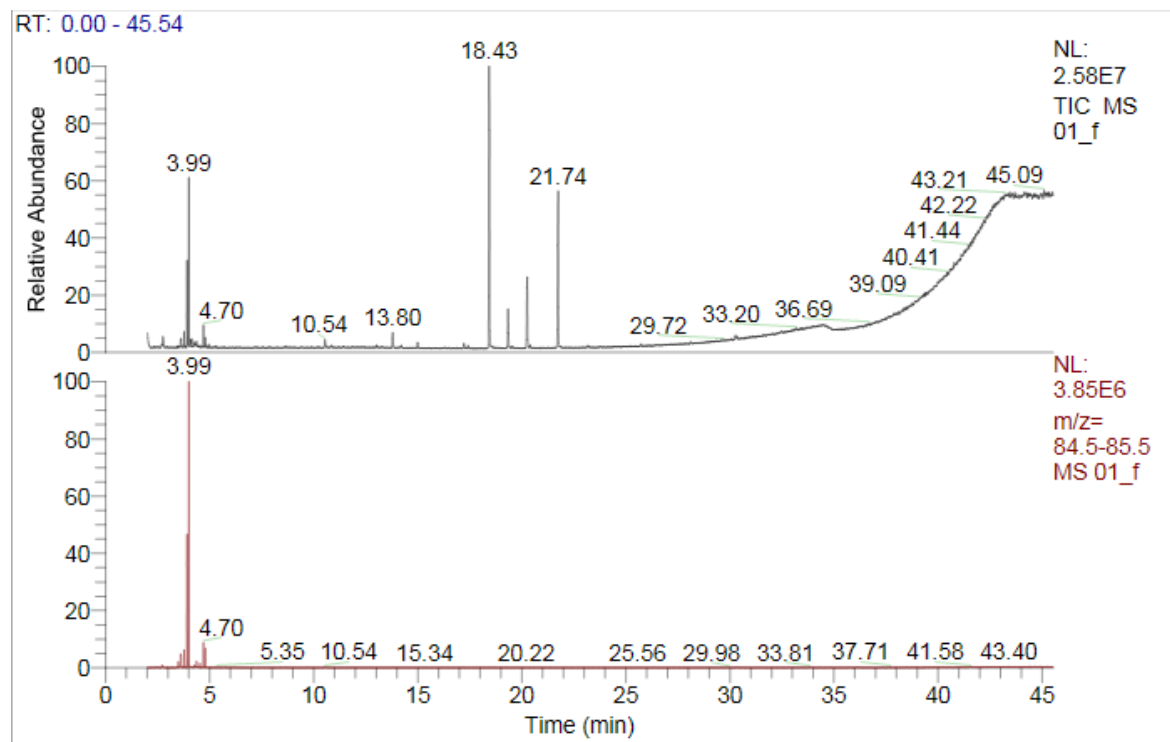
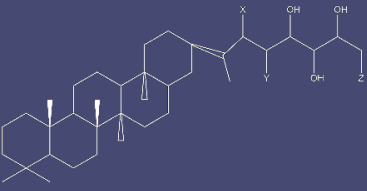
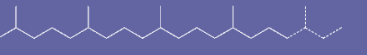
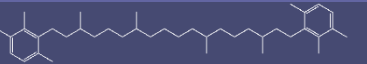
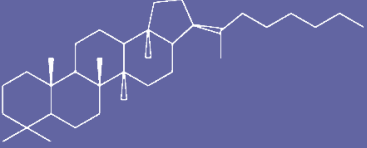
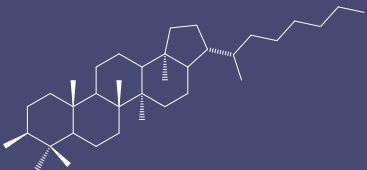
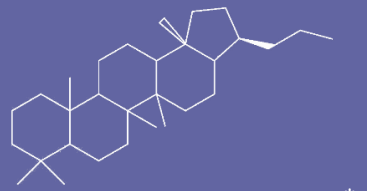
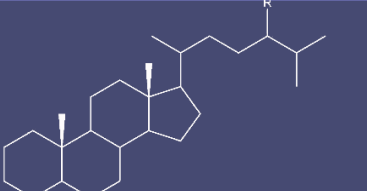

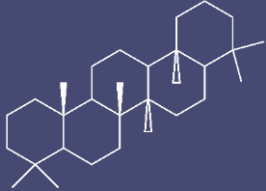
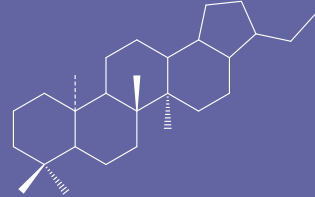
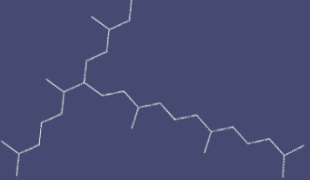
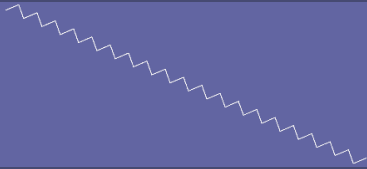
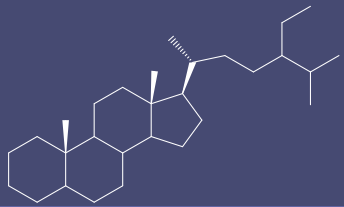

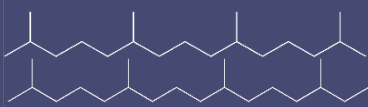
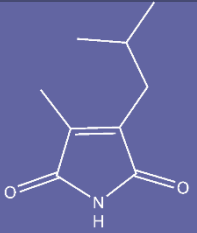




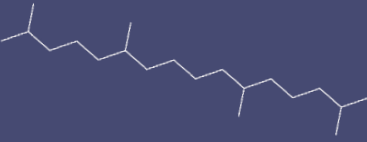
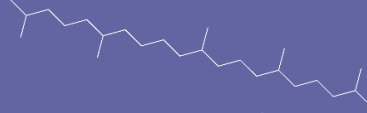
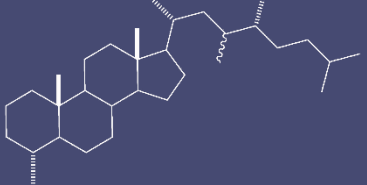

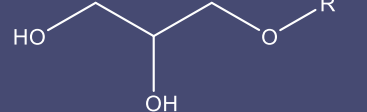
Figure 79. Chromatogram and n-Alkane trace for Sample 1f

Appendix C: Biomarker reference table

Table 7. Biomarkers identified in Neoproterozoic hydrocarbons; structure images were created in ChemDraw

Molecule(s)	Structure	Associated taxa/environment	Reference
Pentacyclic terpanes of the C ₃₁ to C ₃₅ extended hopane series		Bacteria	Ourisson and Albrecht (1992), Rohmer et al. (1984)
C ₂₁ – C ₂₅ regular isoprenoids		Halophilic archaea	Grice et al. (1998)
Isorenieratane		Phototrophic sulfur bacteria	Koopmans (1996)
Extended C ₃₂ – C ₃₆ 2 α -methyl hopanes		Cyanobacteria and prochlorophytes	Bisseret et al. (1985), Summons et al. (1999)
Extended 3 β -methyl hopanes		Aerobic methanotrophs	Gaines et al. (2009)
17a(H),21b(H)-Hopane C ₂₇ , C ₂₉ -C ₃₂		Cyanobacteria	Tosti et al. (2014), Li et al. (2006), Chen, Z. et al. (2017) *National center for Biotechnology information. PubChem compound database; CID=6431253
Steranes		Eukaryotes	Brocks & Summons (2003), Li et al. (2006), Chen (2017)
24 – isopropylcholestane		Demosponges (definitive in pre-Silurian)	Gold et al. 2016

Gamacerane		Anoxia and/or hypersaline environment	Grice et al. (1998), Li et al. (2006)
28, 30 – bisnorhopane (BNH) and 25, 28, 30 – trinorhopane (TNH)		Anoxia	Summons & Walter (1990), Peters et al. (1993)
C₂₀, C₂₅, and C₃₀ highly branched isoprenoid (HBI) hydrocarbons		Diatoms and photosynthetic algae	Sinnenghe Damsté et al. (1999a), Volkman et al. (1994), Belt et al. (2000), Rowland et al. (2001)
C₄₀-Alkane		Chlorophytes, marine eustigmatophytes	Allard et al. (2002) and Killips et al. (2000)
24 – ethylsterane		Green algae	Briggs & Summons, 2014
Monomethylalkanes (MMA) and dimethylalkanes (DMA)		Cyanobacteria in hypersaline and hydrothermal environments	Dembitsky et al. (2001), Kenig et al. (1995), Shiea et al. (1990)
Pristane (Pr) and Phytane (Ph)		Cyanobacteria, algae, phototrophic bacteria	Peters et al. (1993), Tosti (2014), Li et al. (2006), Chen, Z. et al. (2017)
3-isobutyl-4-methyl maleimide		Green sulfur bacteria	Grice (1996)
Okenane		Purple sulfur bacteria	Gaines et al. (2009)
Squalane		Archaea	Grice et al. (1998)

Crocetane		Anaerobic methane-oxidizing Archaea	Bian et al. (2001) and Thiel et al. (1999)
PMI (2,6,15,19-pentamethyleicosane)		Methanogenic and methanotrophic archaea	Elvert et al. (1999), Schouten et al. (1997), and Thiel et al. (1999)
Dinosterane		Dinoflagellates	Summons & Walter (1990)
Iso- and anteiso-branched fatty acids (C₁₅ & C₁₇)		Sulfate-reducing bacteria (not definitive)	Tosti et al. (2014), Heindel et al. (2010, 2012)
Mono-O-alkylglycerol ethers (MAGEs)		Sulfate-reducing bacteria (not definitive)	Heindel et al. (2010, 2012); Gaines et al. (2009)

Appendix D: Supplemental geochemical data statistics

Table 8. Statistic breakdown of T_{max} , Oxygen Index (OI), S1, S2, S3, and Free Oil by outcrop site.

T_{max}	dn MCS	do DBS-1	dn DBS-1	do site 3	All dn	All do	All
Mean	385	346	426	321	393	333	364
Median	418	335	428	316	419	320	340
Stdev	52	44	8	16	49	34	52

OI	dn MCS	do DBS-1	dn DBS-1	do site 3	All dn	All do	All
Mean	74	89	156	170	90	129	109
Median	27	94	152	13	84	70	84
Stdev	80	35	56	363	82	251	182

S1	dn MCS	do DBS-1	dn DBS-1	do site 3	All dn	All do	All
Mean	0.11	0.06	0.06	0.07	0.10	0.06	0.08
Median	0.11	0.05	0.06	0.07	0.06	0.06	0.06
Stdev	0.07	0.02	0.01	0.03	0.06	0.03	0.05

S2	dn MCS	do DBS-1	dn DBS-1	do site 3	All dn	All do	All
Mean	0.05	0.02	0.06	0.00	0.05	0.01	0.03
Median	0.05	0.01	0.06	0.00	0.06	0.01	0.02
Stdev	0.04	0.03	0.02	0.01	0.04	0.02	0.03

S3	dn MCS	do DBS-1	dn DBS-1	do site 3	All dn	All do	All
Mean	0.20	0.38	0.19	0.55	0.20	0.47	0.33
Median	0.19	0.28	0.18	0.15	0.19	0.24	0.19
Stdev	0.03	0.36	0.02	0.77	0.03	0.58	0.42

Free Oil	dn MCS	do DBS-1	dn DBS-1	do site 3	All dn	All do	All
Mean	19	19	45	10	24	15	20
Median	9	17	51	5	16	13	13
Stdev	15	12	10	12	18	12	16

Appendix D: Comparison of biomarker analysis methods

Table 9. Hydrocarbon extraction and other methods used in other studies on the Dengying Formation, compared to Seiden, 2020. "Conc." refers to the ratio of rock powder to solvent in grams per milliliter.

	Conc.	Solvent	extraction method	Other methods
Seiden, 2020	3 : 5 (g/ml)	DCM/Methanol 9:1 (v/v)	Microwave-assisted (35 min)	n/a
Duda et al., 2014	99 : 100 (g/ml)	DCM, DCM/hexane 1:1 (v/v), hexane	Ultrasonication (15 min)	decalcification with HCl; HyPy; desulfurization with copper
Chen et al., 2017	n.d.	DCM/Methanol 93:7 (v/v)	Soxhlet (24hrs)	Liquid chromatography on silica gel and alumina using hexane/DCM 1:1 (v/v)
Li et al., 2006	3 : 5 (g/ml)	DCM/Methanol 83:17 (v/v)	72hrs @ 50°C	desulfurization with copper; deasphaltation with petroleum ether; column chromatography on silica gel and aluminum 9:1 (v/v)

Table 10. GCMS instrumentation used for analysis of hydrocarbons in other studies on the Dengying Formation, compared to Seiden, 2020.

	GC	Capillary column	MS
Seiden, 2020	ThermoFinnigan Trace GC-DSQ	fused silica, 30 m x 0.25 mm i.d. x 0.25 µm	ThermoFinnigan Trace GC-DSQ
Duda et al., 2014	Varian CP-3800 GC	fused silica, 30m x 0.32mm i.d. x 0.25 µm film thickness	Varian 1200L triple quadrupole MS
Chen et al., 2017	Agilent 6890 GC	methyl silicone DB-1 column, 60m x 0.25mm i.d. x 0.25µm	Agilent 5975i MS
Li et al., 2006	n.d.	fused silica 60m x 0.32mm i.d. x0.25 µm film thickness	Finnigan Model SSQ- 710 MS